Status Report
KfK Contribution to the Development of

DEMO-relevant Test Blankets for NET/ITER
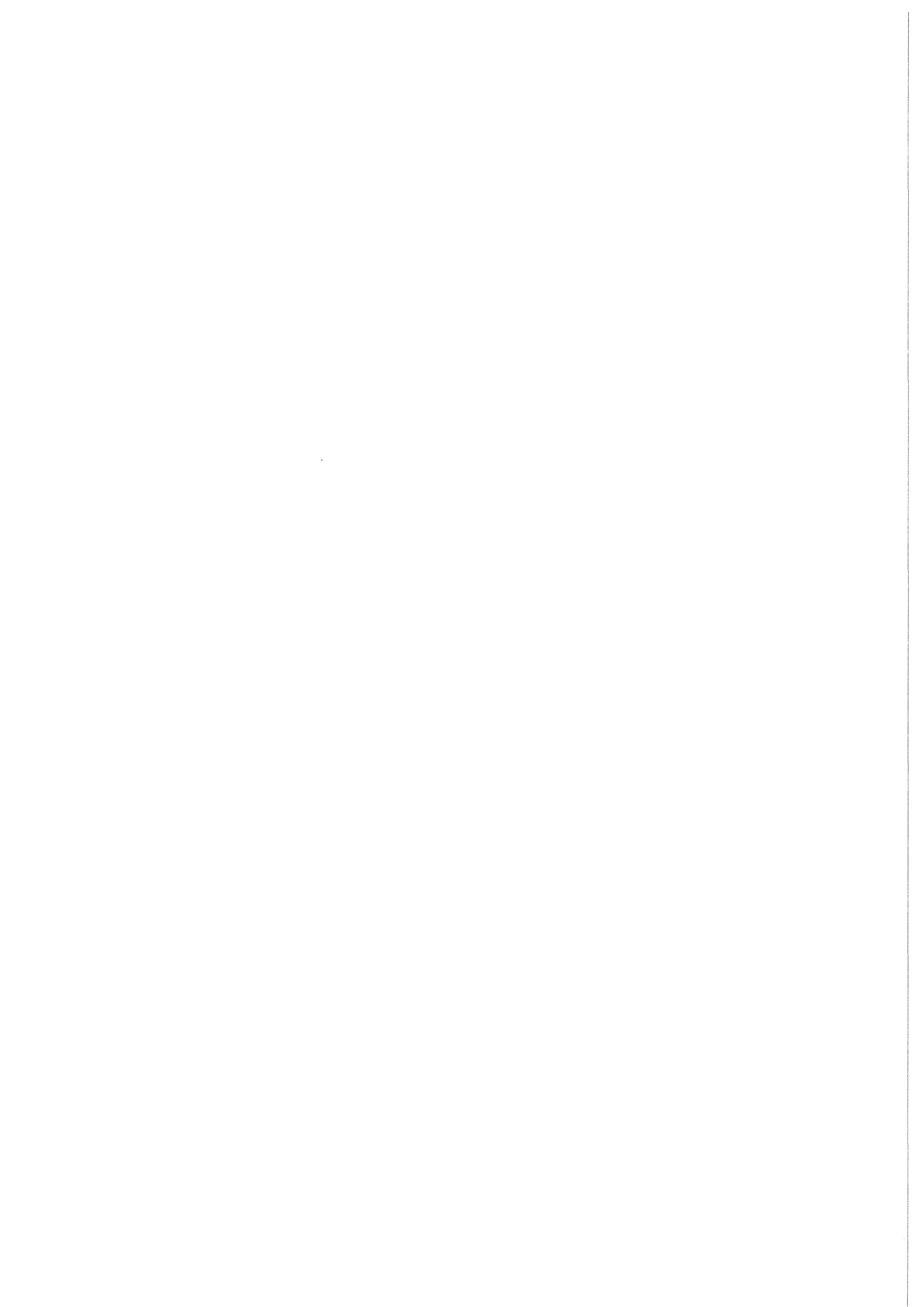
Part 2:
BOT Helium Cooled Solid Breeder Blanket
Volume 2:
Detailed Version

Compiled by: M. Dalle Donne

Contributors: C. Adelhelm, H. D. Baschek, L. V. Boccaccini,
E. Bogusch, E. Bojarsky, M. Dalle Donne, H. Deckers,
W. Dienst, L. Dörr, U. Fischer, W. Fritsch, H. Giese,
E. Günther, H. E. Häfner, P. Hofmann, F. Kappler,
R. Knitter, M. Küchle, U. von Möllendorf, P. Norajitra,
R.-D. Penzhorn, G. Reimann, H. Reiser, B. Schulz,
G. Schumacher, A. Schwenk-Ferrero, G. Sordon,
T. Tsukiyama, H. Wedemeyer, P. Weimar, H. Werle,
E. Wiegner, H. Zimmermann

Association KfK-Euratom
Projekt Kernfusion

Kernforschungszentrum Karlsruhe

KERNFORSCHUNGSZENTRUM KARLSRUHE

Association KfK-EURATOM
Projekt Kernfusion

KfK 4929

Status Report
KfK Contribution to the Development of
DEMO-relevant Test Blankets for NET / ITER
Part 2: BOT Helium Cooled Solid Breeder Blanket
Volume 2: Detailed Version

Compiled by: M. Dalle Donne
Contributors: C. Adelhelm, H.D. Baschek*, L.V. Boccaccini, E. Bogusch*,
E. Bojarsky, M. Dalle Donne, H. Deckers, W. Dienst, L. Dörr, U. Fischer,
W. Fritsch*, H. Giese, E. Günther, H.E. Häfner, P. Hofmann, F. Kappler,
R. Knitter, M. Küchle, U. von Möllendorf, P. Norajitra, R.-D. Penzhorn,
G. Reimann, H. Reiser, B. Schulz, G. Schumacher, A. Schwenk-Ferrero,
G. Sordon, T. Tsukiyama, H. Wedemeyer, P. Weimar, H. Werle,
E. Wiegner, H. Zimmermann

*Interatom GmbH, 5060 Bergisch Gladbach

Kernforschungszentrum Karlsruhe GmbH, Karlsruhe

Status Report
KfK Contribution to the Development of Demo-relevant Test Blankets for NET / ITER
Part 2: BOT Helium Cooled Solid Breeder Blanket
Volume 2: Detailed Version

Abstract
The BOT (Breeder Outside Tube) Helium Cooled Solid Breeder Blanket for a fusion Demo reactor and the status of the R & D program is presented. This is the KfK contribution to the European Program for the Demo relevant test blankets to be irradiated in NET / ITER. Volume 1 (KfK 4928) contains the summary, volume 2 (KfK 4929) a more detailed version of the report.

In both volumes are described the reasons for the selected design, the reference blanket design for the Demo reactor, the design of the test blanket including the ancillary systems together with the present status of the relative R & D program in the fields of neutronic and thermohydraulic calculations, of the electromagnetic forces caused by disruptions, of the development and irradiation of the ceramic breeder material, of the tritium release and recovery, and of the technological investigations. An outlook is given on the required R & D program for the BOT Helium Cooled Solid Breeder Blanket prior to tests in NET / ITER and the proposed test program in NET / ITER.

"This work has been performed in the framework of the Nuclear Fusion Project of the Kernforschungszentrum Karlsruhe and is supported by the European Communities within the European Fusion Technology Program."

Status Bericht
KfK Beitrag zur Entwicklung der Demo-relevanten Test Blankets für NET / ITER
Teil 2: BOT Heliumgekühltes Feststoff-Brutblanket
Band 2: Detaillierter Bericht

Zusammenfassung
Es wird ein heliumgekühltes Feststoffbrutblanket für einen Demo-Fusionsreaktor mit Brutstoff außerhalb von Kühlrohren (BOT) beschrieben und der Stand der F und E Arbeiten wird vorgestellt. Dies ist der Beitrag des KfK zum Europäischen Entwicklungsprogramm für die Demo-relevanten Testblankets, die in NET / ITER bestrahlt werden sollen. Band 1 (KfK 4928) enthält die Zusammenfassung und Band 2 (KfK 4929) den detaillierten Bericht.

In den beiden Berichten werden die Gründe, die zum gewählten Entwurf geführt haben, beschrieben. Es werden der Referenzentwurf für das Demo-Reaktor-blanket und der Entwurf für ein Testblanket in NET / ITER mit den dazugehörigen externen Kreisläufen vorgestellt. Der Stand der Forschungs- und Entwicklungsarbeiten bezüglich: Neutronen- und Thermohydraulikrechnungen, Rechnungen der elektromagnetischen Kräfte verursacht durch Plasmazusammenbrüche, Entwicklung und Bestrahlung der keramischen Brutstoffe, Tritiumfreisetzung und -gewinnung sowie technologische Untersuchungen werden aufgezeigt.

Es wird ein Ausblick gegeben auf die noch vor dem NET / ITER Test notwendigen F. & E.-Arbeiten für das BOT Heliumgekühlte Feststoff-Brutblanket und das zugehörige Testprogramm, das in NET/ ITER durchgeführt werden soll.

"Die vorliegende Arbeit wurde im Rahmen des Projekts Kernfusion des Kernforschungszentrums Karlsruhe durchgeführt und ist ein von den Europäischen Gemeinschaften geförderter Beitrag im Rahmen des Fusionstechnologieprogramms."

TABLE OF CONTENTS

1. PREVIOUS STUDIES AND REASONS FOR THE SELECTED DESIGN (M. Dalle Donne)

1.1 Introduction

In the frame of the European Technology Programm (EFTP) the Karlsruhe Nuclear Center (KfK) is performing design and related R. and D. work for the Breeder Out of Tube (BOT) Helium Cooled Solid Breeder Blanket (HCSBB) for the Demonstration Reactor (Demo).

Demo is the next step after NET / ITER. Its blanket should be Demo-relevant, i.e. it should demonstrate the capability of producing tritium in the blanket with a breeding ratio higher than one. Furthermore the blanket coolant temperature should be sufficiently high so that a plant efficiency of at least 30 % for the heat estracted from the blanket should be possible [1]. Beside the BOT-HCSBB three other Demo-relevant blanket types are being investigated within the EFTP frame: one is the Breeder Inside Tube (BIT)-HCSBB, the other two are with a liquid metal breeder (liquid metal or water cooled respectively). Common specifications for the Demo-reactor and the Demo-relevant blanket have been proposed by the European Test Blanket Advisory Group [1, 2]. Table 1.1 and Fig. 1.1 show the most important of these specifications. Coolant tubes for the outboard blanket should come from the top, while for the inboard blanket and the divertors the coolant tubes can come from the bottom as well. Blanket material can be placed also behind the divertors. In the neutronic calculations, ten ports, 3.4 m high and 1 m wide, placed in the equatorial region of the central outboard blanket segment should be assumed. Although twin loops are presently favoured for passive plasma stabilization in ITER, the same saddle loops proposed so far for the NET-design were specified for the Demo blanket [1, 2].

The main objective of the European R. and D. work for the Demo-relevant blankets is to choose two blanket types (one with solid and the other with a liquid breeder) and prepare the related test modules to be irradiated in NET / ITER.

Testing in NET / ITER is very expensive. Space available for testing and test duration is relatively limited. A considerable amount of R. and D. work is required prior to testing in NET / ITER to reduce the risks of failures in NET / ITER and to make choices on the base of sound arguments.

The present report describes the design work performed at KfK in collaboration with Siemens-Interatom for the Breeder Out of Tube (BOT) Helium Cooled Solid Breeder Blanket for the Demonstration Reactor (Demo), and for the relative test modules to be irradiated in NET / ITER (Chapters 2 and 3). Chapter 4 gives a review of the R. and D. work performed at KfK so far to support the design and the design choices. Chapter 5 illustrates the remaining R. & D. program prior to the tests in NET / ITER. Finally Chapter 6 shows the proposed test program for the test modules in NET / ITER.

1.2 Previous Studies

The first helium cooled solid breeder blanket investigated at the Karlsruhe Nuclear Research Center (KfK) was with a lead multiplier integral with the first wall and toroidally arranged pressure tubes containing the breeder material. Due to the low melting point of lead the first wall region had to be cooled by a separate helium circuit at low temperature [3].

Subsequently, a design with poloidally running pressure tubes containing the ceramic breeder material and the beryllium multiplier in the form of a pebble bed was investigated [4]. The resulting one-dimensional tritium breeding ratio (TBR) was 1.08 (based on 100 % torus surface coverage) which would imply a real tridimensional breeding ratio lower than one. Therefore, it was decided to investigate other blanket forms with higher breeder and multiplier amounts per unit volume. Indeed, the investigated poloidal solution was rather leaky for the neutrons, which was the main reason for the rather modest breeding ratio.

In 1988 the conceptual design of a blanket with a tridimensional TBR higher than one was published [5]. This design was based on the use of radial canisters containing the breeder material and the multiplier. However, this blanket was designed for NET, i.e. for a considerably lower neutron flux at the first wall (1 MW/m^2 against 2.2 MW/m^2 for the Demo blanket) and a lower neutron fluence (0.8 MWy/m^2 against 5 MWy/m^2 for the Demo blanket)

The here proposed design for the Demo blanket is similar to the canister design for NET. There are however differences, the main one is the use of a martensitic steel as a structural material (Manet) in place of the austenitic steel 316 L. Manet is able to withstand the high neutron fluence in the Demo blanket (70 d.p.a.) without swelling.

1.3 Reasons for the Selected Design

The present design is based on the following choices:

- the use of small lithium orthosilicate pebbles as breeder material

- the use of high pressure helium as coolant

- the use of beryllium as neutron multiplier

- the use of the martensitic steel Manet as structural material.

The combination ceramic breeder material and helium coolant was an early choice (1983 - 1984) of the European Fusion Technology Program (EFTP).

Ceramic materials have high melting points. They are not very chemically active and of course do not present MHD problems. The best known lithiated ceramics are lithium oxide

Li$_2$O or the ternary ceramics Li$_x$M$_y$O$_z$ (M = metal). These materials have been extensively used in some countries for tritium production in the frame of their military programmes. Tritium extraction from the ceramics by means of a helium purge gas flow has been extensively and successfully used. A further earlier decision within the EFTP was to concentrate on the ternary ceramics, because Li$_2$O is more chemically active, with possibly more compatibility problems with structural and breeder materials, and also because Li$_2$O tends to swell more when subjected to neutron irradiation [6]. Among the ternary lithiated ceramics, aluminates and silicates are the most actively studied so far, thus it was decided that CEA-ENEA would concentrate on aluminate investigations and KfK on the silicates. Recently both groups have started some activity on lithium metazirconate Li$_2$ZrO$_3$ as well. Namely on metazirconate pellets (CEA) or pebbles (KfK).

Early during the KfK ceramic breeder R. & D. program it was established that tritium release from orthosilicate was much faster than from metasilicate [7], lithium orthosilicate Li$_4$SiO$_4$ was therefore chosen as reference breeder material. This material however has a relatively low thermal conductivity and high thermal expansion coefficient and might break up due to excessive thermal stresses when irradiated at high power densities. This is confirmed by irradiation experiments at high burn-ups, which show that Li$_4$SiO$_4$ pellets break up in smaller pieces due to excessive thermal stresses [8]. Obviously the use of sufficiently small Li$_4$SiO$_4$ pebbles would avoid this problem and this is the solution which was chosen for the present design.

Helium is better suited than water as the coolant of a lithium ceramic blanket. Water reacts with lithiated ceramics producing lithium hydroxide, which has a relatively high vapor pressure. This could cause unduly high lithium transport due to the temperature gradients present in the blanket. Helium, on the contrary, is an inert gas and, as the experience with helium cooled fission reactors shows, can be kept extremely pure (total amount of impurities <1 ppm) even in large and complex circuits. Unlike water, helium can be kept at high temperatures without need to increase the pressure, thus the problem of keeping the minimum temperature in the breeder material above a certain level, to ensure low tritium inventories in the breeder, becomes much easier, as thermal insulating gaps between breeder and coolant are not required. A further advantage of helium is that leakages to the plasma chamber have much less severe consequences than water leakages.

The only two elements which in practice could be used as neutron multiplier are lead and beryllium. Due to the low melting point (327 °C), it is very difficult to keep lead in the solid state in a ceramic blanket: changes of phase during operation are practically unavoidable. For this reason beryllium is generally the preferred choice. This material has been extensively studied 25 - 35 years ago as a possible cladding material for fission reactors and it has been used as reflector in various material testing reactors. It is an excellent neutron multi-

plier. Its high melting point, high thermal conductivity and low specific weight are considerable advantages. There are however problems related to its behaviour under neutron irradiation.

Due to the high neutron fluence in the structural material expected in the Demo blanket ($\approx$ 70 dpa) an austenitic steel cannot be used as it would swell too much under irradiation. Within the European Fusion Technology Program the martensitic steel Manet has been chosen as the structural material. This steel is similar to the martensitic steels which are being investigated within the various fast reactor programs and promises to be able to withstand very large neutron fluences with very small amounts of swelling. The R. & D. work for Manet is part of a separate program within the EFTP, parallel to the blanket program and will not be discussed in the present report.

In summary the present design is based on the following principles:

a) The use of lithium orthosilicate (Li_4SiO_4) as breeder. This offers the advantage to have a fast tritium release and thus a low tritium inventory in the breeder material. Lithium orthosilicate is quite stable at high temperatures: in vacuum or dry pure helium the total lithium pressure above Li_4SiO_4 at 1120 °C is only 10^{-2} Pa. Of the considered lithiated ceramics, lithium orthosilicate, together with Li_2O, is the one which has the lower induced radioactivity after short (compared to aluminate) and very long (compared to aluminate and zirconate) times. This offers safety advantages (low after-heat) and makes the waste disposal easier. Finally, lithium orthosilicate has considerably more lithium per unit volume than lithium aluminate $LiAlO_2$ (a factor 2) and than lithium metazirconate Li_2ZrO_3 (a factor 1.5). This offers the advantage of having a proportionally smaller lithium burn-up for the same fluence.

b) The use of small Li_4SiO_4 pebbles. This avoids the thermal stress problem in the breeder material. With full or annular pellets, cracks, caused by thermal stresses and high burn-ups, are more likely, as pellets are necessarily of greater size. These cracks, if large enough, may cause uncontrolled and very high temperature increases in the ceramic, especially for the pieces which are displaced away from the tube walls. In case of a pebble bed, these large displacements are not possible and the deterioration of the thermal conductivity of the ceramic, likely at high burn-ups, has little effect on the thermal conductivity of the bed, as this is mainly controlled by the thermal conductivity of the helium purge gas. Furthermore, a bed of pebbles allows for a large volume for the flow of the purge helium gas. This reduces the tritium partial pressure in the purge gas and, consequently, the tritium losses from the purge flow system.

c) The use of a helium purge flow at a pressure below atmospheric: This of course reduces the amount and probability of tritium losses by leakage. Furthermore, as the tritium partial pressure in the purge gas in the blanket depends on the purge helium

volume flow and not on its density, the low pressure reduces the mass flow rate of the purge helium and thus the dimensions of the purge gas system.

d) <u>The use of the Breeder Out of Tube (BOT) solution:</u> The coolant helium gas at high pressure is contained inside tubes, the breeder material and the low pressure purge gas is placed outside the pressure tubes. This avoids the instability problems (tube collapsing) which could occur, in the case of higher pressure being outside the tubes (Breeder Inside Tube solution) especially in presence of thermal and / or irradiation creep. Furthermore the use of a BOT solution allows to use flat outer surfaces and thus to pack more breeder and multiplier in the limited space available in the blanket.

e) <u>Good temperature conditioning of the blanket components:</u> This requires that the first wall, where the highest heat flux and power density occur is cooled by the inlet helium. The blanket is cooled by the helium preheated in the first wall region, so that the minimum temperature of the breeder is 380 °C, which allows to have a very low tritium inventory in the breeder material. The beryllium temperature is kept as low as possible to reduce the beryllium swelling under irradiation. Beryllium and breeder are well mixed to increase the tritium breeding ratio.

f) <u>The use of relatively small radial canisters:</u> The coolant moves essentially in radial direction thus producing a more uniform temperature distribution in the blanket due to the large power density gradients in radial direction. The use of radial canisters allows a good filling with breeder and multiplier of the space available in the blanket region. The subdivision of the blanket in small modules reduces the thermal stresses and the stresses caused by the plasma disruptions, makes a precise construction easier and gives the possibility of making significant tests starting from the smallest submodules.

g) <u>The use of a redundant convective cooling system:</u> The use of two completely separate coolant systems with the helium flowing alternatively in two opposite directions renders more uniform the temperature distribution in the first wall and in the blanket. The use of a redundant convective cooling system offers safety advantages and is particularly important with helium, which has not as good natural convection cooling capabilities as other, more dense, fluids.

h) <u>The use of a double containment against tritium losses:</u> This is realized in the blanket region by the presence of the canister and of the segment box walls. Obviously, the control of the tritium losses is an important safety issue.

i) <u>The use of a double containment against high pressure coolant helium losses:</u> This is realized in the blanket region by the presence of the high pressure tube and of the canister walls. Also this point has important safety implications.

References

1. Minutes of the 4th Meeting of the Test Blanket Advisory Group. CCR Ispra, March 14th, 1990.

2. Minutes of the 5th Meeting of the Test Blanket Advisory Group, Karlsruhe, June 26th, 1990

3. M. DALLE DONNE, S. DORNER, and S. TACZANOWSKY, " Conceptual Design of Two Helium Cooled Fusion Blankets (Ceramic and Liquid Breeder) for INTOR", KfK - 3584, EUR-7978e, Kernforschungszentrum Karlsruhe (1983).

4. M. DALLE DONNE, U. FISCHER, and M. KÜCHLE, "A Helium-Cooled, Poloidal Blanket with Ceramic Breeder and Beryllium Multiplier for the Next European Torus", Nucl. Technol., 71, 15 (1985).

5. M. DALLE DONNE, U. FISCHER, M. KÜCHLE, G. SCHUMACHER, G. SORDON, E. BOJARSKY, P. NORAJITRA, H. REISER, H.D. BASCHEK, E .BOGUSCH, "Pebble-bed canister: The Karlsruhe ceramic breeder blanket design for the Next European Torus", Fusion Technol., 14, 1357 (1988).

6. G.W. HOLLENBERG and D.L. BALDWIN, "The Effect of Irradiation on Four Solid Breeder Materials", I. Nucl. Mater., 133 & 134, 242 (1985).

7. H. WERLE, J.J. ABASSIN, M. BRIEC, R.G. CLEMMER, H. ELBEL, H.E. HÄFNER, M. MASSON, P. SCIERS and H. WEDEMEYER, "The LISA-1 Experiment: In-Situ Tritium Release Investigations", J. Nucl. Mater. 141-143 (1986) 321.

8. G.W. HOLLENBERG, "Swelling of Lithium Ceramics During Irradiation", presented at American Ceramic Society Mtg., Pittsburgh, Pennsylvania, May 1987.

Table 1.1	Demo Specifications

Geometry: Double null
Number of sectors: 16
Number of segments: 48 outboard, 32 inboard
Plasma major radius: 6.3m
Blanket thickness: 0.85 m outboard, 0.55 m inboard, for the other dimensions see Fig. 1.1

Operation: Neutron wall load: 2.2 MW/m^2 average
Surface heat flux: 0.4 MW/m^2 average
0.5 MW/m^2 peak
Operation time of segment: 20000 hours
Continous operation: reference mode
Pulsed operation: optional mode with
burn time = 1 hour
number of cycles = 2.10^4
Disruptions: linear decay of plasma current from 20 MA to zero in 20 ms.

Blanket requirements: **Tritium breeding:** TBR > 1.0 in 3D neutronic calculations with 10 ports and the geometry of Fig. 1.1
Coolant conditions: As required for electricity production with a thermal efficieny η > 30 % where:

$$\eta = \frac{electrical\,power\,output\,from\,the\,blanket}{(neutron\,power + surface\,heat)\,to\,the\,blanket}$$

Resistance to disruptions: After one disruption the blanket may be deformed and non operational but it must be removable from the port.
First Wall protection: no special first wall protection is required.
Materials: Structural material: Manet
Breeder material: temperature and blanket design so that the tritium residence time in the blanket is less than 10 days,
Divertor thickness (for neutronic calculations): tungsten 5mm, copper 30 mm, stainless steel 20 mm.

Fig. 1.1 Vertical section across theDemo-blanket.
The dimensions are in millimeters.

2.   DEMO BLANKET REFERENCE DESIGN

2.1   Design

2.1.1   The blanket configuration (M. Dalle Donne, H.D. Baschek, E. Bogusch, E. Bojarsky, G. Reimann, H. Reiser)

Fig. 2.1.1 at page 314 (at the end of the report) shows a vertical cross section of the Demo blanket surrounding the plasma. Various horizontal sections are shown as well. The poloidal magnetic field has two points where it equals zero, and thus it is called a double-null configuration. The blanket is divided into two parts: an outboard and an inboard blanket.

As in the NET / ITER case the Demo plant has 16 toroidal field (TF) coils. On the outboard side there are three blanket segments for each TF coil, two of them adjacent to the magnets and one in the middle. On the inboard side there are two segments. Altogether there are 48 outboard segments with an opening angle of 7.5 ° in respect of the torus axis of simmetry and 32 inboard segments with an opening angle of 11.25 °. These arrangements facilitate the loading and unloading of the blanket segments. In order to increase the breeding capability, the blanket of the inboard segment is extended to the area behind the divertors and the blanket ot the outboard blanket is prolonged by a vertical part arranged at the upper segment section on opposite location to the upper divertor. This is in accordance with the specifications of the European Test Blanket Advisory Group (see Section 1.1).

The radial shielding forms part of the blanket segments. The radial thickness at the midplane of the inboard segment amounts to 856 mm and of the outboard segment to 1856 mm. The total length of the blanket segments amounts to approx. 16m. The blanket segments except the lower part of the inboard segment are suspended from the flange of the upper access port. This port serves for the exchange of blanket segments. The following considerations concern a lateral inboard and a central outboard blanket segment.

2.1.1.1 The outboard blanket segment

The outer blanket segment is illustrated in Figs. 2.1.1 through 2.1.5 and exhibits the following basic design features:

1.   The ceramic breeder material (Li_4SiO_4 pebbles) and beryllium multiplier are contained in 28 separate, nearly rectangular canisters, which are mounted on a back plate (Figs. 2.1.1 and 2.1.3).

2.   The whole arrangement of canisters is contained in a tightly closed box called a blanket box (Fig. 2.1.4).

3. The plasma facing surface of the blanket box consists of the first wall. The back side of the blanket box is the plate on which the canisters are mounted. This back plate is formed by poloidal coolant helium feeding manifolds (Fig. 2.1.4).

4. At the back of the blanket box there are the main coolant helium feeding tubes. These are contained in a closed box which is fixed to the back of the blanket box. Blanket box plus feeding tubes box form the segment box (Fig. 2.1.2).

5. A helium cooled vertical radial shield is provided at the back of the segment box (Fig. 2.1.1)

6. A horizontal shield is installed inside the segment box upper part above the blanket (Fig. 2.1.1).

7. The blanket box and blanket structure are cooled by helium at 8 MPa. The coolant flows in series through the blanket box and the blanket structure.

8. The blanket structure consists of vertically arranged 21-mm-thick beryllium plates with 6-mm slits in between. The slits are filled with a bed of Li_4SiO_4 pebbles of diameter in the range 0.35 to 0.6 mm. A coolant coil of the shape seen on Fig. 2.1.5 is embedded in each beryllium plate.

9. A separate purge gas system at 0.08 MPa carries away the tritium generated in the breeding material.

10. For safety reasons, the coolant flow is divided into two completely independent coolant systems, which alternately feed consecutive coolant tubes.

11. Passive plasma stabilization requires a saddle loop of high electrical conductivity. This is achieved with 13-mm-thick copper plates attached on the side walls of the segment box and an increased thickness of the first-wall plate in two 500-mm-wide regions at the poloidal angle of 60 deg from the plasma magnetic axis (Fig. 2.1.3).

The general arrangement of the cooling systems is shown in Fig. 2.1.1. The blanket box is formed by first wall / radial walls equipped with radial / toroidal / radial cooling tubes and the back wall with integrated poloidally running cooling gas manifolds. It is a closed box with helium-cooled cover plates at top and bottom. Inside the blanket box the 28 blanket canisters are arranged one stacked above the other. The canisters are positioned by connecting tubes and fixing rods to the coolant outlet manifolds. The blanket box has a radial thickness of 850 mm. The main coolant feeding tubes (A/D) are connected to the manifolds at the bottom, the main outlet tubes (B/C) at the top of the blanket. The purge gas inlet and outlet lines are connected to the respective manifolds at the top of the blanket box. The cooling and the purge gas main tubes inside the segment box are routed in such a way

(e.g. with expansion bends) that stresses due to different thermal expansion are well below allowable limits.

The cooling gas feed tubes are fixed to the segment side walls by semi-fixed points (clamps) to withstand forces from plasma disruptions and to keep the stresses in the pipe walls within acceptable limits (see Fig. 2.1.1). To reduce the induced electrical currents in the structures caused by plasma disruptions, the clamps are electrically insulated from the pipes (Fig. 2.1.2). The piping outside the blanket box is surrounded by the segment box, of which the first wall and the side walls of the blanket box are an integral part.

The segment box side walls are helium-cooled by brazed poloidal cooling tubes. The cooling gas inlet is at the bottom also providing coolant to the bottom plate. The outlet collectors are arranged at the segment top below the horizontal shield. The segment box is stiffened by horizontal U-shaped stiffening plates to provide stronger resistance against forces from plasma disruptions. The pipe fixing clamps are connected to the stiffening plates (Fig. 2.1.1 and 2.1.2).

A horizontal shield is installed inside the segment upper part above the blanket to protect flange region and piping arrangement located there from neutron irradiation and to limit the radiation level at the space above the flange. This shield consists of a helium-cooled welded structure filled with granulated shielding material. Cooling is provided by embedded cooling tubes (Fig. 2.1.1).

The pipings for blanket cooling gas, purge gas and coolant for the segment walls penetrate the horizontal shield, and are routed with expansion bends to the segment flange. The penetration through the flange plate has to be a gas-tight welded structure, also providing the fixing points for the supply lines (Fig. 2.1.1).

A radial shield is provided at the back of the segment box. The function of this shield is to protect the vacuum vessel and the magnetic field coils from excessive radiation. The radial shield is mechanically attached to, but electrically insulated from the back wall of the segment at the outside. It is a welded steel structure of 500 mm total thickness provided with poloidally running cooling channels and helium cooling. The cooling gas inlet and outlet pipes are arranged at the top of the shield and are connected in parallel to the cooling system of the segment walls inside the segment box (Fig. 2.1.1). The coolant flow in the shield structure is directed downwards in the front part and upwards in the rear part. The radial shield of the outboard segment is designed in such a way that it can be disconnected from the segment box and be possibly re-used without cutting and re-welding of welds between segment box and shield, except the cooling tubes.

The blanket box cooling tubes depart from the poloidal manifold feeding tubes and run first toroidally, then radially, then again toroidally to cool the first wall, and eventually ra-

dially and toroidally again up to poloidal short manifolds. The helium flows in opposite directions in the two cooling systems. This allows a more uniform temperature field in the first wall and avoids the nonsymmetrical thermal expansion in poloidal direction of the blanket box due to the helium temperature increase in the first-wall region (Fig. 2.1.4).

There are two poloidal short manifolds per canister. The helium is carried through the canister wall radially, then it goes into toroidal distribution tubes contained in the canister (Fig. 2.1.4) and finally in radially-poloidally running tubes, which cool the ceramic material and the beryllium multiplier (Fig. 2.1.5). After that, the helium is collected in toroidal manifolds contained in the canister, and then it flows first to two poloidally running manifolds which form a part of the back plate of the blanket box and finally to the two outlet tubes (Fig. 2.1.1). The purge gas system follows a similar path and flows in and out of the segment flange in smaller double-walled tubes (Figs. 2.1.1 and 2.1.5).

Fig. 2.1.4 shows a radial toroidal cross section of a segment of the outboard blanket. It looks similar to an earlier design which was performed for the NET reactor [4], however, there are some significant differences mainly due to the choice of the structural material. As already mentioned due to the higher neutron fluence in the Demo-reactor, the martensitic steel Manet has been chosen rather than austenitic steel like for the NET blanket. This dictates the choice of the coolant helium temperature of 250 °C at the blanket inlet to keep the Manet at temperatures above the DBTT (Ductile-Brittle-Transition-Temperature) level [1]. The reduced difference between outlet and inlet helium temperature, and the better thermal conductivity of Manet allow to have the inlet and outlet helium feeding manifolds welded together (Fig. 2.1.4). Thus they make the back wall of the blanket box, allowing a considerable simplification at the back of the box in respect of the NET solution.

In Fig. 2.1.5, one can see the stiffening plates that connect the opposite flat walls of the canisters. The canisters have to contain the helium purge system pressure of $\sim$ 0.08 MPa.

The structure inside the canisters can be seen in Figs. 2.1.4 and 2.1.5. The stainless steel cooling tubes are brazed to beryllium plates. To avoid large thermal stresses due to differential thermal expansion, these plates are divided into smaller segments (not shown in the figures). The 6-mm-wide slit between two adjacent beryllium plates is filled with 0.35 $\div$ 0.6 mm lithium orthosilicate (Li_4SiO_4) pebbles. The beryllium plates and the pebble beds are contained in a stainless steel casing. Figure 2.1.5 shows the small tubes that bring the helium purge flow on the plasma side of the canisters. Afterward, the purge helium flows in radial direction through the pebble bed and carries away the tritium produced in the Li_4SiO_4 pebbles. Figure 2.1.5 shows that in the present canister design the coolant tubes of the canister outer walls are round and do not need an outer square section to ease the brazing to the walls. Brazing tests performed at the KfK show that the brazing provides a very good thermal contact also in the case of round tubes if a groove is provided on the wall. The radi-

al toroidal flat walls of the canisters are cooled by tubes of square section manufactured by milling grooves in a thick plate and covering this plate with a metal sheet welded to the plate by a surface diffusion welding (see Subsection 4.5.2.2).

Fig. 2.1.3 shows the chosen configuration for the first wall. The helium cooling tubes are obtained either by deep boring a thick Manet plate or by surface diffusion welding. Both solutions appear, in principle, possible. Investigations are under way to decide which solution is better from a practical point of view. (Section 4.5.2).

2.1.1.2   The inboard blanket segment

The inboard blanket segment mainly consists of blanket box, piping and radial shield, all contained in the segment box. A horizontal shield is installed in the upper segment region to protect the TF-coils, the flange region and the piping above from neutron irradiation (Fig. 2.1.1).

The inboard blanket segment is divided into a main part comprising 17 canisters and a small part consisting of 4 canisters arranged behind the lower divertor. The canisters have a poloidal length of 614 mm. The lower small blanket has the same layout as the upper main part but is supplied with cooling and purge gas through the bottom of the vacuum vessel. However, it has to be exchanged also through the upper access port (Fig. 2.1.1).

The inboard blanket segment has the same general arrangement of blanket box and shield as the outboard blanket segment. However, the radial shield of the inboard segment is integrated into the segment box. The blanket box with poloidal running manifolds for the twofold redundant cooling system encloses completely the blanket canisters (Fig. 2.1.6).

Coolant and purge gas supply lines are connected at the top to the respective manifolds. The supply lines penetrate the horizontal shield above the blanket and exite the segment through bellows welded to the segment flange to allow thermal expansion of the pipings (Fig. 2.1.1). Due to the small place available at the neck in the upper region of the inboard boxes (see view A in Fig. 2.1.1), the diameter of the coolant helium feeding tubes is relatively small (126 mm o.d.), thus the helium pressure has to be higher than in the outboard blanket (10 MPa against 8 MPa) to keep the pressure drops within reasonable limits.

The radial shield consists of steel blocks with cooling channels which are welded together. The steel blocks should contain 10 ÷ 20 % zirconium hydride pellets to reduce the neutron fluence in the vacuum vessel and in the magnets below allovable limits (see Section 2.2.4). The radial shield is cooled by a bypass flow of helium which is separated from the main coolant flow above the horizontal shield. The downward flow is at the front part of the shield, turned at the bottom into opposite direction and the upward flow is at the rear side. The lower shield structure is extended below the blanket box to provide enough

shielding at that area because there is an empty space which is needed for different thermal expansion of the large inboard segment and lower small inboard blanket (Fig. 2.1.1).

Fig. 2.1.6 shows a toroidal-radial cross section of the inboard segment at the equatorial plane. The general arrangement in the blanket region is similar to that of the outboard segment. However, the coolant coils, the beryllium plates and the pebble beds are placed in toroidal-radial planes, rather than poloidal-radial ones like in the outboard blanket. This is due to the fact that the segment cross section in this plane is unchanged in poloidal direction, thus allowing the use of the same unit cell of breeder, multiplier and coolant channel for the whole inboard blanket. For the outboard blanket segment this is only possible by placing the breeder-multiplier-coolant channel unit cells in poloidal-radial planes, due to the variation of the segment width in toroidal direction.

2.1.2 Considerations on the design choices for the Li_4SiO_4 pebbles (M. Dalle Donne)

The choice of small lithium orthosilicate pebbles as breeder material has been already discussed in Section 1.3. The reason of the choice of the proposed diameter range of the pebbles is given in the present Section.

The maximum tensile stress in a sphere subject to a uniform volumetric power production is:

$$\sigma = \frac{\alpha E}{1-\nu} \frac{9}{15\,k} R^2$$

with
α = thermal epansion coefficient

E = Youngs's modulus

ν = Poisson number

q = power density in the sphere

k = thermal conductivity of Li_4SiO_4

The data for α and k are taken from Section 4.2.1 and for E and ν from Section 4.2.2 for a temperature of 600 °C (average temperature of the pebbles in the present blanket design). Assuming that the maximum allowable tensile stress is equal to the ultimate bending stress, from the data of Section 4.2.2 we obtain a maximum allowable thermal stress of 33 MPa for a porosity of the pebble of 3 % and an average grain size of 50 µm (pessimistic value, probably corresponding to the maximum value at temperature of 1000 °C). The maximum power density in a pebble for the present design is 76 W/cm³ (referred to the pebble volume). With these data one obtains a maximum allowable diameter of the pebble of 2.8

mm. To allow for a possible deterioration of the pebble properties due to irradiation at high burn-ups, this diameter should be probably smaller.

The thickness of the pebble bed adopted in the present design is only 6 mm, because for the given thermal conductivity of the bed and the power produced in the bed, a greater thickness would result in too high temperatures in the bed (see Section 2.3).

A maximum pebble-bed width of 6 mm means that the pebble diameter should be equal or smaller than 0.6 mm. This minimum ratio between bed width and pebble diameter of ~ 10 is required to avoid problems of pebble bridge formations and consequent unduly high mechanical stresses in the pebbles, and too strong variations of the pebble-packing factor in the bed [2].

The reference orthosilicate pebbles are fabricated by Schott Glaswerke, Mainz, Germany by spraying molten material. By this method pebbles are obtained in the range 0.05 to 1.2 mm. To improve the production yield it was decided to use the pebbles in the diameter range 0.35 - 0.6 mm rather that the previously used range of 0.45 - 0.56 mm. By this choice production yield is improved by a factor 3, and at the same time the presence of small pebbles does not increase too much the pressure drop in the purge gas flow (see Section 2.3).

2.1.3 Results of the neutronic, thermohydraulic and stress calculations (M. Dalle Donne)

These calculations are described in more detail in Section 2.2 and 2.3, here only the results will be summarized and evaluated.

The power distribution, the local tritium production and the tritium breeding ratio have been evaluated by means of three dimensional Monte Carlo calculations using the code MCNP. These calculations account also for the presence of 10 ports placed at the equatorial plane of ten outboard blanket segments. The neutronic calculations have allowed to design properly the shields behind the blankets to maintain the radiation loads on the TF-coils within acceptable limits. The blanket temperatures and stresses in the structural material (first wall and boxes) have been evaluated by tridimensional calculations using the computer code ABAQUS. Temperatures and stresses are within acceptable limits.

Table 2.1.1 shows the main results of these calculations. The helium temperatures of the cooling system (inlet 250°C, outlet 450°C) are modest compared to those obtained in high temperature gas-cooled fission reactors. Although detailed calculations have not yet been performed, preliminary estimates show that these temperatures would be sufficient to allow a plant efficiency comparable to that of a pressurized water reactor ($\approx$ 33 %). The helium temperature limitation is given by the conservative choice of the structural material (martensitic steel) and the relative limitation of 550°C maximum operation temperature.

Higher temperatures could be achieved by the use of a more advanced structural material, such as for instance a molybdenum alloy as proposed for a Japanese blanket design [3].

While the temperatures in the first-wall region must be kept as low as possible due to the steel temperature limitation, in the blanket region the minimum ceramic breeder material temperature should be high enough to permit a rapid tritium release and hence to allow a reasonably low tritium inventory (see Section 2.1.4). This temperature, however, is mainly dependent on the helium temperature at the inlet of the blanket region. Due to the choice of series cooling first-wall blanket, this inlet helium temperature is thus limited by the maximum allowable temperature in the first-wall. The use of a series cooling reduces the number of helium supply tubes. The use of two separate first-wall and blanket cooling systems would imply a doubling of the number of these supply tubes. For the outboard blanket, this could be just about possible as far as space limitations at the upper neck of the segment box are concerned; however, one would expect problems to make room for the tube valves and supports above the segment box. As far as the inboard blanket is concerned, doubling of the supply tubes would be impossible due to the space limitation at the upper neck of the segment box.

The pressures and pressure drops in the cooling system of the inboard blanket are considerably higher than those required by the outboard blanket. This is mainly due to the relatively small diameters allowed for the helium supply tubes caused by the above mentioned space limitation at the upper neck of the segment box.

The obtained tritium breeding ratio (TBR) value of 1.11 (which accounts for the presence of ten ports on the outboard blanket) is high enough to ensure a sufficient margin against the uncertainties in the TBR calculations (estimated at 5 %) and the reserve to compensate for the tritium decay and tritium inventories in the system (estimated at 1 - 2 %).

The total amount of beryllium is rather high (228 tonnes). The neutronic calculations show that this value could be reduced to 100 tonnes with a loss in TBR of only 4 %. However, design work for this alternative has not yet been performed.

2.1.4 Tritium inventories and control (M. Dalle Donne)

The evaluation of the tritium inventories and the tritium control in the blanket are particularly important as the Demo blanket has to show the capability of producing sufficient tritium for a continuous plasma operation (TBR > 1). Similarly to the blanket design for NET [4], the tritium extraction and control are based on a tritium purge flow system using helium plus 0.1 % hydrogen at subatmospheric pressure to extract the major fraction of the tritium produced in the blanket. Furthermore, 0.1 % of the helium mass flow is continuously extracted from the main helium coolant circuit and sent to a helium purification plant for

the extraction of the impurities and of the tritium coming by permeation from the purge flow or directly injected from the plasma. The assessment of these tritium quantities has been performed with the methods illustrated in Ref. [4] and [5]. The permeation data for Manet are based on the experimental results of Ref. [6].

Table 2.1.2 shows the main results of these calculations. As in Ref. [4], the tritium inventory has been calculated from the measured tritium residence time τ for the Li_4SiO_4 reference pebbles Schott 86 (see Section 4.6.3.2). The measured data can be approximated by the following equation:

$$\tau(s) = 2.182 \times 10^{-7} \exp \left| \frac{17636}{T(K)} \right|.$$

As the residence time τ is the ratio between tritium inventory and tritium production rate, the blanket tritium inventory is given by

$$I = \frac{1}{3} \frac{\dot{m}}{T_{max} - T_{min}} \times \int_{T_{min}}^{T_{max}} \left| 2.182 \times 10^{-7} \exp\left(\frac{17636}{T(K)} \right) \right| dT = 10 \text{ g},$$

where

$\dot{m}$ = 4.51 x 10-3 g/s = 390 g/day (total tritium production rate in the blanket, obtained by the neutronic calculations)

T_{max} = 1093 K = maximum temperature of the pebbles in the blanket

T_{min} = 653 K = minimum temperature of the pebbles in the blanket.

This equation is obtained assuming a linear variation of temperature over the pebble bed volume in the blanket and neglecting the variations of tritium local production rates. This method results in too high tritium inventories, as the temperature distribution in the breeder is not linear and the tritium production in the high temperature regions is higher. Therefore the correction factor 1/3 has been used. This has been obtained by comparing the tritium inventory obtained by the linear variation assumption and the exact calculation performed by numerical integration of the local production rates at the local temperatures in the breeder. This was done for the similar BOT-HCSBB design for NET [7].

The greatest tritium inventory is in beryllium. This has been calculated on the assumption that all the tritium produced in the beryllium is trapped in it as the beryllium temperature is everywhere $\leqslant$ 600 °C. Recent experimental information shows that beryllium irradiated to a total fluence of 5 x 10^{22} cm-2 (E $\geq$ 1 MeV) releases 99 % of tritium only at temperatures

above 600 °C [8]. These data might not be completely relevant to the present blanket as the beryllium of Ref. [8] was irradiated at low temperatures (< 75 °C), was probably considerably anisotropic and contained a relatively large amount of BeO.

The tritium purge system data appear quite feasible. The tritium losses by leakage are negligible. The tritium losses by permeation from the purge flow system to the main helium system are considerably higher than in the case of NET. This is due to the fact that the permeability of tritium through Manet is considerably higher than through austenitic steels [6].

The tritium inventory in the first wall and the tritium direct losses from the plasma to the main helium cooling system are known only very roughly. They have been calculated with the code DIFFUSE for a similar blanket [9]. The amounts of tritium coming directly from the plasma by permeation may be very large (estimated at 1-100 g/d). Only with an effective oxidizing atmosphere in the helium main cooling system and / or permeation reducing coatings on the permeating surfaces could it be possible to reduce the tritium losses to the environment to the desired value of less than 10 Ci/d (0.37 TBq/d).

References

1. K. EHRLICH, Private communication, Kernforschungszentrum Karlsruhe, 1989.

2. "Problems of the Pebble Bed and Granular Materials", Proc. THTR Symp., Jülich, FRG, March 6 - 7, 1968, European Atomic Energy Community.

3. T. KURODA, K. SATO, T. SUZUKI, T. TONE and M. SEKI, "Technical Considerations on the Tritium Breeding Blankets for a Fusion Power Reactor", Fusion Engineering and Design 8, (1989) 219 - 226.

4. M. DALLE DONNE, U. FISCHER, M. KÜCHLE, G. SCHUMACHER, G. SORDON, E. BOJARSKY, P. NORAJITRA, H. REISER, H.D. BASCHEK, E .BOGUSCH, "Pebble-bed Canister: The Karlsruhe Ceramic Breeder Blanket Design for the Next European Torus", Fusion Technol., 14, 1357 (1988).

5. M. DALLE DONNE, S. DORNER, "Tritium Control in a Helium Cooled Ceramic Blanket for a Fusion Reactor", Fusion Technol. 9, (1986) 484 - 491.

6. K. FORCEY, D. ROSS, I. SIMPSON, D. EVANS, "Hydrogen Transport and Solutbility in 316 L and 1.4914 Steels for Fusion Reactor Applications", J. Nucl. Mat. 160, (1988) 117 - 124.

7. G. SORDON, unpublished report, KfK, 1989.

8. D. BALDWIN, G. GELLES, O. SLAGLE, "Tritium Release from Irradiated Beryllium at Elevated Temperatures", 4th. Int. Conf. Fusion Reactor Materials, Kyoto, Dec. 5 - 8, 1989, J. Nucl Mat. <u>179 - 181</u> (1991).

9. E. PROUST, CEA, April 1990, unpublished.

Table 2.1.1   Main characteristics of BOT Helium Cooled Solid Breeder Blanket for the Demo reactor.

Breeding material:	0.35 - 0.6 mm Li_4SiO_4 pebbles (90 % ^6Li enrichment), total amount = 60 tonnes
Multiplier:	Beryllium, total amount = 228 tonnes
Total blanket power:	2500 MW (+ 300 MW in the divertors)
Coolant helium temperature:	inlet = 250 °C outlet = 450 °C
Coolant helium pressure:	8 MPa outboard, 10 MPa inboard
Coolant helium pressure drop (first wall, blanket, feeding tubes):	0.26 MPa outboard, 0.4 MPa inboard
First wall maximum steel temperature:	550 °C
Max. temp. in beryllium:	600 °C
Max. temp. in pebble bed:	820 °C
Min. temp. in pebble bed:	380 °C
Peak thermal and pressure load:	437 MPa (Von Mises, primary plus secondary stress, at first wall, outboard equatorial plane, T = 481 °C)
Real tridimensional tritium breeding ratio (assuming ten 3 x 1 m ports on outboard blanket for heating systems and others):	1.11
Tritium production rate:	390 g/d
Peak burnup in Li_4SiO_4:	10 at% referred to total lithium, 22 dpa
Peak fluence in Manet:	70 dpa
Peak fluence in beryllium:	2.2×10^{22} n/cm^2 (E > 1 MeV), 15000 appm He

Table 2.1.2   Tritium inventories and control

Tritium inventories:

- Tritium inventory in Li_4SiO_4 pebbles $= 10$ g

- Tritium in first wall: 3 to 300 g

- Tritium in beryllium at the end of blanket life: 2080 g

- Tritium in solution in blanket structural material: 0.15 g

Tritium purge system:

- Total purge helium mass flow: 0.67 kg

- Average helium pressure: 0.08 MPa

- Purge helium velocity in the bed: 0.3 m/s

- Pressure drops in the bed: 0.011 MPa outboard, 0.006 MPa inboard

- HT partial pressure in purge helium: 0.85 Pa outboard, 0.44 Pa inboard

- H/HT ratio: 94 outboard, 182 inboard

Tritium losses (neglecting the direct losses from plasma to main helium cooling system)

by permeation from purge system to main helium coolant system $= 2.9$ g/d

by permeation from the main helium coolant system to water /steam circuit:

   reducing atmosphere in He-system : 175 Ci/d (6.5 TBq/d)

   oxidizing atmosphere in He-system $<$ 10 Ci /d (0.37 TBq/d).

7.5°

1307.9

Electrically
insulating
layer

∅219×10

500

Radial shield

ELECTRIC INSULATED

1856

U-shaped
stiffening
plates for
the segment
box

Coolant
helium
feeding
tubes

BREEDER
CANISTER

Coolant
helium
poloidal
manifolds

1064.6
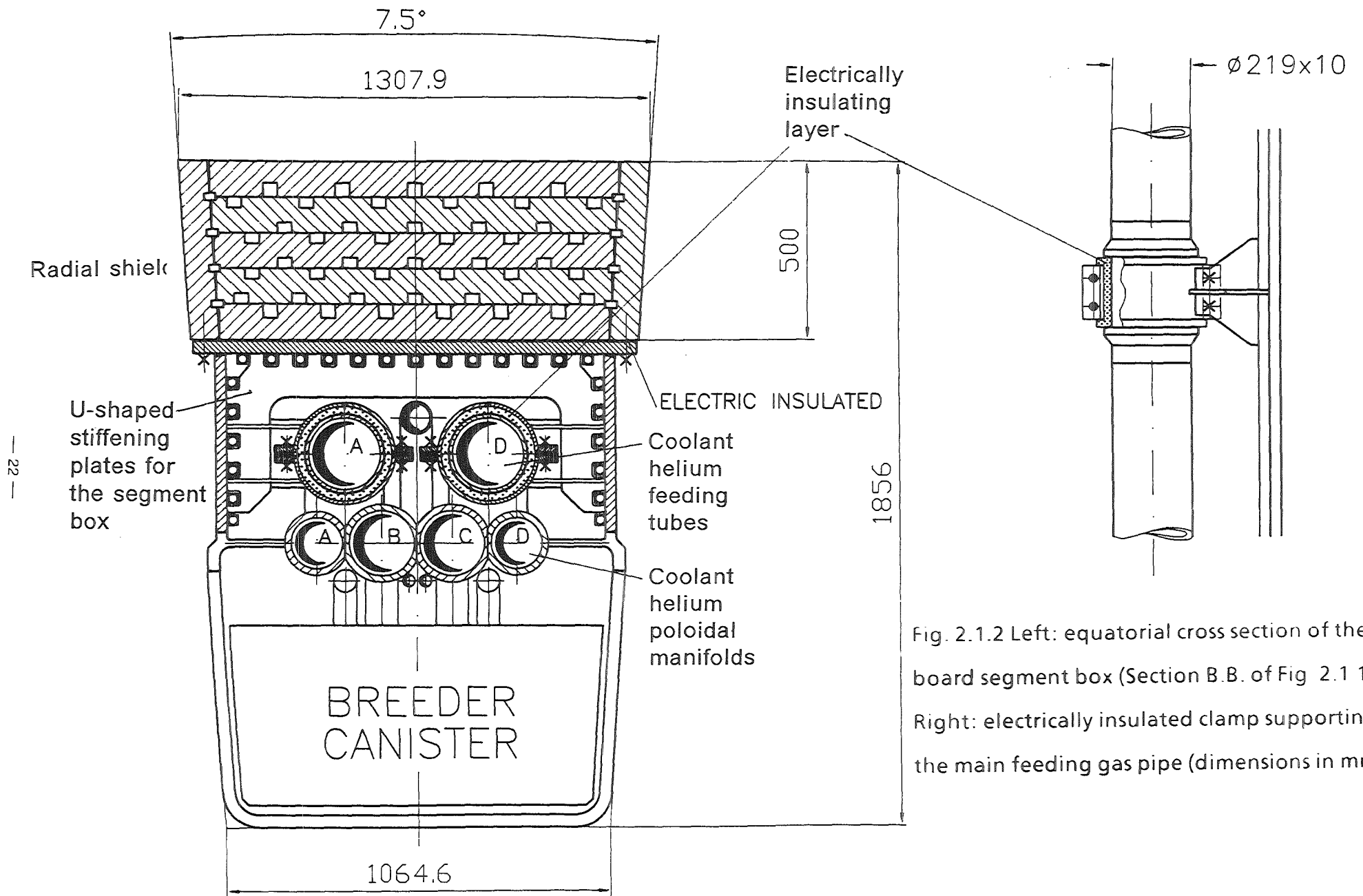
Fig. 2.1.2 Left: equatorial cross section of the out-
board segment box (Section B.B. of Fig 2.1 1).
Right: electrically insulated clamp supporting
the main feeding gas pipe (dimensions in mm).
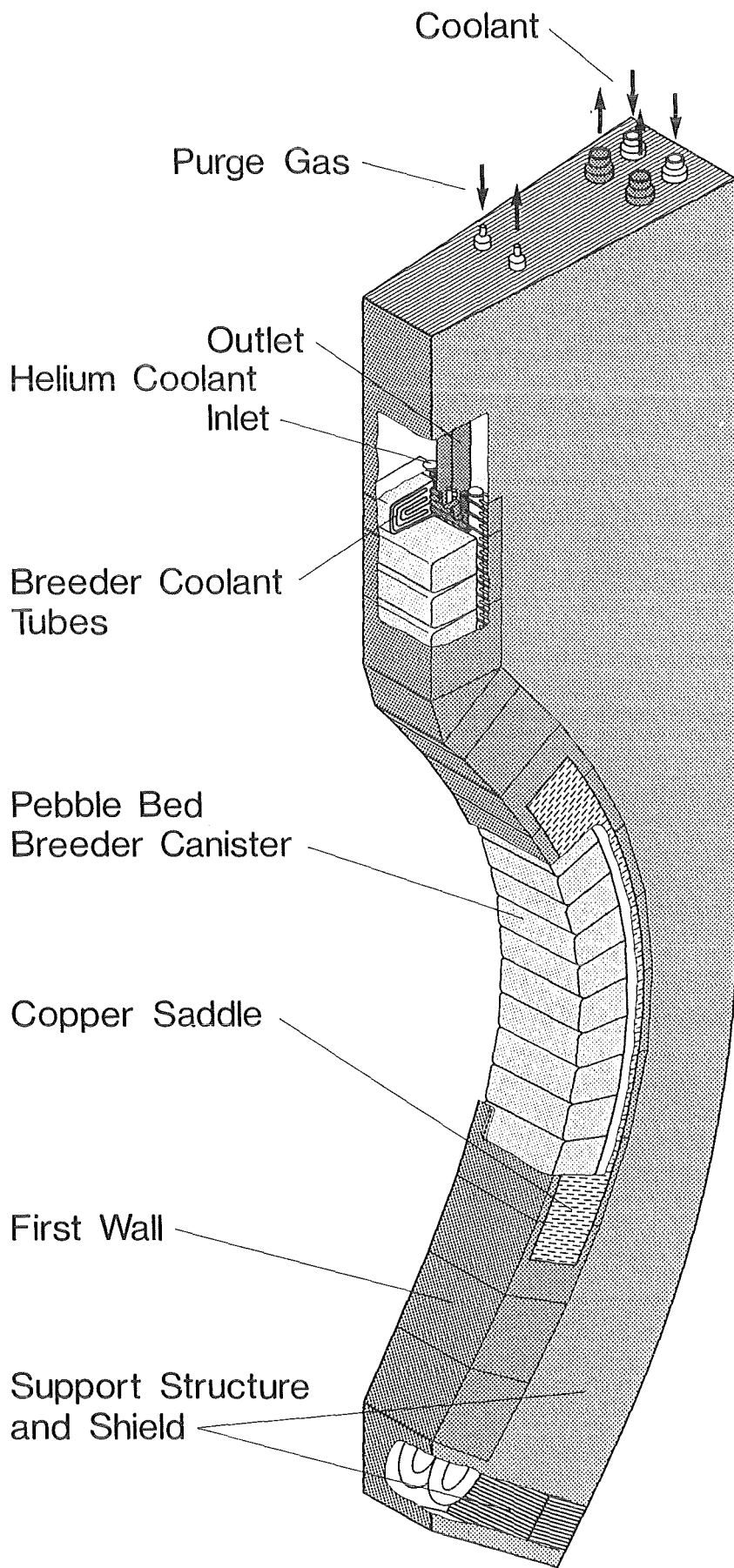
Fig. 2.1.3 Isometric view of the outboard blanket segment.

Poloidal feeding manifolds

He Cooling System 1   EB Welded   He Cooling System 2

Short poloidal manifolds

850

Blanket Canister

Li Ceramic Pebbles

Beryllium Plates

Cooling Tubes

Purge Gas Supply

Blanket Box with First Wall

18,5   19,75

34

24

Fig. 2.1.4 Radial-toroidal cross section at the equatorial plane of the outboard blanket box and (below) radial-poloidal section of the first wall (dimensions in mm)
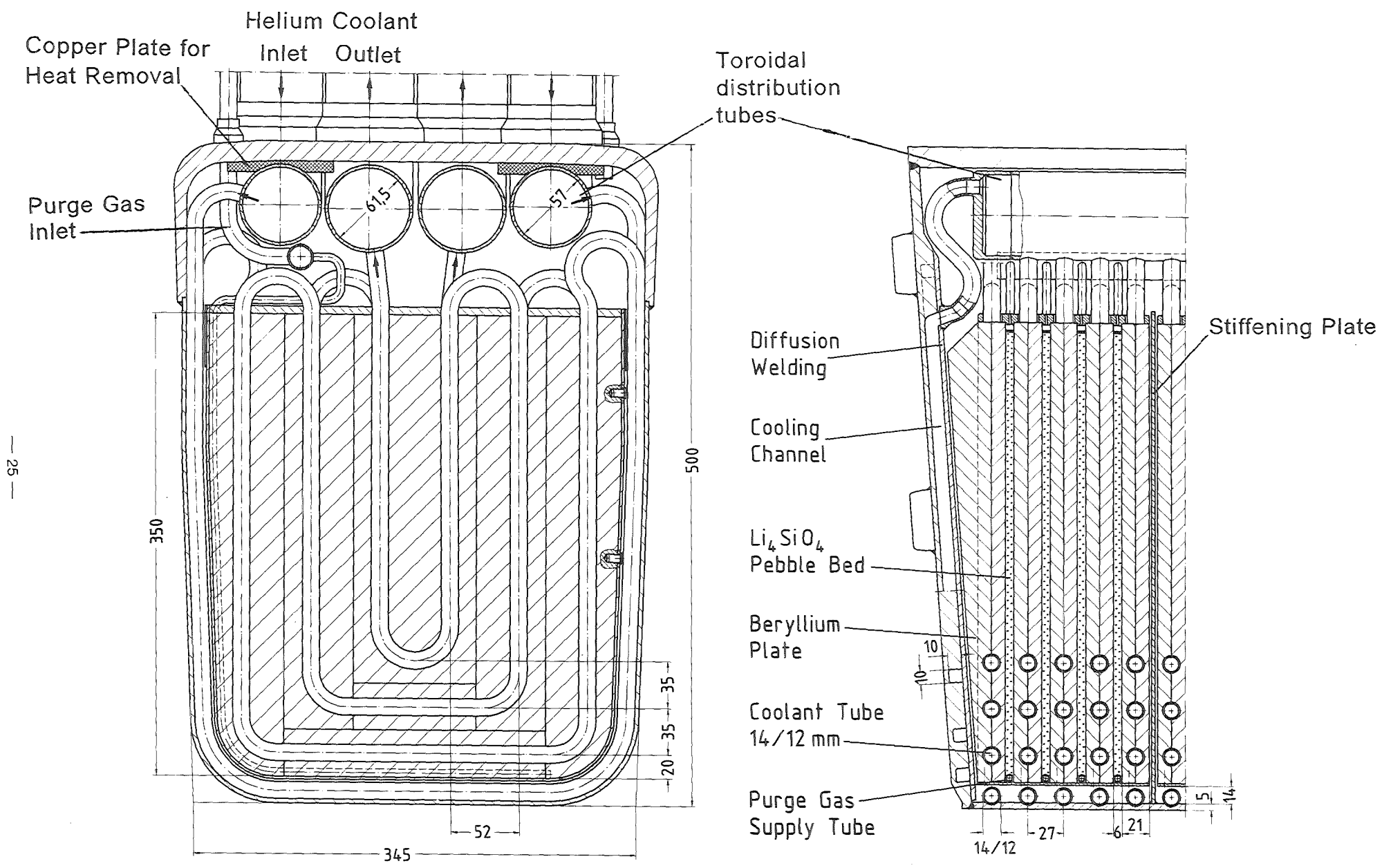
Fig. 2.1.5 Radial-poloidal (left) and radial-toroidal (right) cross section of a outboard canister (dimensions in millimeters).
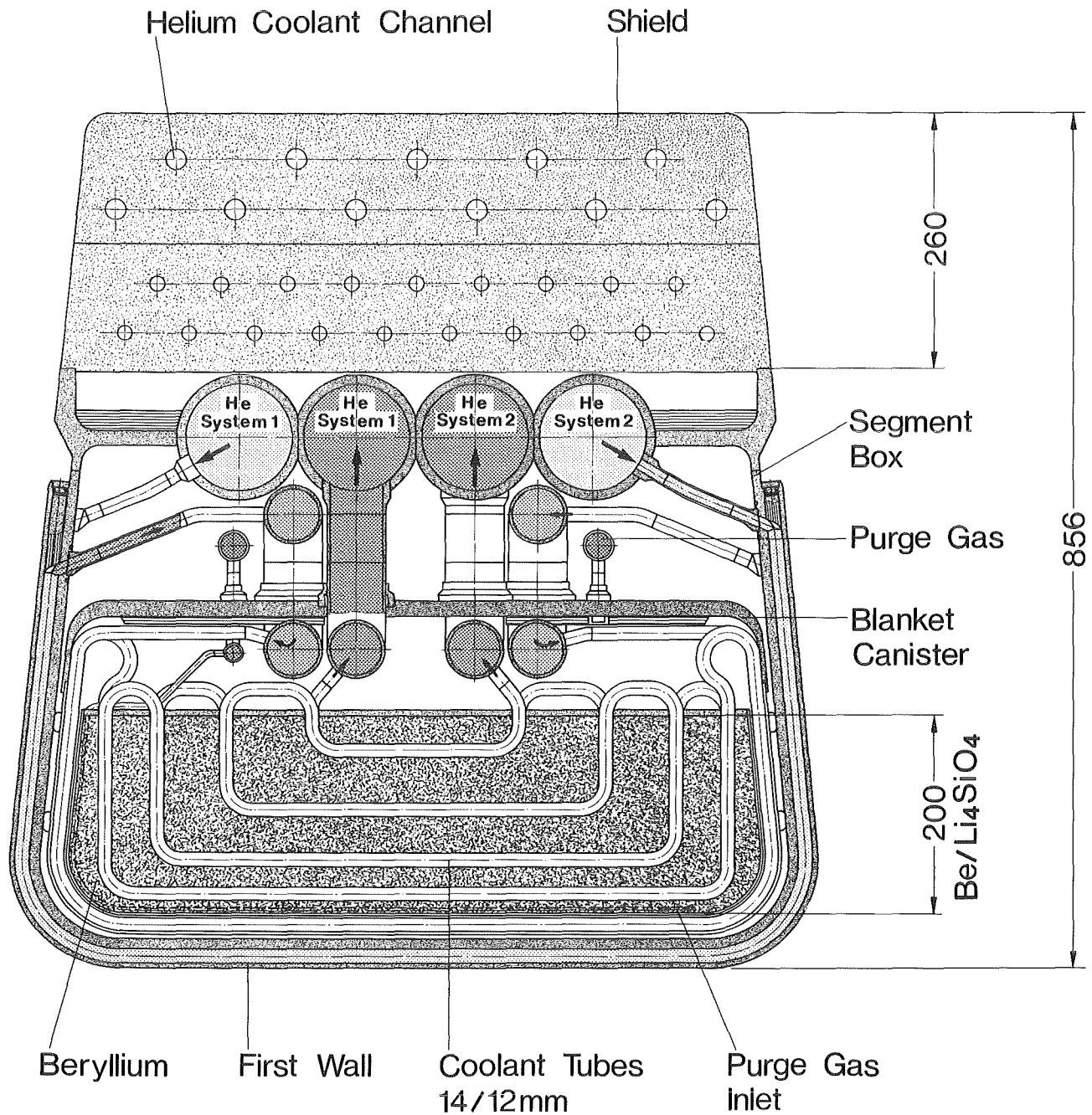
Fig. 2.1.6 Radial-toroidal cross section of the inboard segment box (dimensions in millimeters).

2.2 Neutronics   (U. Fischer)

The solid breeder blanket is characterized by the use of the neutron multiplier beryllium: for an optimal breeding performance a large volume fraction of beryllium (typically 80 to 90 %) is needed; ideally it should be arranged in a homogeneous mixture with the breeding material /1/. In the present design of the canister blanket a quasi-homogeneous solution near the optimum has been achieved by arranging 21 mm thick beryllium plates with 6 mm thick slits in between in vertical (i.e. radial-poloidal) direction. Li_4SiO_4, enriched to 90 % in ^6Li, is used as breeding material; it is filled in form of small pebbles into the slits between the beryllium plates. The effective density of the breeding ceramics the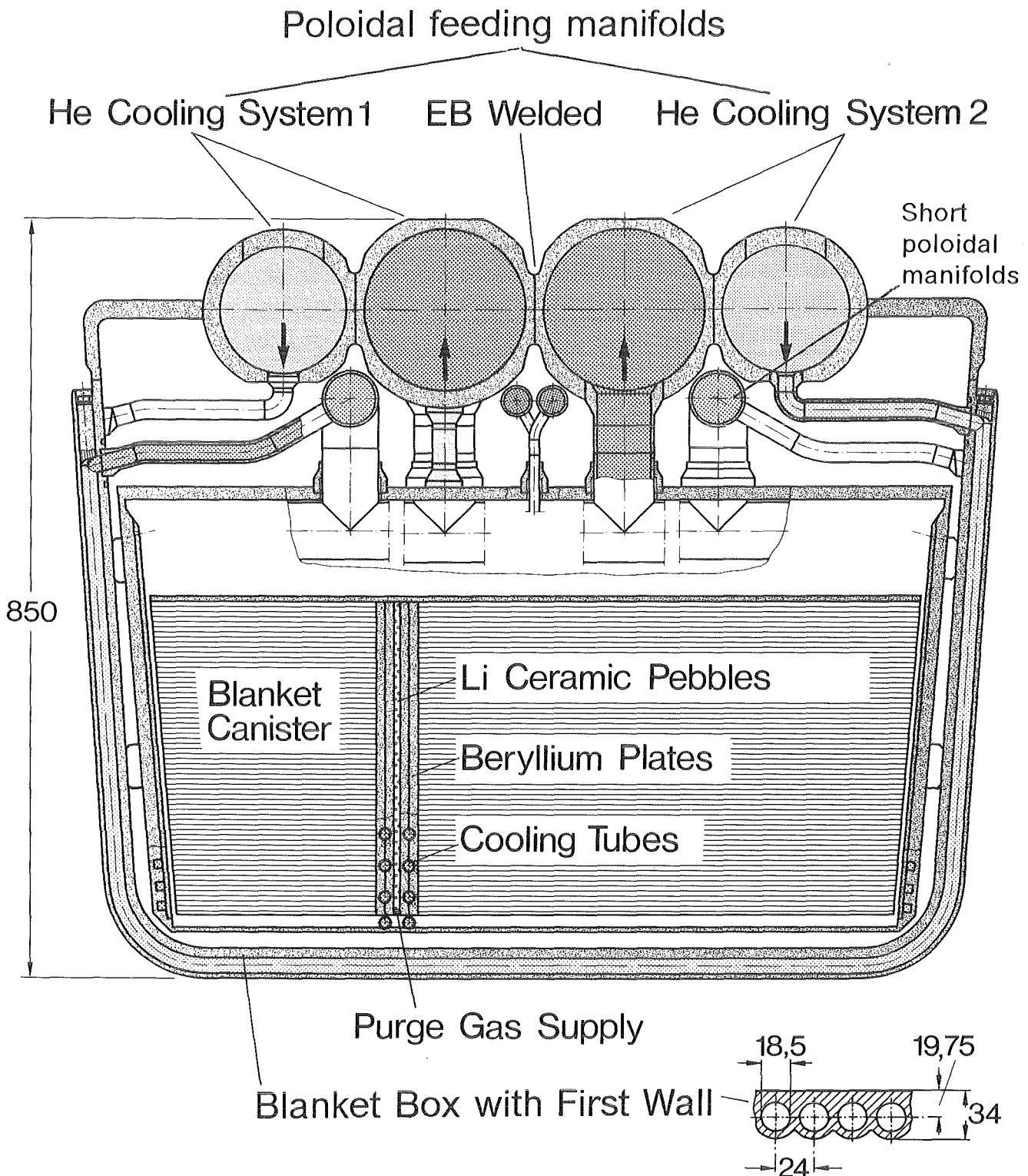reby is reduced from 2.39 g/cm^3 to 1.49 g/cm^3. For beryllium the theoretical density of 1.84 g/cm^3 is maintained. For the Demo blanket, the radial thickness of the beryllium plates is 35 cm and 20 cm on the outboard and inboard side, respectively. The total amount of beryllium inventory is about 230 tons. This includes "divertor breeding", i.e. the utilization of the space behind the divertors for breeding, and, additionally, the arrangement of breeding canisters in the upper region of the outboard blanket segments to reduce the neutron losses through the upper divertor openings.

For the neutronic analysis of the solid breeder blanket a three-dimensional torus sector model of the Demo reactor has been set up. The Demo reactor is composed of 16 torus sectors (22.5^0), each consisting of two inboard and three outboard segments. Due to its toroidal symmetry it is sufficient to model a torus sector of 11.25^0 and applying reflective boundary conditions (Fig. 2.2.1). Within this torus sector the model follows very closely the geometrical arrangement of all relevant reactor components (blanket segments, divertors, vacuum vessel, etc.), as they are given in the technical layout. The geometrical modelling of the blanket segments is illustrated by radial-toroidal cross-sections of the inboard (Fig. 2.2.3a) and outboard (Fig. 2.2.3b) segments. Their poloidal arrangement can be taken from Fig. 2.2.2. The Monte Carlo code MCNP /2/ has been used to set up the torus sector model and for performing all neutronic calculations presented here. The nuclear data used in these calculations originate from the European Fusion File EFF-1 and have been processed into a MCNP working library at PSI Würenlingen /3/.

In the Monte Carlo calculation the spatial plasma source distribution is described by a probability distribution of the 14 MeV neutron source density s (a). The normalized neutron source density is given by:

$$s(a) = \left[1 - \left(\frac{a}{A} \right)^2 \right]^4 \qquad 0 \leq a \leq A$$

The parameter a fixes a contour line at constant neutron source density. It corresponds to a magnetic flux line which can be represented by:

$$R = R_0 + a \cdot \cos(t + \delta \sin t) + e \left| 1 - \left(\frac{a}{A} \right)^2 \right|$$

$$z = E \cdot a \cdot \sin t$$

$$\delta = \delta_0 \cdot \frac{a}{A} \qquad 0 \leq a \leq A \, , \, 0 \leq t \leq 2\pi$$

R gives the radial distance to the torus axis and z the poloidal distance to the torus mid-plane.

This plasma source representation has been adopted from neutronic calculations for the NET-reactor /4/. For the Demo reactor the following parameters are used:

R_0 = 635 cm   major plasma radius

A = 182 cm   minor plasma radius

E = 2.17   elongation

e = 16.2 cm   excentricity

δ_0 = 0.57   maximal triangularity

2.2.1 Tritium breeding ratio

For the calculation of the tritium breeding ration (TBR) in the 11.25^0 torus sector model of the Demo blanket about 70 000 neutron histories have been followed. Table 2.2.1 shows the neutron balance and the associated statistical errors obtained in these calculations. The rather high global breeding ratio of TBR = 1.167 ± 0.3 % is due to the high blanket cover-

age achieved by arranging breeding canisters in the space behind the divertors and in the upper region of the outboard blanket segments. If these "upper canisters" would be replaced by non-breeding material components, the global breeding ratio would drop to TBR = 1.128 ± 0.5 %; if additionally the divertor breeding canisters would be removed, the breeding ratio would decrease further to TBR = 1.054 ± 0.6 %. In both cases the neutron multiplication would not change significantly: the breeding material mixture contained in these canisters does not act as neutron multiplier (although 60 % of the available volume is occupied by beryllium) but rather as useful neutron absorber. This observation suggests to replace the breeding material mixture (beryllium, Li_4SiO_4 pebbles and steel) by a pure Li_4SiO_4 pebble bed (a mixture of 80 % by volume pebble bed and 10 % steel is used in the calculations). Actually, the tritium breeding ratio would not be affected by this measure (Table 2.2.2), while on the other hand about 56 tons of beryllium would be saved. From the view of beryllium saving it would be beneficial, furthermore, to restrict the radial thickness of the beryllium plates both at the outboard and the inboard side by replacing the beryllium/ceramics mixture correspondingly by a pure Li_4SiO_4 pebble bed. Without any loss in the global TBR the radial beryllium thickness could be reduced to 27 cm at the outboard and to 14 cm at the inboard side. This would result in a further beryllium saving of about 43 tons (Table 2.2.2). Thus the total beryllium inventory in the Demo blanket could be reduced from 230 tons to about 130 tons. If one would admit a small TBR loss with respect to the reference case (Table 2.2.1) the total beryllium inventory even could be limited to about 100 tons at a global TBR of 1.13 (Table 2.2.2). In this case the radial beryllium thickness would amount to 14 and 21 cm, inboard and outboard, respectively.

The calculations of the global TBR rely on the use of reflective boundary conditions at the lateral walls of the 11.25^0 torus sector model, i.e. it is assumed that the Demo reactor is composed of 2 x 16 = 32 identical torus sectors. In reality there will be torus sectors with complete blanket segments and, in between, torus sectors with blanket ports for plasma heating, remote handling, pellet injection, diagnostics etc., which reduce the tritium breeding. The Demo reactor design provides horizontal ports in a total of 10 outboard blanket segments. To assess their impact on the breeding performance a torus sector model of $4 \times 11.25^0 = 45^0$ with 4 inboard and 6 outboard segments has been devised /5/. It represents the whole reactor with 32 inboard and 48 outboard segments by applying reflective boundary conditions. In this model 8, 12 and 16 horizontal ports of the Demo reactor are simulated. Each port covers an area of 340 cm height times the full segment width in the centre of an outboard segment. The model relies on a simplified geometrical representation of the solid breeder blanket. Fig. 2.2.4a shows a radial-toroidal cross-section through the 45^0 torus sector with 1 + 2 x 1/2 = 2 ports, simulating a total of 2/6 x 48

= 16 ports. Fig. 2.2.4b shows a radial-poloidal cross-section through a torus sector including a blanket port.

A blanket port has two different effects on the breeding performance: it reduces the breeding ratio due to a loss of breeding (and/or multiplying) material and it modifies the albedo of the blanket segment. Depending on the specific port configuration the latter property can lead to reduced or enhanced out-scattering losses through the blanket port. Therefore, three different port configurations are considered: a partially voided port with a steel plate at the level of the blanket back side (see Fig. 2.2.4a), a port plugged with steel, and a completely voided port (i.e. voiding also the steel structure between the blanket port and the vacuum vessel, see Fig. 2.2.4a). Fig. 2.2.5 shows the dependence of the TBR on the number of ports for all port configurations considered. Obviously the TBR decreases smoothly with the number of ports and therefore it can be interpolated linearly on this number. In the cases of the plugged port and the partially voided port ("steel plate option") the reduction of the outboard TBR roughly corresponds to the loss of breeding material, i.e. it is not affected by out-scattering losses through the blanket port. The inboard TBR strongly depends on the albedo of the outboard blanket segments: the plugged port enhances the in-scattering gains to the vacuum chamber, increasing thereby the inboard TBR; the partially and, of course, the completely voided port reduce the in-scattering gains, leading to a reduced inboard TBR.

For 10 blanket ports a total TBR loss of 0.08 can be taken from Fig. 2.2.5 in case of the partially voided port ("steel plate option"), corresponding to an 8.4 % reduction of the outboard and a 7 % reduction of the total TBR. In case of the plugged port 10 blanket ports would lead to a total TBR loss of 0.06, corresponding to an 8.4 % reduction of the outboard TBR and a 5 % reduction of the total TBR. The solution with the plugged ports is the one which most approaches the real situation, as the ports will be full of metallic apparatus (mostly of steel). Furthermore shields will be provided to protect the TF-coils. Thus it can be expected that the global TBR of the solid breeder blanket in the actual Demo reactor with a total of 10 blanket ports would decrease from TBR = 1.167 (Table 2.2.1) to about TBR = 1.11.

Neglecting the effect of the modified albedo, the TBR loss due to the inclusion of blanket ports can be estimated from the reduction of the blanket coverage. One blanket port covers about 48 % of the first wall area of an outboard blanket segment of 7.5^0. In case of 10 ports a TBR loss of 10 x 0.48 / 48 = 10 % could be expected for the outboard segments. This would result in an estimated total breeding ratio of TBR = 1.09, which is in fairly good agreement

with the above deduced values. Thus it can be concluded that the impact of the blanket ports on the tritium breeding ratio can be estimated by the reduction of the outboard blanket coverage within sufficient accuracy. This holds for the plugged port and the "steel plate option". In case of the completely voided port this does not hold; there the outboard TBR loss is enhanced due to out-scattering losses through the blanket ports. The completely voided port, however, is not a realistic option for the port configuration.

2.2.2 Power production

For the thermal-hydraulic blanket layout a detailed evaluation of the spatial power density distribution is needed. This is achieved by performing coupled neutron-photon Monte Carlo transport calculations with up to 370 000 source neutrons. In these calculations the material zones of the torus sector model are appropriately segmented in radial and poloidal direction. Based on a fusion power of 2216 MW of the Demo reactor the calculated power production of single blanket segments and the complete reactor, equipped only with solid breeder blanket segments, is given in Table 2.2.3. Typically about 70 % of the power is produced in the breeder material zones of the blanket segments. The breeding ceramics, of course, is the major heat source; due to its low volume fraction the power density in the breeding ceramics is rather high (see, for example, the radial profiles of the power densities for the various material components at the outboard torus mid-plane, Fig. 2.2.6a, or the poloidal profiles of the ceramics power densities, Fig. 2.2.6b). The maximum value is about 46 W/cm^3 at the front of the outboard breeding zone at the torus mid-plane. The maximum power density of steel, on the other hand, is not more than 25 W/cm^3 (outboard first wall at torus mid-plane), the maximum power density of beryllium, the major component of the breeding material mixture, is restricted to 15 W/cm^3 (front of outboard breeding zone at torus mid-plane).

2.2.3 Tritium production

The ^6Li (n, α) t-reaction in the breeding ceramics is the main source of the tritium production. Additionally tritium is produced in the beryllium plates of the solid breeder blanket due to the ^9Be (n, t)^7Li-reaction. The spatial distribution of the tritium production rate in the breeding ceramics and in the beryllium plates again has been estimated on the basis of three-dimensional Monte Carlo calculations in the 11.25^0 torus sector model of the Demo reactor. For this purpose about 70 000 neutron histories have been followed assuring a statistical uncertainty less than $\pm$ 1 % for the calculated reaction rates. Table 2.2.4 gives the results of these calculations assuming again a fusion power of 2216 MW for the Demo reactor.

2.2.4 Shielding

Radiation shielding is most crucial at the inboard side of the Demo reactor: although the total thickness of the blanket/shield system amounts to 115 cm, the thickness of the vacuum vessel, acting as major shielding component, is only 30 cm, whereas the total thickness of the blanket segment is 85 cm. The shielding performance of a breeding blanket in general is poor (with the exception of aqueous salt solution blankets); this also holds for the solid breeder blanket with beryllium: the total neutron flux density decreases, for instance, from $8.78 \cdot 10^{14}$ cm^{-2} s^{-1} at the inboard first wall to $5.25 \cdot 10^{13}$ cm^{-2} s^{-1} at the rear wall of the inboard blanket segment, i.e. by not more than a factor 17 across the total thickness of 85 cm. Although large amounts of the neutron multiplier and moderator beryllium are present in the blanket, the slowing-down power is too poor for an efficient neutron moderation, which is the precondition for an efficient shielding.

Therefore it is questionable, if the shielding requirements can be met in the actual configuration of the Demo reactor. To clarify this question, appropriate shielding calculations have been performed in the 11.25^0 torus sector model of the Demo reactor. The MCNP-code has been applied for performing the shielding calculations making use of the importance sampling technique. About 150 000 neutron histories have been followed in the shielding calculations to assure a sufficient statistical accuracy in the region of the TF-coil. For the vacuum vessel the layout shown in Fig. 2.2.3a has been used: a steel layer (SS-316) of 5 cm thickness, a layer of borated water (40 g H_2 BO_3 per liter of water) with a thickness of 2 cm, a steel layer of 7 cm, again a layer of borated water (5 cm) and a steel layer of 11 cm. Such a material configuration shows a high shielding performance; however, no attempt has been made for its optimization.

Various design options have been used for the inboard blanket segment:

- the reference design option with helium-cooled steel plates ("steel plate option") of 23 cm total thickness at the backside of the blanket segment (see Fig. 2.2.3a)

- a design option with improved shielding performance: the helium-cooled steel plates are replaced by a mixture of 70 % steel and 10, or 20 % ZrH ("ZrH option"). In this case the solid metal hydride ZrH acts as efficient neutron moderator: the atomic number densities of hydrogen are on the same order of magnitude than those of pure water.

- a design option with improved breeding performance to reduce the neutron leakage into the shield components: In this case the beryllium/ceramics/steel breeder mixture is partially replaced by a pure ceramics/steel mixture ("ceramics option"). Actually the thickness of the beryllium zone is kept at 14 cm, but the thickness of the pure ceramics zone is increased to 16 cm; thus the total thickness of the breeding zone amounts to 30 cm.

For the "steel plate" and the "ZrH option" Fig. 2.2.7a) and Fig. 2.2.7b) show the poloidally averaged radial profiles of the total and the fast (E > 0.1 MeV) neutron flux densities across the inboard blanket segment and the vacuum vessel respectively. Obviously the inclusion of the solid neutron moderator ZrH greatly reduces the penetrating neutron radiation: if 20 % ZrH are inserted into the steel plates, the total neutron flux density at the front of the vacuum vessel decreases by about one order of magnitude. There is still room for a further improvement of the shielding efficiency, as can be deduced from Fig. 2.2.7: solid ZrH could also be inserted into the rear part of the blanket segment itself, i.e. between the shielding steel plates and the breeding zone. The radial thickness of this part amounts to about 30 cm with an overall void fraction of about 80 %. Thus it would be easily feasible from a technical point of view to fill some ZrH into the void space there.

Actually it is sufficient to insert ZrH only into the shielding steel plates: assuming an integral operation time of 20 000 h, the radiation design limits for the TF-coild can be met by the Demo blanket configuration (Table 2.2.5). In case of the reference design ("steel plate option"), the radiation design limits are exceeded by about a factor 2 to 3. This factor, however, could also be eliminated by a vacuum vessel design optimized for shielding, or, simply by a vacuum vessel with an increased thickness of 5 to 7 cm. The blanket design option with a pure ceramics pebble bed in an enlarged breeding zone, on the other hand, does not improve the shielding efficiency with respect to the reference design, although it reduces the neutron leakage out of the breeding zone. This observation shows the great importance of the neutron moderation for the shielding efficiency: it is not sufficient to keep the neutron radiation at a low level, but it is necessary, furthermore, to obtain a well moderated neutron spectrum. In this case, the emerging neutron radiation is easily absorbed in the structural components of the blanket segment, or, subsequently, in the vacuum vessel.

References:

1. U. FISCHER: "Optimal Use of Beryllium for Fusion Reactor Blankets, Fusion Technology", 13 (1), 1988, 143 - 152

2. J.F. BRIESMEISTER (Ed.): "MCNP - A General Monte Carlo Code for Neutron and Photon Transport, Version 3A", Report LA-7396-M, Rev. 2, Sept. 1986

3. P. VONTOBEL: "Generation of an EFF-1 Based Monte Carlo Neutron Library for MCNP", Paul Scherrer Institut, Villigen, Switzerland, 1990

4. U. FISCHER: "Die neutronenphysikalische Behandlung eines (d, t)-Fusionsreaktors nach dem Tokamakprinzip (NET)", KfK-4790, Oktober 1990

5. U. FISCHER: "Impact of Ports on the Breeding Performance of Liquid Metal and Solid Breeder Blankets in the DEMONET-configuration", 2. Int. Symp. on Fusion Nuclear Technology, June 2 - 7, 1991, Karlsruhe, F.R. Germany

neutron multiplication M	1.676 ± 0.2 %
tritium breeding ratio TBR	
outboard segment	0.771 ± 0.4 %
upper canisters	0.064 ± 1.7 %
inboard segment	0.244 ± 1.2 %
divertor region	0.089 ± 1.5 %
total TBR	1.167 ± 0.3 %

Table 2.2.1: Neutron balance of the solid breeder blanket in the Demo reactor configuration

	Replacing of beryllium/ceramics mixture in the divertor region and the "upper canisters" by a pure ceramics pebble bed	Additionally: reducing outboard beryllium thickness to 27 cm by replacing beryllium/ceramics mixture accordingly	Additionally: reducing inboard beryllium thickness to 14 cm by replacing beryllium/ceramics mixture accordingly
M	1.652 ± 0.2 %	1.636 ± 0.2 %	1.624 ± .2 %
TBR	1.172 ± 0.5 %	1.164 ± 0.5 %	1.161 ± 0.5 %
Beryllium savings [tons]	56.5	88.0	99.6

Table 2.2.2: Various measures for reducing the beryllium inventory

inboard segment (11.25⁰)	
central part	14.47
divertor breeding region	4.00
total inboard	18.47
outboard segment (7.5⁰)	
central part	27.93
upper canisters	2.26
total outboard	30.19
total power production	2040

Table 2.2.3: Power production [MW] in single blanket seg-
ments and in the complete Demo reactor with
a fusion power of 2216MW

	^{6}Li (n, α) t	^{9}Be $(n, t)^7$Li
<u>inboard segment (11.25^0)</u>		
central part	2.58	$1.54 \cdot 10^{-2}$
divertor breeding region	0.94	$1.79 \cdot 10^{-3}$
total inboard	3.52	$1.72 \cdot 10^{-2}$
<u>outboard segment (7.5^0)</u>		
central part	5.42	$3.16 \cdot 10^{-2}$
upper canisters	0.45	$9.12 \cdot 10^{-3}$
total outboard	5.87	$4.1 \cdot 10^{-2}$
<u>total tritium production rate</u>	394.4	2.50

Table 2.2.4: Tritium production rate [g/d] in single blanket segments and in the complete Demo reactor with a fusion power of 2216 MW

	Radiation design limits	Reference design ("steel plate option")	"ZrH-option" 10 % ZrH 70 % steel	"ZrH-option" 20 % ZrH 70 % steel	"ceramics option"
Epoxy radiation dose [rad]	$\sim 5 \cdot 10^9$				
torus mid-plane		$1.29 \cdot 10^{10}$	$7.96 \cdot 10^9$	$5.27 \cdot 10^9$	$1.39 \cdot 10^{10}$
poloidal average		$7.50 \cdot 10^9$	$4.08 \cdot 10^9$	$2.63 \cdot 10^9$	$7.39 \cdot 10^9$
Fast neutron fluence [cm^{-2}]	$\sim 10^{18}$				
torus mid-plane		$3.76 \cdot 10^{18}$	$3.50 \cdot 10^{18}$	$2.84 \cdot 10^{18}$	$3.75 \cdot 10^{18}$
poloidal average		$2.17 \cdot 10^{18}$	$1.65 \cdot 10^{18}$	$1.20 \cdot 10^{18}$	$2.31 \cdot 10^{18}$
Maximum power density [mW/cm^3]	~ 1.0				
torus mid-plane		3.19	1.96	1.30	3.44
poloidal average		1.85	1.0	0.65	1.82
Total power production in the TF-coil [kW]	~ 20	26.0	14.6	9.8	25.6

Table 2.2.5:   Radiation loads on the inboard TF-coil for various design options (20 000 h integral operation time)
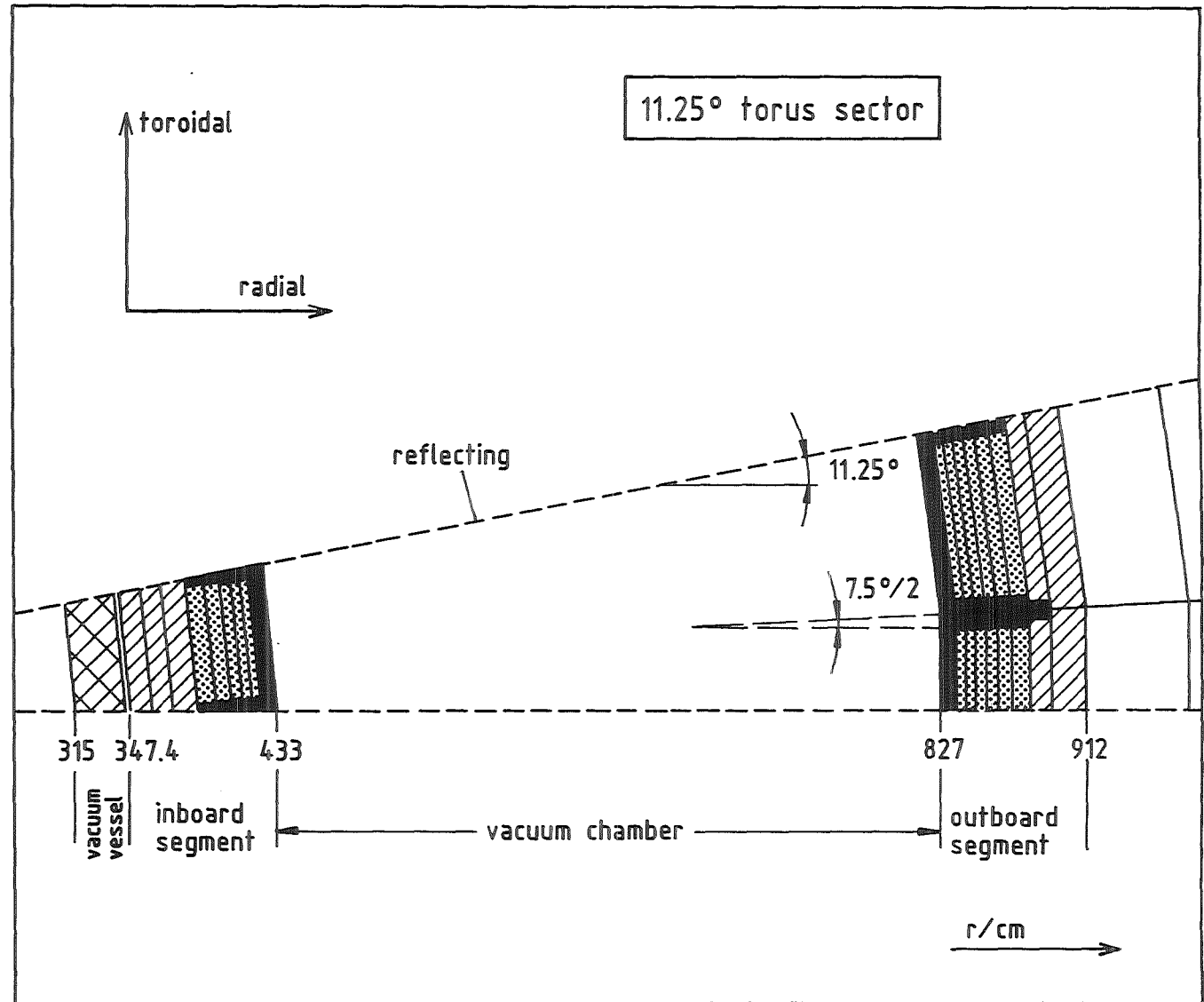
Fig. 2.2.1   Radial-toroidal cross-section of the 11.25⁰ torus sector model

poloidal

radial

upper divertor

inboard blanket segment

lower divertor

upper canisters

outboard blanket segment

structure (MANET)

vacuum vessel

vacuum chamber
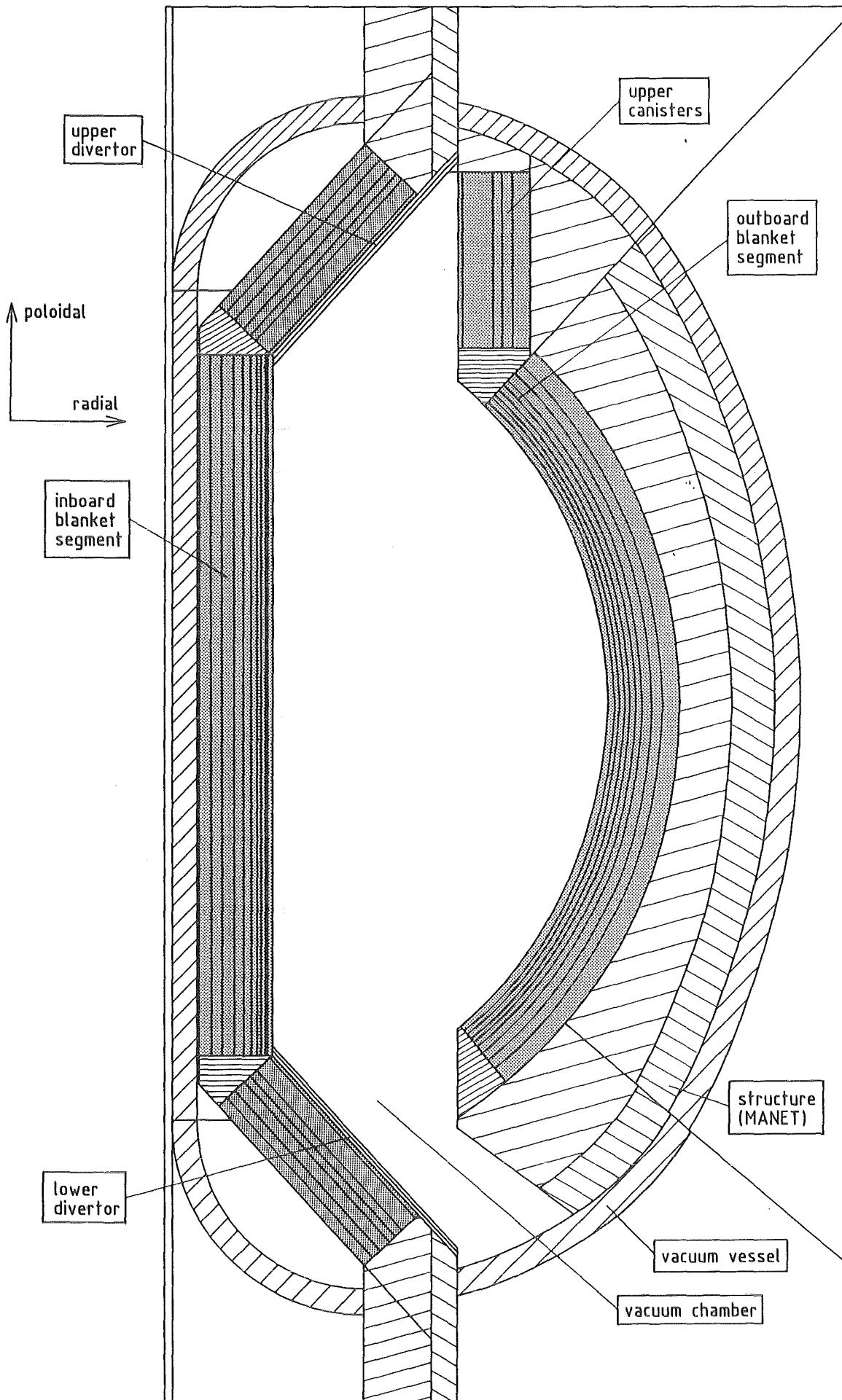
Fig. 2.2.2   Radial-poloidal cross-section of the 11.25⁰ torus sector model
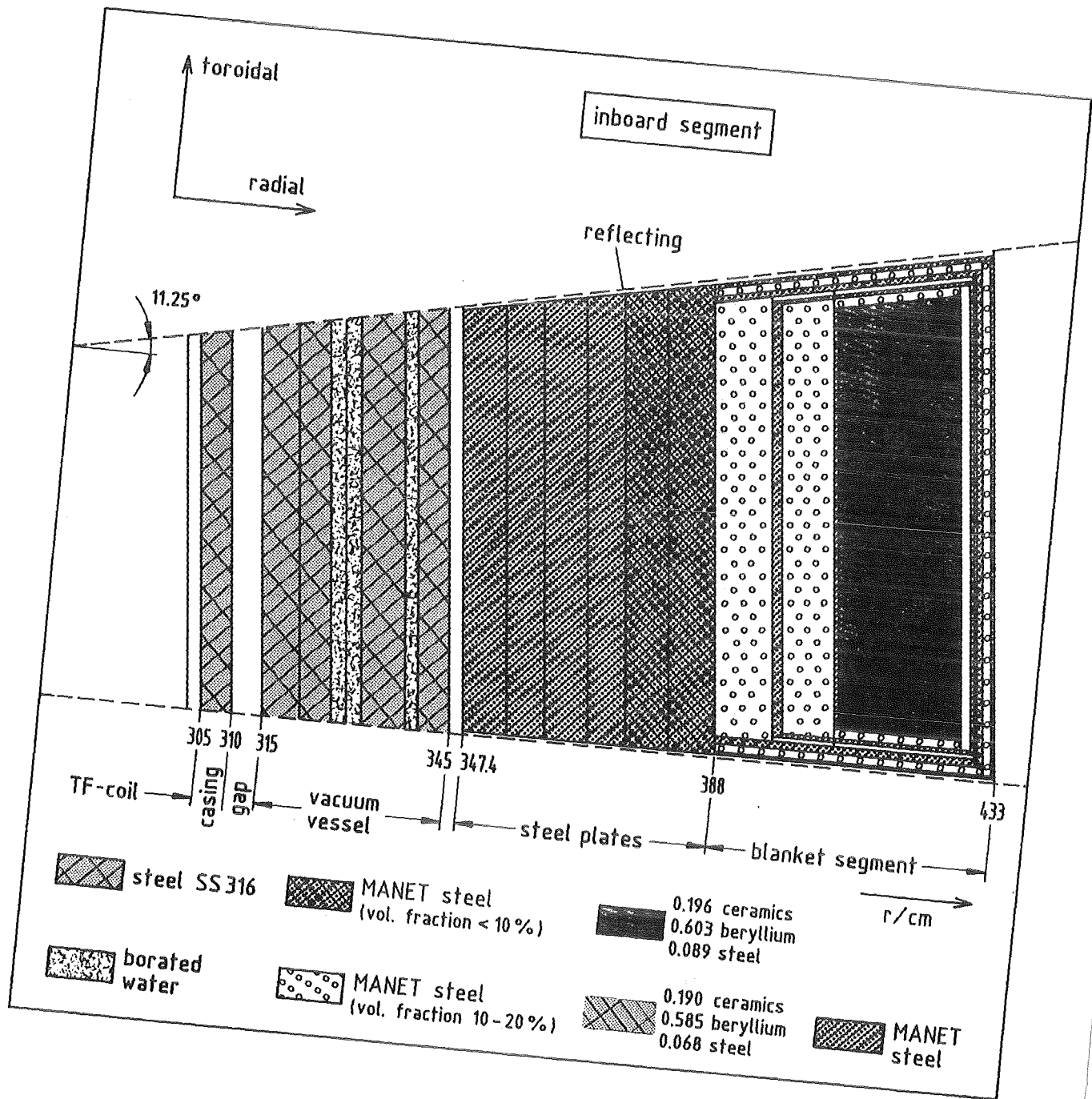
Fig. 2.2.3 a)   Material composition in the inboard segment
(radial-toroidal cross-section).
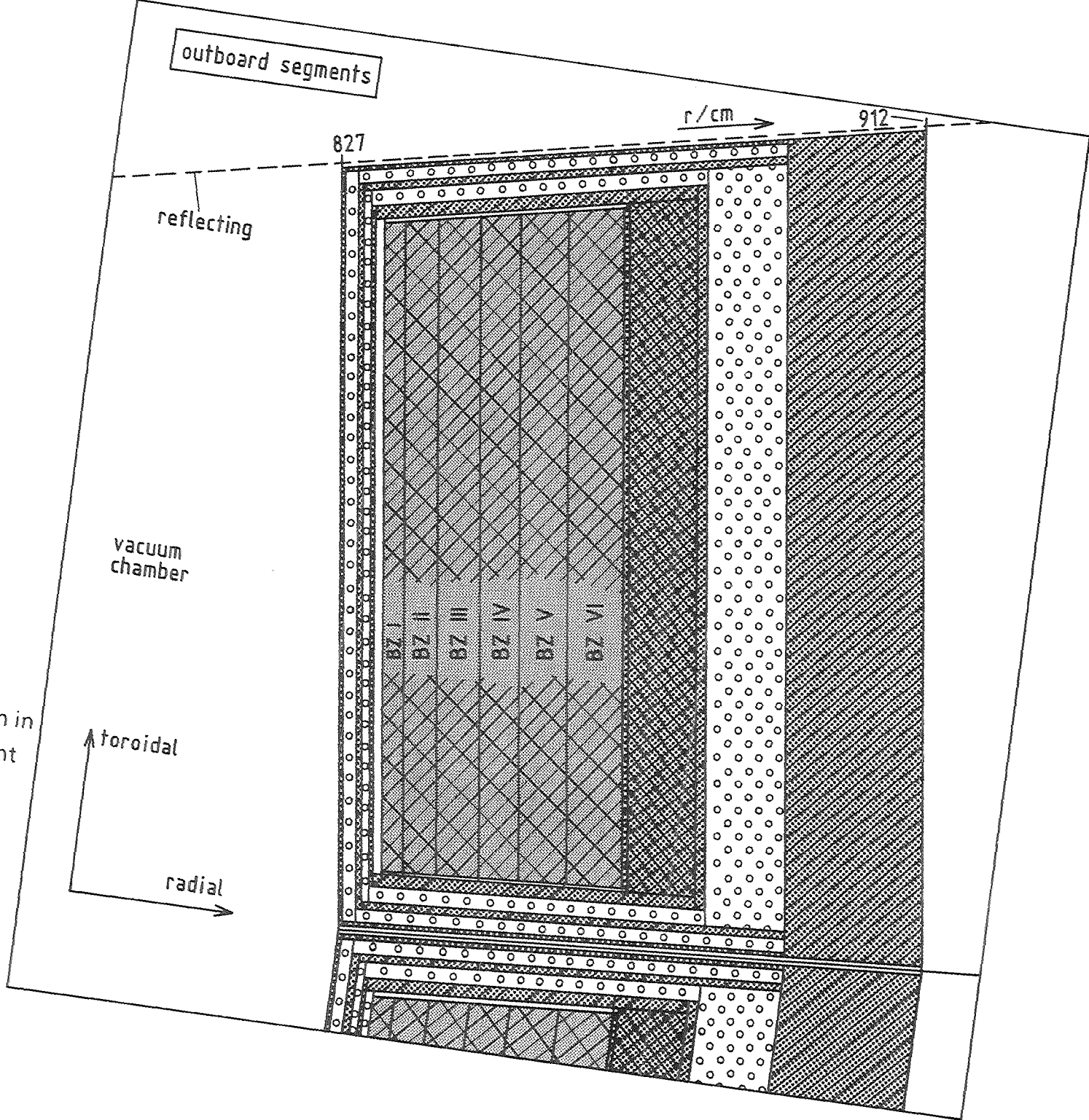
Fig. 2.2.3b)   Material composition in the outboard segment (radial-toroidal cross-section)
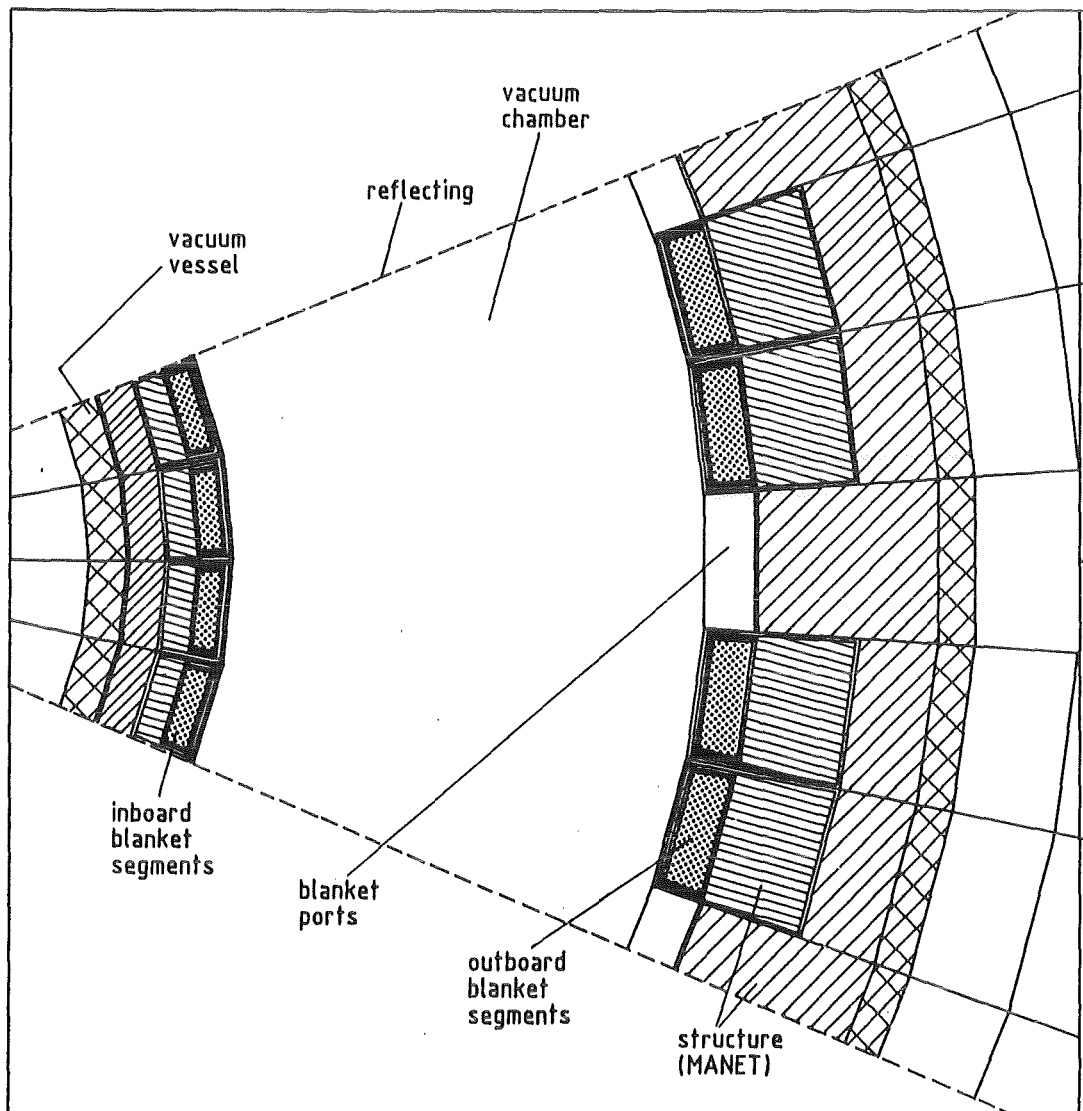
Fig. 2.2.4 a)   4 x 11.25⁰ torus sector model for analyzing the port effect.

Radial-toroidal cross-section at torus mid-plane.

Fig. 2.2.4b) 4×11.25^0 torus sector model for analyzing the port effect. Radial-toroidal cross-section at the centre of the torus sector
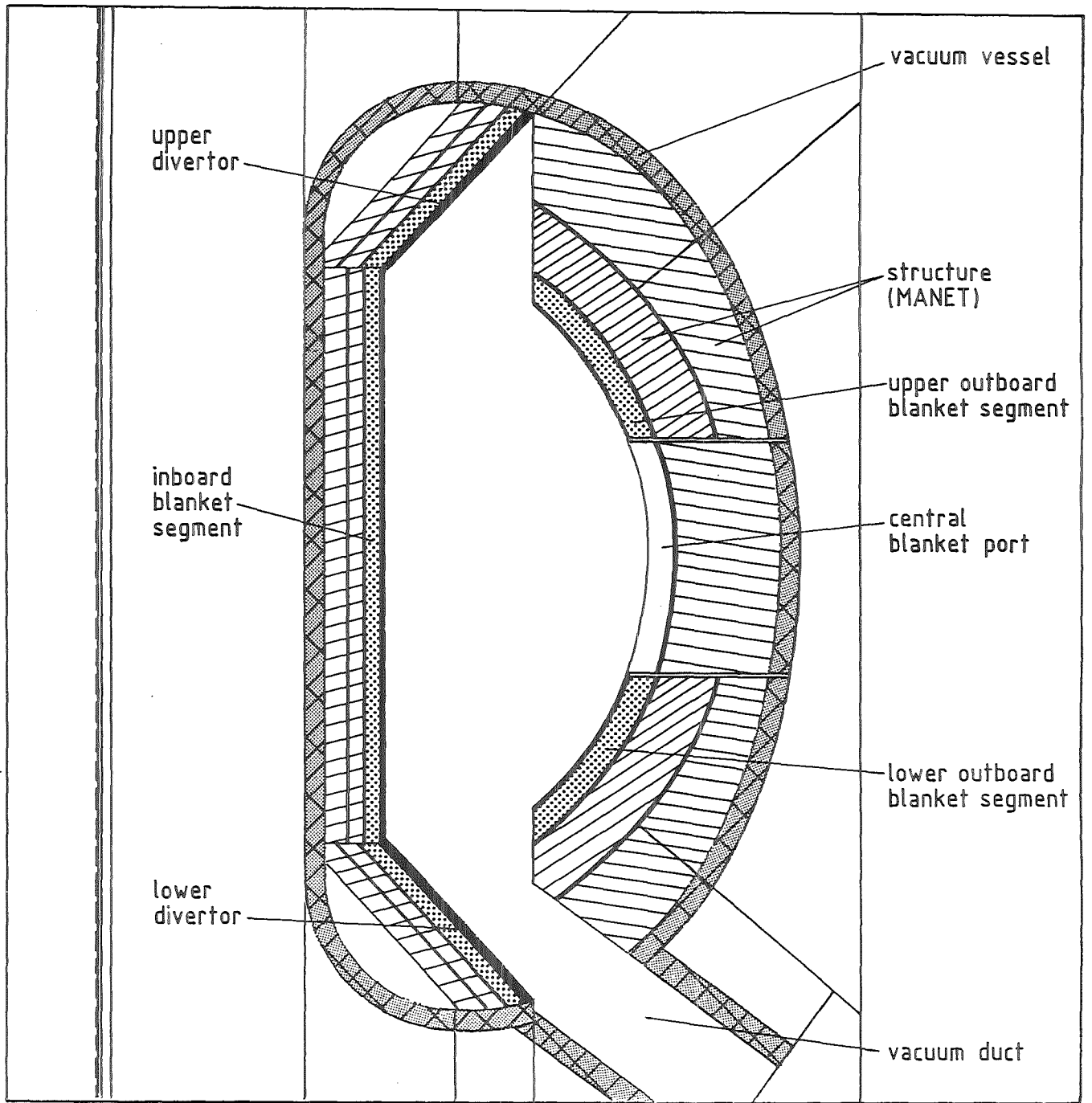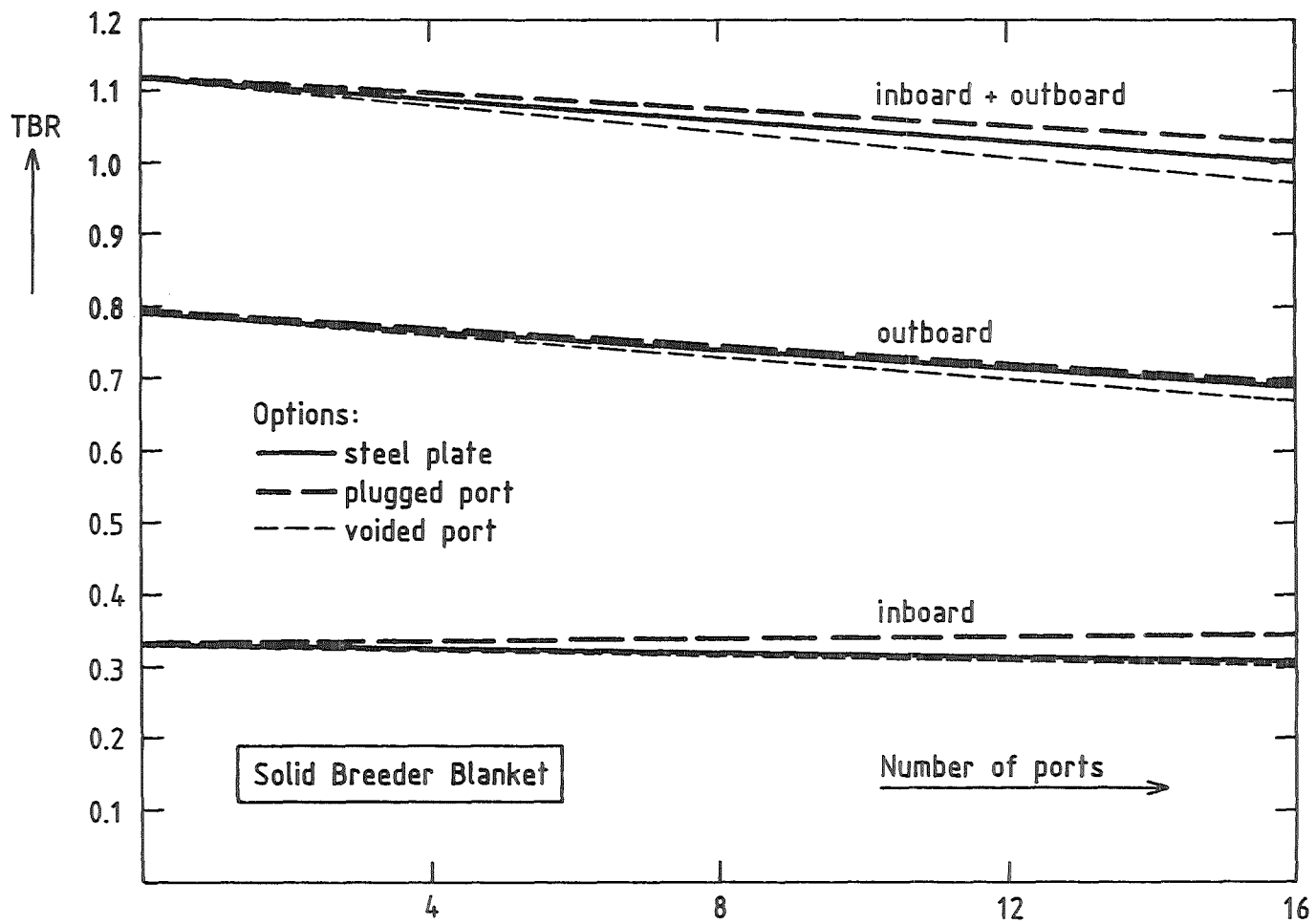
Fig. 2.2.5   Dependence of the tritium breeding ratio (TBR) on the number of outboard blanket ports
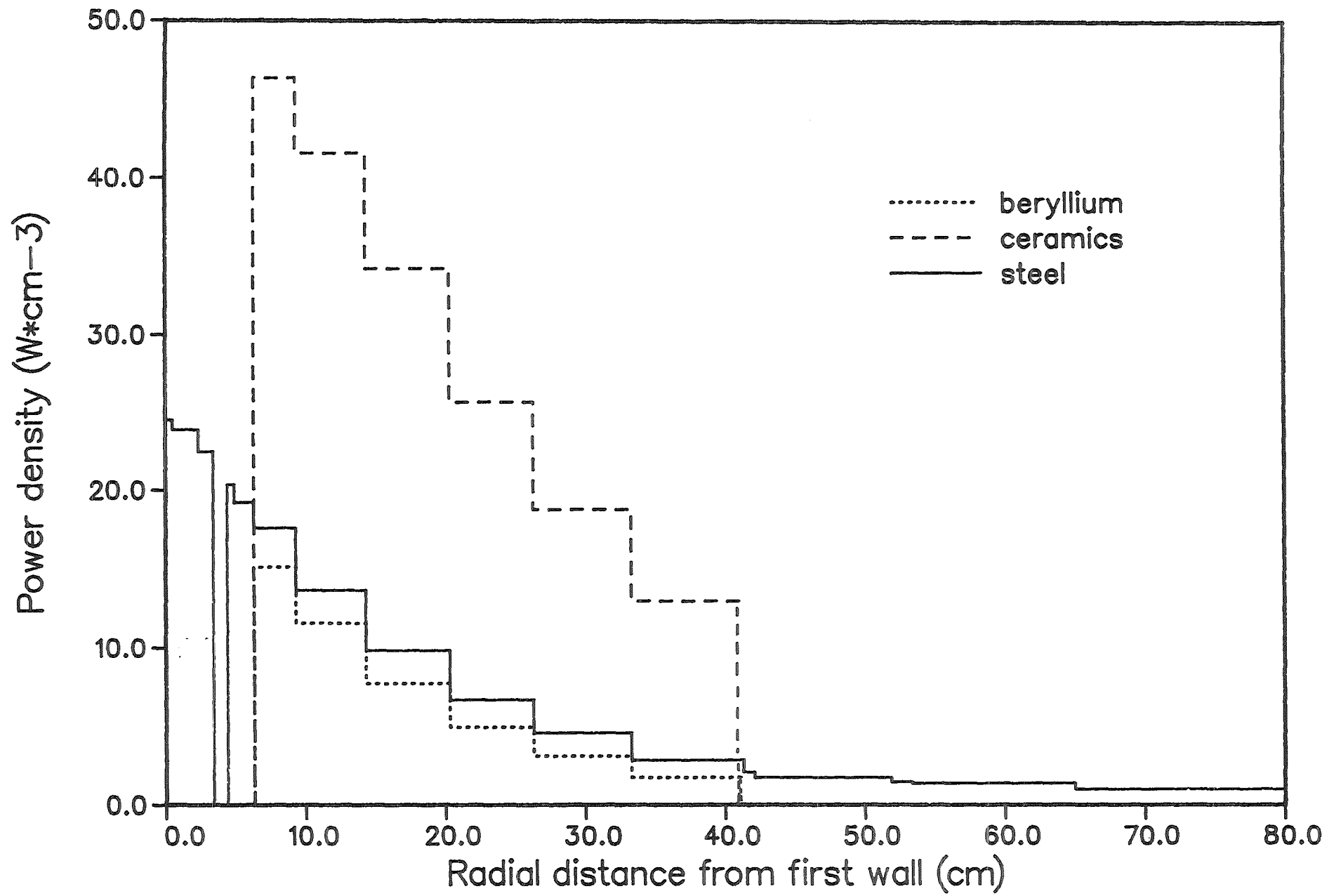
Fig. 2.2.6a)   Radial profiles of the power density at the torus mid-plane of the outboard segment.
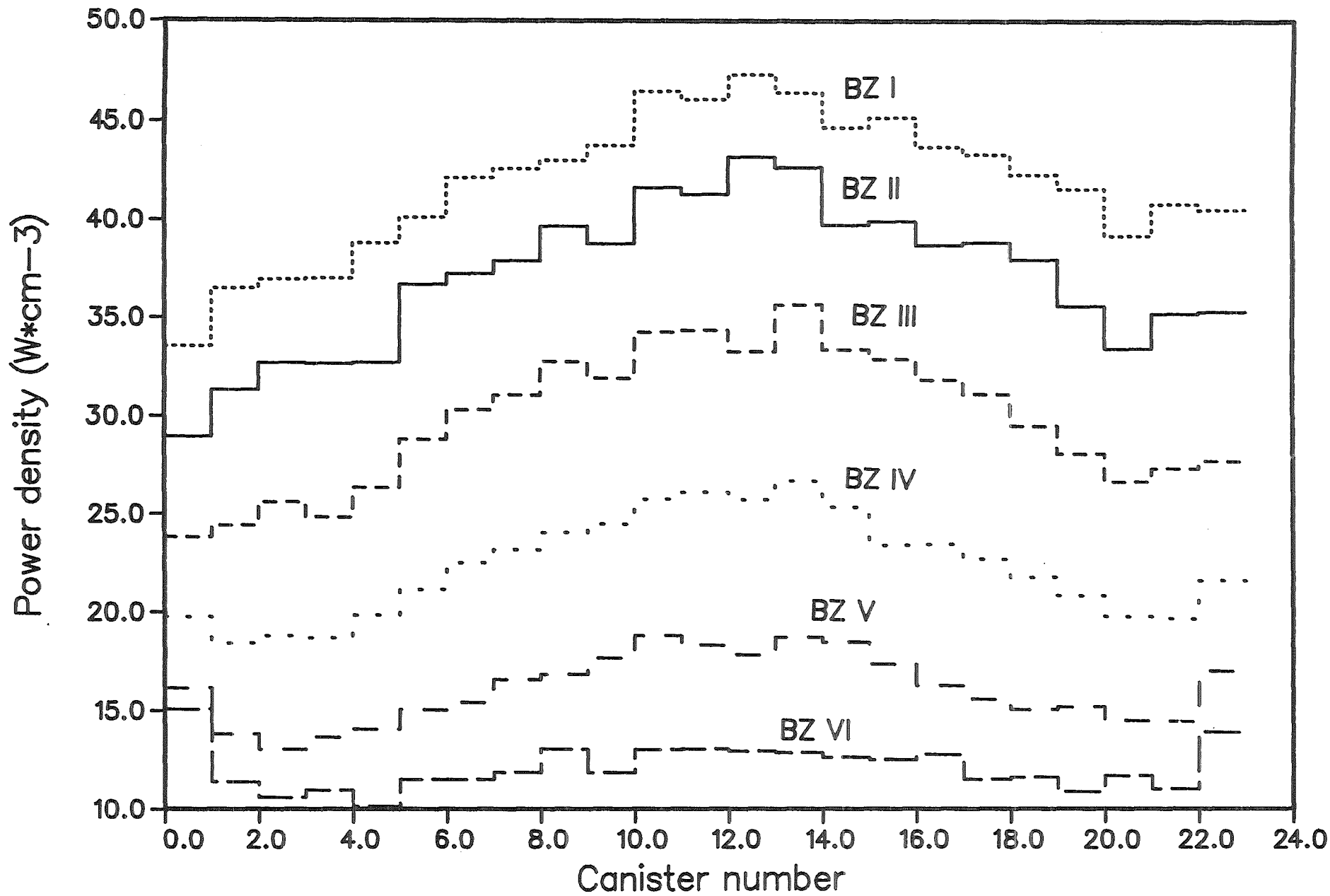
Fig. 2.2.6b) Poloidal profiles of the ceramics power density in the outboard blanket segment
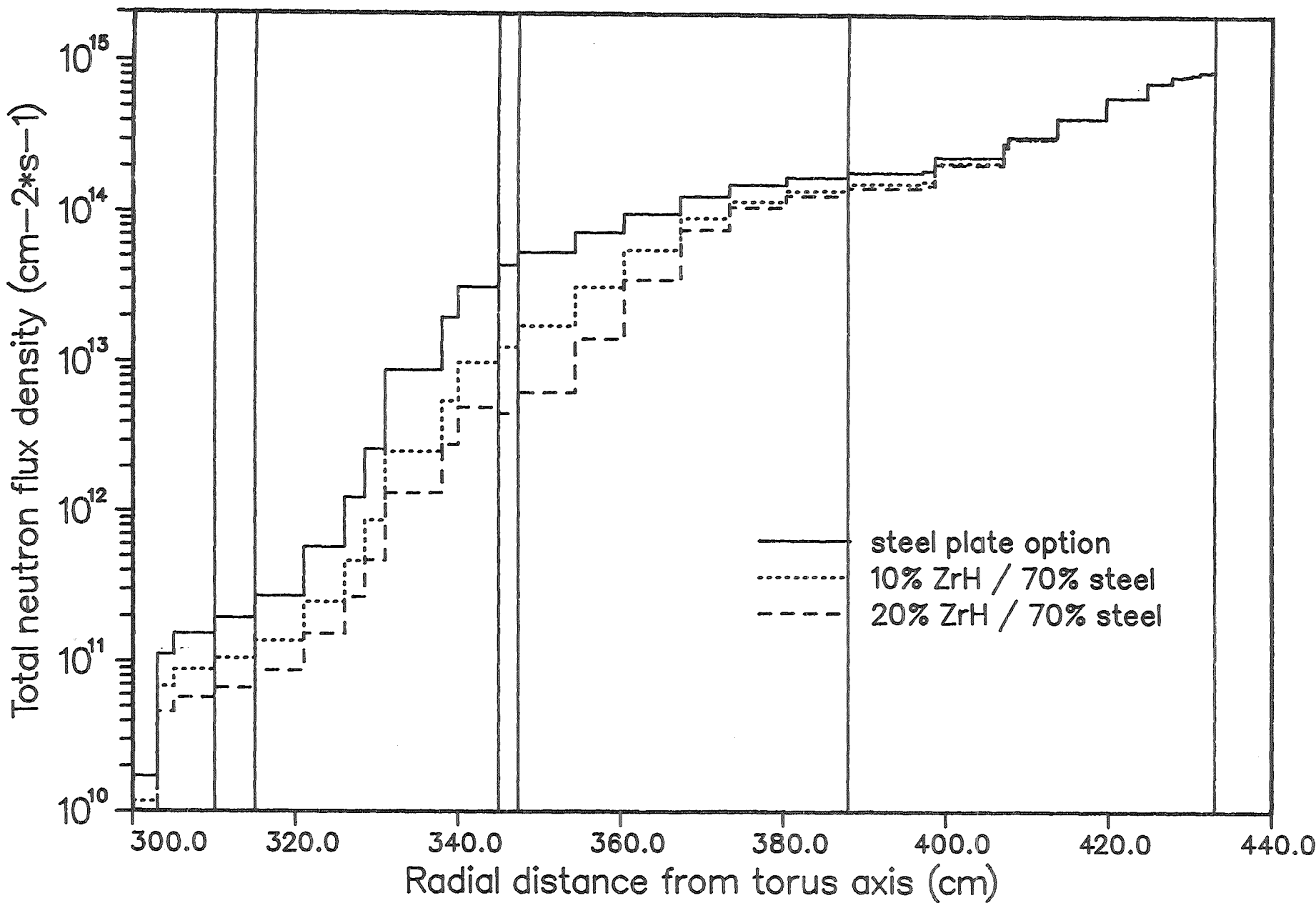
Fig. 2.2.7a)   Radial profiles of the total neutron flux density across the inboard blanket
segment and the vacuum vessel (poloidal average)
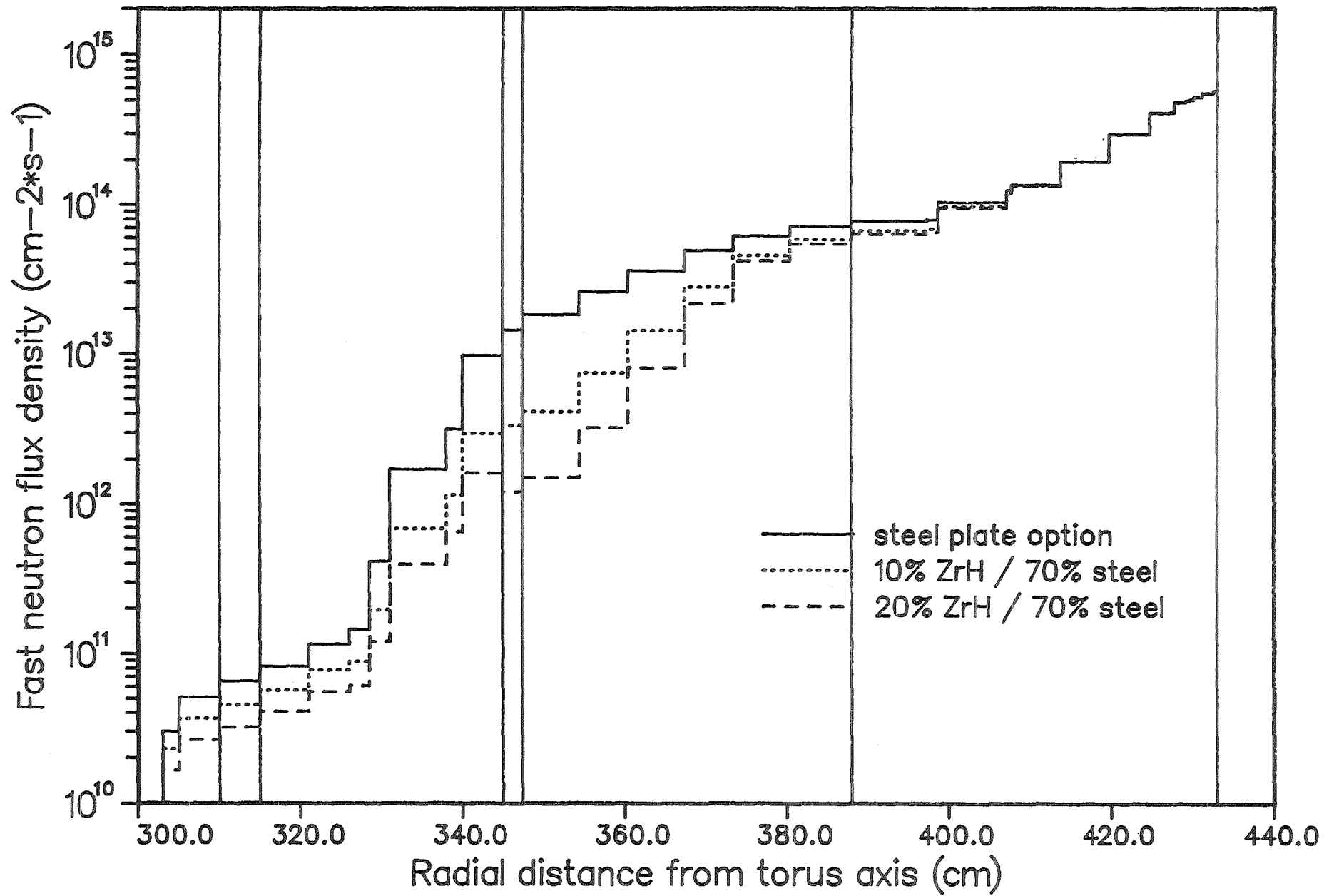
Fig. 2.2.7b)   Radial profiles of the fast (E > 0.1 MeV) neutron flux density across the
inboard blanket segment and the vacuum vessel (poloidal average)

2.3   Thermohydraulics and Stress Calculations (M. Dalle Donne, P. Norajitra)

2.3.1   Assumptions

In Ref. [1] more details are given on the methods used for the thermohydraulic calcula-
tions. Here, it will suffice to recall the main assumptions used. They are listed below.

1.   The convective heat transfer coefficient between coolant channel walls and flowing
      helium has been calculated using the correlation of Ref. [2]. The relevant thermohy-
      draulic properties of helium are taken from the correlations proposed in Ref. [3].

2.   The effective thermal conductivity of the bed of Li_4SiO_4 pebbles has been measured
      at KfK (Section 4.5.4). For the bed of 0.5 mm Li_4SiO_4 in helium the measured effec-
      tive thermal conductivity data may be correlated by the equation:

$$K_e\,[W/mK] = 0.85 + 2.5 \times 10^{-4}\,T - e^{-0.00776T}, \quad T\,[°C] \tag{1}$$

      The measured heat transfer coefficient between particle bed and bed wall is equal
      to 0.45 W/cm^2 °C. Recent measurements for a bed with Li_4SiO_4 pebbles in the diame-
      ter range 0.35 ÷ 0.6 mm indicate that the thermal conductivity of this pebble bed is
      correlated by the same equation, while the heat transfer coefficient at the bed wall
      is higher, i.e. equal to 0.62 W/cm^2 °C.

3.   The friction pressure drops in the coolant helium channels have been calculated with
      the usual Prandtl-Nikuradse equation [4]. The pressure drops due to bends and flow
      cross-section changes have been calculated with equations given in Refs. [5, 6 and 7].
      The pressure drop caused by the flow of purge helium in the pebble bed has been
      calculated with the correlation of Ref. [5].

4.   The radial and poloidal power distribution has been obtained by the three-dimen-
      sional neutronic calculations (Section 2.2). To obtain a uniform helium outlet tem-
      perature, the helium mass flow per canister has been assumed proportional to the
      power produced in the canister itself. This means that the helium flow to each canis-
      ter should be controlled by proper gagging.

2.3.2   Results

Fig. 2.3.1 shows the tridimensional temperature distribution in the beryllium and in the
Li_4SiO_4 pebble bed in a radial / poloidal slab of an outboard blanket canister placed at the
equatorial plane of the torus. This is the highest rated canister. The temperatures shown
in the figure are the highest in the outboard blanket, and they are also equal or higher
than the maximum values occurring in the inboard blanket.

The temperature calculations have been performed with the computer code ABAQUS [8]. The maximum temperature in the pebble bed is 823 °C. It has been calculated assuming a heat transfer coefficient at the interface beryllium-steel coolant tubes of 3 W/cm² °C, which allows for a small gap of a few µm between beryllium and steel coolant tubes: In case of a heat transfer coefficient of 1 W/cm² °C, corresponding to a gap of 20 µm, the temperature would increase to 850 °C. These values are probably slightly pessimetric, as they have been calculated with the old value of the heat transfer coefficient at the interface pebble bed / beryllium (0.45 /cm²°C) rather than the new one (0.62 W / cm²°C) obtained with the bed of pebbles with variable diameter.

The maximum temperature in the beryllium is 600 °C, while the maximum temperatures at the beryllium / pebble bed interface is 610 °C. The maximum temperatures at the interface steel / beryllium and in the steel pressure tubes are 550 °C and 540 °C respectively. All these temperatures appear to be within acceptable limits.

Fig. 2.3.2 shows a more detailed temperature distribution in the radial-toroidal section A-B of Fig. 2.3.1. The local power densities in the pebble bed, in the steel and in the beryllium are shown as well.

Fig. 2.3.3 shows a poloidal-radial cross section of the outboard first wall at the equatorial plane of the torus, where the power densities are the highest. Also shown are the boundary conditions used for the temperatures and thermal stress calculations. These values have been obtained with the general thermohydraulic calculations, while the power densities are from the three-dimensional neutronic calculations. The heat flux from the plasma is 50 W/cm² i.e. the peak value specified by the European Test Blanket Advisory Group (see Section 1.1).

The von Mises stresses in the first wall, given by the thermal stresses and the helium pressure inside the cooling tubes, are calculated with the assumption of generalized plain strain elements [8]. At the peak temperature of 551 °C the von Mises stress is 228 MPa while the primary stress is only 15 MPa at this point. All the stresses are within the ASME limits.

Figure 2.3.4 shows the results of the tridimensional temperature calculations for a radial / toroidal section of the outboard box, again at the equatorial plane of the torus. This is formed by the first wall, by the radial walls and at the back by the poloidal feeding manifolds welded together. Fig. 2.3.5 shows the temperatures and the stresses for these manifolds. Also here are the temperatures and stresses within the allowable limits.

The minimum temperature in the breeder material has been calculated with the pessimistic, as far as tritium inventory is concerned, assumption of perfect contact between beryllium and coolant tubes (heat transfer coefficient = ∞). The resulting value is 380 °C.

References

1. M. DALLE DONNE, S. DORNER, and S .TACZANOWSKI, "Conceptual Design of Two Helium Cooled Fusion Blankets (Ceramic and Liquid Breeder) for INTOR", KfK-3584, EUR-7987e, Kernforschungszentrum Karlsruhe (1983).

2. M. DALLE DONNE and F.W. BOWDITCH, "Experimental Local Heat Transfer and Friction Coefficient for the Flow of Air or Helium in a Tube at High Temperatures", OECD Dragon Project, Report 184, Organization for Economic Cooperation and Development (1963).

3. H.J- PFRIEM, "Der turbulente Wärmeübergang an Helium und Wasserstoff in beheizten Rohren bei großen axial steigenden Temperaturdifferenzen und das sich daraus ergebende Temperaturprofil", KfK-1860, Kernforschungszentrum Karlsruhe (1973).

4. H. SCHLICHTING, "Boundary Layer Theory", 4th ed., McGraw-Hill, Inc., New York (1969).

5. VEREIN DEUTSCHER INGENIEURE, "VDI-Wärmeatlas", VDI-Verlag, Düsseldorf (1984).

6. W. KALIDE, "Strömungslehre", Carl Hansen Verlag, München (1971).

7. I.E. IDEL'CHIK, "Handbook of Hydraulic Resistance, Coefficients of Local Resistance and of Friction", AEC-TR-6630, Atomic Energy Commission (1960).

8. "ABAQUS-A General Purpose Linear and Non Linear Finite Element Code, Update to Version 4.5", Hibbit Karlsson and Lorensen, Inc., Providence, Rhode Island (1986).

He - INLET
313°C
①

He - OUTLET
446°C
⑩

⑦   ④

389   419   464   477   460   431   431

BERYLLIUM PLATE
21 mm

467

431

408   441   486   499   482   452   446

COOLANT TUBE
14/12 mm

515

446

437   476   522   534   518   486   470

577

470   475   530   576   561   571   539   503

663

592   587

503   520   578   558   594   544

775   539   529   550   600   563

541   546   547   543   551   565

813   823   818   805   802   805   818   823

563   565   551   543   542   546   541

RADIAL

TOROIDAL

POLOIDAL

q (R) [W/cm³]

2 3 13
3 5 18
5 7 26
8 11 33
12 15 43
15 18 47

STEEL
BERYLLIUM
CERAMIC

3D - TEMPERATURE DISTRIBUTION

MAX. CERAMIC TEMPERATURE

Li - CERAMIC PEBBLE BED
6 mm

MAX. BERYLLIUM TEMPERATURE

— 52 —

Fig. 2.3.1   Temperature distribution in a radial / poloidal slab of an outboard blanket canister placed at the equatorial plane of the torus

POINT	1	2	3	4	5	6	7	8	9	10
He - TEMP. (°C)	313	332	363	380	394	410	421	431	437	446

He - MASS FLOW PER TUBE: 43.5·10⁻³ kg/s (COUNTER FLOW IN ADJACENT COILS OF TUBE)
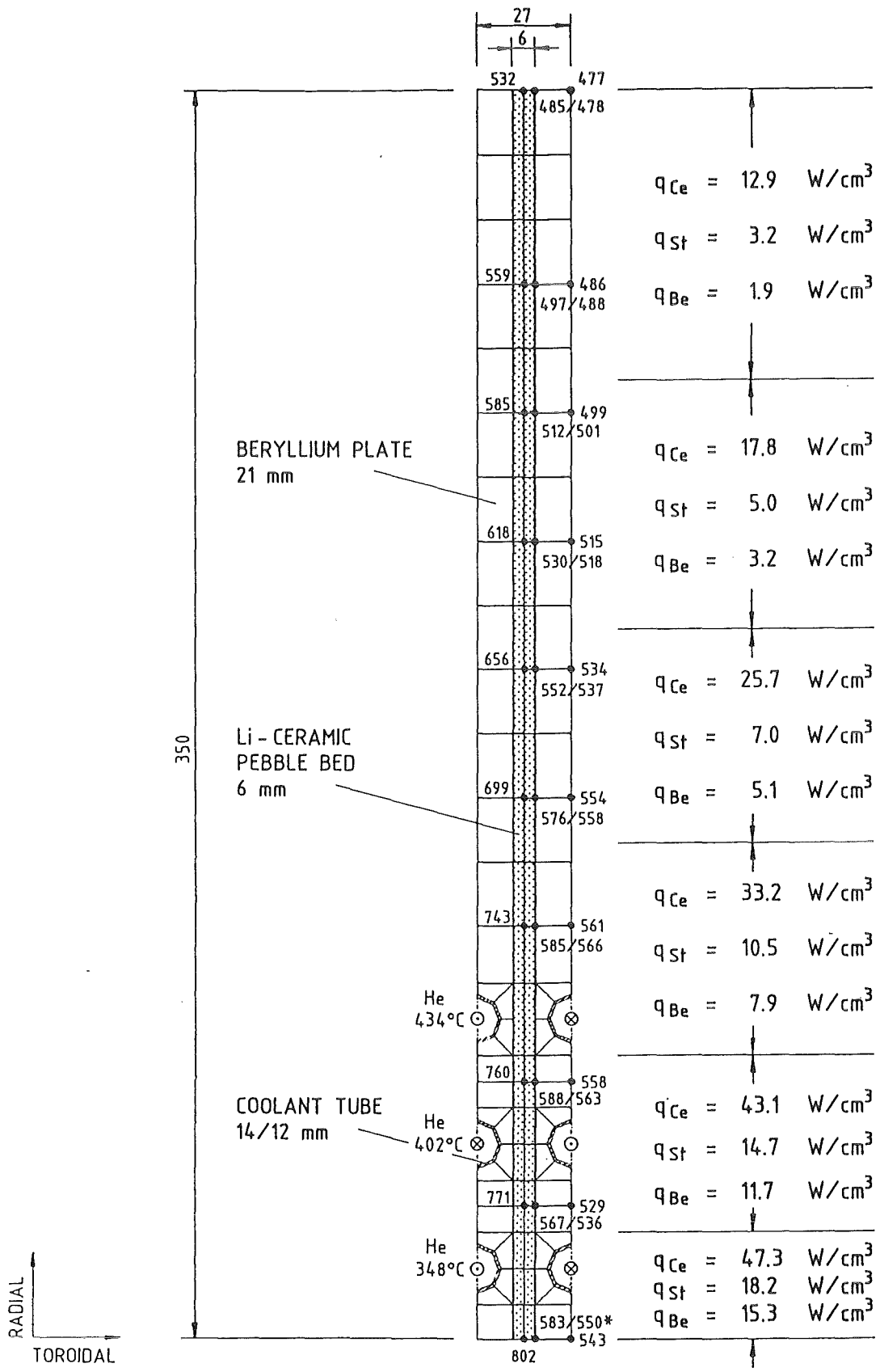
Fig. 2.3.2   Temperature distribution in the radial / toroidal cross section A-B of Fig. 2.3.1 (temperatures in °C).

TEMPERATURE DISTRIBUTION (2D)

SURFACE HEAT LOAD: 50 W/cm²

	(°C)
K	550
J	525
I	500
H	475
G	450
F	425
E	400
D	375
C	350
B	325
A	300

HELIUM

299 °C   256 °C   299 °C

TORUS MIDPLANE

FIRST WALL (MANET) q = 24 W/cm³

POLOIDAL

RADIAL
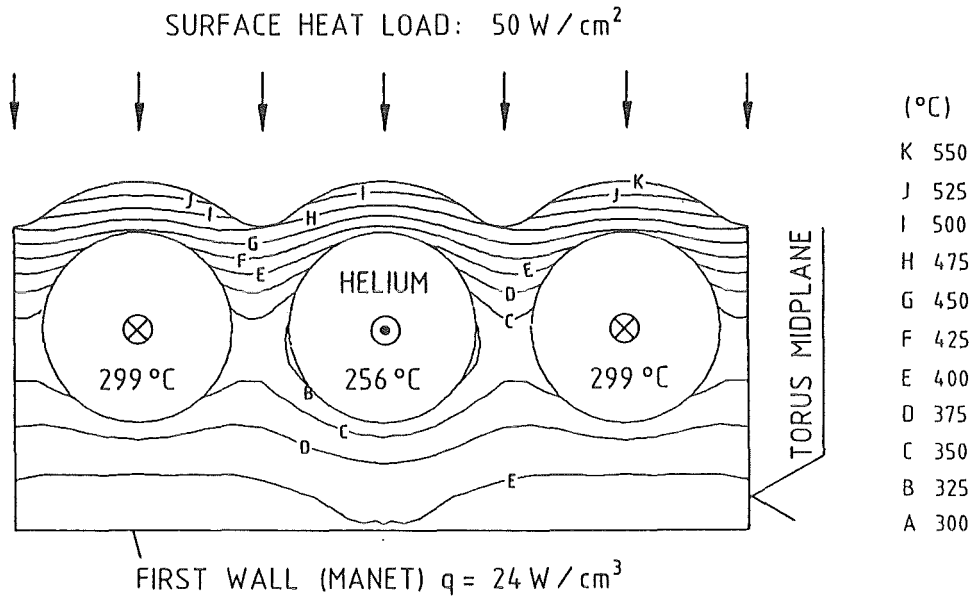
VON MISES STRESS DISTRIBUTION (2D)

	(MPa)
G	400
F	350
E	300
D	250
C	200
B	150
A	100

HELIUM

80 bar   80 bar   80 bar
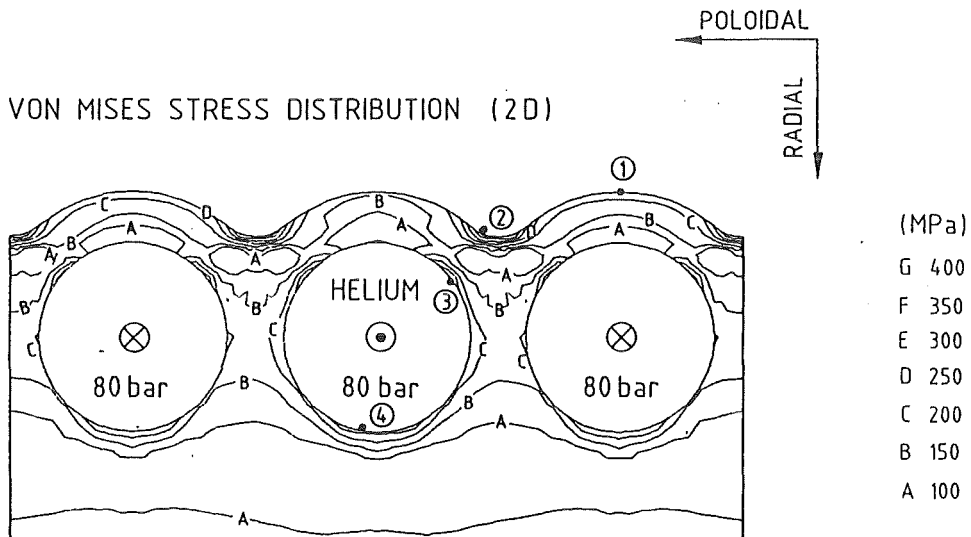
Point	Temperature [°C]	prim. + sec. Stresses [MPa]	allowable Stresses [MPa]
1	551 (max.)	228	430
2	481	437 (max.)	516
3	379	307	620
4	333	286	657

Fig. 2.3.3   Temperature and stress distribution of the outboard first wall at the torus equatorial plane, where the power densities are the highest.

HELIUM MAIN TUBE
q = 1 W/cm³

INLET
250°C

OUTLET

450°C

TEMPERATURE DISTRIBUTION (3D)

SIDE WALL
q = 1 - 23 W/cm³

467
458
265
256
279
288
303°C
401
362
265
300
304
455
251°C
292
458
467
He 303°C
332
465
458
467
300
332
425
382
458
467
410

FIRST WALL
q = 24 W/cm³
PLANE OF SYMMETRY

479
547
410
524
479
567
410
541
479
530
410
536
541
536
He
277°C
406
536

MAX. FW - TEMP.

112·10⁻³ kg/s

TORUS MIDPLANE

50 W/cm²

RADIAL   POLOIDAL   TOROIDAL

— 55 —

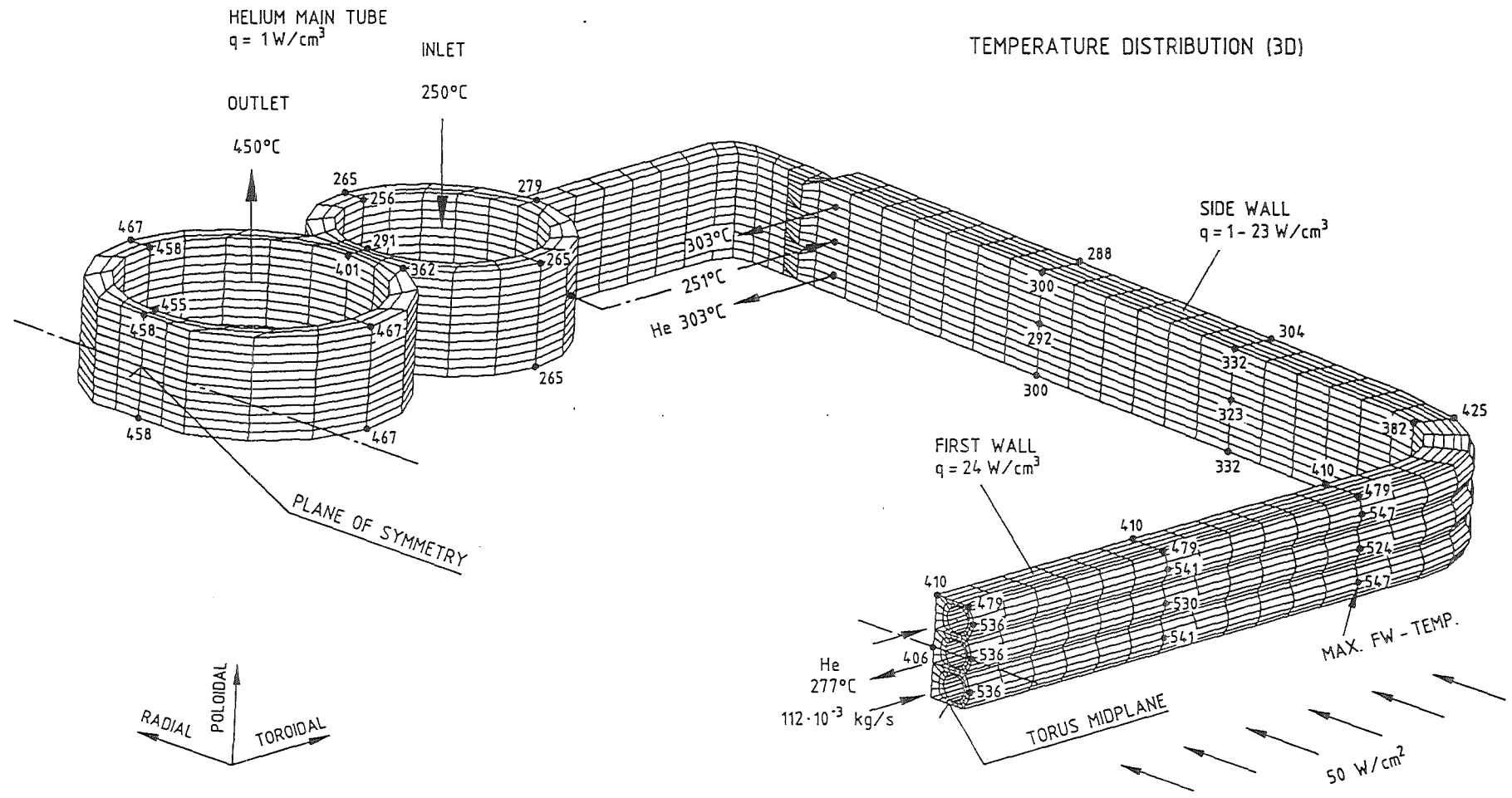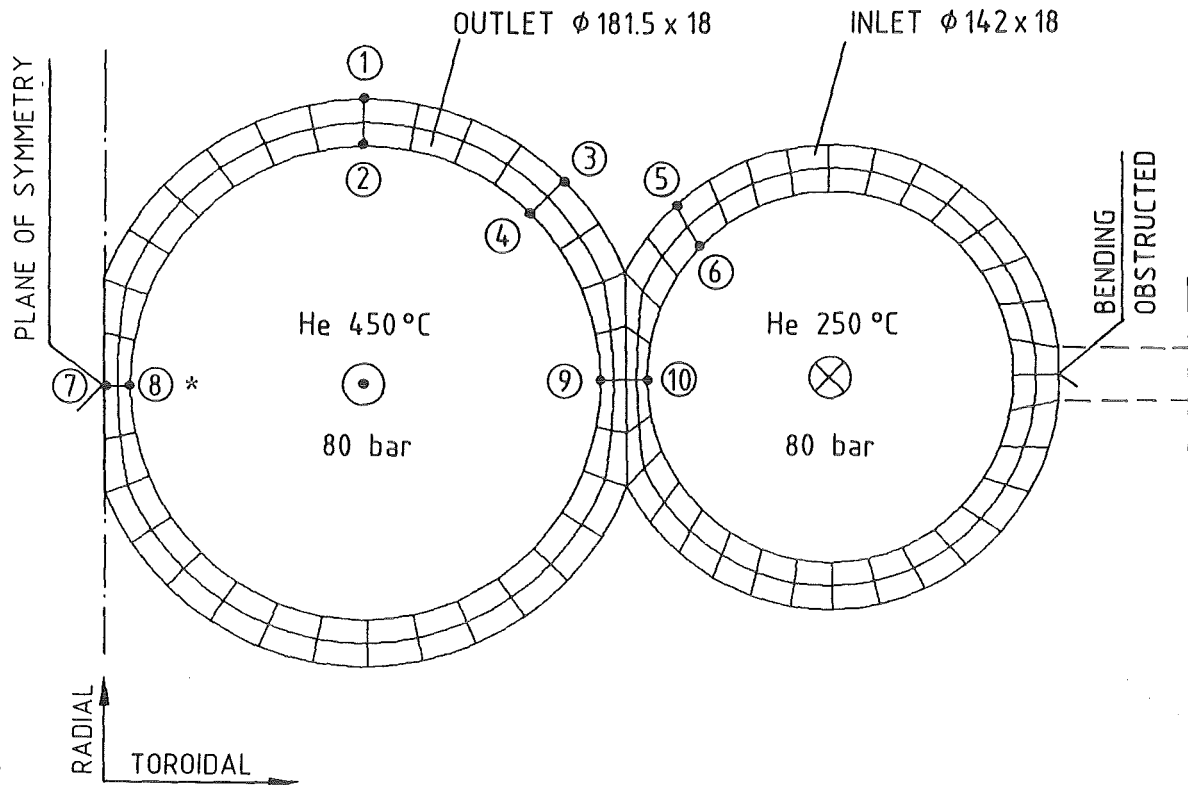Fig. 2.3.4   Temperature distribution in a radial toroidal section of the blanket box at the outboard torus equatorial plane (temperatures in °C).

HELIUM MAIN TUBES, q = 1.25 W / cm³

OUTLET Ø 181.5 x 18   INLET Ø 142 x 18

He 450°C

80 bar

He 250 °C

80 bar

PLANE OF SYMMETRY

BENDING OBSTRUCTED

RADIAL

TOROIDAL

Point	Temperature [°C]	prim. + sec. Stresses [MPa]	allowable Stresses [MPa]
1	467 (MAX.)	114	532
2	458	94	542
3	458	242 (MAX.)	542
4	454	186	546
5	276	181	697
6	262	197	706
7	458	114	542
8	455	112	545
9	401	232	599
10	291	94	687

*   Max. primary membrane stress 75 MPa (allowable 175 MPa)

Fig. 2.3.5   Temperature and stress distribution in a radial / toroidal section of the poloidal feeding manifolds.

2.4 Magnetic Forces in the Blanket Structures Caused by Disruptions (L.V. Boccaccini)

In all operating tokamaks it has been observed that, under certain circumstances, the plasma collapses and the plasma current decreases very rapidly to zero. The rapid current variation produces induced eddy currents in the surrounding metallic structures. These currents, together with the strong stationary magnetic fields present in the tokamak, produce large magnetic forces in the structures surrounding the plasma. In particular, plasma disruptions have a significant impact on the design of the blanket, since large currents can be induced due to its proximity to the plasma.

In the frame of the Karlsruhe Helium Cooled Solid Breeder Blanket development a computational system has been developed to calculate eddy currents and the resulting forces and stresses in the structures [1] . Calculations have been already performed for the blanket design for NET/ITER (plasma current 10.8 *MA*) [2] . The main conclusion of that work [1, 3] was that, during a main plasma disruption event, load distributions can arise able to endanger the structural integrity of the blanket. It was also pointed out that further work was required to modify the design in view of improving the mechanical behaviour of this blanket concept against the postulated disruptions.

For the Demo Blanket development the mechanical effects of plasma disruptions remain one of the critical issues, in spite of the assumption that only one main disruption event should occur in the whole life of the Demo Reactor [4]. The knowledge of load distributions, that can arise on the blanket structure during disruptions, is of primary importance particulary in the design phase where one has to compare different constructive options.

In this section a preliminary analysis of the force distribution induced during a main plasma disruption event on the segment box of the Demo blanket is presented. Owing to many simplifying assumptions used in the calculation, the presented study is not intended as a detailed engineering analysis of the consequences of a plasma disruption on the segment box. Nevertheless the results should provide a general guide to the design of this component.

As mentioned above, a computational system for the calculation of the mechanical effects of disruptions has been developed. The main element of this system is the computer program CARIDDI for the calculation of the induced eddy currents and of the magnetic forces. CARIDDI is a finite element three-dimensional program for the electromagnetic analysis of nonmagnetic materials, originally developed at the University of Naples-Salerno [5] . In the present computational system the modified version CARIDDI/KFK has been used. Two new models have been developed and introduced in this version: an improved plasma model to describe plasma motion and a magnetic stiffness and damping model to calculate eddy currents produced by the movement of a conducting structure in a magnetic field.

2.4.1 Electromagnetic calculations for the insulated outboard blanket

In the present section the results of the electromagnetic calculation for an "insulated model" of the outboard blanket are given, namely eddy currents and magnetic forces. In this model each of the 48 segment boxes of the outboard blanket is electrically insulated from the other components of the reactor. Furthermore, only the magnetic interaction among the boxes is taken into account. While the first assumption is in accordance with the reactor design, the second one is only a first approximation. The latter assumption is discussed in further detail in Sub-section 2.4.2.

In Fig 2.4.1 a schematic picture of the Demo blanket is shown with the coordinate system and geometrical definitions. Fig. 2.4.2 shows the model of the blanket that has been used in the calculation. The parts that have been included in the model are numbered in this picture and listed in Tab. 2.4.1. In the same Table the reference thickness for each plate and the corrective factor for the specific electric resistivity - to take into account the particular structure of the walls (for instance the cooling tube of the first wall or the multilayer structure of the vertical shield) - are also listed. The vertical shield (parts 9 and 10) is electrically insulated from the rest of the blanket structure.

As the program CARIDDI cannot take into account the magnetic properties of the martensitic steel Manet, a material magnetic permeability equal to the vacuum permeability has been implicitly assumed in the calculation. Furthermore, a value

of 0.9 10^{-6} Ωm has been used for the specific resistivity of the material at 350°C (average temperature of the structural material in the blanket).

The main input required by CARIDDI is the plasma current as a function of time and space during the disruption. A filamentary plasma model without motion has been used in the present calculation. The plasma current varies linearly from an initial value of 19.8 MA to zero in 20 ms, while the position of the magnetic axis remains unchanged. This is in accordance with the specifications proposed by the Test Blanket Advisory Group [4] .

The stationary magnetic fields produced by the toroidal field (TF) and poloidal field (PF) coil systems has been taken into account in the calculation of the magnetic forces. A function inversely proportional to the distance from the torus axis - with a value of 6 Tesla at the radius 6.3 m - has been used for describing the toroidal field. As the final configuration of the PF coils for Demo and the related currents are not yet fixed, the PF coils for ITER and the proposed operating scenario have, therefore, been adapted to the slightly different geometry of Demo. The positions and sizes of the PF coils, that have been used in the calculation, are given in tabular form in Tab. 2.4.2. The currents, that are assumed to flow in the coils, are shown in this Table too. These currents refer to the "end of burn (EOB)" phase for the ITER operating scenario with 22 MA [6] . The time dependent contributions of the magnetic fields produced by the plasma and by the eddy currents have been also taken into account in the calculation of the magnetic forces.

The main results of the electromagnetic calculations are illustrated in Fig. 2.4.3, 2.4.4 and 2.4.5. The time behaviour of the induced currents is shown in Fig. 2.4.3. Caused by the linear decay of the plasma current, the currents start at zero, reach a maximum determined by the time constant of the structure at the end of the quench (20 ms) and then decay back to zero. This picture shows the time dependence of the "toroidal box current" defined as integral on the vertical middle plane (see Fig.2.4.1) of the absolute value of the toroidal component of the current density.

The Fig. 2.4.4 illustrates schematically the induced current distribution on the segment box. Streamlines - each of them shows the pattern of a 100 kA current - are drawn on the different parts in which the structure has been divided. At the

equatorial plane the streamlines flow toroidally on the first wall and on the back walls, and radially on the side walls to form closed loops. This distribution - close patterns normal to the poloidal magnetic field produced by the plasma current - is more or less followed on the other parts of the structure. Owing to the geometric symmetry of the blanket in respect to the middle vertical plane and owing to the axial symmetry of the plasma in respect to the torus axis, the eddy current distribution is antisymmetric in respect to the vertical middle plane.

Fig. 2.4.5 shows the time dependence of the absolute value of the resultant magnetic forces on the segment box. As the force distribution has no symmetry in respect to the vertical middle plane, two curves are drawn on this picture for both the halves in which the structure is divided by this plane.

A more detailed force distribution at time 20 ms is given in tabular form in Tab. 2.4.3 and 2.4.4. The resultant forces and torques calculated for each of the different parts, in which the structure has been divided, are shown here. The results are presented in these tables for each half of the structure respectively. The torques are calculated on the geometrical center of each part. The coordinates of these centers are listed in the tables as well.

2.4.2 Conclusions and future work

The results of the present electromagnetic calculation based on an "insulated model" of the outboard blanket give only a rough picture of the eddy current and magnetic force distribution. Further work is required to obtain load distributions suitable to the design of the component. The main points that need to be improved are listed and briefly discussed below.

As regards to the electromagnetic interaction of the reactor components, it has been shown [7, 8] that the first wall behavior is strongly affected by the presence of the vacuum vessel, that produces a significant shielding of the field changes. However, a complete calculation of the tokamak reactor (vacuum vessel, outboard and inboard blankets, divertors and coil systems) requires a considerable number of mesh elements. This number is limited by the computer memory availability, so that only calculations of simplified structures can be performed.

The choice of the martensitic stainless steel Manet as structural material for the blanket causes great difficulties in the actual electromagnetic calculations. As already pointed out, the computer program CARIDDI cannot take into account the presence of magnetic materials. On the other hand, Manet has a complicated magnetic behaviour, because its relative permeability is high and the B-H curve is nonlinear and followed by saturation of the magnetization. As at the present time there are no satisfactory computer programs for the calculation of eddy currents and magnetic forces in presence of magnetic materials, this effect is neglected in the first approximation calculations. The expected increase of the force values will be roughly taken into account using a separately estimated safety factor.

In the present calculation only a linear decay model of the plasma current without motion has been assumed. Nevertheless, there is experimental evidence that in case of failure of the active control system, instabilities can arise, so that the plasma moves with exponential increasing velocity in vertical direction. This motion is typically followed by a current quench, when the plasma hits the divertor plates. It has been shown [1, 3] that this kind of event can produce higher loads than the linear model without motion. Furthermore, the produced load distributions are essentially different in the motion phase from those occurring in the quench phase, so that a separate assessment is required.

In the calculation of the eddy currents in the segment box, particular attention has to be paid to the effect of the passive plasma stabilizer elements. The function of these elements is to slow down the vertical movement of the plasma during normal operation. They are in electrical contact with the segment boxes and are mechanically supported by these. It has been shown [1, 3] that the presence of these loops with low electrical resistance cause a strong increase of the eddy currents and magnetic forces in the NET blanket.

A static stress analysis at the time of occurence of the maximum forces will be performed in the future to compare different support options. Furthermore, due to the impulsive character of the magnetic forces during disruptions, a dynamical structural analysis of the segment box will be carried out. In fact,in the mentioned analysis of the NET blanket, the dynamical stresses were greater than the static ones by about 70%.

Finally, also the coupling of mechanical dynamics and induced currents should be analysed. In this case a change in the mechanical frequency in the elastic structure and a effective damping might be observed, that could modify the dynamic behaviour of the blanket. In the mentioned analysis of NET Blanket, the damping effect has been calculated, however the reduction of the maximum stresses was relatively modest [1].

References

1. L.V. BOCCACCINI,"Berechnung der elektromagnetischen Kräfte im Blanket eines Tokamakreaktors beim Plasmastromabbruch und Bestimmung der dadurch hervorgerufenen mechanischen Spannungen", KfK-4757, EUR-11399DE, Kernforschungszentrum Karlsruhe (1990).

2. M. DALLE DONNE, U. FISCHER, M. KÜCHLE, G. SCHUMACHER, G. SORDON, E. BOJARSKY, P. NORAJITRA, H. REISER, H.D. BASCHECK and E. BOGUSCH: "Pebble-bed canister: the Karlsruhe ceramic breeder blanket design for the Next European Torus", Fusion Technol., 14, 1357 (1988).

3. L.V. BOCCACCINI and M. DALLE DONNE, "Electromagnetic forces and stresses in Ceramic Breeder Blankets caused by disruptions", Proc. 14th Symp. Fusion Technology, London, UK, September 3-7, 1990.

4. Minutes of the 4th Meeeting of the Test Blanket Advisory Group, Ispra, March 14th, 1990.

5. R. ALBANESE and G. RUBINACCI, "Integral formulation for 3D eddy-current computation using edge elements", IEE Proceedings, 135A, 457 (1988).

6. "ITER Poloidal Field System", ITER documentation series No.27, IAEA, Vienna 1991.

7. R. ALBANESE, L. BOTTURA, E. COCCORESE, R. MARTONE and G. RUBINACCI, "Electromagnetic effects induced by plasma disruptions in the NET vacuum vessel", to be published in Fusion Engineering and Design.

8. "Study of the Reactor Relevance of the NET Design Concept", CLM-R278, Culham Laboratory, Abingdon, UK (1987).

n.	structure part	reference thickness	corrective factor
1	First Wall (top)	30 mm	1.5
2	First Wall (bottom)	30 mm	1.5
3	Back Wall (top)	30 mm	1
4	Back Wall (bottom)	30 mm	1
5	Cover Plate (top)	20 mm	1
6	Cover Plate (bottom)	20 mm	1
7	Side Wall (top)	20 mm	1.5
8	Side Wall (bottom)	20 mm	1.5
9	Vertical Shield (top)	500 mm (*)	1.2
10	Vertical Shield (bottom)	500 mm (*)	1.2
11	Horizontal Shield	500 mm (**)	10
12	Box Back Wall (top)	40 mm	1
13	Box Back Wall (bottom)	40 mm	1
14	Front Box Wall (top)	40 mm	1
15	Front Box Wall (bottom)	30 mm	1
16	Box Side Wall (top)	30 mm	1
17	Box Side Wall (bottom)	30 mm	1

Note (*) : in this case the dimension in radial direction is listed

Note (**) : in this case the dimension in vertical direction is listed

Tab. 2.4.1: List of the parts, into which the blanket model of Fig. 2.4.2 has been divided, with reference thickness and corrective factor for the specific resistivity.

Coil No.	Center Co-ordinates		Dimensions		Currents at EOB
	R	z	R	z	
PF1U/L and PF2U/L	1.84 m	±1.6 m	0.6 m	3.2 m	-44.6 MA
PF3U/L	1.84 m	±4.0 m	0.6 m	1.6 m	-9.1 MA
PF4U/L	1.84 m	±6.4 m	0.6 m	3.2 m	0.0 MA
PF5U/L	4.3 m	±8.6 m	1.0 m	1.0 m	7.7 MA
PF6U/L	12.3 m	±6.0 m	0.5 m	1.0 m	-7.0 MA
PF7U/L	12.3 m	±3.0 m	1.0 m	1.0 m	-5.6 MA

Tab. 2.4.2: Positions, sizes and currents of the poloidal field coil system used in the Lorentz force calculation.

| No.	Force (kN)			Torque (kNm)			Co-ord. Center (m)		
	x	y	z	x	y	z	x	y	z
1	-1941	-204	-549	53	411	145	7.317	0.220	2.936
2	466	-49	-400	-80	-653	-28	7.730	0.233	-1.865
3	-1904	-240	-574	91	-497	178	8.227	0.250	2.983
4	868	-87	-554	-144	-793	-28	8.450	0.258	-2.201
5	3	-23	-121	-7	6	-1	6.959	0.208	6.255
6	21	2	9	0	8	-2	6.878	0.205	-3.982
7	-7177	-456	813	2114	-4081	763	7.711	0.480	3.121
8	4513	617	1508	-591	-2936	362	8.079	0.504	-2.124
9	-11200	-1152	558	1833	2147	2005	9.882	0.319	3.875
10	8383	-550	-2084	-1938	-8159	-1138	9.180	0.296	-2.891
11	58	-117	-575	-36	-173	23	8.159	0.247	7.500
12	-1468	-164	101	94	26	212	9.712	0.298	5.168
13	1505	-88	-522	-202	-498	-62	8.946	0.273	-2.789
14	-330	-79	-155	-42	282	38	6.520	0.194	8.108
15	491	-7	32	-3	105	-12	6.827	0.204	-4.773
16	-18311	-3602	-5894	2829	12238	1419	8.425	0.527	6.411
17	5953	99	-559	-946	-3772	631	8.219	0.513	-3.335
TOT	-20065	-6099	-8970	21492	-235630	10106	6.942	0.329	2.210

Tab. 2.4.3: Calculated force distribution on the left half (positive y-direction) of the blanket in respect to the vertical middle plane.

No.	Force (kN)			Torque(kNm)			Co-ord. Center (m)		
	x	y	z	x	y	z	x	y	z
1	1232	81	453	-82	1393	62	7.317	-0.220	2.936
2	-1337	119	451	56	177	-94	7.730	-0.233	-1.865
3	1539	104	521	-107	1253	85	8.227	-0.250	2.983
4	-1205	169	587	104	518	-139	8.450	-0.258	-2.201
5	17	23	113	-8	-7	2	6.959	-0.208	6.255
6	-22	0	-9	1	-13	-2	6.878	-0.205	-3.982
7	7151	-435	-815	-1573	4393	-770	7.711	-0.480	3.121
8	-4590	-49	-1508	957	2813	-356	8.079	-0.504	-2.124
9	11311	-8	-866	-1645	1548	2138	9.882	-0.319	3.875
10	-8439	1416	2352	1988	6197	-2151	9.180	-0.296	-2.891
11	58	117	524	-37	121	-23	8.159	-0.247	7.500
12	2010	14	5	-197	-2477	211	9.712	-0.298	5.168
13	-475	175	465	149	928	-177	8.946	-0.273	-2.789
14	941	29	-59	19	-165	37	6.520	-0.194	8.108
15	1	26	145	-16	-197	-16	6.827	-0.204	-4.773
16	18666	1290	5875	-4306	-11839	-1427	8.425	-0.527	6.411
17	-5862	638	571	1418	363	-624	8.219	-0.513	-3.335
TOT	20997	3710	8804	2946	240160	-1872	6.942	-0.329	2.210

Tab. 2.4.4: Calculated force distribution on the right half (negative y-direction) of the blanket in respect to the vertical middle plane.
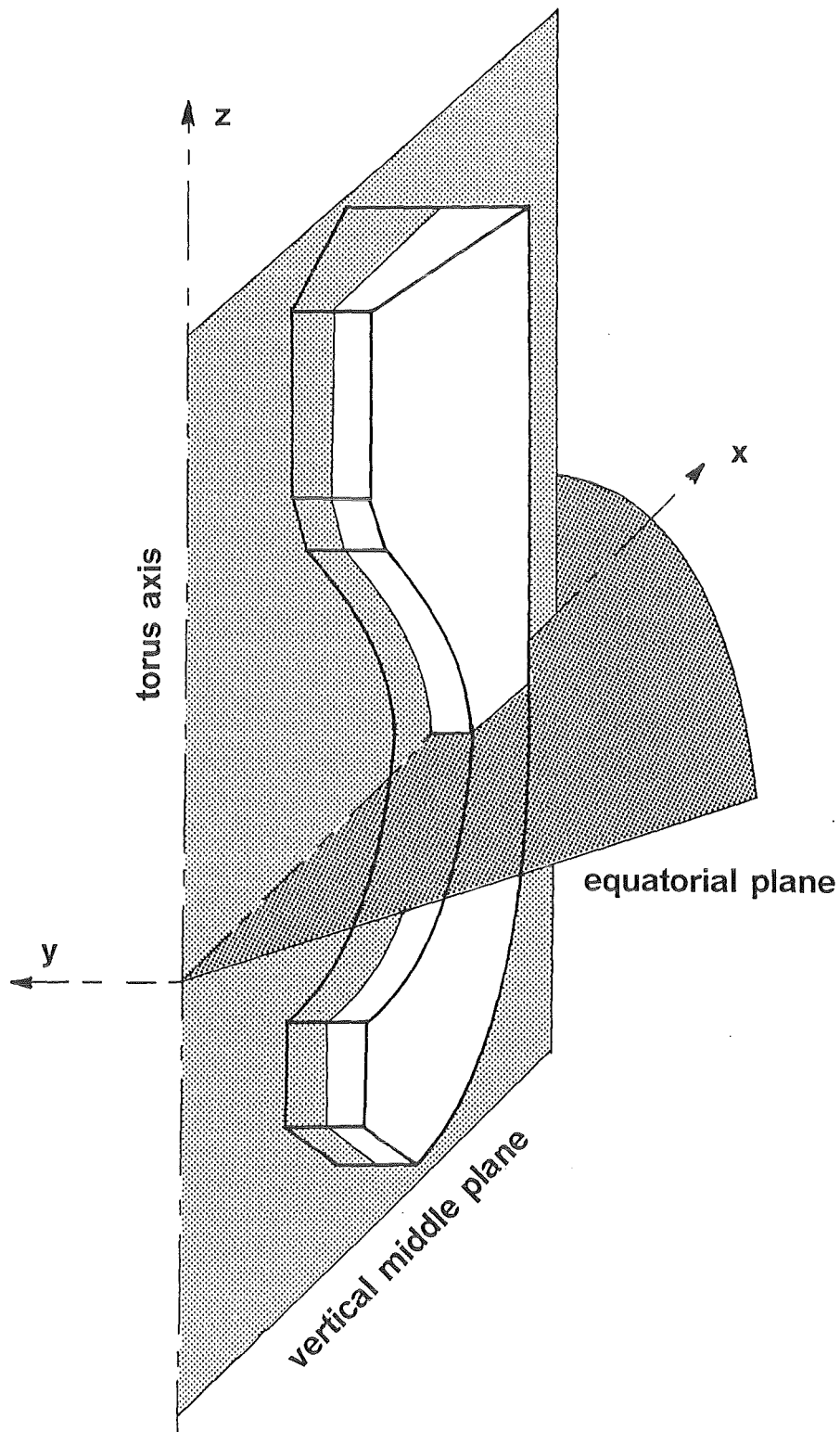
Fig. 2.4.1: Schematic picture of an outboard segment of the Demo blanket with the coordinate system and the geometrical definitions. The proportions between the different parts are not respected in the picture.
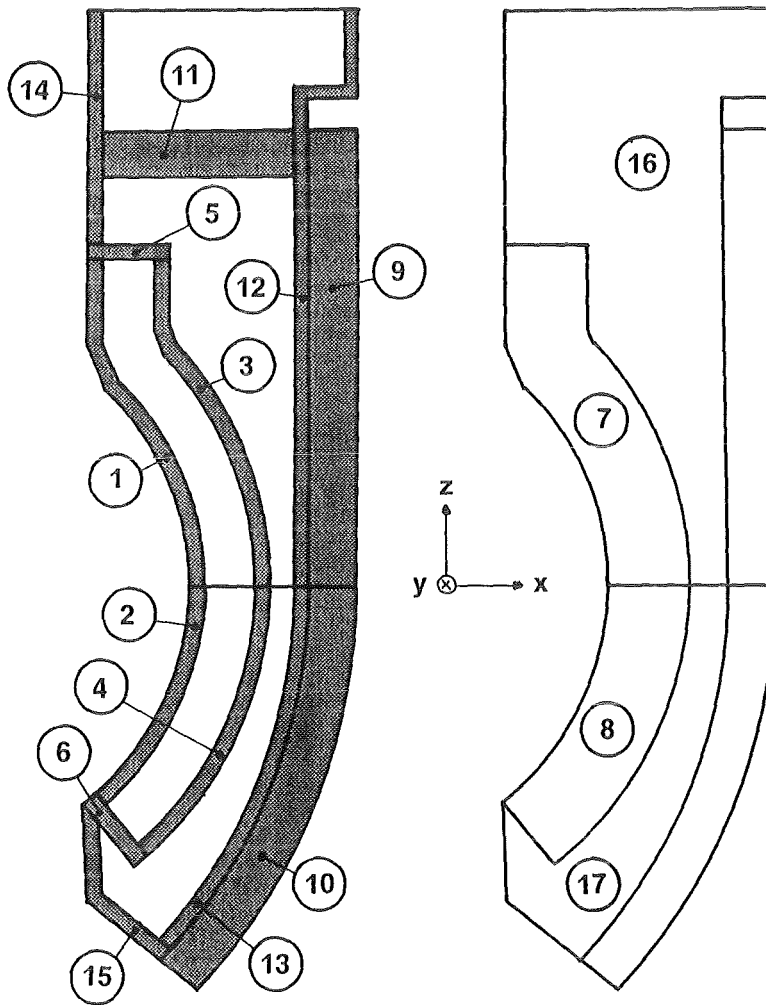
Fig. 2.4.2: Demo blanket model used in the electromagnetic calculation: vertical section and lateral view. The proportions between the different parts are not respected in the picture.
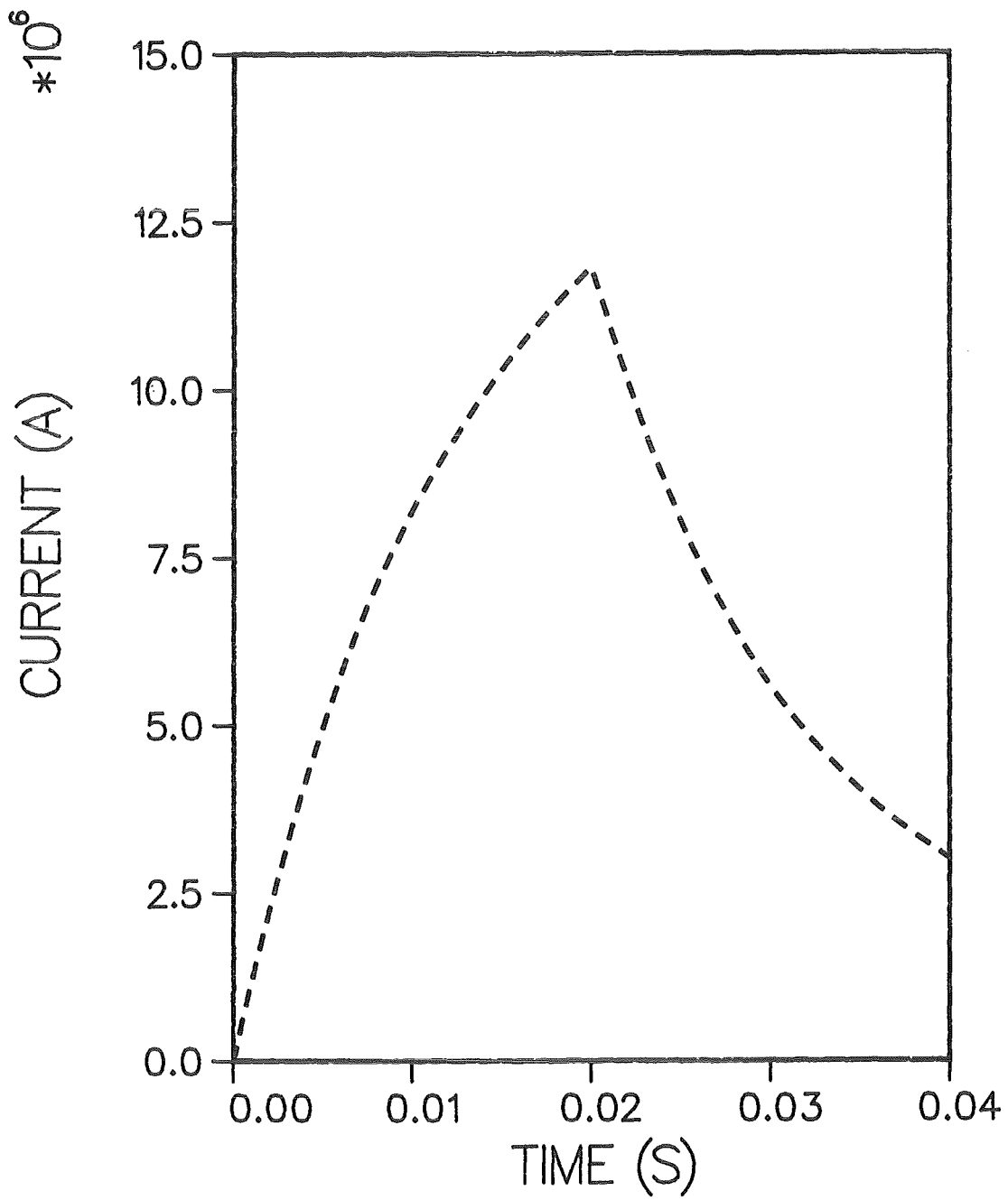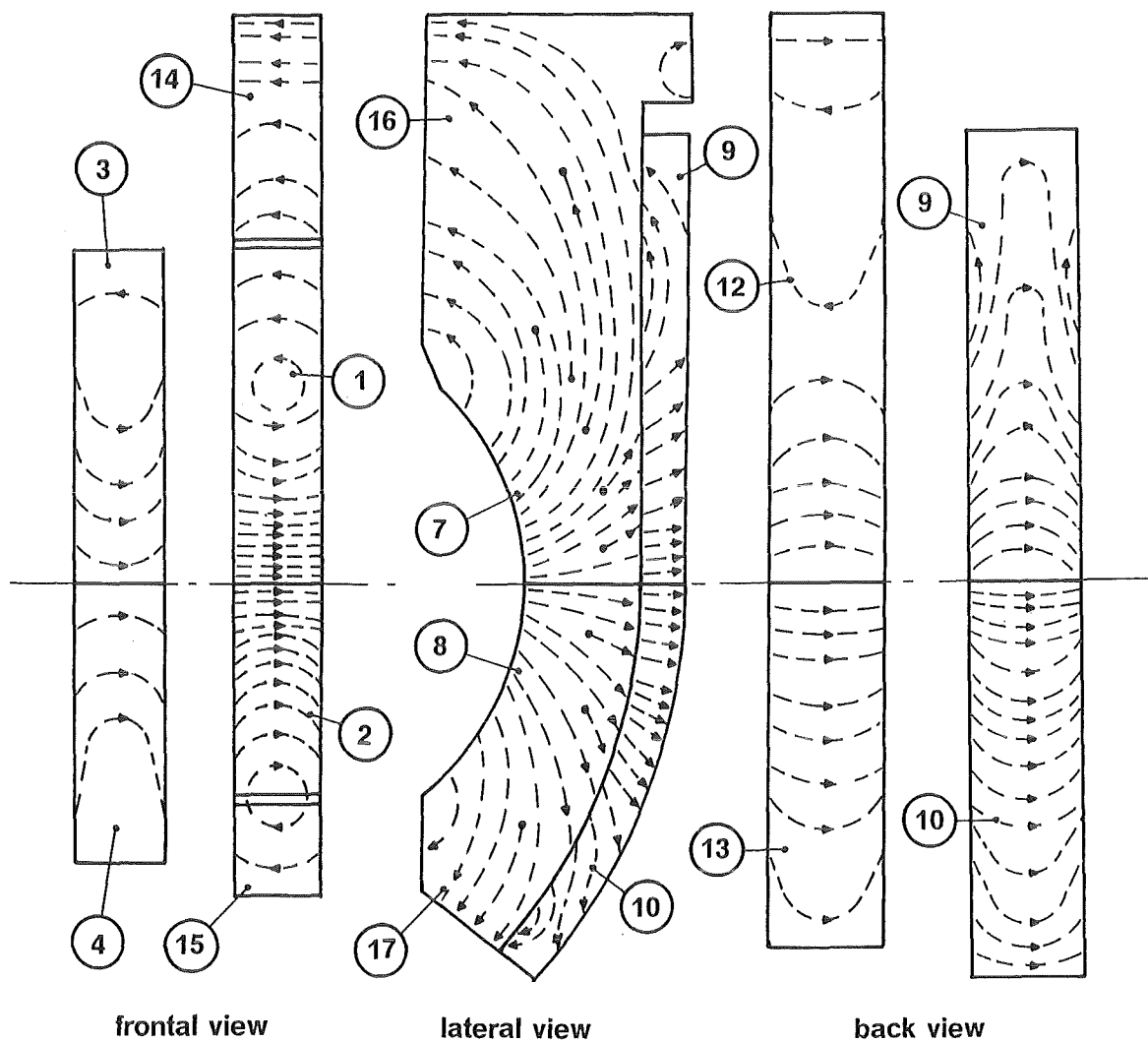
Fig. 2.4.3: Time behaviour of the calculated "toroidal box current".

frontal view   **lateral view**   **back view**

Fig. 2.4.4: Calculated eddy current distribution at 20 ms (end of the plasma quench). Each dotted line shows a 100 kA streamline. The proportions between the different parts are not respected in the picture.

— 70 —
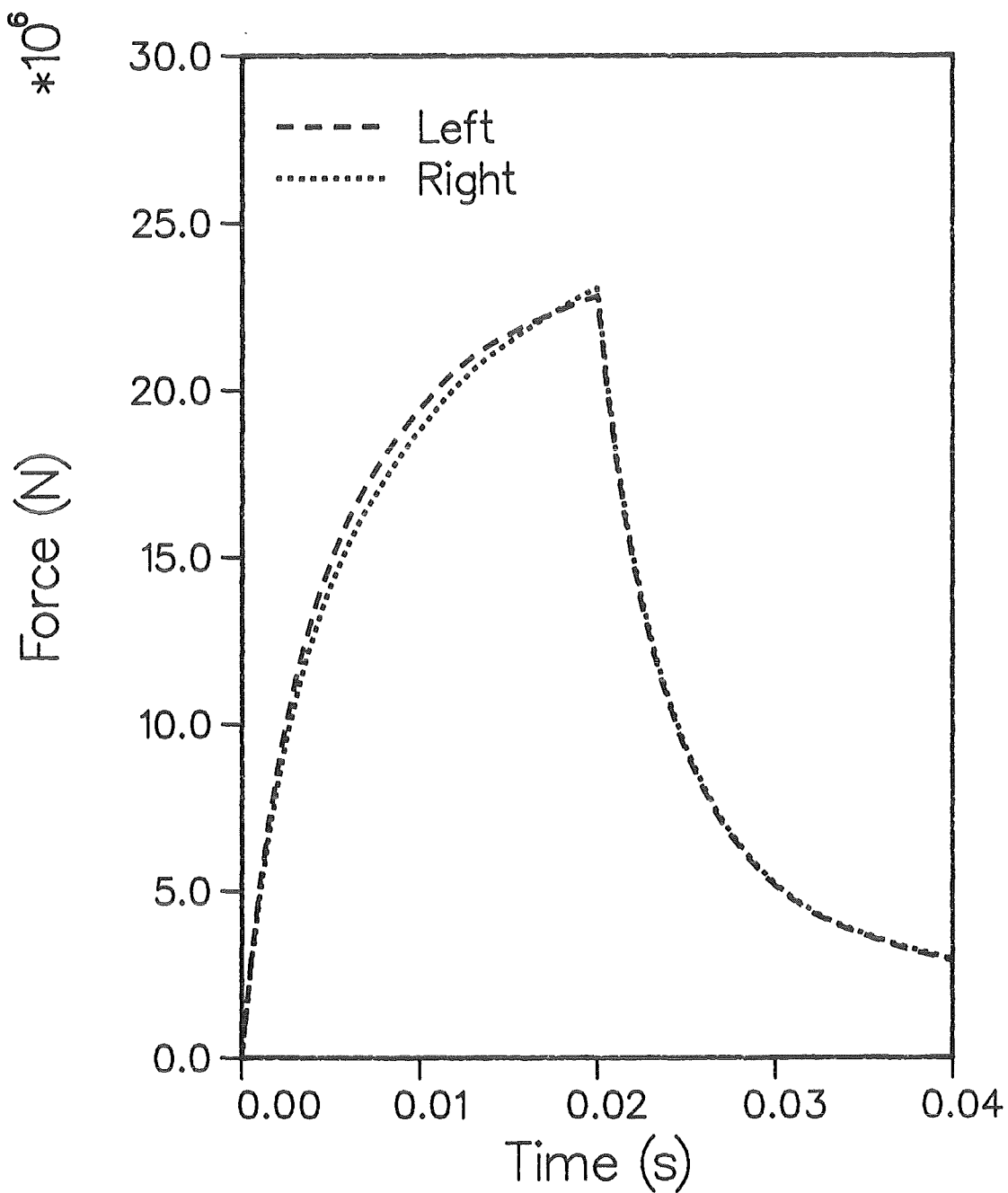
Fig. 2.4.5: Time behaviour of the calculated absolute value of the resultant magnetic forces on the Demo segment box. Each curve refers to a half of the blanket structure in respect of the vertical middle plane: "left" in the positive y-direction and "right" in the negative y-direction.

2.5 Tritium Extraction from the Blanket (R.-D. Penzhorn)

As described in Section 2.1 the BOT Helium Cooled Solid Breeder Blanket for the Demo reactor consists of beds of small lithium orthosilicate pebbles and cooled beryllium plates contained in radial canisters placed in 80 inboard and outboard tightly closed segment boxes [1, 2]. In each canister tritium is bred in the solid breeder material and, to a much lesser extent, in the beryllium plates ($\approx$ 0.6 %). It is estimated that only a small fraction (less than 1 $\div$ 2 %) of the tritium bred in the beryllium is released, the rest will accumulate in the beryllium over the total period of operation. The total tritium production rate in the blanket is specified to 390 g/d.

To extract tritium from the blanket a Tritium Extraction System (TES) must be designed capable of removing tritium at an average rate equivalent to the tritium breeding rate. In this way the desired tritium inventory can be maintained constant.

Some basic design requirements concerning the purge gas of the lithium ceramic pebbles / beryllium containing canisters have been compiled in Table 2.5.1.

Table 2.5.1 Process requirements: Composition, flows, and other parameters of the purge gas of the lithium ceramic / beryllium zone of a solid breeder blanket.

Ceramic blanket purge gas	inlet	outlet
Temperature °C	250	450
Pressure [kPa]	81	80
He flow [kmol /d]	603	603
Q_2 flow [kmol /d]	0.603	0.603
Q_2O flow [mol /d]	0.6	0.6
Total impurities [mol /d]*	0.6	0.6
Total tritium flow [kCi /d]	200	4100

* Impurities: Ar, N_2, O_2, CO, CO_2, Kr, Xe

Q = T, H

The Demo breeder blanket design stipulates temperatures for the breeder material in the range 380 - 800 °C and for the beryllium temperatures not exceeding 600 °C. The blanket is to be purged with helium at 80 kPa, containing 0.1 % of hydrogen. The swamping ratio is specified to $H/T \approx 100$. The blanket tritium recovery system must produce a stream of dry hydrogen with a dew point of < -100 °C (< 0.014 µbar H_2O) containing less than 1 ppm total impurities, so that it can be fed directly into the Isotope Separation System. Criteria for the selection of TES components are low tritium inventory and minimum tritium waste. Filters are to be placed between the blanket and the various TES subsystems to remove particulates.

In the following several options for the extraction of tritium from a helium cooled solid breeder blanket are discussed.

2.5.1 Cryoadsorption / permeation / electrolysis concept

One TES option comprises cryoadsorption, permeation, and electrolysis as main process steps [3, 4]. A basic assumption is that most of the tritium in the purge gas is in the form of molecular hydrogen. While it has been postulated from thermodynamic considerations [5] and shown in release experiments [6] that tritium bred in Li_4SiO_4 is released mainly as T_2O, in the presence of excess hydrogen in the purge gas most of the tritium will exist as HT [7]. A simplified block diagramm of the tritium extraction process concept is given in Fig. 2.5.1.
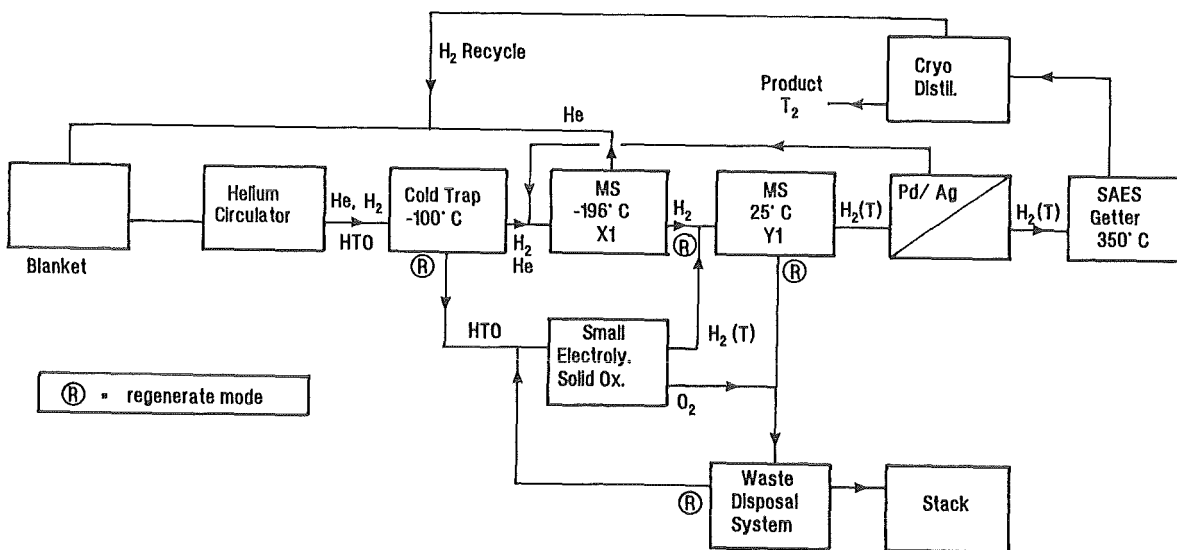
Fig. 2.5.1   Functional scheme of the TES

In a first step water (H2O/HTO) is removed employing a cold trap at -100 °C. The other tritium product, i.e. H2/HT, is separated from the helium purge gas together with all other tritiated and non-tritiated impurities and about 1 % of the helium by sorption on a molecular sieve bed at liquid nitrogen temperature (-196 °C). To illustrate this separation, the adsorption isotherms at liquid nitrogen temperature of pure hydrogen and pure helium on zeolite 5A are shown in Fig. 2.5.2. The regeneration of the molecular sieve bed is carried out periodically and sequentially employing an appropriate temperature programm: a) to recover the hydrogen the beds are cycled between -196 and -100 °C every two hours using warm H2 gas to assiste the desorption of isotope hydrogens and coadsorbed helium, b) to desorb the more volatile impurities the adsorber bed is heated about once a week to 25 °C while purging with hydrogen, and c) to liberate water and carbon dioxide the molecular sieve is heated up to 250 °C.
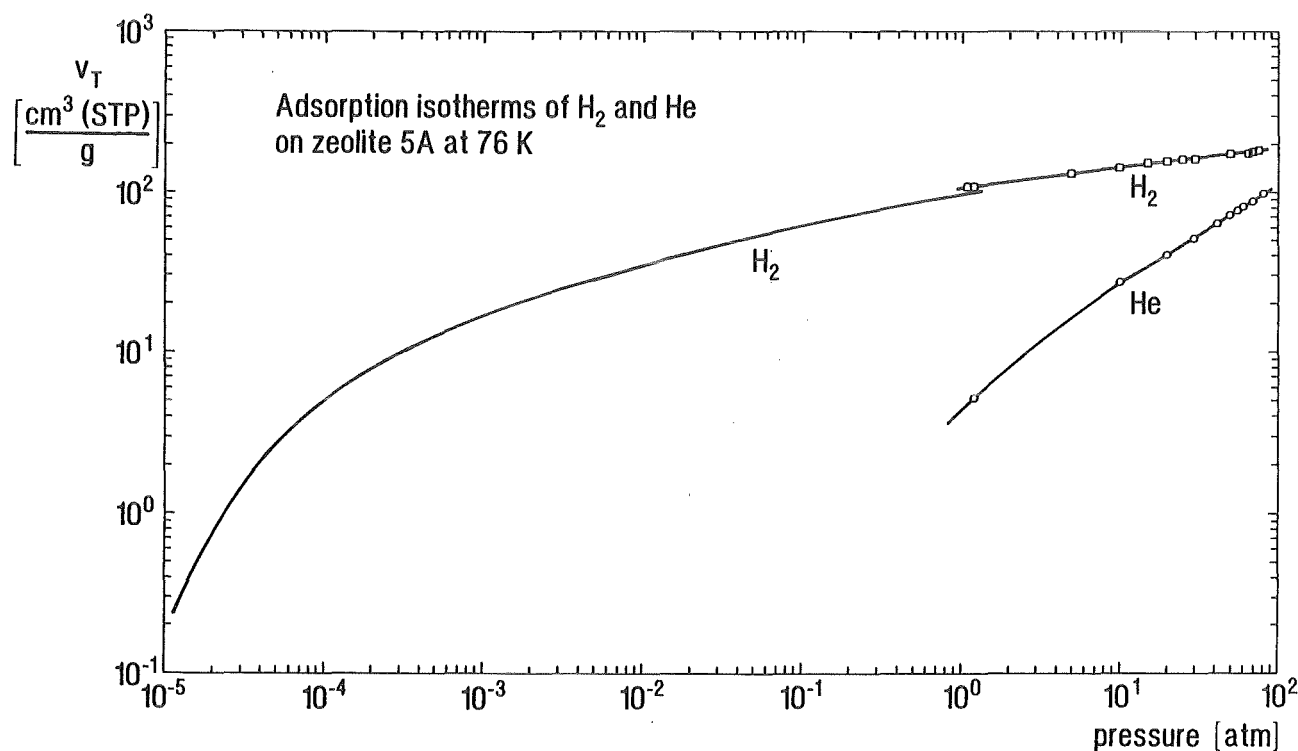
Fig. 2.5.2   Adsorption isotherms of hydrogen and helium on zeolite 5A at 76 K.

The isotope hydrogens recovered from the molecular sieve bed in high concentration are removed batchwise and with high efficiencey employing a palladium / silver permeator of comparatively small permeation area [8]. A particularly efficient permeator design is shown schematically in Fig. 2.5.3. The hydrogen-rich process gas is forced with the aid of insert tubes through the inside of a bundle of permeation tubes closed at one end. Under these

conditions highly efficient plug flow gas transportin is achieved. Vacuum is applied to the outside of the tube bundle (large cross section) with an oil-free pump combination. The permeated tritiated hydrogen, which has a purity of 99.9999 % is fed directly into the isotope separation system. To prevent that impurities from a possible leakage through one of the permeation tubes clog the cryogenic isotope separation system, a guard bed is installed between the permeator and the cryogenic columns.

Impurities, including those containing tritium are sent to an interfacing impurity processing system. Water collected in the cooler is recovered periodically and decomposed into the elements hydrogen and oxygen using an electrolysis cell. A ceramic electrolysis cell operating at 870 K having a throughput of 0.18 mol/h of water has been developed and tested with tritium at JAERI [9]. Another electrolysis cell concept having a hollow palladium / silver cathode has been developed at Valduc and tested succesfully with up to $1.2 \cdot 10^{13}$ Bq/ml water [10]. Preparations at Chalk River Laboratories for the test of an electrolytic cell developed at Mol to electrolyze water with up to 1 MCi tritium per liter are well advanced [11]. While the electrolytical hydrogen is recycled into the TES, the oxygen is sent to the waste detritiation system.
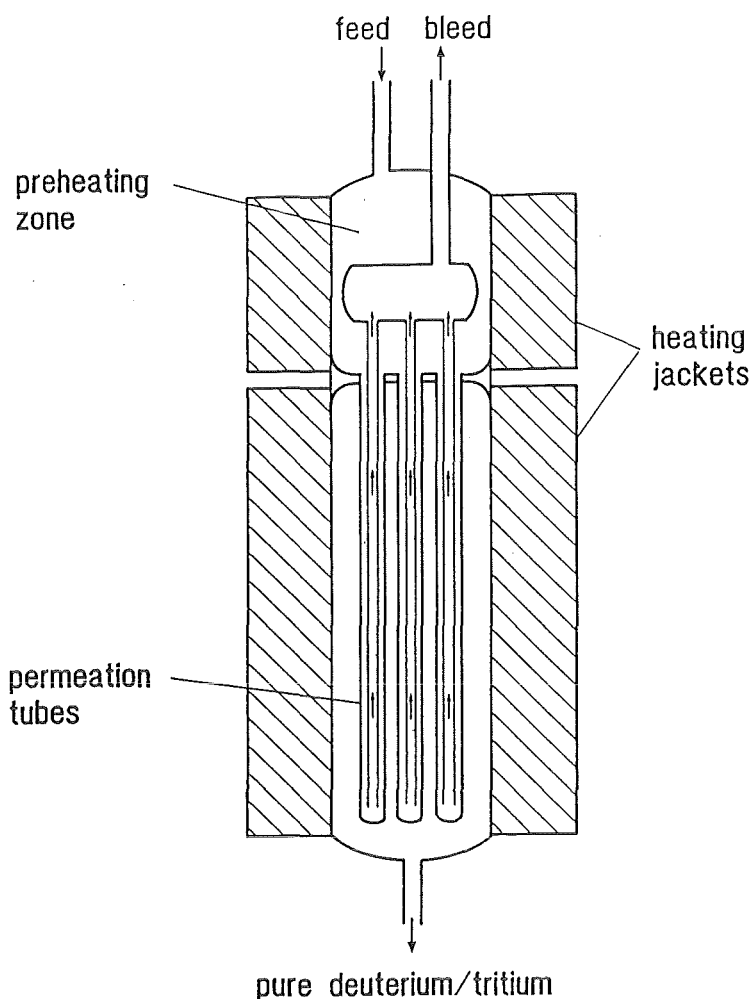

Fig. 2.5.3

Scheme of a

palladium-silver

permeator

Tritiated water produced from the oxydation of impurities such as ammonia and / or hydro-carbons in the waste disposal system is processed electrolytically together with the water collected in the cold trap.

2.5.2   Freezer / adsorption process concept

The freezer / adsorption option assumes no physical separation between the breeder zone and the beryllium zone [12]. The purge helium from the breeder ($2.4 \cdot 10^5$ - $3.6 \cdot 10^5$ mol/d) containing tritium as tritiated water and tritiated hydrogen is first cooled down by counter current to room temperature and then compressed to 10 bar (see Fig. 2.5.4). A process pressure of 10 bar is used to optimize the freezing operations and to reduce the size of the components.

After removal of the compression heat the gas is passed through a prefreezer, in which essentially all the water is frozen out. The water partial pressure is further reduced down to a dew point of -120 °C employing a freezer panel cooled to 150 K with liquid nitrogen. The water freezer is regenerated every 24 hours. To recover the tritiated water (1 kCi/g) in the prefreezer panels, the panels are warmed up and the vaporized gases sent via a degassing column into an electrolyser. Hydrogen and oxygen produced from the electrolysis of water (about 21 mol/d throughput) are directly returned into the loop and compressed together with the helium purge gas coming from the breeder. In this way, drying of both gases is circumvented and oxygen is removed together with the other impurities condensed in the cryoadsorption trap.
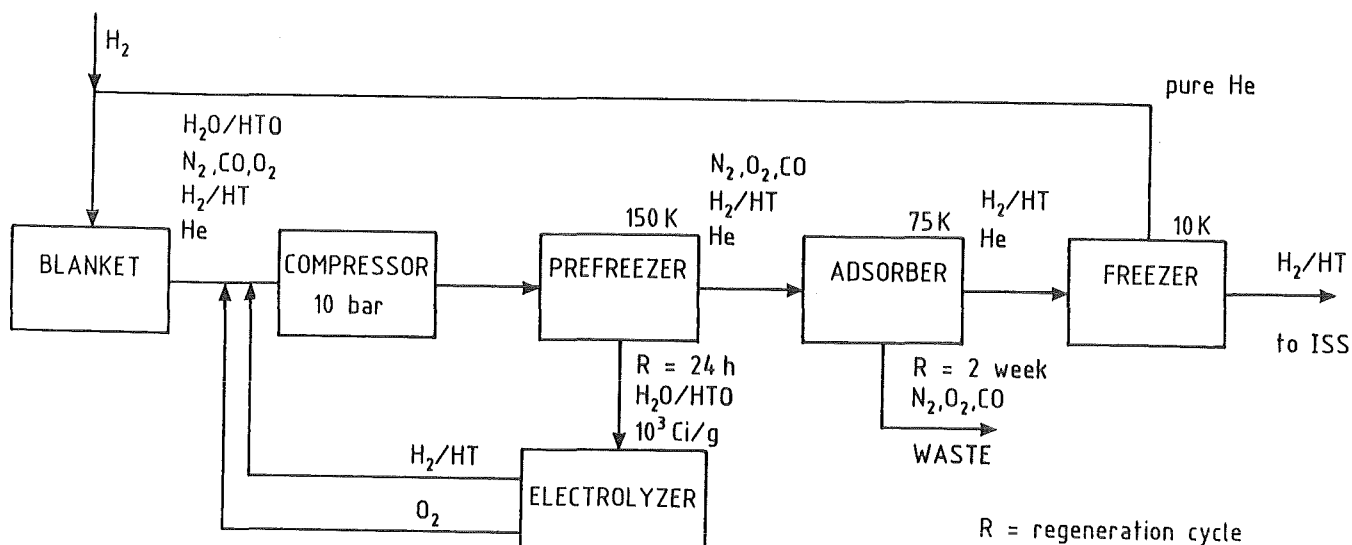

Fig. 2.5.4   Simplified scheme of the Freezer / Adsorption concept

Low boiling point gases, such as N_2, O_2, CO, CO_2, CH_4, and residual H_2O, present as impurities in the purge gas (total impurities < 1.2 mol/d) are removed by adsorption at liquid nitrogen temperature (- 196 °C). Regeneration of the adsorbers is carried out every two weeks at 150 - 200 °C.

Hydrogen (22.8 mol/h) is separated from the purge gas helium in a freezer panel cooled to < 10 K with liquid helium. The clean purge gas is returned through several counter current heat exchangers to the blanket. The hydrogen recovered from the freezer, which contains only helium as a minor impurity, can be fed directly into the isotope separation system.

2.5.3 Direct extraction of tritium via permeation

When most of the bred tritium is in the form of molecular hydrogen the use of a large permeator or of an array of permeators to extract directly and continuously the hydrogen isotopes from the purge gas appears to be an attractive alternative. However, calculations have shown that for this purpose palladium / silver permeators with up to 36 m^2 will have to be developed [14].

If, on the other hand, a significant fraction of the tritium in the purge gas exists in the oxide form, it appears preferable to convert all the hydrogen into tritiated water and process the latter by liquid phase / vapor phase catalytic exchange.

References

1. M. DALLE DONNE, E. BOJARKSY, U. FISCHER, M. KÜCHLE, P. NORAJITRA, G. REIMANN, H. REISER, G. SORDON, The Karlsruhe Helium Cooled Ceramic Breeder Blanket Design for the Demonstration Reactor, 16th Soft Conf., London Sept. 3-7 (1990)

2. M. DALLE DONNE, E. BOJARKSY, U. FISCHER, M. KÜCHLE, P. NORAJITRA, G. REIMANN, H. REISER, H.D. BASCHEK, E. BOGUSCH, The Karlsruhe Solid Breeder Blanket and the Test Module to be irradiated in ITER / NET, Int. Symp. Fusion Nucl. Technol. Karlsruhe, June 2-7 (1991).

3. P.A. FINN, D.K. SZE, R.G. CLEMMER, Conceptual Design Description for the Tritium Recovery System for the U.S. ITER Li_2O/Be Water Cooled Blanket, ANL / FPP / TM-249 (1990)

4. H. YOSHIDA, Tritium Recovery System for an ITER Driver Blanket, ITER Fuel Cycle Experts Meeting, Aug. (1989)

5. H.R. IHLE, R.-D. PENZHORN, P. SCHUSTER, The Thermochemistry of Lithium Silicates in View of their Use as Breeder Materials, Nucl. Eng. Design 8 (1989) 393.

6. H. KUDO, K. OKUNO, S. O'HARA, Tritium Release Behaviour of Ceramic Breeder Candidates for Fusion Reactors, J. Nucl. Materials 155 - 157 (1988) 524.

7. W. BREITUNG, R. HUBER, H. LEBKÜCHER, M. MÖSCHKE, G. SCHUMACHER,H. WERLE, internal KfK report, unpublished, (1989).

8. R.-D. PENZHORN, M. GLUGLA, Behandlung der Abgase für NET II, KfK-Nachrichten 21 (1989) 273.

9. S. KONISHI, M. INOUE, T. HAYASHI, K. OKUNO, Y. NARUSE, J.W. BARNES, J.L. ANDERSON, Development of the JAERI Fuel Clean up System for Tests at the Tritium System Tests Assembly, 9th Topical Meeting on Technol. of Fusion Energy, Oak Brook, Oct. 7-11, (1990).

10. P. GIROUX, T. PELLETIER, P. BOUCQUEY, J. BRESIEUX, Electrolysis Cell for Highly Tritiated, 16th Symp. on Fusion Technol., Sept. 3 - 7, (1990).

11. A. BRUGGEMAN, A. RAHIER, R. CORNELISSEN, J.M. MILLER, R.E. JOHNSON, R.J. KEYES, Testing of a Capillary Electrolysis System for Highly Tritiated Water, 16th Symp. on Fusion Technol., Sept. 3-7, (1990).

12. M. ISELI, Design Requirements: Tritium Recovery from the Purge Gas of the Water Cooled Ceramic Blanket, ITER Fuel Cycle Experts Meeting Aug. (1990).

13. M. ISELI, M. SCHAUB, ITER Ceramic Breeder Blanket Tritium Recovery System, Conceptual Design Description, ITER Fuel Cycle Work Shop, Garching Feb. (1990).

14. M. ISELI, personal communication

2.6 Safety and Reliability Considerations (M. Dalle Donne)

The safety problems of a helium cooled solid breeder blanket are similar to those of a helium cooled fission reactor, so that a lot of experience is available. In respect of fission reactors the fusion reactor has, however, considerable safety advantages:

a. Generally an accident causes an increase of the impurities in the plasma, which cause a plasma disruption. The power production in the blanket is rapidly switched off.

b. The after-heat in the blanket is much smaller than in a fission reactor, (it is essentially produced in the steel, the after-heat produced in the orthosilicate and in the beryllium is negligible), after a very short time it is only about 1 % of the full power production.

Helium, an inert, one-phase and transparent coolant, offers considerable safety advantages. However, it loses its good heat transfer properties by the decrease of pressure and velocity. For this reason the safety investigations have the objective of maintaining the high pressure and mass flow of the helium coolant. Detailed safety investigations for the Demo blanket and its helium and water / steam circuits have not yet been performed. They will be carried out during 1992 - 1994.

However preliminary estimates and considerations can be already mentioned at this stage:

a. The blanket is cooled by two completely separate helium cooling systems. Each of these systems is able to carry away the after-heat by temperatures lower than those by normal operation. By the full power production , the operation of a single coolant circuit would result in blanket temperatures higher than the normal operation temperatures. However the resulting deformations in the blanket are such that a blanket segment can still be replaced.

b. The helium / water-steam heat exchangers can be placed sufficiently above the blanket, so that the after-heat in the blanket can be carried away by the natural convection of helium, provided the helium pressure is maintained.

c. For the blanket module to be tested in NET / ITER it has been shown that even in the case of failure of both main helium cooling systems, the tritium purge gas system is able to carry away the blanket after-heat (see Section 3.2).

d. Preliminary investigations show that, in case of failure of both main helium cooling systems, it is possible to remove the blanket after-heat by introducing a heavy gas (argon or CO_2) in the gaps between the segment box and the inner structures (canisters, tubes, shields).

e. The canisters have to contain the helium purge system pressure of ~ 0.08 MPa. Calculations show that for pressures up to 0.6 MPa, the stresses in the canister walls remain in the elastic region. If one allows plastic deformation, the canisters can even withstand the pressure of 6 MPa [1]. Recent experiments confirm the calculations and show that the canisters fail at 9 MPa [2], which is greater than the maximum pressure that would occur in the canister due to the failure of one or more cooling tubes. Of course, excessive pressurization of the helium purge flow system and plastic deformation of the canisters during an accident should be avoided; thus, a pressure limitation system,. for instance a burst membrane acting at ~ 0.3 MPa, should be provided. Furthermore, the canister walls under the effect of the fast neutrons could become brittle and allow only a small plastic deformation. However, the calculations and experiments show that even a complete pressurization of the canisters at relatively high pressures would not produce a catastrophic failure of the blanket.

f. The purge gas sytem, which contains the major part of the tritium, is relatively small, is operating at subatmospheric pressure and relatively low temperatures and has a double containment.

Detailed reliability investigations have not yet been performed. However also here it is possible to make some preliminary considerations. It has been frequently stated that the number of welds has an important effect on the reliabily of a system. In the present blanket design there are about 54000 tubes contained in 2016 canisters, as against 60000 tubes and 8000 modules for the CEA-ENEA Breeder Inside Tube Demo blanket. These numbers are comparable with the number of fuel rods in a fission reactor of equivalent power (the German standard PWR of 1300 MWe has about 59000 fuel rods, while the fast reactor Superphenix with 1180 MWe has about 100000 rods in the core and 20000 in the blanket). Both for the standard German PWR of 1300 MWe and the Superphenix reactor a failure rate of 10^{-5} rods / year ($\approx 10^{-9}$ rods / hour) has been achieved [3, 4]. The two welds of each coolant tube in the present design are placed in the back region of the blanket where the smallest neutron fluences are expected, as in the case of the fission reactors. A failed weld causes a leakage of coolant helium in the purge flow system, which can be detected by the local increase of helium pressure. If the crack is small enough, this increase in pressure is small and operation with the damaged element can be continued until the next planned blanket discharge operation.

References

1. E. WEHNER, R. KRIEG, and B. DOLENSKY, "Load Carrying Capacity of Canister Type Blanket Elements for NET Under Accident Conditions", presented at 9th Int. Conf.

Structural Mechanics in Reactor Technology (SMIRT 9), Lausanne, Switzerland, August 17 - 21, 1987.

2. E. WEHNER, R. KRIEG and B. DOLENSKY, "Canister Type Blanket Elements for NET Under Accident Overpressure. Theorectical and Experimental Investigations", Fusion Eng. Design, 6, 69 (1988).

3. P. RAU, Siemens Kraftwerk Union, Private communication, 1990.

4. E. FRANCILLON, Framatome, Private communication, 1991.

3. TEST OBJECT DESIGN FOR NET / ITER

One of the main objectives of NET / ITER is to test Demo-relevant blankets. Presently the NET / ITER testing program foresees first module or submodule tests in ports placed at the equatorial plane of outboard blanket segments and later tests of whole segments or sectors. The testing philosophy for the Demo-relevant BOT-HCSBB (Breeder Out of Tube, Helium Cooled Solid Breeder Blanket) foresees that the module testing should be made in three stages in order to reduce the risk of malfunction. First the module should be made of austenitic steel 316 L, rather than Manet, and placed behind the standard water cooled NET / ITER first wall. Then, a 316 L module should be placed with its helium cooled wall directly facing the plasma. Finally, a Manet module facing the plasma should be tested (see Chapter 6).

In this Chapter the design of the test module placed behind the first wall and of its extraction system will be presented (Section 3.1). Section 3.2 explains in detail the design and functioning of the required out-of-reactor ancillary systems (two helium cooling systems, one purification system for the cooling helium and one purge gas system) and shows their space requirements around the NET / ITER machine.

This design work has allowed to estimate the time constants of the various components and thus allowed to assess the requirements given by the testing of the modules on the NET / ITER machine (burn time, duty cycle and duration of continuous operation) (see Chapter 6.)

3.1   Design (H.D. Baschek, E. Bogusch)

3.1.1   Overview

Fig. 3.1.1 at page 315 (at the end of the report) shows a vertical and horizontal cross section of the test module placed behind the first wall. The module composed of a box containing six canisters, the neutron shields and the various pipes, is contained in an adapter box.

Access to the inside of the vacuum vessel is possible via the adapter box flanged to the respective horizontal port. The adapter box allows access to the plasma volume from the torus hall without breaking the cryostat vacuum. So it can also serve as a lock for inspection and maintenance purposes to be performed inside the vacuum vessel. Supply and removal of test blankets can be executed by the manipulator box attached to the adapter box by a lock system.

In the first phase the test blankets will not directly face the plasma but will be enclosed and protected by a plug box equipped with a first wall of the same design as the main ITER-first wall.

The plug box is also flanged to the vacuum vessel wall. It has a smaller cross section than the adapter box so it can be inserted and removed through the adapter box without disconnecting that box from the vessel wall.

3.1.2   Box system

The box system consists of three components, the plug box housing the test blanket proper, the adapter box to provide a channel between vacuum vessel port and the torus hall, and the manipulator box as transporting unit. The inner volume of plug box and adapter box is filled with helium at low pressure under normal operating conditions (plant operation).

3.1.2.1 Plug box

The plug box is a water-cooled steel box of welded structure flanged to the vacuum vessel thus closing the horizontal port opening. It is electrically insulated from the vacuum vessel.

The flange bolts are covered by a weld seal to provide a vacuum tight barrier between the vacuum of the vacuum vessel and the adapter box atmosphere, in addition to the mechanical seal of the flanges. By the design a double barrier (1. mechanical seal, 2. weld seal) to the inner vacuum vessel can be achieved. The plug box has a poloidal length of 2520 mm and a width of 1088 mm constant in poloidal direction.

The plug box wall facing the plasma is of the same design as the first wall of the permanent blanket segments. Plating of the first wall with graphite tiles is foreseen.

Cooling of first wall and side walls is provided by bored cooling channels in radial / toroidal direction, while the horizontal walls are cooled by toroidal oriented cooling channels. The coolant supply lines are connected to the plug box at the vertical flanges and are guided along the side walls of the adapter box leaving it at the upper wall in an area outside the cryostat.

3.1.2.2 Adapter box

The adapter box serves as already mentioned as a channel between the vacuum vessel port and the torus hall through the cryostat vessel wall providing a barrier to the torus hall atmoshpere. The penetration of the adapter box through the cryostat vessel wall is sealed by

a bellow-type structure to allow the adapter box to follow the movement of the vacuum vessel, e.g. by thermal expansion, without affecting the cryostat vessel.

At the bottom of the adapter box a channel is installed housing the main supply lines for the lower part of the central outboard blanket segment.

The front of the adapter box is flanged to the vacuum vessel and is electrically insulated from the vessel. The flange connection is equipped with a weld seal for vacuum tightness, in addition to the mechanical flange sealing. ·

At the rear of the adapter box a lock with horizontally sliding door and inflatable seals is installed. The door is equipped with welded seal strips and circumferential sealing frame with two inflatable seals on both sides. It is moving in guiding elements with ball bearings. The drive mechanism consists of two threaded spindles connected to gear motors. The lock is permanently connected to the adapter box.

Inside the adapter box, a rail system for the test blankets is installed at the ground wall. The side walls are equipped with rails to guide and position the supply lines for the test blanket. In addition they serve for stiffening the box to withstand loads from electromagnetic forces.

3.1.2.3 Manipulator box

The manipulator box serves for the transport of test blankets between the torus hall and the hot workshop. It is equipped with remotely-controlled manipulators to perform all necessary handling operations to exchange test blankets.

The design of the manipulator box has only been investigated basically. It is a closed steel box with a lock at one side compatible with the adapter box. The manipulator box can be connected tightly to the adapter box to allow exchange of test blankets or maintenance work inside the vacuum vessel. As a result, possible release of activity to the torus hall can be avoided on opening the adapter box or the vacuum vessel.

The manipulator box has to be large enough to house the test blanket and the manipulator unit necessary for remote handling operations. It has also to be designed to be moved on the floor of the torus hall, e.g. on rails by a transport vehicle, and by a crane. The transport vehicle has to be equipped with vertical and horizontal adjustments devices to facilitate the connection of flanges between adapter box and manipulator box.

3.1.3 Test plug

The test plug mainly consists of blanket unit, shield unit and supply lines for helium coolant, purge gas, water coolant and instrumentation and control.

The blanket units is mounted to the shield unit at the back center by a rigid structure as anchor point and at top and bottom by a hinge joint to allow thermal expansion of the blanket structure and simultaneously provide a solid connection against forces from disruptions. The blanket unit consists of six canisters of the helium-cooled pebble bed design as for Demo enclosed by a casing with a Demo-type first wall.

The casing is segmented in poloidal direction. Front (first) wall and the side walls are made of one sheet bent into the required shape to minimize the number of welds. First wall and side walls are cooled by helium at 80 bar.

The canisters are supported from the back of the blanket unit by a rigid structure composed of poloidally running coolant inlet and outlet tubes and a back wall. This rigid structure also forms the back of the casing. The blanket is equipped with a twofold redundant cooling system. From the poloidally running inlet tubes (the outer tubes of the four-tube-arrangement), the cooling gas first flows through the cooling channels of the casing and then through the cooling tubes of the canisters. Leaving the canisters the cooling gas is collected in the two central tubes of the a.m. four-tube-arrangement. The supply lines for the cooling gas are connected to the poloidal tubes at the lower rear. In that area also the purge gas lines penetrate the back wall of the blanket unit. They are connected to the purge gas (helium) manifolds which themselves are connected to the individual canisters. All this is the same as for the outboard Demo blanket.

From the blanket unit, helium coolant and purge gas lines are guided through shield unit in such a way that no direct neutron irradiation of components behind the shield is possible.

Behind the shield unit the supply lines are guided to the flange area where they are connected to the supply lines outside the adapter box by remotely removable pipe connections. The flanges of pipes connected to the test plug are kept in a fixed position by a movable support device to facilitate remote handling. The support device moves on a rail system arrangement at the side wall of the adapter box.

The counterpart of each supply line penetrates the adapter box at the top behind the cryostat wall at a defined position. The penetrations are designed in such a way that electrical insulation between pipes and box wall is guarenteed.

The shield unit is a box containing two water-cooled shielding elements. The shielding elements are arranged in a way to achieve a good shielding performance and leave enough space for the supply line going through. The shield unit also has to carry the weight of the

blanket unit. It is equipped with wheels to be moved on the rails of the adapter box. The verical stability is achieved by a side roller system also guided on rails. The roller systems are also electrically insulated from the adapter box. At the rear the shield unit is equipped with a mechanical interlock system to keep the test plug in a fixed position. The water-coolant supply lines are arranged in parallel and designed similar to the blanket supply lines. Table 3.1.1 summarizes the main technical data of the test plug.

Table 3.1.1

Number of canisters	6
Main dimensions	approx. 2.5 m x 1.2 x 2.8 m
Total weight	appros. 12.5 t
Weight of blanket	appros. 2.3 t
Total weight at vacuum vessel flange	appros. 120 t
Dimensions of vacuum vessel opening	1.2 m x 2.56 m
Piping dimensions	
- Poloidal cooling tubes	193.7 x 18 mm
- First wall cooling channels	18.5 mm
- Cooling gas intermediate collectors	60.3 x 2.6 mm
- Cooling gas supply lines	88.9 x 3.2 mm
- Purge gas supply lines	25 x 2 mm

3.2   Ancillary Equipment (E. Bogusch, W. Fritsch)

3.2.1   Helium cooling system

3.2.1.1   System description

The cooling system has the following functions:

- Removal of the heat generated in the test plug (cooling)

- Heating of the test plug from room temperature to 400 °C (dry-out of breeder material, bake-out)

- Decay heat removal by means of forced circulation

- Decay heat removal by means of natural circulation

An operating pressure of 60 bar is assumed for both normal operation (cooling and heating) and for decay heat removal operating conditions.

The cooling system illustrated in Fig. 3.2.1 consists of two redundant cooling loops (2x50% design).

Apart from connecting piping and fittings, each cooling loop contains the following components:

- Dust filter in the main cooling line
- Recuperative heat exchanger
- Helium/water heat exchanger (main cooler)
- Blower
- Electrical heater

The following operating conditions must be considered:

Cooling

The helium leaving the test plug at a temperature of 450 °C is filtered (dust filter) and then cooled to 300 °C in the recuperative heat exchanger. The main cooler reduces the cooling gas inlet temperature into the blower to 50 °C.

After reheating in the recuperative heat exchanger from approx. 50 °C to 200 °C, the cooling gas flows through the switched-off electrical heater and is returned to the test plug at a temperature of 200 °C.

Heating

In the operating mode "heating", the recuperative heat exchanger which is positioned in the return line to the test plug and the main cooler are bypassed (heating bypass) and the electrical heater is put into operation.

Decay heat removal by means of forced circulation

If the blower is operable, the decay heat is removed as in the cooling mode. For adaptation to the decay heat power, an entire cooling loop can be switched off and the flow can be reduced by means of the speed-controlled blower. Further possibilities to cope with lower power are operation via the heating bypass and change-over to decay heat removal by means of natural convection.

Heat removal by means of natural circulation

For simultaneous failure of the blowers in both cooling loops or in the case of substantially reduced decay heat, the cooling loop can be operated in the natural convection mode. For this purpose the heat source (test plug) and the heat sink (main cooler) are arranged with a difference in height as driving force.

3.2.1.2 Design

The design is based on the data presented in Table 3.2.1.

Cooling

The operating mode "cooling" is the design case for the cooling loop and its components.

As shown in Table 3.2.1, the helium mass flow amounts to 0.924 kg/s for each cooling loop.

The helium volume of a cooling loop including the test plug is estimated at approx. 3 m³. The helium mass of a cooling loop amounts to about 15.5 kg.

The design of the loop components is described in the following:

Main cooler

The main cooler (selected design: U-tube heat exchanger) is installed downstream of the recuperative heat exchanger. This means that the helium is pre-cooled and enters the main cooler at a temperature of 300 °C. The inlet temperature into the blower is 50 °C during

cooling operation. A heat transfer surface of approx. 21 m² was calculated to remove 1.2 MW.

Recuperative heat exchanger

The recuperative heat exchanger (similarly of U-tube design) transfers 0.72 MW with a selected heat transfer surface of 4.5 m². The cold helium flows around the outside of the heat exchanger tubes and the hot helium is conveyed in the heat exchanger tube.

Blower

A single-stage radial blower of encapsulated design is planned for circulation of the cooling gas. It has a volumetric flow rate of 382 m³/h, a pressure increase of 1.8 bar and a drive power of approx. 27 kW. The use of magnetic bearings eliminates the need for lubrication with oil and hence the risk of oil ingress in the case of accidents.

During heating operation the He mass flow drops with increasing temperature (volumetric flow almost constant). The maximum temperature at the blower inlet is 400 °C in this case.

Piping

Assuming a distance of 40 m from the test plug to the wall penetration of the installation room, a total pipe length of approx. 118 m is estimated for each cooling loop for the DN 125 piping. The pipe lines are made of austenitic steel.

The pressure loss in the cooling loop without test plug amounts to approx. 0.64 bar including a 30% safety margin. Therefore a pressure increase of at least 1.78 bar (selected 1.8 bar) in the blower is necessary.

Heating

The test plug structures must be heated for bake-out from 20 °C to 400 °C within a period of 20 to 24 hours. For this purpose, an electrical heater with a heating power of 100 kW is installed in each cooling loop. The design power includes heat losses during heating and the power required for heating the concerned piping of the cooling loop.

3.2.2 Purification system

3.2.2.1 System description

The tasks of the purification system are as follows:

-   Removal of gaseous impurities, in particular H_2, HT, T_2, N_2, from the helium in the cooling system

-   Reduction of the tritium partial pressure in the cooling loops to limit tritium permeation into the rooms or the cooling water system

-   Removal of radioactive impurities from the helium before transferring it to the He supply and He storage system

-   Pressure control in the cooling system together with He supply and He storage.

The purification system for the cooling system consists of one purification loop for the two cooling loops, see Fig. 3.2.2.

As a result of connection of the purification loop to the pressure (inlet) and to the suction (outlet) side of the cooling loop, no blower is necessary during normal operation. To cover special cases such as decay heat removal with small flows in the cooling loop, a blower is provided in the purification loop in the bypass.

Apart from connecting piping and fittings, the purification loop consists of the following components:

-   Fine filter
-   Electrical heater
-   Copper oxide beds with integrated filters
-   Helium/water heat exchanger
-   Water separator
-   Room temperature adsorbers with integrated filters
-   Recuperative heat exchanger
-   Low-temperature adsorbers with integrated chillers and integrated filters
-   Hydrogen getter (U-bed)
-   Blower

The gas purification process is performed at three temperature steps:

- High temperature range for the oxidation of reducing impurities
- Room temperature range for the adsorption of water
- Low temperature range for the adsorption of nitrogen

A partial flow is removed from the respective cooling loop and conveyed to the gas purification system.

Dustlike impurities from the cooling loops are retained in the sintered-metal filter. Before entering the copper oxide bed, the helium is preheated to the necessary operating temperature. In the copper oxide bed the hydrogen isotopes H_2, HT and T_2 are converted to H_2O, HTO and T_2O by means of oxidation. After cooling and possible water separation, water in the steam state is adsorbed at molecular sieves (zeolite) in the room temperature adsorber. For nitrogen separation the helium is subsequently passed through a low-temperature adsorber with recuperative heat exchanger positioned upstream and downstream of it. The purified helium is returned to the respective cooling loop at approximately room temperature.

After being shut off, the redundant copper oxide beds, room and low-temperature adsorbers can be regenerated during purification operation.

While separate He auxiliary systems are necessary for the adsorbers, the copper oxide beds can be regenerated by a discontinuous input of oxygen diluted with helium. The end of the life of a copper oxide bed is indicated when hydrogen can be significantly detected in the helium after leaving the copper oxide bed.

In the subsequent cooler, the helium to be purified is cooled to room temperature.

The condensate occurring in the cooler and the downstream separator is collected and conveyed to the water extraction facility of the helium auxiliary systems.

The remaining water in the steam state is adsorbed in the room temperature adsorber so that the helium flow is almost free of hydrogen and water before entering the low temperature range.

The recuperative heat exchanger is used to bring the gas to be purified to low temperature by the vaporized nitrogen of the nitrogen-cooled chiller integrated in the downstream low-temperature adsorber. Thus the remaining moisture content is frozen in the heat exchangers and the nitrogen impurities are retained by adsorption in the low-temperature adsorber. Abrasion from the adsorber filling of the low-temperature adsorber is retained in two filters during purification operation (forward flow - downwards) and regeneration

(reverse flow - upwards). These filters are integrated at both ends of the low-temperature adsorber.

The purified helium leaving the recuperative heat exchanger at approximately room temperature is then conveyed directly to the cooling loops or, if the hydrogen content is still too high, it can be passed through a hydrogen getter (uranium bed). The getter is installed in the bypass to the main line.

3.2.2.2 Design

The mass flow rate through the purification loop is assumed to be 1 ‰ of the total cooling gas flow of both cooling loops, i.e. 1.848×10^{-3} kg/s. This corresponds to a purification constant of 0.22 h^{-1}.

The following hydrogen partial pressures are calculated for the cooling loop as a result of the tritium balance:

- p_{H_2}	5.2 Pa
- p_{HT}	5.3×10^{-2} Pa
- p_{T_2}	1.6×10^{-4} Pa

Only the H_2 partial pressure is of relevance for the process-engineering design. A design value of 10 Pa is selected conservatively for the hydrogen partial pressure.

Corresponding to anticipated HTR values, the nitrogen impurity is assumed to be 1 vpm (p_{N_2} = 6 Pa).

The purification system contains the following components:

Copper oxide bed

A copper oxide quantity of approx. 15 l is required (BASF catalyst R3-11, copper in highly-dispersed form on a carrier material, tablets 5 x 3 mm). The working temperature in the copper oxide bed is 150 to 250 °C (nominal). The acceptable upper limit is around 300 °C.

In the design case, the hydrogen flow amounting to 1.55×10^{-9} kg/s results in an oxygen consumption of 1.23×10^{-8} kg/s and an occurring water mass of 1.4×10^{-8} kg/s. This means that approx. 50 g water occur after oxidation in a period of 1000 h.

He/water heat exchanger upstream of the room temperature adsorbers

A double-tube heat exchanger with helium in the inner tube and cooling water in the gap between inner and outer tube is selected for the design. A surface of approx. 0.15 m^2 is necessary for the approx. 2 kW heat transfer capacity.

Room temperature adsorber

The occurring water quantity of 1.4×10^{-8} kg/s must be adsorbed by an adsorption agent in the room temperature adsorber at a water partial pressure of 10 Pa (design value). An adsorption agent mass of approx. 1.45 kg (Bayer Zeolite W894) is required for a service life of 1000 h at an operating temperature of 40 °C.

Recuperative heat exchanger

A helical coil type double-tube heat exchanger with the colder helium in the inner tube and the warmer helium in the gap to the outer tube is selected. A heat transfer surface of 4.82 m^2 is necessary for a heat transfer capacity of approx. 2 kW.

Low-temperature adsorber

The N_2 impurity of 1 vpm resp. 6 Pa N_2-partial pressure postulated for the design corresponds to an N_2 impurity mass flow of 1.29×10^{-8} kg/s which must be adsorbed at the adsorption agent (selected: activated charcoal) at an operating temperature of -177 °C. A quantity of approx. 1.40 kg of activated charcoal is necessary for a service life of 1000 h.

Hydrogen getter (U-bed)

A uranium bed operated at room temperature which can be switched on is provided as an additional measure for removing hydrogen from the cooling gas to be purified.

Blower

An additional blower is provided in the pipe bypass for special operating conditions such as decay heat removal. It is designed for a volumetric flow rate of 0.695 m³/h and a pressure increase of 5000 Pa.

Piping

The pipe lines are made of austenitic steel. The pressure loss of the piping system (minimum nominal size selected for the design DN 10) is negligible when compared to the pressure difference at the connection point of the respective cooling loop amounting to approx. 1.14 bar (pressure loss via test plug). During normal operation of the cooling and purification systems, the flow rate through the purification loop must be adjusted by throttling.

3.2.3 Tritium balance

The tritium balance for the cooling system including the purification system was drawn up for one loop using the data in Table 3.2.2. Conservatively it was assumed that there is no hydrogen injection into the cooling system.

However, permeation of hydrogen isotopes from the purge gas system into the cooling system inside the blanket canister was considered.

The partial pressures of H_2, HT and T_2 were established by means of the three principal equations given below:

- Balance of all hydrogen isotope (H_2, HT and T_2)

- Balance of the hydrogen isotope H (H balance) for H_2 and HT

- Law of mass action between the hydrogen isotopes

The H_2 partial pressure was calculated to be 5.2 Pa, the HT partial pressure 5.3×10^{-2} Pa and the T_2 partial pressure 1.6×10^{-4} Pa.

The tritium inventory in the circulated helium of one cooling loop amounts to approx. 1.05×10^{-7} kg for a loop volume of approx. 3 m³ and an average loop temperature of 280 °C. This corresponds to a tritium activity of 3.72×10^{10} Bq (1.01 Ci).

The tritium permeation rates per cooling loop, see Fig. 3.2.3, for the tritium balance are listed in Table 3.2.3 taking into account the partial pressures p_{T_2} and p_{HT}, tritium permeation, and tritium separation in the gas purification system.

A separation efficiency of 100 % was assumed for the purification system.

With respect to the tritium balance of the complete cooling system, 86.7 % (10.4 Ci/d) of the tritium activity flow of 12 Ci/d flowing into the two cooling loops is separated out in the gas purification system under the boundary conditions given above.

Approx. 13.2 % (1.6 Ci/d) permeate into the surrounding rooms.

In relation to one cooling loop, approx. 0.21 Ci/d of this (approx. 3.5 % of the input activity flow) is released in the installation room for components of the respective cooling loop.

For an air exchange rate of approx. 6.4 h^{-1} in the installation room of a cooling loop, the acceptable radiological limit values for personnel occupationally exposed to radiation in the controlled zone of 10 mSv/a (1 rem/a) are not exceeded.

Via the supply and return pipes, approx. 0.58 Ci/d are released per cooling loop.

A total of approx. 1.2 x 10^{-4} Ci/d permeates on the cooling water side. The activity flow therefore remains clearly below the target maximum value of 0.1 Ci/d.

The above data are naturally dependent on the specifications, the selected boundary conditions and the assumptions.

Thus, for example, the hydrogen partial pressure which reduces the tritium loss is assumed exclusively on the basis of simultaneous hydrogen permeation from the breeding material, i.e. hydrogen permeation as a result of corrosion on the water side of the cooler is not taken into account although the value for this is expected to be in a similar order of magnitude. Furthermore, no permeation-impeding layers were considered when determining the permeation rates. Consequently the results must be evaluated conservatively.

Table 3.2.1: Main Design Data for One Cooling Loop

Cooling power	1.2	MW
Temperatures	200	°C
Test plug inlet	200	°C
Test plug outlet	450	°C
Coolant pressure	60	bar
Pressure drop of test plug	1.14	bar
Helium mass flow rate	0.924	kg/s

Table 3.2.2: Data Basis for the Tritium Balance of One Cooling Loop

Temperature of pipings between

Test plug - recuperative HX	450	°C
Recuperative HX - main cooler	300	°C
Main Cooler - recuperative HX	50	°C
Recuperative HX - test plug	200	°C
Mean He-Temperature	280	°C
He-Volume	3	m^3

Partial pressures

p_{HT}	0.264	Pa
p_{H_2}	100	Pa
He mass flow rate (cooling loop)	0.924	kg/s
He mass flow rate (purification loop)	$0.924 \cdot 10^{-3}$	kg/s

Tritium permeation rate into the cooling loop   6 Ci/d

Table 3.2.3: Tritium Permeation Rates for One Cooling Loop

	Tritium Mass Flow Rate [kg/s]	Activity Flow Rate [Ci/d]
In via first wall	$6.03 \cdot 10^{-12}$	5.0
In from purge gas system	$1.21 \cdot 10^{-12}$	1.0
Losses into components room	$2.54 \cdot 10^{-13}$	0.21
Losses through piping walls outside components room	$7.04 \cdot 10^{-13}$	0.58
Losses into water loop at main cooler	$7.35 \cdot 10^{-17}$	$6.10 \cdot 10^{-5}$
Separation in the cooling gas purification system	$6.27 \cdot 10^{-12}$	5.2

3.2.4 Purge gas system

3.2.4.1 System description

The tasks of the purge gas system are as follows:

- Removal of produced tritium from the breeding material bed
- Intermediate storage of tritium before transfer to an isotope separation system
- Emergency cooling for loss of decay heat removal via the cooling loops

The purge gas system consists of a purge gas loop and a sweep gas loop which is connected to the secondary side of a Pd/Ag-permeator, see Fig. 3.2.4, to convey the permeated hydrogen isotopes (incl. tritium) to the U-beds for intermediate storage.

The main design data for the purge gas system are listed in Table 3.2.4.

Apart from connecting piping and fittings, the purge gas system contains the following components:

- Main.cooler (He/water heat exchanger)
- Fine filter
- Room temperature adsorber with integrated filters
- Electrical heater upstream of the permeator
- Pd/Ag-Permeator (permeation cell consisting of Pd/Ag-membranes)
- Aftercooler downstream of permeator
- Recuperative heat exchanger
- Low-temperature adsorber with integrated chiller and integrated filters
- Purge gas blower
- Blower aftercooler
- Vacuum pump ⎤
- Hydrogen getter (U bed) ⎦ sweep gas loop

The purge gas system can be operated in the operating modes "purging" and "emergency cooling".

Purging

The helium purge gas flow with a pressure level of approx. 1 bar is doped with H_2 to reduce tritium permeation losses. On being discharged from the test plug the He gas flow can contain slight quantities of water moisture in addition to hydrogen. This water moisture is separated out in adsorbers at room temperature (main cooler upstream). The redundant design of the room temperature adsorbers permits regeneration of these components during continuation of the purging operation.

In the permeator the hydrogen, and hence tritium, permeates from the purge gas loop into the sweep gas loop where it is stored in the U-bed. The vacuum pump in this sweep gas loop is used to support gas transport.

The purge gas is re-enriched downstream of the permeator by injection of H_2. It is then cooled and conveyed to the low temperature section of the loop for the separation of impurities such as nitrogen which do not condense easily.

At the same time, residual water contents are trapped in the low temperature components (in the recuperative heat exchanger and in the chiller which is integrated in the low-temperature adsorber).

The purge gas which has been heated to room temperature by the recuperative heat exchanger is transported by a blower to the test plug.

The purge gas passes through the blower aftercooler during purging without the cooling function being operative (cold water flow shut off). As a result, the purge gas can be returned to the test plug at room temperature or with a slight temperature increase due to the rise in temperature in the blower.

In addition to bypasses of the redundant components, the low temperature section of the purge gas loop and the permeators can be bypassed if required.

The gas pressure in the purge gas loop is regulated at the pressure reference point upstream of the blowers to attain a slight overpressure in relation to the installation room. This is effected by an input from the He supply and He storage system or by an output to the pressure relief system for He auxiliary systems.

Emergency cooling

During emergency cooling via the purge gas system (after loss of the decay heat removal functions via the cooling system) the flow only passes through the components main cooler, blower and blower aftercooler. For this purpose, the emergency cooling bypass is opened and the fittings upstream of the room temperature adsorbers are closed.

In the emergency cooling case, both blowers are in operation to attain the elevated flow rate.

The temperature increase in the blower is essentially reduced by aftercooling.

3.2.4.2 Design

Main cooler

The operating mode "emergency cooling" is the design case for the He/water heat exchanger. Despite the temperature reduction via the non-insulated double pipe upstream of the main cooler, the full temperature reduction is assumed conservatively in the main cooler.

On the basis of this assumption, a heat transfer surface of 1.32 m^2 is necessary to transfer a power of 10.2 kW for a selected double tube heat exchanger with cold water in the jacket tube and helium in the inner tube.

Room temperature adsorber

The room temperature adsorber for the separation of water from the purge gas flow is designed for the normal purging case. The elevated quantity of water occurring during preliminary drying and power start-up (final drying) is covered by the elevated loading capacity at higher water partial pressure at the inlet into the adsorber or by the possibility of interim regeneration.

In the purging case, an HTO mass flow of 4.5×10^{-9} kg/s must be separated out.

An adsorption agent mass of 38.3 kg (zeolite Baylith T144) is necessary for this purpose for a service life of 1 year.

Electrical heater

A heating capacity of approx. 4 kW is necessary to heat up the purge gas flow from 40 °C to 300 °C (operating temperature of the permeator). A capacity of 4.5 kW was selected.

Pd/Ag-Permeator

A permeation coefficient of

$$K_p = 2.5 \cdot 10^{-7} \frac{mol\,(H_2) \cdot cm}{cm^2 \cdot min \cdot (kPa)^{\frac{1}{2}}} = 2.6 \cdot 10^{-11} \frac{kg\,(H_2) \cdot m}{m^2} \cdot s \cdot Pa^{\frac{1}{2}}$$

is used as the basis for permeation of hydrogen isotopes through a Pd-25 % Ag membrane at an operating temperature of 300 °C [1].

As the permeation of hydrogen isotopes is dominated by the H_2-content, design calculations were performed considering H_2 only.

At almost complete hydrogen permeation via the permeator, the total hydrogen mass flow of 1.5 x 10-6 kg/s (p_{H_2} = 100 Pa, $\dot{m}_{He}$ = 0.003 kg/s) must be permeated.

The counter partial pressure of the hydrogen isotopes at the secondary side of the permeator is disregarded to calculate the permeation rate.

Using an average partial pressure of approx. 30 Pa, the necessary permeation surface per mm wall thickness is calculated as 10.5 m2 (surface)/mm (wall thickness).

With a safety margin of 50 %, a surface of 1.58 m2 is necessary for a wall thickness of s = 0.1 mm.6
In the case of a tube bundle design and a bundle length of 1 m, this results in 50 tubes with a diameter of 10 mm and a wall thickness of 0.1 mm.

Aftercooler downstream of permeator

The aftercooler downstream of the permeator recools the purge gas flow from 300 °C to 40 °C. Consequently, a power of approx. 4 kW must be transferred in the cooler. A heat transfer surface of 1.62 m2 is necessary for this purpose for the selected double tube heat exchanger design.

Recuperative heat exchanger

A helical coil type double tube heat exchanger with the colder helium in the inner tube (33 to -177 °C) and the warmer helium in the outer tube (-170 to 40 °C) is selected. A surface of 14.5 m2 is necessary for the transfer capacity of 3.27 kW.

Low-temperature adsorber

The postulated N_2 impurity of 1 vpm resp. 0.1 Pa N_2 partial pressure corresponds to an N_2 impurity mass flow of 2.1 x 10-8 kg/s. A quantity of approx. 15 kg of activated charcoal is

necessary as adsorption agent for a service life of approx. 4000 h at an operating temperature of -177 °C.

Blower

During the operating mode "purging", 68.7 m^3/h helium at 1 bar, 33 °C must be transported with a pressure increase of 0.24 bar.

During the operating mode "emergency cooling" (both blowers are simultaneously in operation during emergency cooling), approx. 56.2 m^3/h helium at 1 bar, 40 °C must be transported by each blower with a pressure increase of 0.35 bar.

Aftercooler downstream of blower

In the operating condition "emergency cooling", the aftercooler downstream of the blowers cools the helium flow from approx. 100 °C to 50 °C by means of a temperature increase in the blowers.

For the selected double tube heat exchanger design (helium in inner tube and cold water in outer tube), a surface of 0.46 m^2 is necessary for the heat transfer capacity of 1.25 kW.

Vacuum pump

The hydrogen flow rate of 1.5 x 10^{-6} kg (H_2)/s permeating through the permeator is conveyed to the hydrogen getter by a helium flow circulated in the sweep gas loop.

In order to be able to disregard the counter partial pressure of H_2 during permeation through the permeator (error smaller than 10 %), the H_2 partial pressure at the end of the permeator must at least be smaller than 1 Pa.

A helium mass flow of 3 x 10^{-4} kg/s is necessary for this purpose. At a selected suction pressure of 100 Pa = 1 mbar, this corresponds to a volumetric flow (suction capacity) of approx. 7000 m^3/h.

Hydrogen getter (U-bed)

The hydrogen getter is operated at room temperature and approx. 1 bar pressure level (helium) using uranium powder as getter material. The H_2 mass flow to be collected (T_2 mass flow is negligible for the component design) amounts to 1.5 x 10^{-6} kg/s.

In the case of stoichiometric conversion, 12.6 g H_2 react with 1 kg uranium.

For 90 % conversion and a selected service life of 100 h, 72 individual uranium beds (660 g uranium powder, 60 dia. x 120 mm) are necessary according to /2/. The 72 individual beds are joined to form one unit.

Piping

DN 40 is selected as the uniform nominal size of the piping for the purge gas loop. In the operating mode "purging" the flow path is approx. 165 m; in the operating mode "emergency cooling" this distance is reduced to approx. 117 m. At the different mass flows, this results in a pressure loss including safety margin of approx. 0.1 bar for the pipe system in the operating mode "purging" and approx. 0.12 bar in the operating mode "emergency cooling".

In the region from the test plug to the wall penetration into the cooling loop room, the purge gas-carrying DN 40 pipe is enclosed in a DN 65 pipe. The piping of the purge gas system is made of austenitic steel.

3.2.4.3 Tritium considerations for the purge gas system

The calculated tritium permeation losses via the system walls of the purge gas loop for the individual system sections are given in Fig. 3.2.5. The tritium partial pressure upstream of the permeator which is decisive for tritium permeation amounts to 8.24×10^{-5} Pa. Downstream of the permeator, the tritium partial pressure will amount dropped to 1 % of the upstream value.

With reference to the double-walled pipe (DN 40/DN 65), the successive permeation resistances, namely inner pipe and jacket pipe, and the temperature are taken into account.

In this concept of the non-insulated double pipe, the following influences reduce tritium losses decisively in comparison to an insulated single tube:

- Lower inner tube temperature in comparison to purge gas temperature (helium temperature)

- Lower jacket temperature

- Rapid reduction of all temperatures along the pipe section

As a result of the high surface temperature of the jacket tube, the pipe must be protected against inadvertent contact.

The total tritium permeation loss of the purge gas loop amounts to 5.3×10^{-3} Ci/d, whereby the pipe section between the electrical heater and the permeator makes the greatest contribution to the total loss (approx. 90 %) because of the elevated temperature of 300 °C. On the whole the results for the tritium permeation losses are adequately low. The overall concept (high H_2 partial pressure in the purge gas and non-insulated double pipe in the supply and return lines) therefore provides a satisfactory solution.

Table 3.2.4: Main Design Data for the Purge Gas System

Operating Mode "Purging"

Helium mass flow rate	$3 \cdot 10^{-3}$	kg/s
Helium pressure level	1.0	bar
Blanket pressure loss	0.13	bar

He-temperatures

Test plug inlet	$\geqq 20$	°C
Test plug outlet	350	°C
Breeding zone	450	°C

H_2-Injection	0.1	Vol-%

Partial pressure

p_{H_2}	100	Pa
p_{HT}	0.17	Pa
p_{HTO}	0.03	Pa
p_{H_2O}	negligible	

Operating Mode "Emergency Cooling"

Cooling power	10	kW

He-temperatures

Test plug inlet	50	°C
Test plug outlet	450	°C

Helium pressure level	1	bar

3.2.5 Auxiliary systems

The following auxiliary systems are necessary in addition to the main systems, the helium cooling system and the cooling gas purification system and the purge gas system:

- He supply and He storage
- Regeneration system for adsorbers of the purification system
- Regeneration system for adsorbers of the purge gas system
- Evacuation system for He auxiliary systems
- Water extraction system for He auxiliary systems
- Pressure relief system for He auxiliary systems including the storage of gaseous radioactive waste

Other connected ancillary systems are:

- Cold water system
- Cooling water system
- Nitrogen supply and storage (liquid nitrogen)
- Isotope separation
- Ventilation
- Compressed air supply

3.2.6 Layout studies

The layout studies were performed on the basis of the NET building plan.

With reference to the cooling system and its cooling gas purification system and the purge gas system, preliminary installation studies were performed for the main components. Installation rooms were established for the auxiliary systems and the space required was roughly estimated.

The layout studies were basically performed to determine the space required and to notify NET of this requirement.

Fig. 3.2.6 gives an overview of the layout of the main systems.

The length of the pipes between cooling system and purge gas system and test plug was estimated at 40 m.

3.2.6.1 Helium cooling system and cooling gas purification system

The components of the two cooling loops were accommodated in two separate rooms. These rooms are on a higher level than that of the test plug so that natural circulation is possible in the cooling loops.

Fig. 3.2.7 shows the component layout for a cooling loop and the purification system. The components were arranged to permit optimum pipe routing, taking account of

-       short distances between the components

-       soft installation of the pipes for temperature expansions.

Furthermore, adequate accessibility of the components is guaranteed for inspection, maintenance and repair or replacement.

The purification system is located in a room between the cooling systems. This guarantees short piping connections between the cooling loops and the purification system.

The rooms for the cooling loops and the room for the purification system are monitored for tritium contamination.

3.2.6.2 Purge gas system

The purge gas system is on the same level as the cooling system and the purification system. The room for the purge gas system is located behind the rooms for the cooling and the purification system when viewed from the test plug.

The double-walled pipes of the purge gas system are laid up to the wall of the room. Single-walled pipes are used in the room itself.

With reference to component layout and pipe routing, the prerequisites for inspection, maintenance and repair or replacement which are valid for the cooling system and the purification system are also applicable here.

The selected component arrangement for the purge gas system is apparent from Fig. 3.2.8.

A rough division of the components into components for the treatment of purge gas and components which can be directly allocated to tritium separation (e.g. permeator, vacuum pump, hydrogen getter) is apparent from the figure. The division was selected to improve selective monitoring of components which may have a high tritium inventory.

The room for the purge gas system is also monitored for tritium.

3.2.6.3 Space requirements

In order to notify NET of the requirement, the volumes of rooms for the cooling system and purification system, the purge gas system and the main auxiliary systems for an NET test plug were estimated.

Table 3.2.5 summarizes the different room volumes.

The total volume was estimated at approx. 2100 m^3. This figure does not include stairways, passages, corridors etc.

In order to cover any uncertainties, a total space requirement of 2000 - 2500 m^3 should be used for further planning of the main and auxiliary systems under examination.

Table 3.2.5: Space Requirements for Supply Systems of the NET Test Plug

System	Space requirement [m³]
Cooling loop I	315
Cooling loop II	315
Helium purification system	110
Purge gas system	440
Regeneration system for adsorbers of the purification system	105
Regeneration system for adsorbers of the purge gas system	105
Helium supply and storage	315
Pressure relief system	115
Evacuation system	40
Room for electrical cabinets	70
Control station	60
Water extraction system	35
Gas analysis room	55
Store for gas samples	30

3.2.7   Conclusions

Within the scope of a feasibility study, the objective of this investigation was to consider the conceptual design for systems and components including the determination of the space required for installation of the systems.

3.2.7.1 Helium cooling system and cooling gas purification system

Cooling system

The designed cooling system meets the given requirements using simple, non-problematic technical solutions.

Only the essentially oil-free blowers with their pressure and tightness demands naturally impose more stringent requirements with reference to the tritium problem. These cannot be fulfilled by series aggregates.

Purification system

With respect to the cooling gas impurities hydrogen and nitrogen, the oxidation of hydrogen to water and subsequent adsorption at molecular sieves at room temperature and the low-temperature adsorption of nitrogen at activated charcoal are well-proven techniques.

The design of the room temperature adsorbers (zeolite filling) with a service life of 1000 h offers adequate reserves in conjunction with the possibility of discontinuous regeneration.

The purification flow rate of 1 ‰ of the cooling system flow (purification constant of approx. $0.22\ h^{-1}$) only requires a small piping diameter. DN 10 is selected as minimum nominal size for constructive reasons.

The length of the piping of the cooling system should be reduced if possible in the course of further planning (distance between test plug and installation room).

The low-temperature adsorbers are designed for activated charcoal. When experimentally verified N_2 adsorption isotherms are available for zeolite at low temperatures, the transition to zeolite is recommended because of its advantages over activated charcoal (non-combustible, less abrasion and hence dust).

Tritium balance

From a radiological viewpoint, the tritium balance for one cooling loop results in adequately low values in the installation room for the cooling loop, namely 0.21 Ci/d. An average permeation coefficient from several reference publications, no H_2-injection and the omission of permeation-impeding layers are assumed. An air change constant of ≥ 6.4 h^{-1} is necessary to maintain the radiologically acceptable tritium concentration in the air.

The tritium losses from each of the 40 m long supply and return pipes between the test plug and the installation room for the cooling loop amount to 0.58 Ci/d (for both loops 1.16 Ci/d). The 40 m long, 450 °C hot supply pipes alone make up ≥ 70 % of the total tritium losses. The total 450 °C hot pipe section makes a contribution amounting to approx. 96 %.

As a result of the low pipe wall temperature, the total tritium losses in the cooling water amounting to 1.2×10^{-4} Ci/d are negligible when compared to the target value of 0.1 Ci/d.

3.2.7.2 Purge gas system

In order to remove the tritium produced, helium is flushed through the breeding material at a pressure level of approx. 1 bar. To keep tritium permeation losses through the system walls of the purge gas system low, H_2 is injected into the purge gas to an H_2 partial pressure of 100 Pa.

After the separation of water in the room temperature adsorber, hydrogen isotopes are removed from the purge gas in a Pd/Ag-permeator. The permeated hydrogen is initially stored in a getter (uranium powder as getter material) and transferred to the isotope separation system on regeneration of the getter.

The utilization of a partial section of the purge gas loop (pipes, main cooler, blower) for emergency cooling of the test plug at a pressure level of approx. 1 bar is compatible with the design for the purging case with acceptable effects on the design requirements of main cooler and blowers. Therefore, a separate emergency cooling system is not necessary.

With reference to the permeator and hydrogen getter planned for the purge gas system, additional R + D work must be performed to verify their design.

Tritium losses at the purge gas loop

Low tritium permeation losses of approx. 5.3×10^{-3} Ci/d are determined for the entire purge gas loop.

This is essentially due to the following concept features:

- High H_2 injection and hence low T_2 partial pressure

- Non-insulated double pipe for the pipe section between the test plug and the wall penetration to the cooling loop room with rapid temperature reduction along the pipe section and hence low tritium permeation coefficient

- Omission of reheating of the purge gas on return to the breeding material.

References

1. R.D. PENZHORN, et al., A Catalytic Plasma, Exhaust Purification System, Fusion Technology, 14, 450 (1988)

2. N. P.KHERANI, W. T. SHMAYDA, Gas Handling Systems using Titanium-Sponge and Uranium Bulk Getters, Fusion Technology, Vol. 8, Sep. 1985

Helium Cooling Loop I

Helium Cooling Loop II

1	Test Plug
2	Dust Filter
3	Recuperative Heat Exchanger
4	He/H$_2$O Heat Exchanger
5	Blower
6	Electrical Heater

A	Cooling Water Supply
B	Evacuation System
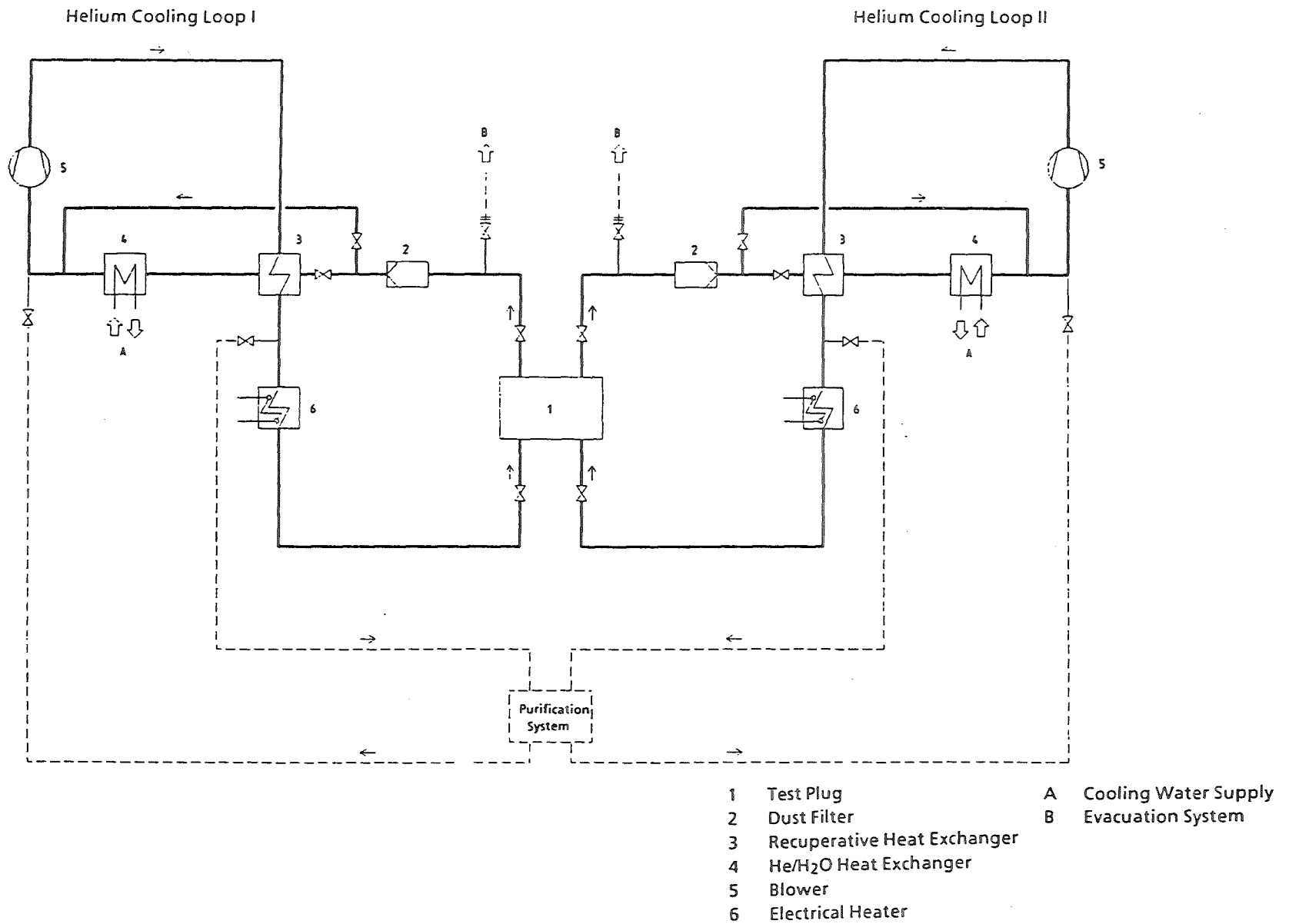
Fig. 3.2.1   Helium Cooling System for NET Test Plug with Canister Blanket

1	Fine Filter	A	Cooling Loop I
2	Electrical Heater	B	Cooling Loop II
3	CuO-Oxidizer	C	Helium Supply and Storage
4	He/H$_2$O Heat Exchanger	D	Cooling Water Supply
5	Water Separator	E	Oxigen Supply and Storage
6	Room-Temperature Adsorber	F	Water Discharge System
7	Recuperative Heat Exchanger	G	Adsorber Regeneration System (Purification System)
8	Low-Temperature Adsorber	H	LN$_2$ Supply and Storage
9	U-Bed (Hydrogen Getter)	I	Evacuation Nozzle
10	Blower		

Fig. 3.2.2   Helium Purification System for the NET Test Plug Cooling System

0.58 Ci/d

0.21 Ci/d

Helium
Purification System

Test Plug

5 Ci/d   1 Ci/d

5.2 Ci/d
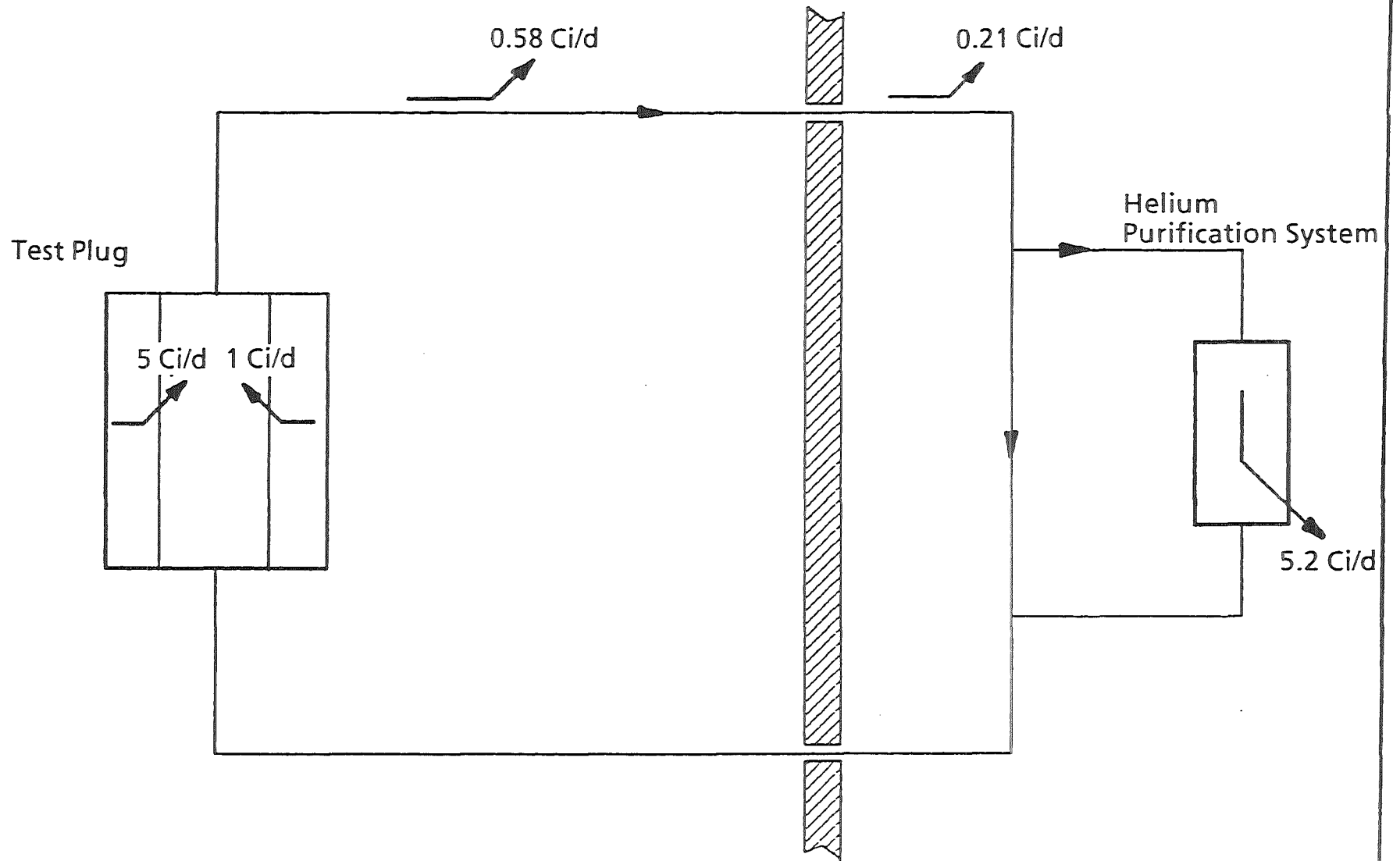
Fig. 3.2.3   NET Test Plug Cooling System;
Distribution of Tritium Loss Rates for one Cooling Loop

1   Test Plug
2   He/H$_2$O Heat Exchanger (Main Cooler)
3   Fine Filter
4   Room-Temperature Adsorber
5   Electrical Heater
6   Pd/Ag-Permeator
7   He/H$_2$O Heat Exchanger
8   Recuperative Heat Exchanger
9   Low Temperature Adsorber
10 Blower
11 He/H$_2$O Heat Exchanger
12 Vacuum Pump
13 Hydrogen Intermediate Storage (U-Beds)

A   Cold Water System
B   Helium Supply and Storage
C   Adsorber Regeneration System (Purge Gas System)
D   Cooling Water Supply
E   LN$_2$ Supply and Storage
F   Evacuation Nozzle
G   H$_2$ Supply
H   Monitoring System of Double-Wall Piping
I   Isotope Separation System
K   Pressure Relief System
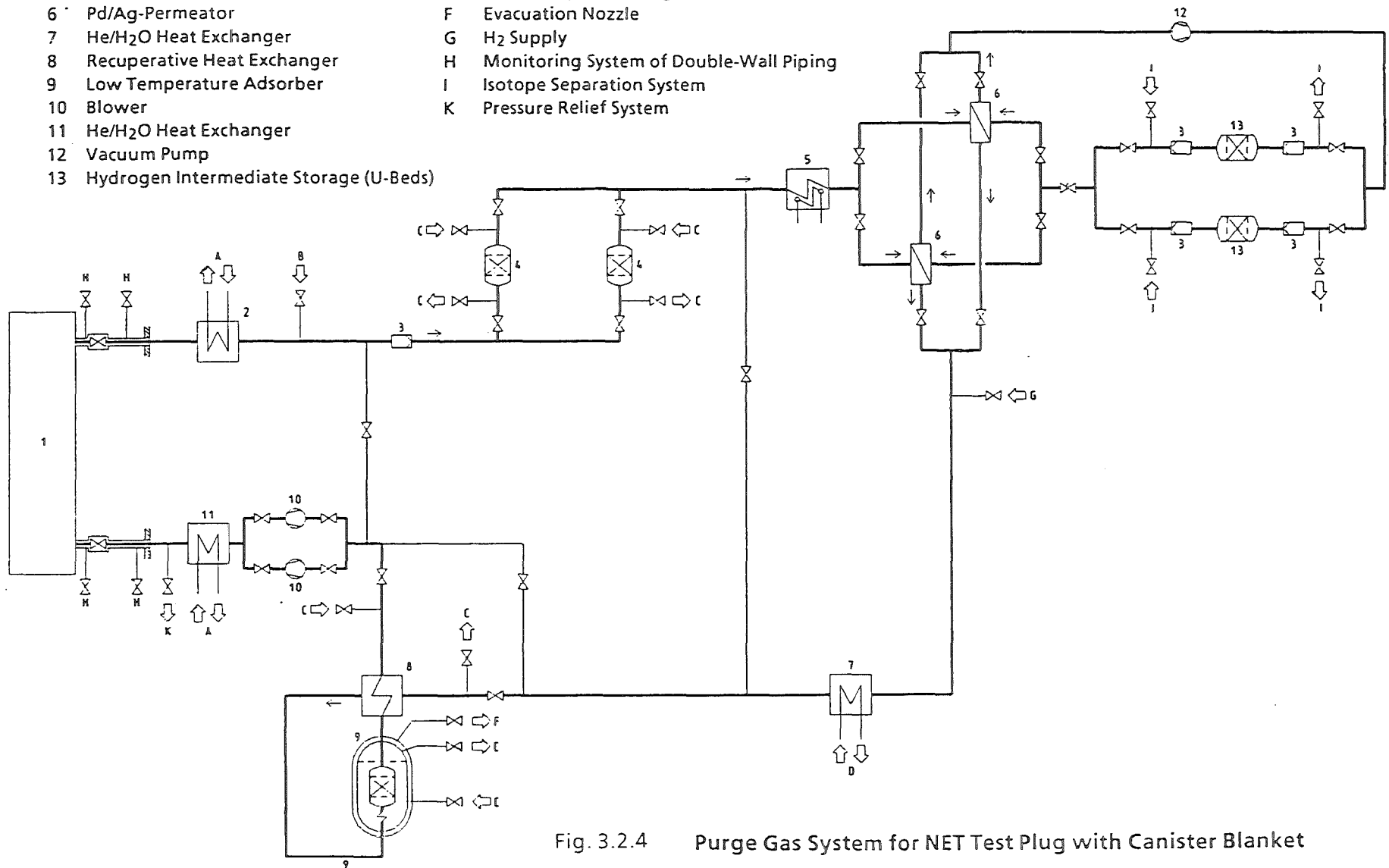
Fig. 3.2.4   Purge Gas System for NET Test Plug with Canister Blanket
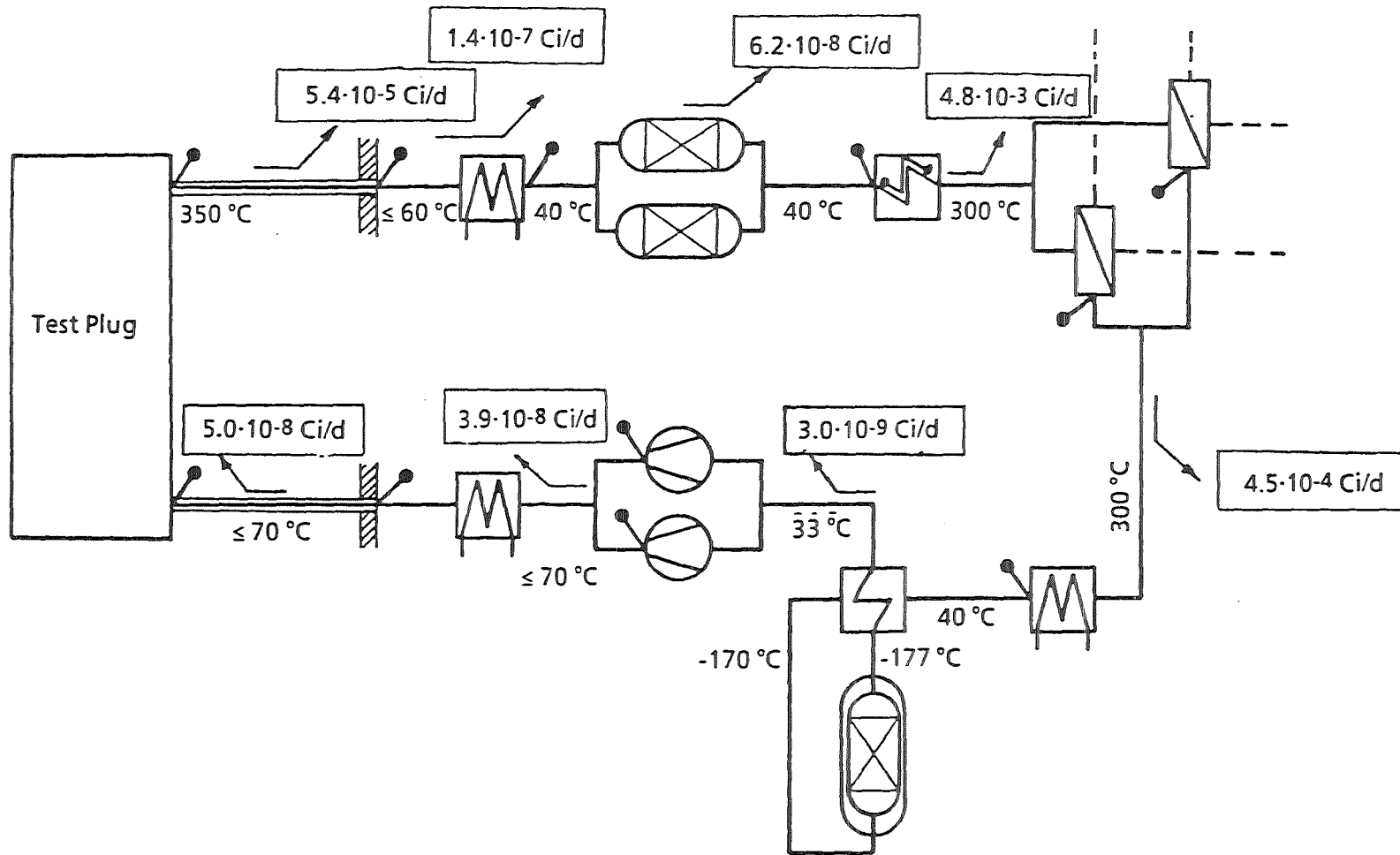
Fig. 3.2.5 NET Test Plug Purge Gas System;
Tritium Loss Rates

Purge Gas System

Cooling Loop I

Purification System
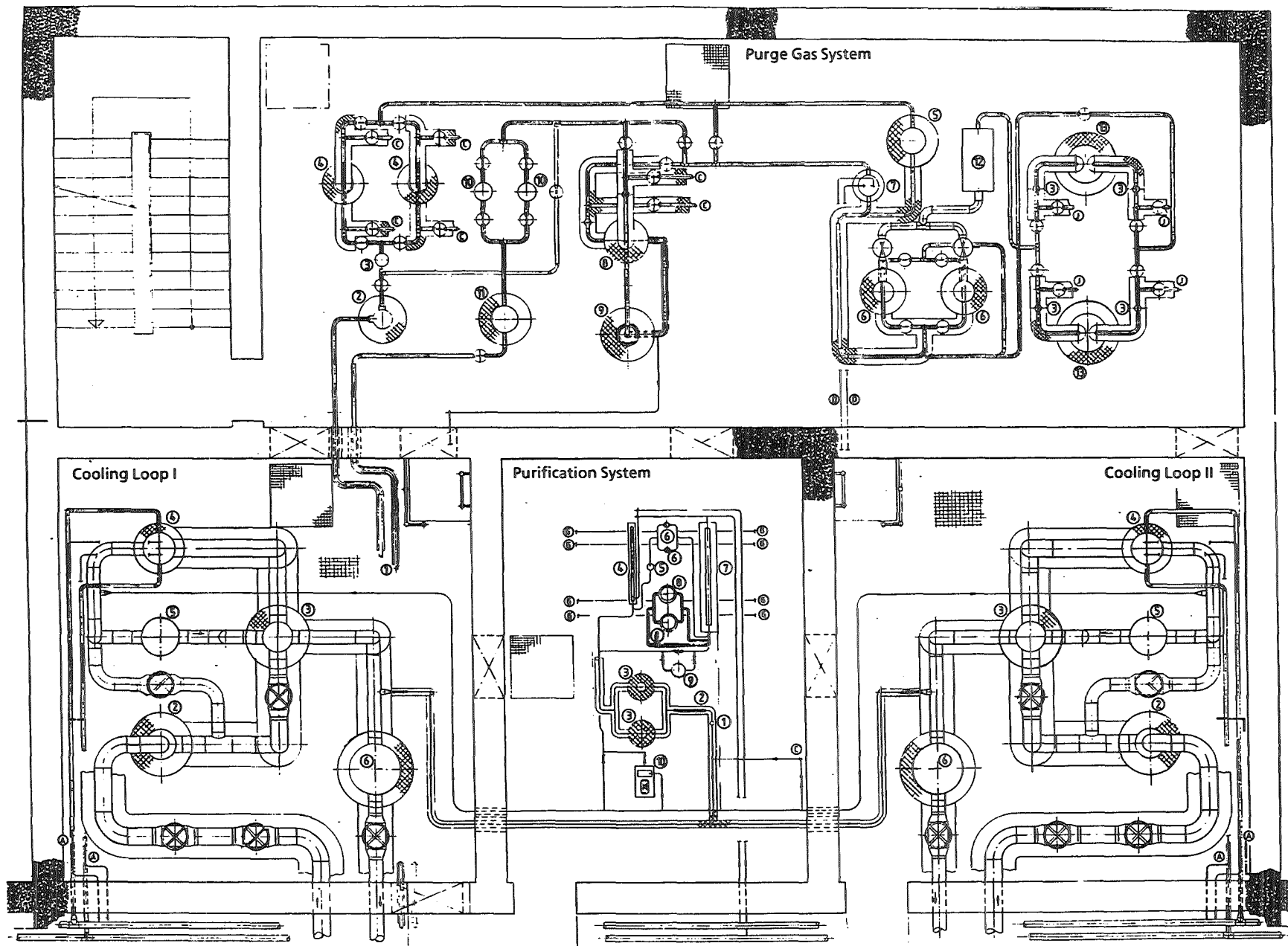
Cooling Loop II

Fig. 3.2.6 **NET Test Plug;**   **Arrangement of Rooms for the Main Systems**

Cooling Loop

1 Test Plug
2 Dust Filter
3 Recuperative Heat Exchanger
4 He/H_2O Heat Exchanger
5 Blower
6 Electrical Heater

A Cooling Water Supply

Purification System

1 Fine Filter
2 Electrical Heater
3 CuO-Oxidizer
4 He/H_2O Heat Exchanger
5 Water Separator
6 Room-Temperature Adsorber
7 Recuperative Heat Exchanger
8 Low-Temperature Adsorber
9 U-Bed (Hydrogen Getter)
10 Blower

C Helium Supply and Storage
D Cooling Water Supply
G Adsorber Regeneration System

Cooling Loop I

Purification System
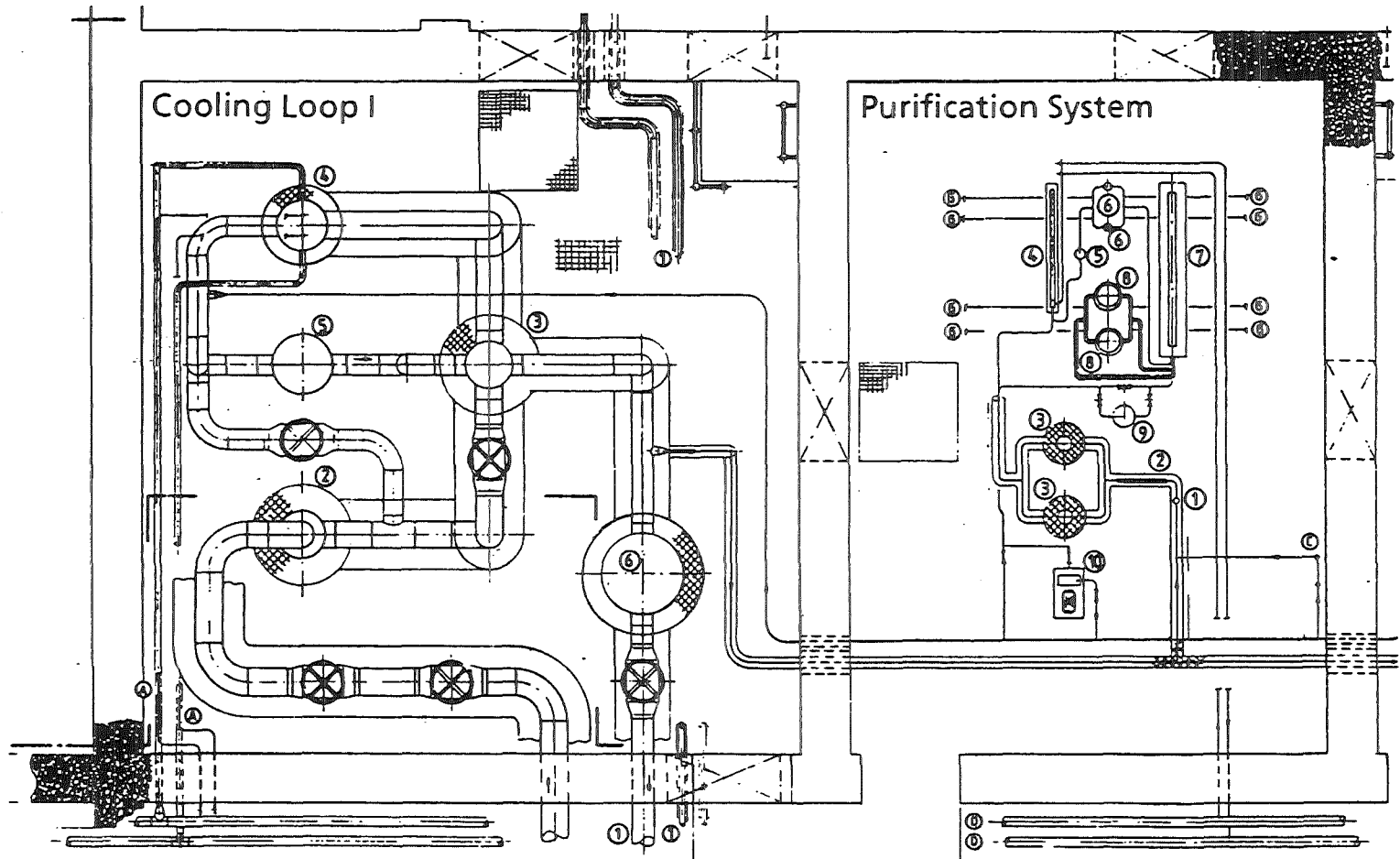
Fig. 3.2.7 **NET Test Plug;**
Arrangement of Components of Cooling Loop I and
Purification System
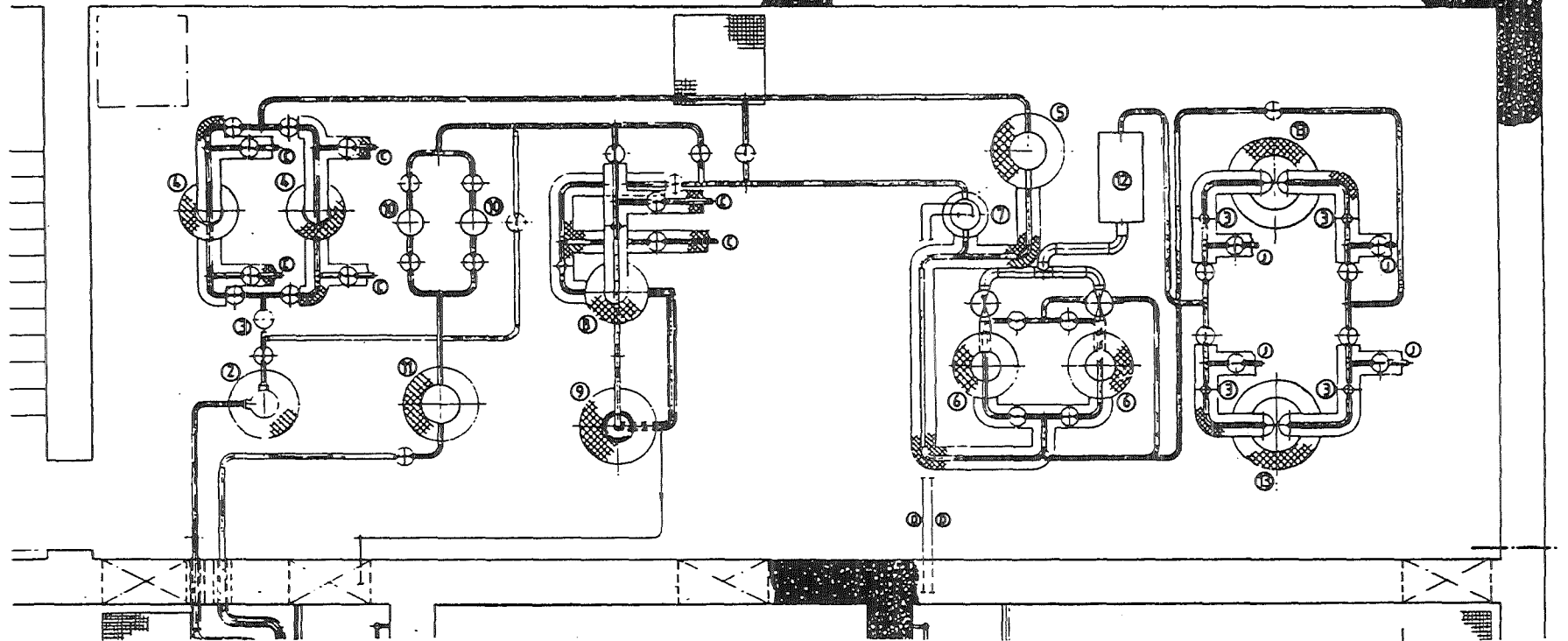
1	Test Plug	8	Recuperative Heat Exchanger	C	Adsorber Regeneration System (Purge Gas System)
2	He/H$_2$O Heat Exchanger (Main Cooler)	9	Low Temperature Adsorber	D	Cooling Water Supply
3	Fine Filter	10	Blower	I	Isotope Separation System
4	Room-Temperature Adsorber	11	He/H$_2$O Heat Exchanger		
5	Electrical Heater	12	Vacuum Pump		
6	Pd/Ag-Permeator	13	Hydrogen Intermediate Storage (U-Beds)		
7	He/H$_2$O Heat Exchanger				

Fig. 3.2.8 **NET Test Plug;**
Arrangement of Components of the Purge Gas System

4. STATUS OF THE R&D PROGRAM

4.1 Neutronics: Methods, Data and Experiments (U. Fischer, A. Schwenk-Ferrero, E. Wiegner, H. Giese, F. Kappler, U.von Möllendorff, T. Tsukiyama (Hitachi Eng. Co.))

4.1.1 General aspects

The neutronic calculations for the blanket layout are performed with the Monte Carlo transport code MCNP and nuclear data from the European Fusion File EFF-1 (see section 2.2). The application of the Monte Carlo transport procedure allows to model the geometrical arrangement of the blanket segments in the three-dimensional configuration of the Demo reactor. This is possible as the Monte Carlo procedure does not solve a transport equation, but it rather simulates individual neutron histories. Actually the Monte Carlo procedure is an appropriate description of the microscopic neutron transport phenomenon, which on principle is a stochastic process, where the interaction probability of a neutron and an atomic nucleus is described by means of the underlying nuclear cross-sections. Anologous to the physical reality the Monte Carlo procedure follows a neutron history from its birth in a (d, t)-fusion reaction to its death in an absorption reaction in the reactor components or by leakage out of the reactor system. All stochastic events (neutron birth, nuclear interaction processes, generation of secondary particles etc.) are simulated by sampling random numbers and taking into account the governing physical laws with their associated data.

In principle there are no restrictions imposed on the quality of this computational procedure: the accuracy of a specific calculational quantity depends on the number of events contributing to this quantity and, of course, on the involved nuclear cross-section data. In practice this means that a large number of neutron histories has to be followed in order to minimize the statistical uncertainty. Thereby use is made of the fact that the real behaviour of a statistical ensemble of neutrons is approached when a large number of neutron histories is considered. On modern large computers this is not a serious limitation for the accuracy; this even holds for "deep penetration problems", e.g. shielding calculations, if sophisticated variance reduction techniques are applied (see section 2.2.4).

Therefore, the accuracy of the calculated quantities (reaction rates, flux densities, power densities etc.) is limited mainly by the accuracy of the applied nuclear cross-section data. Considerable effort is being spent on improving the nuclear data base for neutronic calculations. Within the European Fusion Technology Programme this is performed in the EFF (European Fusion File)-project, while on a supranational level this is performed in the FENDL (Fusion Evaluated Nuclear Data Library)-project under the auspices of the IAEA.

With regard to tritium breeding in the solid breeder blanket, the most important nuclear data are those of ^{6}Li and Be: ^{6}Li acts as tritium breeding material (enriched to 90 atom %), Be serves as neutron multiplier. Thus the most important nuclear interaction processes are the ^{6}Li (n, a)t- and the Be (n, 2n)-reaction. Furthermore, the elastic scattering process of Be plays an important role: it dominates all other competing nuclear reactions in the high energy range and slows down fast neutrons very efficiently. Elastic scattering processes, therefore, determine the neutron transport in beryllium to a large extent.

The nuclear cross-section of the ^{6}Li (n, a)t-reaction is of the well known 1/v-type with a broad resonance at 0.25 MeV neutron energy; its accuracy is surely sufficient. The cross-section data of the Be (n, 2n) reaction are thus the main sources of data uncertainties with respect to the uncertainty of the TBR-calculation for the solid breeder blanket. This holds for the magnitude of the (n, 2n) cross-section itself and, even more, for the angle and energy distributions of the secondary neutrons, which are referred to as double-differential neutron emission cross-sections (DDX-data). Actually the Be (n, 2n)-reaction represents a rather complex system of several two- and three-particle break-up reactions leading to two neutrons and two a-particles. The energy and angle distribution of the two neutrons is crucial for their further history. To a large extent it determines the probability for inducing a further (n, 2n)-reaction, the probability for a useful absorption in ^{6}Li, which usually is mixed with beryllium, and the probability for leaking from the beryllium. A proper description of the energy-angle distribution of the emitted neutrons requires to take into account the angle-energy correlation between incident and emitted neutrons, i.e. the use of DDX-data.

4.1.2 Beryllium DDX-data and their use in transport calculations

The EFF-1 data file, used in the neutronic calculations for the blanket layout, contains the beryllium data evaluation of Young and Stewart /1/. Essentially this is a numerical fit to experimental DDX-data using smooth inter- and extrapolations. The angular dependence is described by a truncated Legendre polynomial series expansion. For representing the DDX-data on the data file the so-called "pseudo-level" representation is used: for a series of excitation energy bins the excitation cross-sections and their associated angular distributions are given. Thus the DDX-data are represented like single-differential (angular) distributions for discrete excitation energies. The EFF-1 beryllium DDX-data therefore can be used in the conventional way both in deterministic and probabilistic transport codes. Note, however, that the pseudo-level representation of DDX-data really is an approximation.

The ENDF/B-VI beryllium data evaluation /2/, released only recently, uses a more appropriate representation of the DDX-data: the correlated energy-angle distributions of the scattered neutrons are given as tabulated functions in the laboratory system, i.e. pointwise in energy and angle. The energy-angle distributions have been obtained by modelling the kinematics of the various many-particle break-up reactions by means of a Monte Carlo technique. Thus the ENDF/B-VI Be data evaluation provides a genuine description of the energy- and angle distribution of the scattered neutrons without making use of the usually applied Legendre fit approximation. At present there are, however, only few possibilities to use these data appropriately in the transport calculations: the Monte Carlo code MCNP /3/, which is the main computational tool for the neutronic blanket layout, is not able to handle DDX-data; deterministic S_N-transport codes (e.g. ONETRAN /4/, ANISN /5/) rely on the use of the Legendre approximation for the scattering kernel. Thus the beryllium scattering matrices have to be provided in the Legendre approximation. This is done by means of the NJOY processing code /6/, which, in the case of the ENDF/B-VI beryllium data, performes a numerical Legendre fit to the angular tabulated DDX-data. Thus a great advantage of the ENDF/B-VI Be-data evaluation is lost in the processing procedure.

At KfK a S_N-transport procedure with rigorous treatment of the neutron scattering has been developed. It avoids the usually applied Legendre approximation of the scattering kernel through the use of angle-dependent scattering matrices. In

this case the scattering integral is numerically integrated using the Gauss-Tchebychev quadrature procedure. Using this calculational method both one- and two-dimensional transport programmes, called ANTRA1 and ANTRA2, respectively, have been developed /7/. A similar calculational procedure originally had been developed by Takahashi and Rusch for one-dimensional spherical geometry /8/. The rigorous S_N-transport procedure takes fully into account the angular dependence of the underlying cross-sections without making use of the Legendre approximation. Therefore it is an appropriate tool for benchmarking methods and data describing the neutron transport in beryllium.

4.1.3 Beryllium benchmark calculations

Benchmark calculations are performed for the neutron leakage spectra of beryllium spherical shells with a central 14 MeV neutron source. Figs. 4.1.1 and 4.1.2 show the neutron leakage spectra, i.e. the lethargy-dependent neutron leakage current per source neutron, for a 30 cm thick beryllium spherical shell, obtained by rigorous S_N (ANTRA1) and approximative S_N/P_ℓ (ONETRAN) calculations using both EFF-1 and ENDF/B-VI beryllium data. In case of the EFF-1 data the spectra of the approximative S_N/P_ℓ-calculations converge towards the spectrum of the rigorous ANTRA1-calculation as the Legendre order is increased. In case of the 30 cm thick spherical shell there is perfect agreement when using the P_3-approximation, for a 5 cm thick spherical shell the P_1-approximation is sufficient /9/. The agreement between rigorous ANTRA1-calculations and approximative S_N/P_ℓ-calculations is due to the use of the Legendre approximation for the microscopic cross-section data on the EFF-1 file, although they are given in the centre-of-mass system. There is also perfect agreement with the leakage spectra calculated by MCNP with EFF-1 beryllium data (not shown). Thus it can be concluded that the rigorous S_N-procedure in spherical geometry is qualified for describing the 14 MeV neutron transport in beryllium.

Using ENDF/B-VI beryllium data there are, however, remarkable differences between S_N/P_ℓ-calculations and the rigorous S_N-calculation: as the Legendre oder is increased, the spectra of the S_N/P_ℓ-calculations converge towards a limit, which is different from the spectrum obtained with the rigorous ANTRA1-calculation (note that the P_3-calculation already agrees with the P_5-calculation). Obviously the P_ℓ-approximation is inadequate for the description of the 14 MeV neutron

transport in beryllium if the underlying nuclear data are given in an appropriate angular representation without making use of the Legendre approximation. The inadequacy of the S_N/P_ℓ-calculations therefore reflects the deficiencies of the numerical Legendre fit approximation to the pointwise tabulated ENDF/B-VI DDX-data, introduced by the data processing procedure. The same behaviour is observed in case of the two-dimensional neutron transport in cylindrical beryllium slabs /10/. Thus there is a clear need to avoid the Legendre fit approximation for beryllium: this holds for both deterministic and probabilistic transport codes. This is not really a problem for the Monte Carlo Code MCNP, as it uses angle-dependent scattering intervals, which in principle is equivalent to using angle-dependent scattering matrices in the rigorous S_N-procedure. The problem for MCNP, however, is that it cannot treat energy-angle correlated neutron emission cross-sections. Therefore, MCNP should be enabled to handle DDX-data.

4.1.4 Comparison to integral experiments

There are only few integral experiments appropriate for benchmarking the 14 MeV neutron transport in beryllium: There are two measurements of the neutron leakage spectrum for a 5 cm thick spherical shell with the time-of-flight method in the energy range 0.35 to 15 MeV /11/ and 6 to 15 MeV /12/. Fig. 4.1.3 shows the exprimental data points along with the neutron leakage spectra obtained with rigorous ANTRA1-calculations using both ENDF/B-VI and EFF-1 data. In the measured energy range the EFF-1 data obviously give slightly better agreement with the measured spectra than the ENDF/B-VI-data. This holds especially for the energy region around 1 - 2 MeV, which is mainly populated by secondary neutrons from the (n, 2n)-reaction. Note, however, that the experimental error, not given in the figure, is rather large in this energy region (typically 10 to 15 %). The more recent experiment /12/ gives a better resolution of the source peak and supports the EFF-1 evaluation also in the high energy region around 10 MeV.

Obviously there is a clear need for more experimental information on the neutron leakage spectra over the whole energy range, from thermal energies to 14 MeV, for thin and, even more, for thick beryllium spherical shells. Actually, such an experiment is underway at KfK /13/. Preliminary results for the leakage spectrum from a 17 cm thick spherical beryllium shell are presented, for the sake of clarity, in two separate figures. Fig. 4.1.4 shows the data in the energy win-

dows 2.45 meV to 100 keV, obtained by a time-of-flight technique, and 3.3 MeV to 15 MeV, obtained by proton-recoil spectroscopy with a scintillation detector. Fig. 4.1.5 shows the data at intermediate energies, obtained with several different proton-recoil proportional counter tubes. The calculated spectrum in both of the figures is a three-dimensional EFF-1 based MCNP result. Quantitative comparison /13/ shows that the calculation overestimates the measured leakage by 12 % in the 2.45 meV to 100 keV window but underestimates it by roughly 10 % in the 10 keV to 3.5 MeV window. In the 3.3 MeV to 15 MeV window, good agreement is found. Calculations with ENDF/B-VI beryllium data could not be performed as MCNP cannot handle them.

It is, however, possible to draw some conclusions on the basis of one-dimensional calculations with EFF-1 and ENDF/B-VI beryllium data /10/. EFF-1 data produce more neutrons in the low energy range than ENDF/B-VI data do due to a higher component of the 14 MeV neutron emission cross-section at low secondary neutron energies. This component, however, is due to the numerical interpolation procedure applied in the beryllium evaluation of Young and Stewart; it does not appear in the ENDF/B-VI evaluation due to kinematic limits. Actually this component is responsible for the overestimation of the low energy neutron leakage spectrum in the KfK-experiment. Using ENDF/B-VI beryllium data, therefore, should result in a better reproduction of this low energy neutron spectrum. On the other hand, the 14 MeV (n, 2n) cross-section in ENDF/B-VI has been reduced by about 15 % with respect to EFF-1. This directly reflects into the population of the neutron leakage spectrum around 1 - 2 MeV (see fig. 4.1.3). The preliminary data from the KfK experiment /13/ in this energy region are roughly 10 % above the EFF-1 result (Fig. 4.1.5). Therefore, even allowing for an experimental normalization uncertainty of these data of about ± 10 %, the Be (n, 2n) cross section value in EFF-1 appears to be closer to reality than the one in ENDF/B-VI. However, it is not possible, on the basis of the presently available leakage spectrum measurements, to draw a final conclusion on the quality of the beryllium data evaluations. This will require more precise experimental data. The corresponding measurements are in progress at KfK and elsewhere.

There are, furthermore, measurements of the angular neutron flux distributions for a cylindrical beryllium slab irradiated with 14 MeV neutrons /14/. This represents a two-dimensional transport problem that can be treated by means of the ANTRA2-code in cylindrical (r, z)-geometry. Fig. 4.1.6 shows the neutron leakage spectra of a 5.08 cm thick beryllium slab at an angle of 41.8° obtained by

rigorous ANTRA2-calculations in S_{16} angular segmentation with both ENDF/B-VI and EFF-1 data. Obviously the reproduction of the experimental spectrum is better with EFF-1 data than with ENDF/B-VI ones. This holds especially for the energy region around 1 MeV. This observation again suggests to increase the 14 MeV (n, 2n) cross-section in ENDF/B-VI.

4.1.5 Neutron multiplication factors

The magnitude of the (n, 2n) cross-section determines directly the neutron multiplication factor, which gives the number of secondary and primary neutrons produced per source neutron in a given material assembly. It is the most important integral quantity with respect to the use of a neutron multiplying material in fusion reactor blankets. Therefore considerable effort is spent on measuring the neutron multiplication factor in integral 14 MeV experiments. This can be achieved most appropriately in spherical shell experiments with a central 14 MeV neutron source by counting the number of neutrons leaking from the spherical shell per source neutron. In case of beryllium, there are, however, parasitic neutron absorptions due to the Be (n, α)- and (n, γ)-reactions; therefore, the number of neutrons leaving the beryllium assembly per source neutron is lower than the actual neutron multiplication factor. We refer to the number of leaking neutrons per source neutron and call it the neutron leakage multiplication factor.

Fig. 4.1.7 shows recent experimental results for the neutron leakage multiplication factors of beryllium spherical shells with thicknesses from 1.5 to 20 cm, along with calculational results obtained with rigorous ANTRA1-calculations using both EFF-1 and ENDF/B-VI data. The results of the INEL manganese bath experiment /15/ are rather well reproduced by the one-dimensional ANTRA1-calculations using ENDF/B-VI beryllium data. Actually this agreement is rather incidental as one-dimensional calculations tend to overestimate the neutron multiplication because they do not take into account neutron beam and detector channels, the neutron target assembly and supporting structures. Actually the results of the INEL-experiment are perfectly reproduced by EFF-1 based MCNP-calculations when using a precise three-dimensional model of the experiment /16/. One-dimensional ANTRA1-calculations, however overestimate the measured leakage multiplication factors by up to 7 % (19.9 cm thick beryllium spherical shell). Thus a precise three-dimensional calculation of the INEL-experiment with ENDF/B-VI

beryllium data clearly will underestimate the measured leakage multiplication factors.

The differences in the leakage multiplication factors calculated by ANTRA1 with EFF-1 and ENDF/B-VI data, on the other hand, amount to not more than 4 %. The (n, 2n)-reaction rates, obtained by summing up the neutron leakage and absorption rates, however differ by 15 %, corresponding to the difference of the 14 MeV (n, 2n) cross-section by the same amount. Thus the parasitic absorptions in beryllium are considerable larger for EFF-1 data than for ENDF/B-VI data: there is a difference of nearly a factor 3 in case of the 19.9 cm thick beryllium spherical shell.

This phenomenon is due to the large low energy component of the secondary energy distribution of the EFF-1 beryllium emission cross-section, leading to enhanced low energy neutron captures. In case of the 19.9 cm thick beryllium spherical shell more than one half of the parasitic absorptions are due to (n, γ)-reactions. Therefore, measurements of the neutron leakage factor are not sufficient for integral tests of the neutron multiplication power of beryllium: there is a need for measuring also the absorption rate in beryllium itself.

With respect to the "boron tank measurements" performed at the Kurchatov Institute of Atomic Energy (KIAE) for beryllium spherical shells with thicknesses between 1.5 and 8 cm /17/ there is agreement for both the EFF-1 and the ENDF/B-VI data within the experimental uncertainty (see Fig. 4.1.7). There is, however, also good agreement with calculations using ENDF/B-IV beryllium data /17/. Thus the differences in the calculated neutron leakage multiplication factors using different beryllium data evaluations actually are smaller than the experimental uncertainties. On the other hand, recent experiments performed at the South West Institute of Nuclear Physics and Chemistry (SWINPC) using the "total polyethylene absorption method" for beryllium spherical shells with thicknesses between 5 and 15 cm /18/ give up to 15 % lower leakage multiplication factors than the EFF-1 based calculations (see Fig. 4.1.7). Note, however, that the agreement between the different experiments is rather good for small thicknesses of the beryllium spherical shells.

4.1.6 Conclusions and recommendations

With respect to the neutron multiplication power of beryllium it has to be con-
cluded that it is presently not possible to draw a final conclusion on the quality of
the EFF-1 and ENDF/B-VI beryllium data evaluations, although their 14 MeV
(n, 2n) cross-sections differ by about 15 %. This is due to the fact that the larger
14 MeV (n, 2n) cross-section in EFF-1 primarily leads to enhanced low energy neu-
tron absorptions in beryllium itself; the neutron leakage multiplication factor,
which is actually measured in integral experiments, therefore differs only by 4 %
with respect to ENDF/B-VI. This difference, however, is within the experimental
uncertainty of neutron leakage multiplication factors. Therefore it is recommend-
ed to perform integral experiments on both the leakage multiplication factor and
the absorption rate in beryllium.

The 15 % difference in the 14 MeV (n, 2n) cross-section will produce, however, a
15 % difference in the beryllium (n, 2n)-reaction rate leading to a neutron multi-
plication factor differing by about 7 % for a typical fusion reactor blanket con-
figuration. A further uncertainty margin has to be added due to the uncertainty
of the Be DDX-data and their impact on the neutron multiplication power. Clearly
this rather large uncertainty of the neutron multiplication power, which is one of
the neutronic key parameters of a fusion reactor blanket, is not satisfactory. Thus
there is a strong need to obtain a more reliable assessment of the quality of the
beryllium data evaluations. This can be achieved on the basis of further integral
experiments. Measurements of the neutron leakage spectra of beryllium spheri-
cal shells with different shell thicknesses covering the whole energy range of the
leaking neutrons, as they are being performed at KfK /13/, are most appropriate
for this purpose.

References:

1. P.G. YOUNG, L. STEWART: "Evaluated Data for n + 9Be Reactions", Los Alamos National Laboratory, LA-7932-MS (July 1979)

2. S.T. PERKINS, E.F. PLECHATY, R.J. HOWERTON: "A Re-Evaluation of the 9Be (n, 2n) Reaction and its Effect on Neutron Multiplication in Fusion Blanket Applications", Nucl. Sci. Eng. 90 (1985), 83 - 98

3. J.F. BRIESMEISTER (Ed.): "MCNP - A General Monte Carlo Code for Neutron and Photon Transport, Version 3A", Report LA-7396-M, Rev. 2, Sept. 1986

4. T.R. HILL: "ONETRAN, a Discrete Ordinates Finite Element Code for the Solution of the One-dimensional Multigroup Transport Equation", Los Alamos National Laboratory, Report LA-5990-MS (1973)

5. W.W. ENGLE: "A User's Manual for ANISN, a One-dimensional Discrete Ordinates Transport Code with Anisotropic Scattering", Report K-1693, Union Carbide Corporation (1967)

6. R.E. MCFARLANE, D.W. MUIR and R.M. BOICOURT: "The NJOY nuclear data processing system", Vols. I, II, III, Los Alamos National Laboratory, Report LA-9303-M (May 1982)

7. A. SCHWENK-FERRERO: "Verfahren zur numerischen Lösung der Neutronen-transportgleichung mit strenger Behandlung der anisotropen Streuung", Kernforschungszentrum Karlsruhe, KfK-4788 (September 1990)

8. A. TAKAHASHI, D. RUSCH: "Fast Rigorous Numerical Method for the Solution of the Anisotropic Neutron Transport Problem and the NITRAN System for Fusion Neutronic Application", Parts I and II, KfK-2832/I, II (1979)

9. U. FISCHER, A. SCHWENK-FERRERO, E. WIEGNER: "Benchmark Analyses of 14 MeV Neutron Transport in Beryllium Using EFF-1 DDX-data", IAEA Advisory Group Meeting on the Nuclear Data for Neutron Multiplication in Fusion Reactor First Wall and Blanket Materials, Chengdu, P.R. China, November 19 - 21, 1990

10. U. FISCHER, A. SCHWENK-FERRERO, E. WIEGNER: "Analyses of 14 MeV Neutron Transport in Beryllium", contribution to 2. Int. Symp. on Fusion Nuclear Technology, June 2 - 7, 1991, Karlsruhe, F.R. Germany

11. A.A. ANDRASENKO et al.: "Measurement and Comparison with Calculations of Neutron Leakage Spectra from U, Pb, Be Spheres with Central 14 MeV Neutron Source", Proc. Specialists CMEA Meeting on Neutronics and Thermohydraulics of OTR Project, Varna, Bulgaria, May 5 - 7, 1987

12. B.E. LESHCHENKO et al.: "Time-of-Flight Measurement of Neutron Leakage Spectrum from a Beryllium Sphere with a Central 14 MeV Neutron Source", Kurchatov Institute of Atomic Energy, Report IAE-5230/8, Moscow 1990 (in Russian), presented at IAEA Advisory Group Meeting on the Nuclear Data for Neutron Multiplication in Fusion Reactor First Wall and Blanket Materials, Chengdu, P.R. China, November 19 - 21, 1990

13. H. EBI, W. EYRICH, H. FRIES, H. GIESE, K. HAYASHI, F. KAPPLER, U. von MÖLLENDORFF, T. TSUKIYAMA: "Measurement of Neutron Transport and Multiplication in Beryllium", contribution to 2. Int. Symp. on Fusion Nuclear Technology, June 2 - 7, 1991, Karlsruhe, F.R. Germany

14. Y. OYAMA, H. MAEKAWA: "Measurement and Analysis of an Angular Neutron Flux on a Beryllium Slab Irradiated with Deuterium-Tritium Neutrons", Nucl. Sci. Eng. 97, 220 - 234 (1987)

15. J.R. SMITH, J.J. KING: "Manganese Bath Measurements of the Neutron Multiplication in Bulk Beryllium", IAEA Advisory Group Meeting on the Nuclear Data for Neutron Multiplication in Fusion Reactor First Wall and Blanket Materials, Chengdu, P.R. China, November 19 - 21, 1990

16. J.W. DAVIDSON, M.E. BATTAT: "Calculation of the INEL Beryllium Multiplication Experiment", IAEA Advisory Group Meeting on the Nuclear Data for Neutron Multiplication in Fusion Reactor First Wall and Blanket Materials, Chengdu, P.R. China, November 19 - 21, 1990

17. V.A. ZAGRYADSKIJ et al.: "Calculated Neutron Transport Verifications by Integral 14-MeV Neutron Source Experiments with Multiplying Assemblies", Proc. First Int. Symp. on Fusion Nuclear Technology, Tokyo, Japan, April 10 - 19 (1988), Part B, 353 - 358

18. Yuan CHEN et al.: "Experiment of Neutron Multiplication in Beryllium", IAEA Advisory Group Meeting on the Nuclear Data for Neutron Multiplication in Fusion Reactor First Wall and Blanket Materials, Chengdu, P.R. China, November 19 - 21, 1990
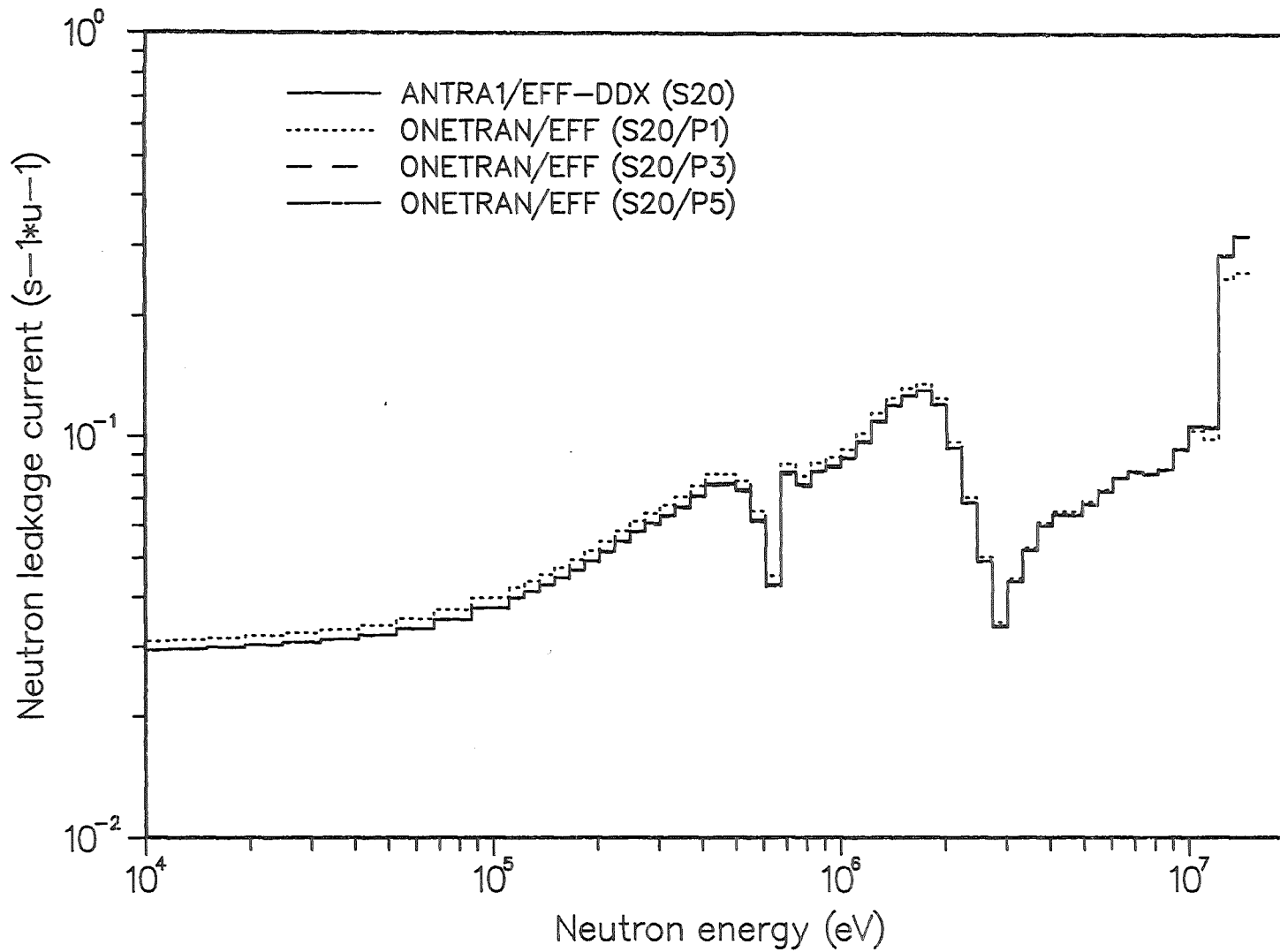
Fig. 4.1.1: Neutron leakage spectra of a 30 cm thick beryllium spherical shell: comparison between rigorous (ANTRA1) and approximative S_N/P_ℓ (ONETRAN)-calculations with EFF-1 DDX-data
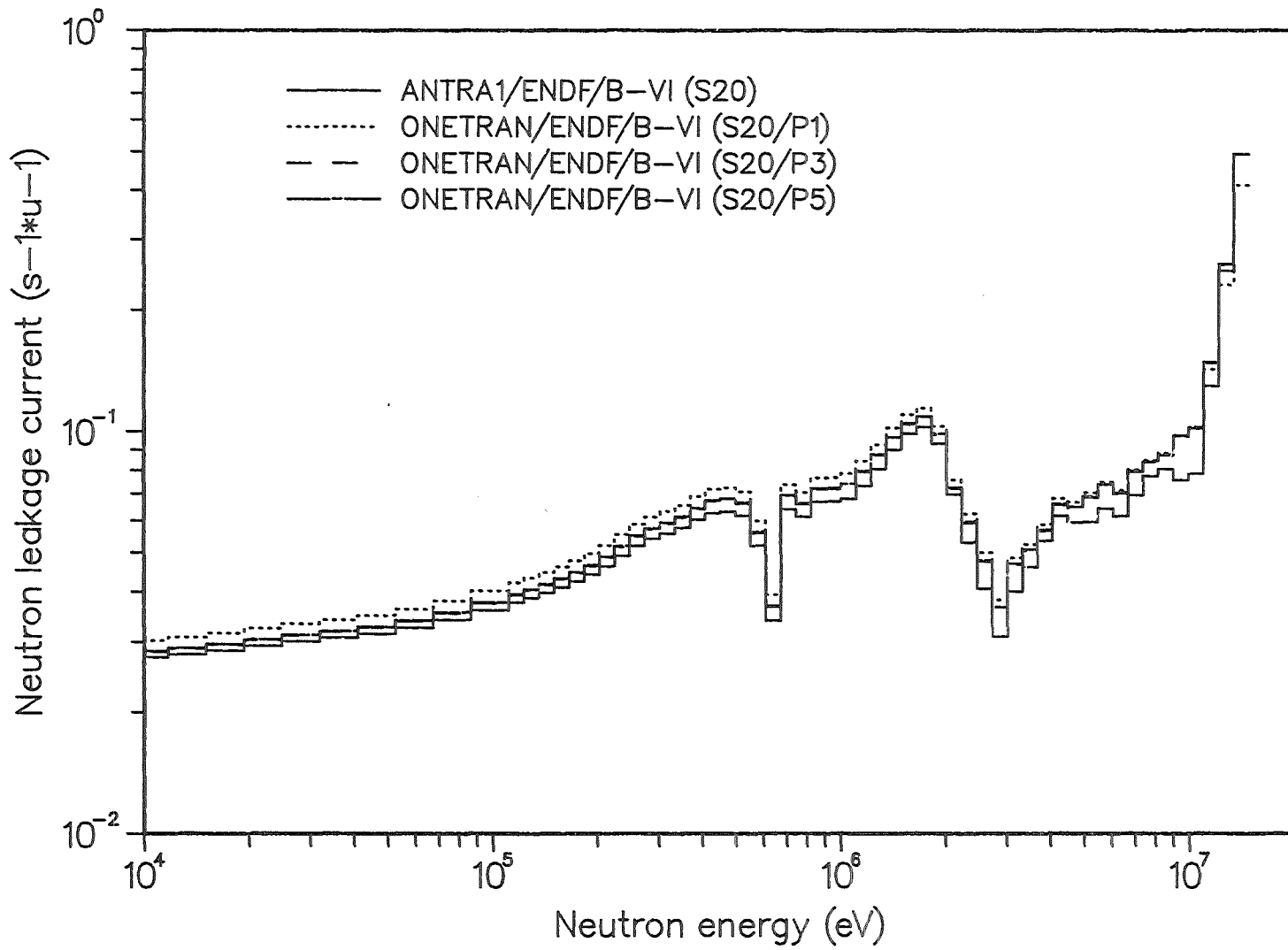
Fig. 4.1.2: Neutron leakage spectra of a 30 cm thick beryllium spherical shell: comparison between rigorous (ANTRA1) and approximative S_N/P_ℓ (ONETRAN)-calculations with ENDF/B-VI DDX-data (Note: the ONETRAN P_3- and P_5-calculations coincide)
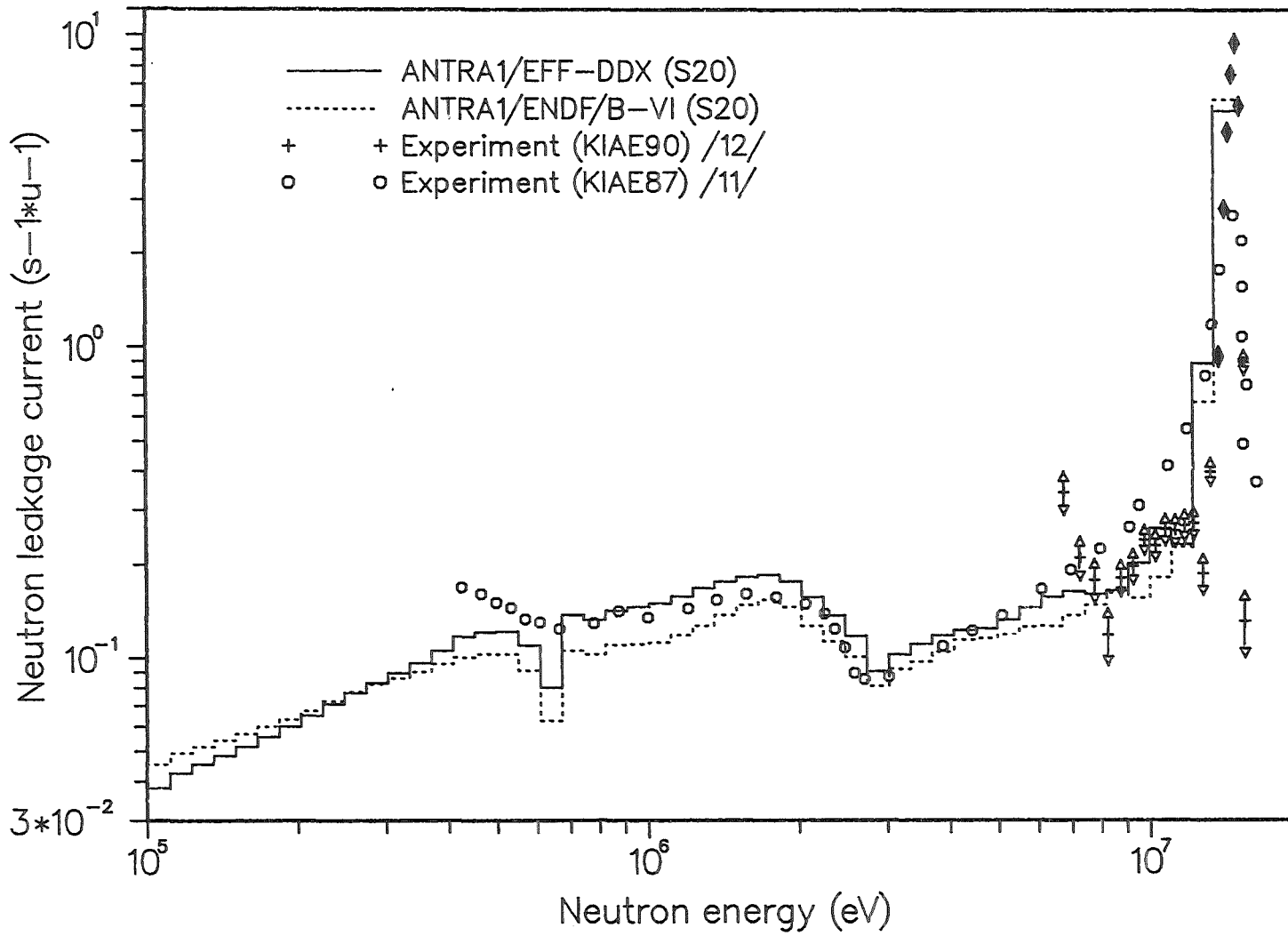
Fig. 4.1.3: Neutron leakage spectra of a 5 cm thick beryllium spherical shell: comparison between experimental data and rigorous ANTRA1-calculations with EFF-1 and ENDF/B-VI DDX-data
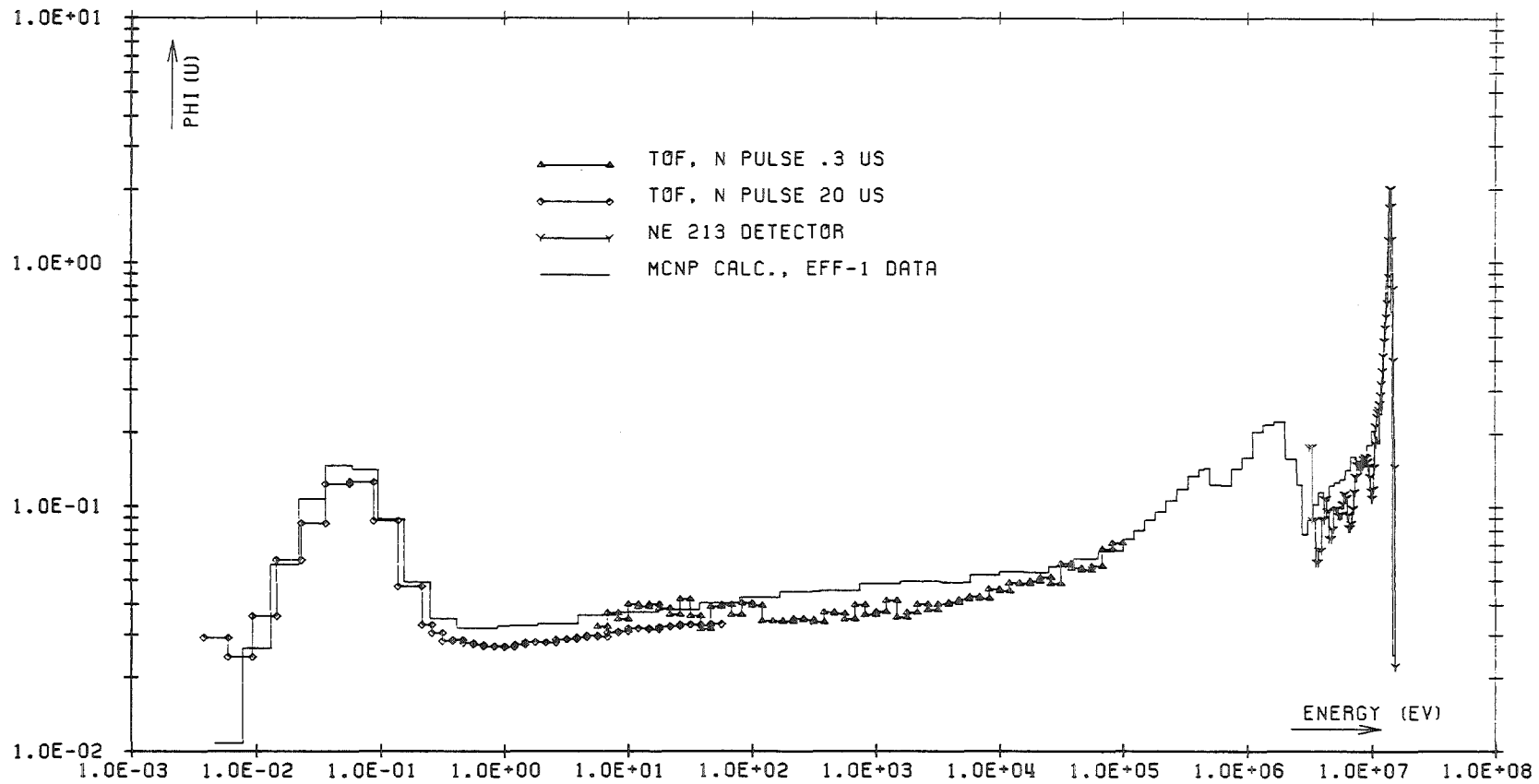
Fig. 4.1.4: Leakage spectrum (only time-of-flight and scintillator data) from 17 cm thick beryllium shell measured at KfK. The ordinate is leakage neutrons per unit lethargy per steradian per source neutron. Data labeled with neutron pulse widths are time-of-flight measurements. Calculated spectrum from MCNP-3A code with EFF-1 data library
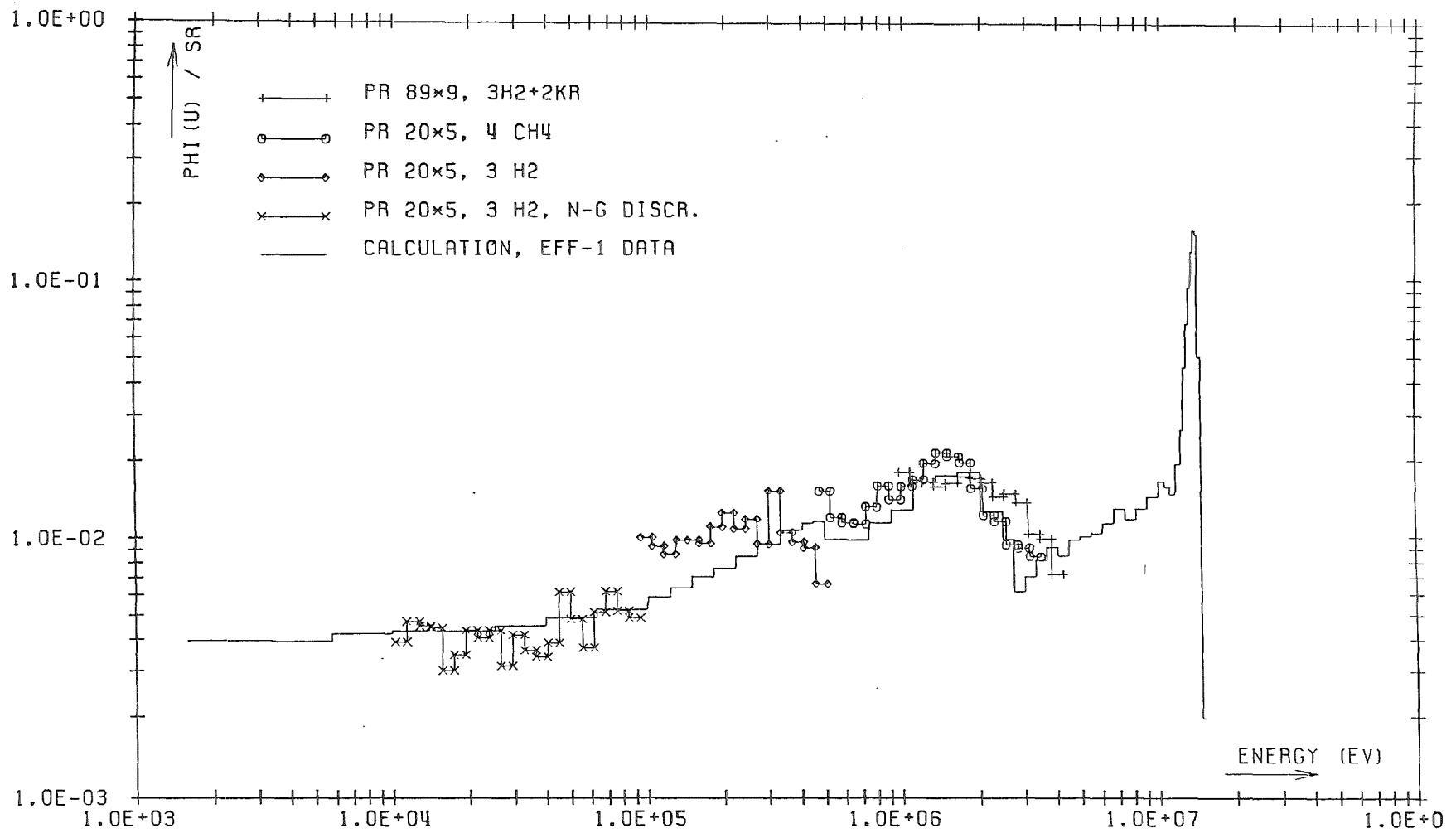
Fig. 4.1.5: Same as Fig. 4.1.4 but counter tube data (labeled PR). Note the different abscissa scale.
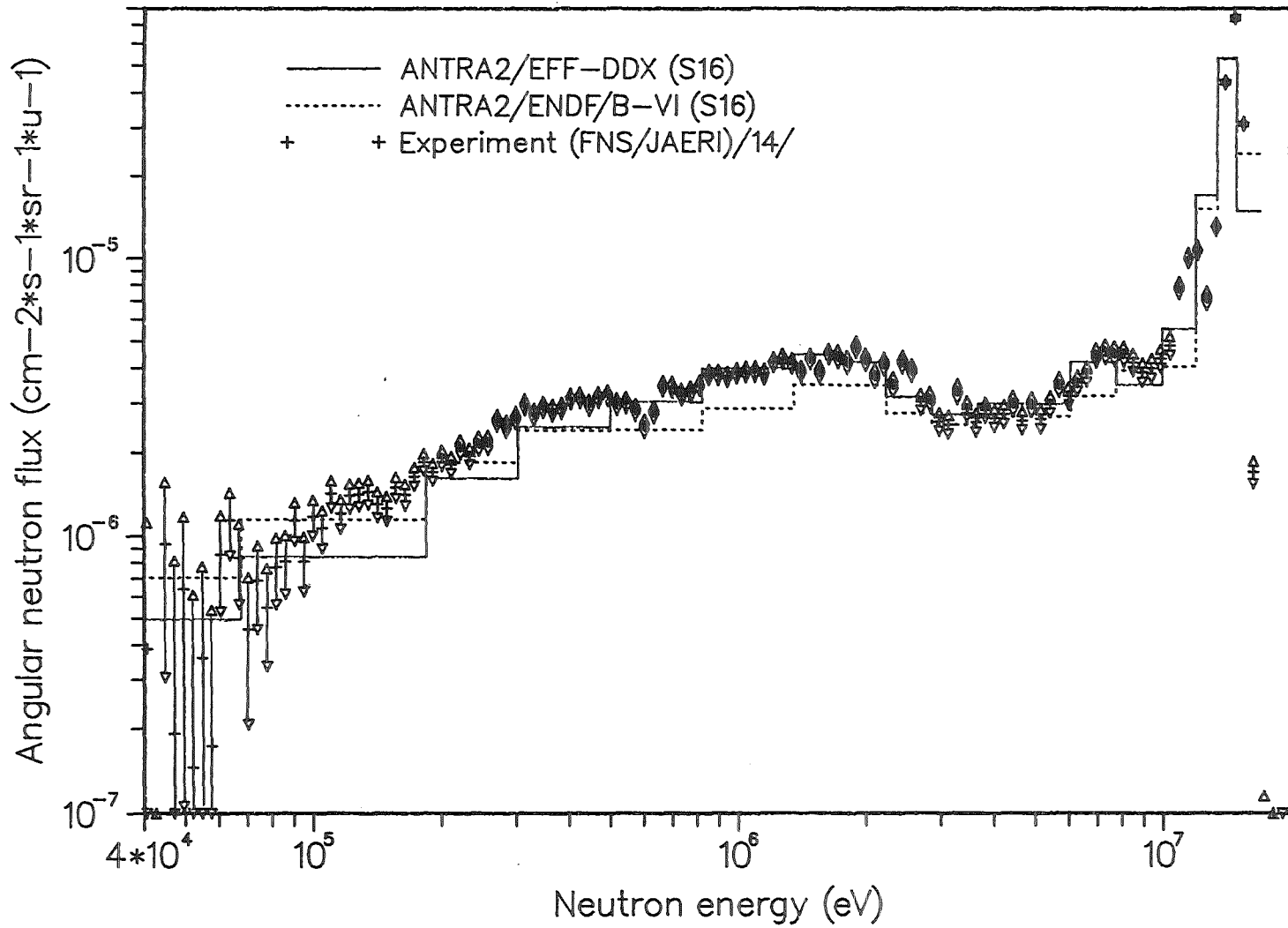
Fig. 4.1.6: Neutron angular flux distribution emitted from a 5.08 cm thick beryllium cylindrical slab at an angle of 41.8°: comparison between experimental data and two-dimensional ANTRA2-calculations

— 136 —
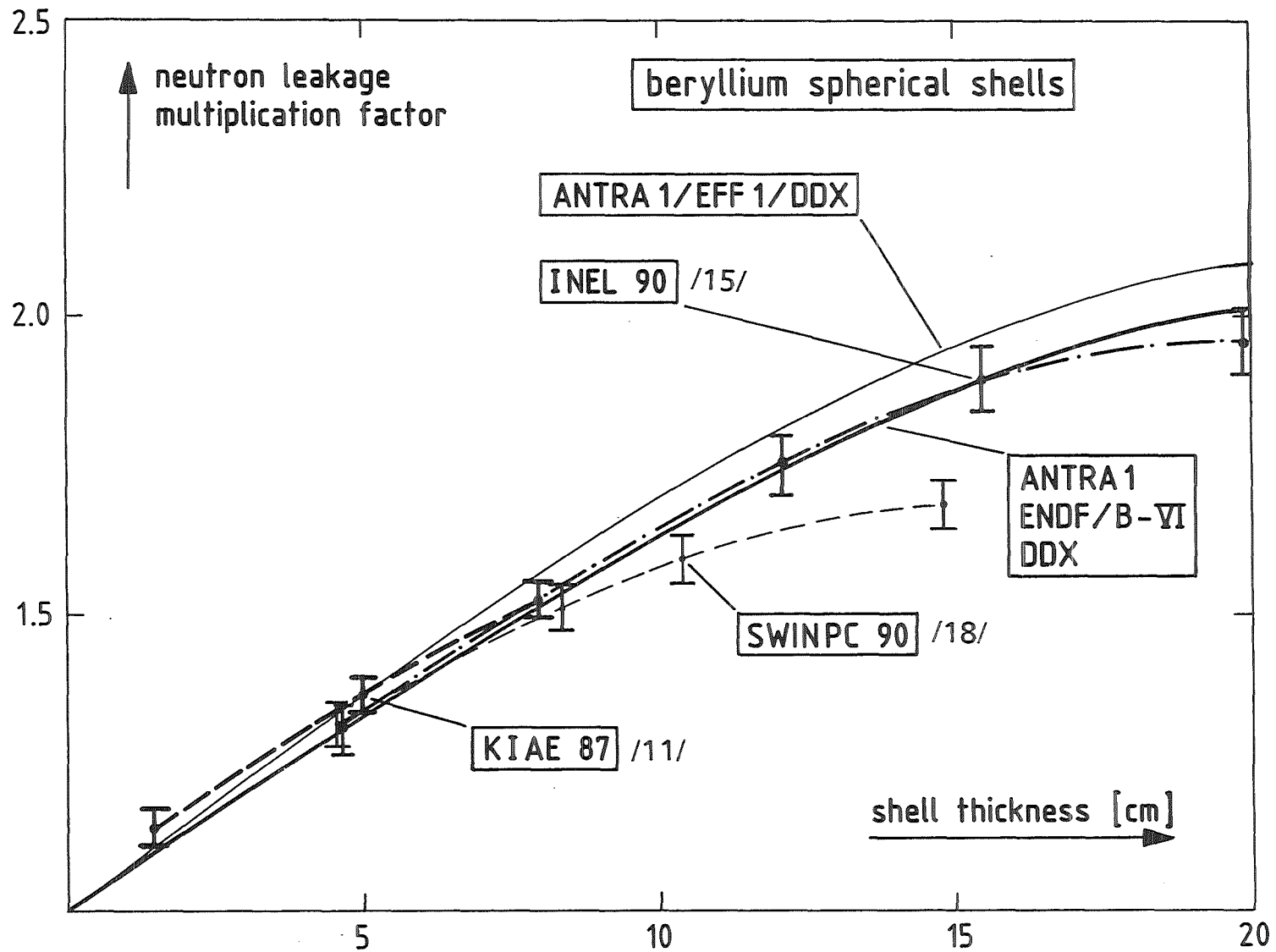
Fig. 4.1.7: Neutron leakage multiplication factors for beryllium spherical shells with a central 14 MeV neutron source: comparison between experimental data and one-dimensional ANTRA1-calculations

4.2　Lithium Orthosilicate (Li_4SiO_4) Properties

4.2.1　Thermophysical properties (B. Schulz)

The thermophysical behaviour of Li_4SiO_4 has to be seen on the background of the Li_2O-SiO_2 phase diagram (Fig. 4.2.1.1) and with respect to the preparation process of the densified material. Temperature and time during densification play a dominant role for the quality and properties of the resulting product. Two kinds of materials were investigated:

I　powder chemically precipitated, pressureless sintered for 6 hours at 1200 °C in air, density $\rho = 0.95\ \rho_{th}$

II　Li_4SiO_4 spheres from the melt, isostatically hot pressed for 10 min at 1200 °C and annealed in air for 4 - 6 h at 800 °C, $\rho = 0.99\ \rho_{th}$

Characterization

The sintered product investigated by differential thermal analysis (DTA) shows always the eutectic peak of the Li_4SiO_4 - Li_2SiO_3 (Fig. 4.2.1.1) - eutecticum at 1022 °C (Fig. 4.2.1.2), indicating a dissociation of Li_4SiO_4 during sintering. This never occurred with hot pressed samples. Correspondingly the microstructural analysis shows two very different products (Fig. 4.2.1.3a,b). Sintered samples (3a) in fact are composites made of two phases Li_2SiO_3 - Li_4SiO_4 (in our samples 13.0 vol.% Li_2SiO_3). The eutectic mainly composed of Li_2SiO_3 forms a matrix, which includes the grains of Li_4SiO_4. This was not observed in the hot pressed samples, but due to high grain size ($\sim$ 55 µm) and the lattice anisotropy of Li_4SiO_4 a widening of grain boundaries is always observed (3b). From these results of characterization it is to be expected:

1.　The sintered samples must have different thermal expansion coefficients α_{th} and thermal conductivity λ compared to the pure Li_4SiO_4 samples as shown in Fig. 3b. Furthermore it must valid

α_{th} (Li_4SiO_4) $</>$ α_{th} (Li_4SiO_4 sintered) $</>$ α_{th} (Li_2SiO_3)

λ (Li_4SiO_4) $</>$ λ (Li_4SiO_4 sintered) $</>$ λ (Li_2SiO_3)

2.　The grain boundary widening of the pure Li_4SiO_4 may influence especially the thermal conductivity, if measurements are carried out in different atmospheres.

Measuring conditions

All samples were preheated in vacuum at 300 °C for 8 - 12 hours to avoid influences of moisture during storage of samples. Property values <u>without</u> hysteresis could be attained by performing the experiments in inert atmosphere (Ar and/or He). For the determination of the thermal conductivity of the pure Li_4SiO_4 a special procedure was applied. After preheating, at 300 °C Ar or He was introduced into the equipment and the sample was held for 1 - 2 days under these conditions. After measurement, the gas was removed by pumping for 3 - 4 days at 300 °C. Then the gas was changed from Ar or He to He or Ar and the procedure as described repeated. Under these conditions we could not find an influence of the nature of the gas atmosphere on the thermal conductivity of the pure Li_4SiO_4, except one sample, the results of which is not shown below.

Specific heat

Specific heat data were measured with a Differential Scanning Calorimeter (DSC2). The results are shown in Fig. 4.2.1.4 and can be expressed as follows [2]:

Li_4SiO_4 $300 < T < 900$ K $c_p = 0.775 + 16.31 \cdot 10^{-4} T + 9000/T^2$ $J/g \cdot K$

Li_2SiO_3 $300 < T < 1000$ K $c_p = 1.504 + 2.803 \cdot 10^{-4} T - 44700/T^2$ $J/g \cdot K$

The data should be correct wihtin $\pm$ 2 %. They agree with experiments described in [3,4].

Thermal expansion

Data were evaluated in using differential dilatometry (Sapphire from NBS was the reference material) at isothermal conditions. Results are given in Fig. 4.2.1.5, showing cleraly the difference in thermal expansion for sintered and pure Li_4SiO_4. The data for $\Delta l/l_0$ should be correct within $\pm$ 3 %.

Conclusions:

Pure Li_4SiO_4 $\alpha_{th} = 1/l_0 \, dl/dT = + 31.2 \cdot 10^{-5}$ K^{-1} $\pm$ 5 %

Thermal conductivity

Measurements were carried out with a laser flash equipment determining the thermal diffusivity

$$\alpha = \frac{\lambda}{c_p \cdot \rho}$$

for conversion to conductivity the given specific heat data(Fig. 4.2.1.4) c_p and the density function according to the thermal expansion (Fig. 4.2.1.5) were used.

No porosity correction was performed for the pure Li_4SiO_4, while for the sintered Li_4SiO_4 the well known equation

$$\lambda_p = \lambda_0 (1 - P)^{3/2}$$

was applied, P - porosity, Index p, 0 refer to porous and dense material.

Fig. 4.2.1.6 shows the results. As was expected the sintered Li_4SiO_4 shows higher thermal conductivity than the pure material. To check for consistancy the equation

$$1 - c_{Li_4SiO_4} = \frac{\lambda_{Li_4SiO_4} - \lambda_{(Li_4SiO_4 + 13\,vol.\%\,Li_2SiO_3)}}{\lambda_{Li_4SiO_4} - \lambda_{Li_2SiO_3}} \cdot \sqrt[3]{\frac{\lambda_{Li_2SiO_3}}{\lambda_{(Li_4SiO_4 + 13\,vol.\%\,Li_2SiO_3)}}}$$

valid for the thermal conductivity of composites with spherical inclusions [5] was applied to calculate the thermal conductivity of pure Li_4SiO_4 in using the data for Li_2SiO_3 and the sintered Li_4SiO_4.

As one can see, the agreement between measured and calculated data for the thermal conductivity is fairly good.

The following value is recommed:

$$300 < T < 800 \text{ K } Li_4SiO_4 \ \lambda = (0.014 \pm 0.002) \text{ W/cmK}$$

In principle there is no difficulty to calculate with the thermal conductivity λ of Li_4SiO_4 and He the thermal conductivity of Li_4SiO_4-spheres surrounded by He. The equation is:

$$1 - c_{Li_4SiO_4} = \frac{\lambda_{Li_4SiO_4} - \lambda}{\lambda_{Li_4SiO_4} - \lambda_{He}} \sqrt[3]{\frac{\lambda_{He}}{\lambda}}$$

References

1. F. C. KRACEK, The binary System $Li_2O\text{-}SiO_2$, J. Phys. Chem. 34 (1930) 2641

2. R. BRANDT, B. SCHULZ, Specific heat of some Li-compounds, J. Nuc. Mater. 152 (1988) 178

3. G.W. HOLLENBERG, D.E. BAKER, Thermal properties of Li-ceramics for Fusion applications Hanford, HEDL-SA-2674FP (1982)

4. B. SCHULZ, Die Abhängigkeit der Feldeigenschaften 2-phasiger Werkstoffe von ihrem Gefügeaufbau, KfK-Report No. 1988 (1974)
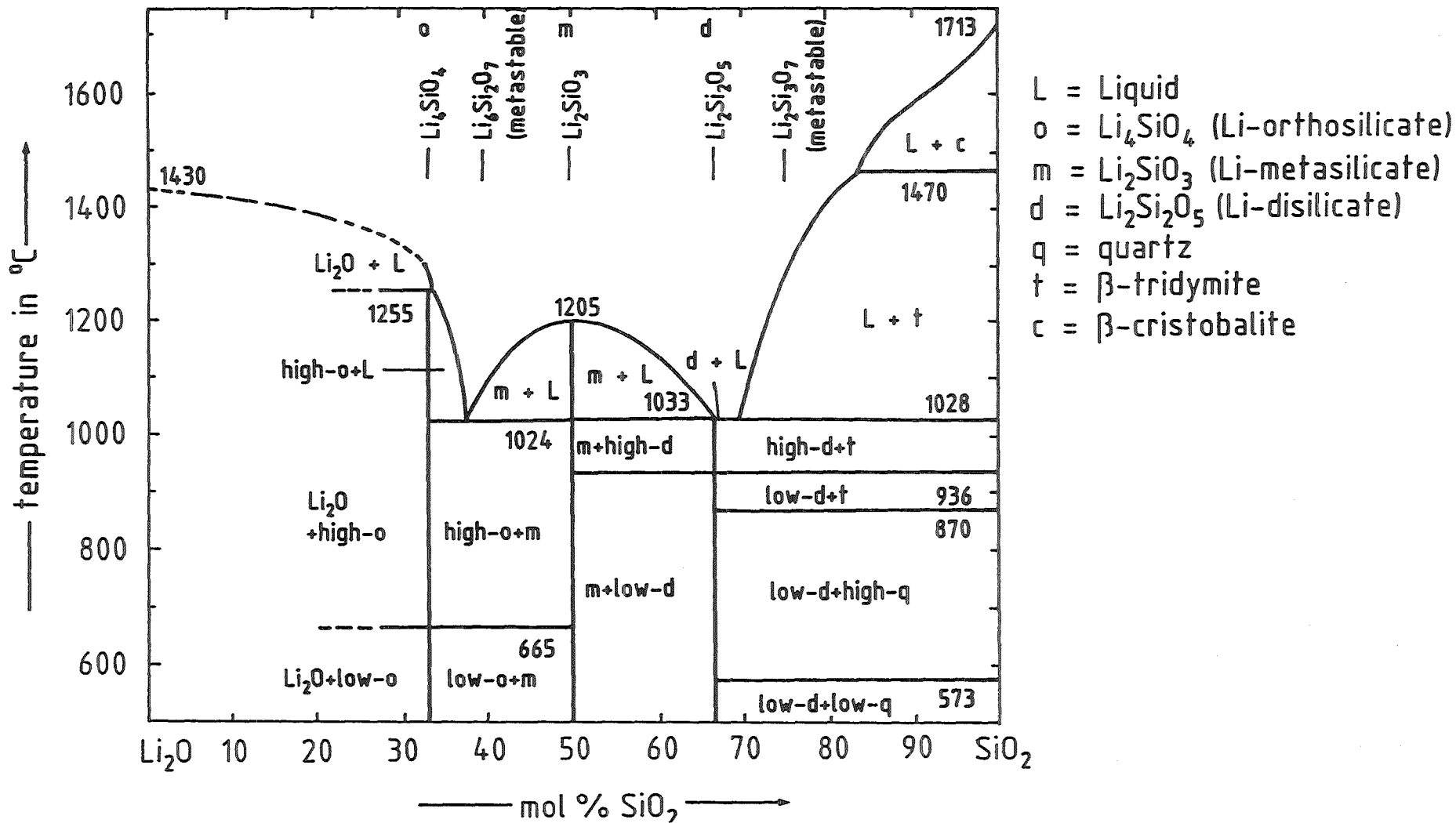
Fig. 4.2.1.1 : Phase diagram of the quasibinary system Li$_2$O-SiO$_2$ [1].
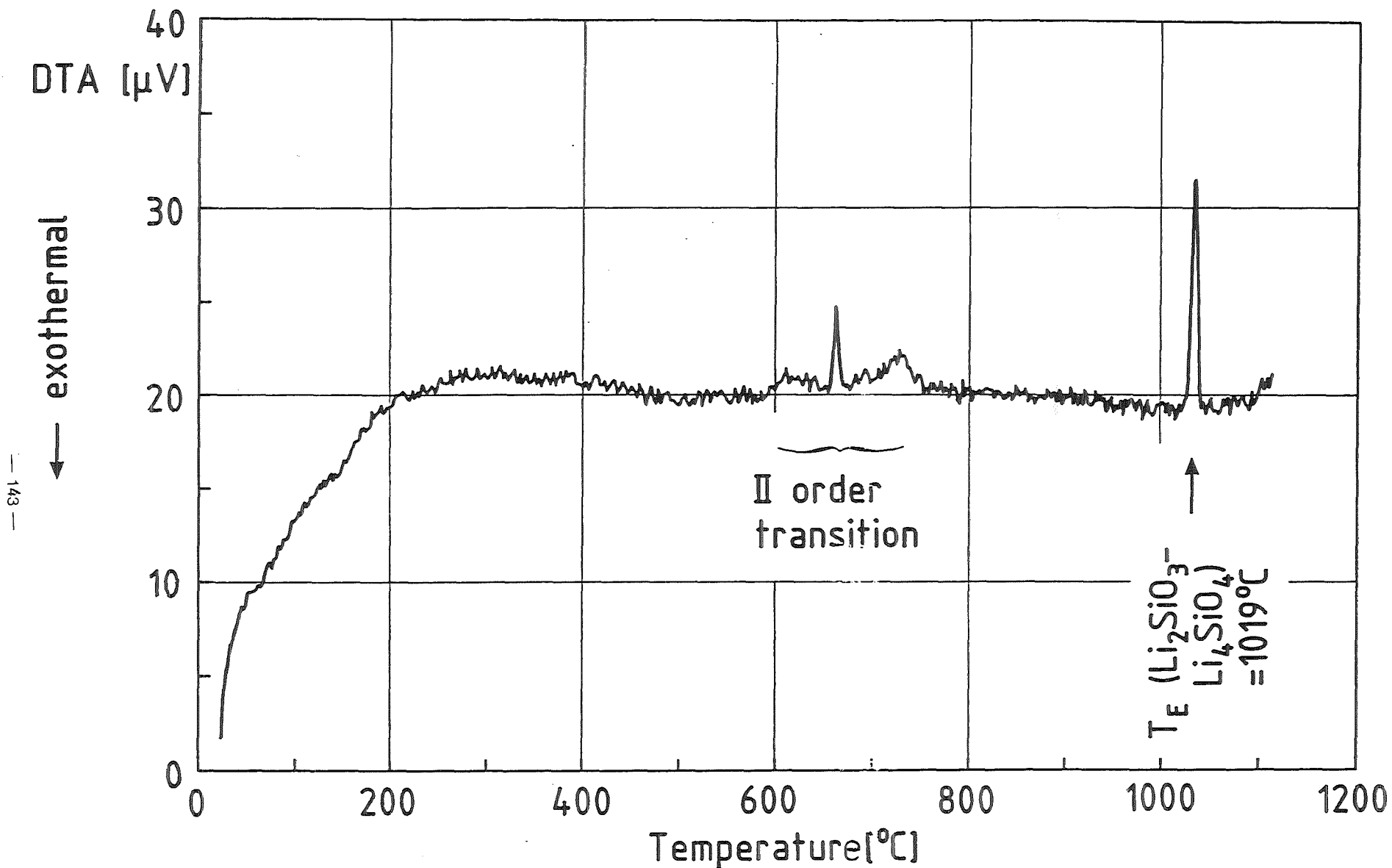
Fig. 4.2.1.2 : DTA of sintered Li_4SiO_4 (heating up) in He, showing eutectic reaction between Li_4SiO_4 and Li_2SiO_3.
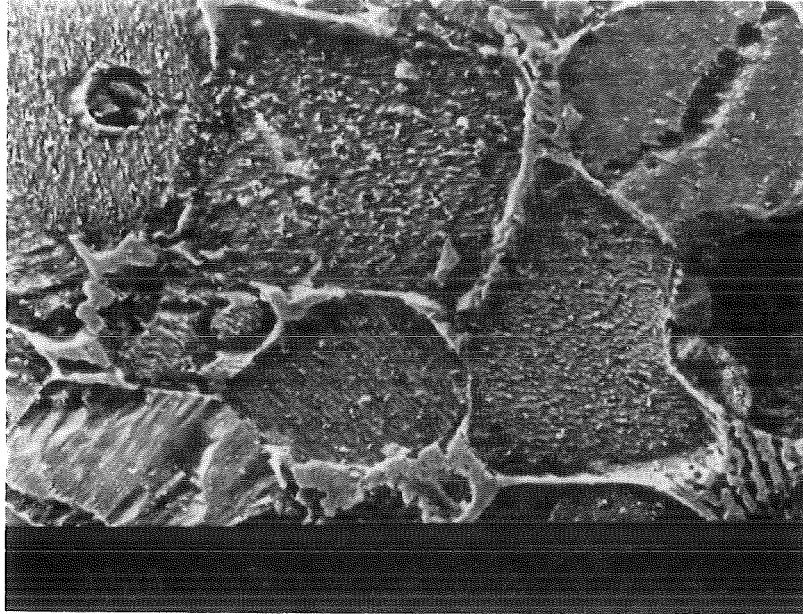
Fig 4.2.1.3a: Microstructure of sintered Li_4SiO_4 with Li_4SiO_4-Li_2SiO_3 eutectic at grain boundaries of Li_4SiO_4.
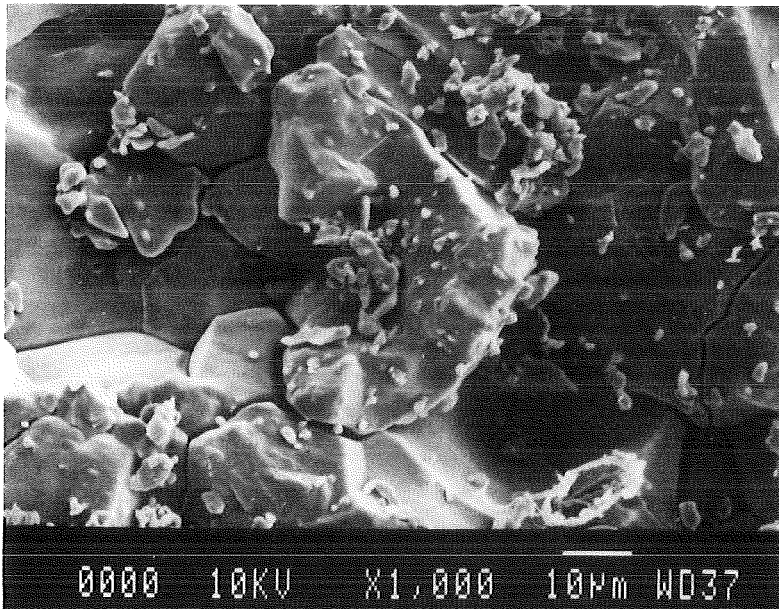
Fig. 4.2.1.3b: Microstructure of pure Li_4SiO_4, showing widening of grain boundaries.
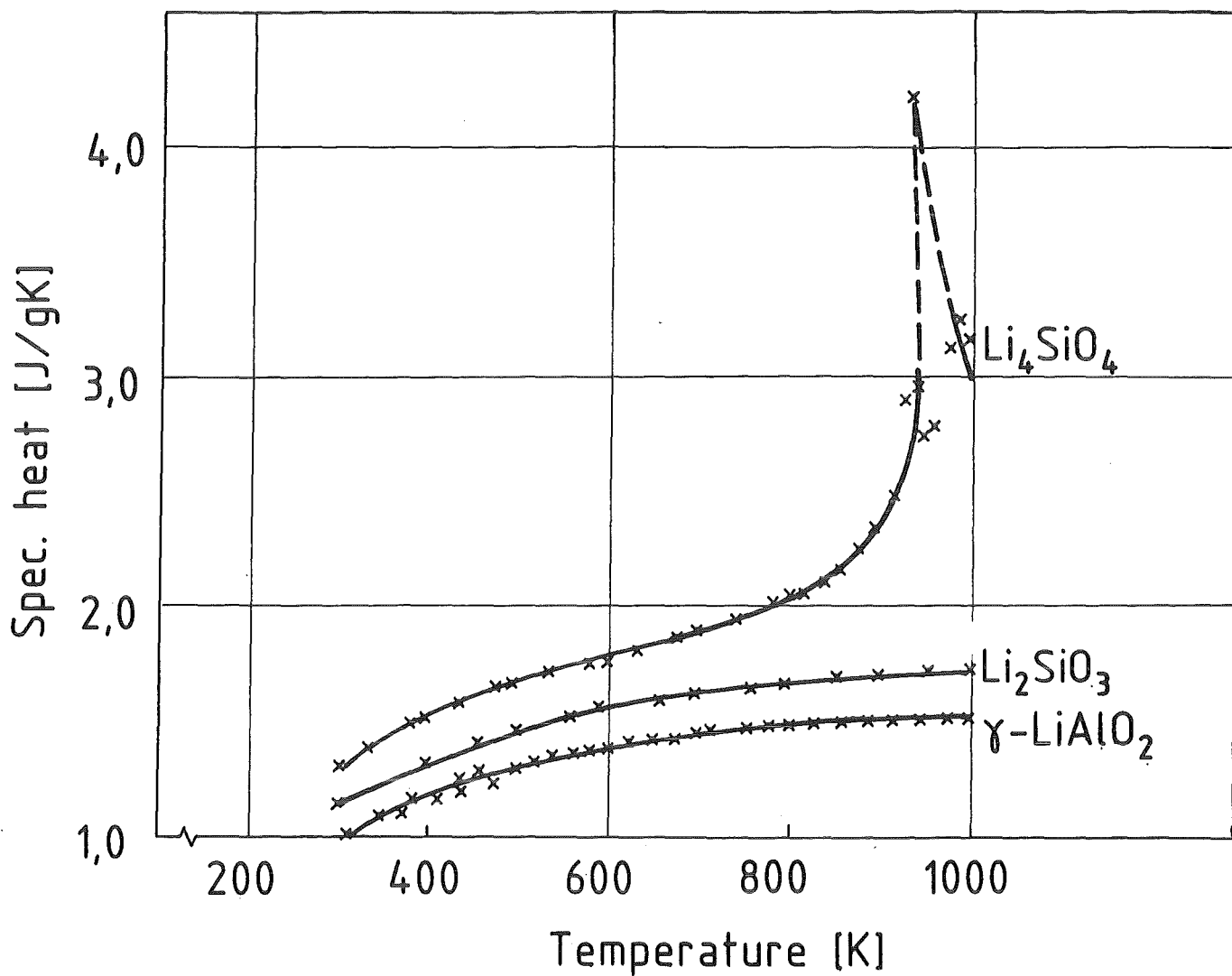
Fig. 4.2.1.4 : Specific heat of pure Li₄SiO₄ and Li₂SiO₃ as function of temperature.
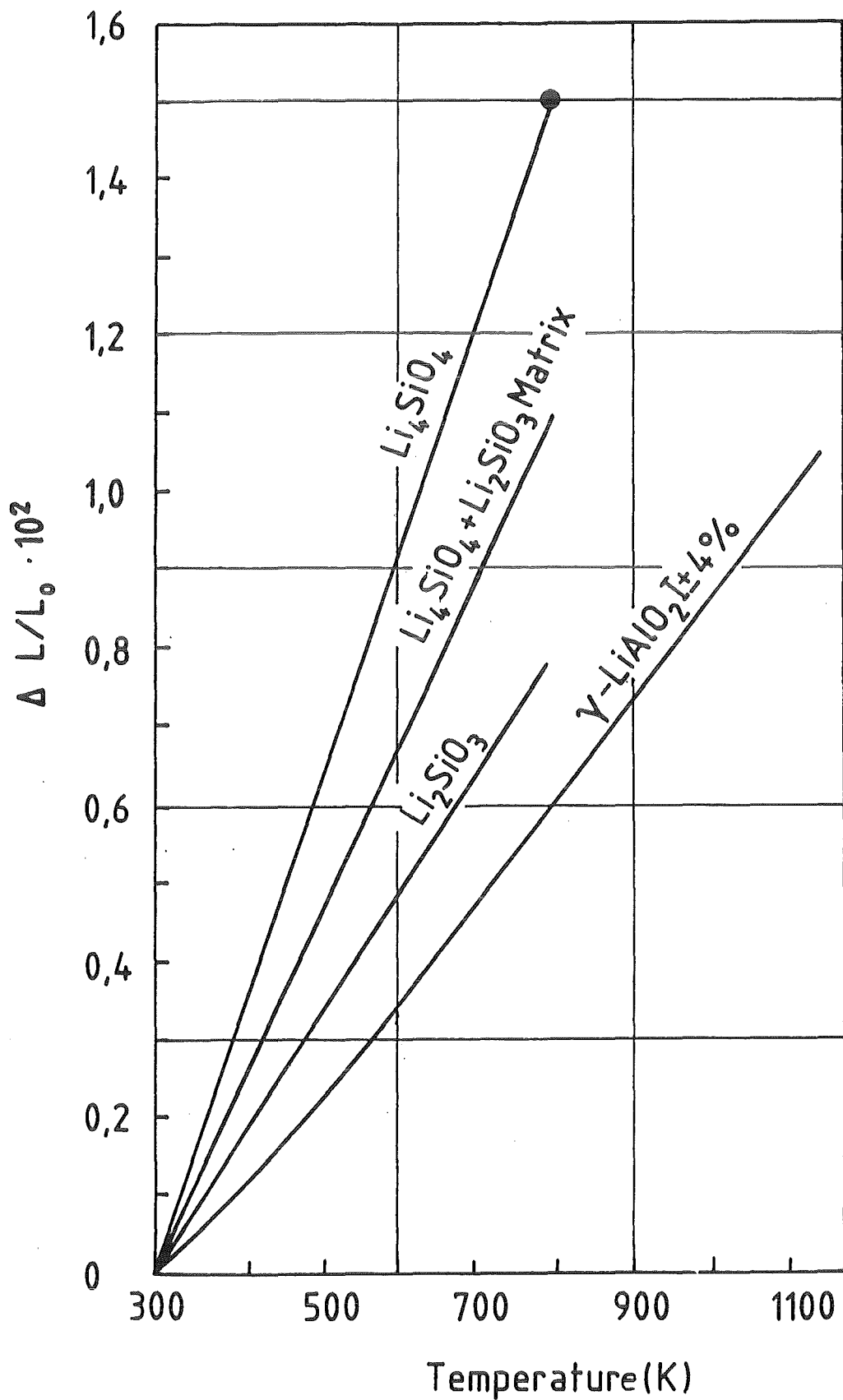
Fig. 4.2.1.5: Thermal expansion of pure Li_4SiO_4, sintered Li_4SiO_4, Li_2SiO_3 and $LiAlO_2$.
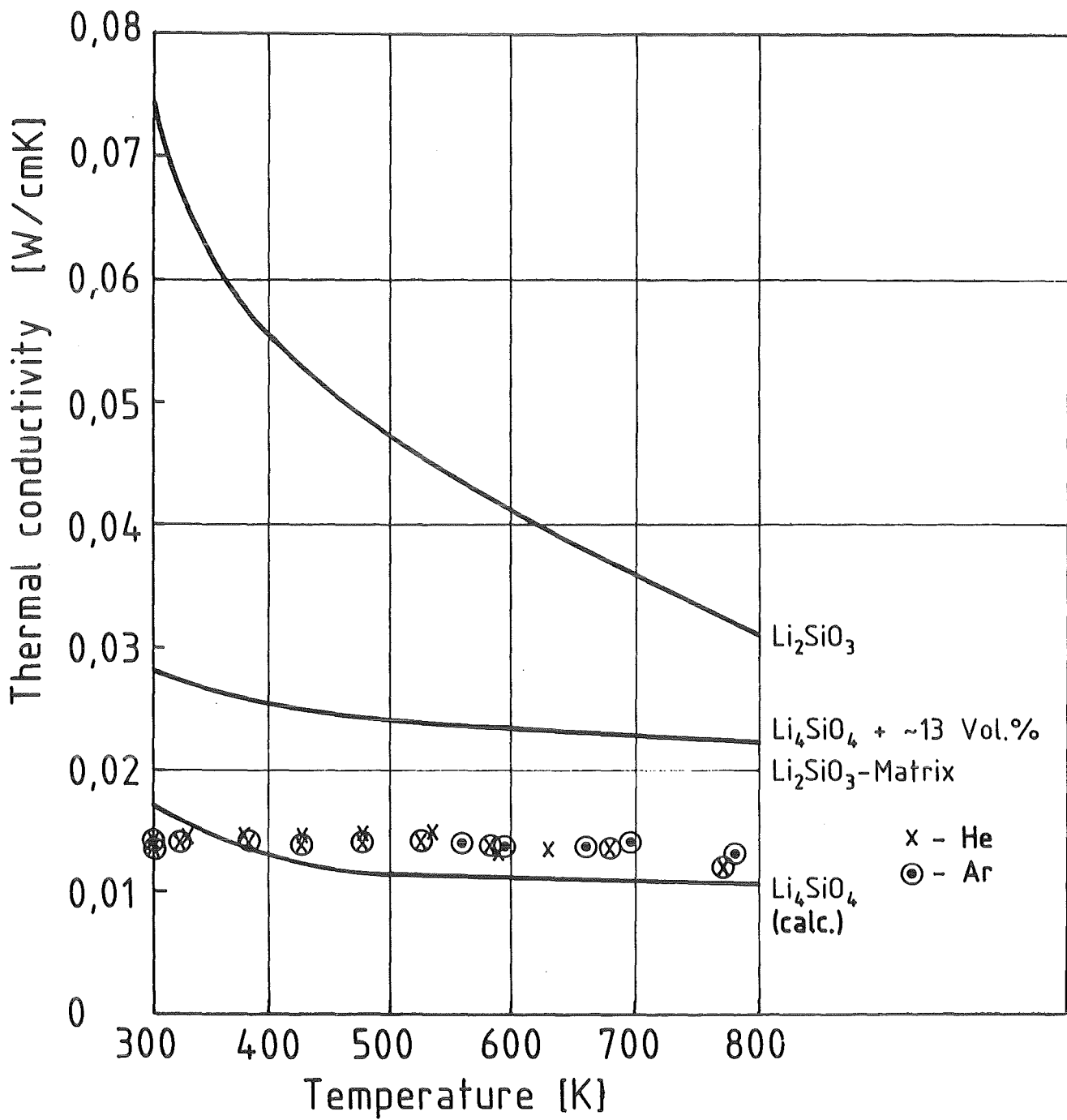
Fig. 4.2.1.6 : Thermal conductivity of Li_2SiO_3, sintered Li_4SiO_4 (+ Li_2SiO_3) and pure Li_4SiO_4.

4.2.2 Mechanical properties (W. Dienst, H. Zimmermann)

This chapter is based on data measured at KfK [1] and on ANL data published in the literature [2,3]. Porosity and grain size of the different sample charges will be given in the following presentation of the experimental results. Elastic properties, compressive strength and creep behaviour were measured on pellet samples of 4 to 10 mm diameter, and bending strength measurements were made on bars of 3 mm x 6 mm x 49 mm dimension.

Young's modulus

The propagation velocities of the longitudinal and transversal waves in ultrasonic pulses were measured in order to determine the Young's modulus. The results are given in Table 4.2.2.1, together with the Poisson number if available. The correlation recommended by KfK, also for the ITER Blanket Materials Data Base, is:

$E = 110 (1 - P)3 [1 - 2.5 \times 10\text{-}4 (T - 293)]$, P = porosity
$0.02 \leq P \leq 0.32$, T in K

The fitting curve is very similar to that of the ANL-recommendation [3]. An influence of microstructural parameters other than porosity could not be recognized. The temperature dependence was only estimated from that of other oxide ceramics and has been adopted from the ANL recommendation.

The Poisson number was found to be about 0.24.

Ultimate compressive strength (KfK)

Most of the compression tests were performed on plane parallel ground pellets. The load was applied at a rate of 30 N/s (pellets with 5 mm diameter) and 100 N/s (pellets with 10 mm diameter). The results are shown in Fig. 4.2.2.1, together with fitting curves to represent their dependence on microstructure parameters. The approach adopted to describe the dependence on porosity and grain size of the strength is expressed by the following formula

$$o = o_0 (1 - P)^b d^{-c}$$

where P = porosity, and d = mean grain size (μm). Using fitting programs the o0 values as well as the exponents were determined. The best fit for the ultimate compressive strength of Li_4SiO_4 in the investigated range of parameters was found to be

$$o_c = 975 (1 - P)^{1.5} d^{-0.44}, MPa$$

which was also recommended for the ITER Blanket Materials Data Base.

As the measured results scatter considerably within the individual fabrication batches, which is attributable to microstructural inhomogeneities, listing of all measured results has been dispensed with here. Only the upper measured values of the respective batch have been presented which are considered as typical of a high-quality material.

Strength measurements (also in bending tests) at elevated temperatures are still lacking. Preliminary tests at 700 °C showed that considerable reduction of the ultimate compressive strength of Li_4SiO_4 has to be expected at this temperature, maybe to values far below 100 MPa in general.

There is no substantial information, up to now, about irradiation-induced strength change.

Ultimate bending strength (ANL)

The above-mentioned fitting approach was also applied to the ANL results of bending tests on Li_4SiO_4 samples [3]. The ultimate bending strength data of the different batches are shown in Fig. 4.2.2.2, together with KfK (IMF) and ANL fitting curves. The KfK approach yields:

$$\sigma_b = 195\,(1 - P)^3 d^{-0.44},\ MPa$$

But a modified version of the ANL correlation was recommended for the ITER Blanket Materials Data Base:

$$\sigma_b = 275\,\exp(-4.3\,P)\,d^{-0.5}$$

$$0.02 \leq P \leq 0.32,\ 4 \leq d \leq 50\,\mu m$$

The ratio of compressive strength to ultimate bending strength in the range of porosities from 2 to 32 % lies between 5 and 10. These are values which frequently can be found also in the literature, especially in the tables prepared by fabricators of ceramics. The porosity exerts a stronger influence on the ultimate bending strength than on the ultimate compressive strength because pores obviously cause a higher increase in local stress and hence a stronger reduction in strength under tensile stress than under compression.

Creep behaviour

The KfK experiments [1] were performed as compression creep tests at constant load (10 and 40 MPa) in vacuum at temperatures between 750 and 950 °C. Depending on the creep rate, the testing periods ranged from 10 to a few 100 hours. Up to about 6 % deformation

strains, a value at which all pellets exhibited cracks, the creep rate depends on the time and on the degree of deformation, respectively, which implies that all tests took place in the primary creep range. The mean creep rates within the first 100 hours of testing (100 h value) as well as the instantaneous creep rates at 1 % deformation (1 % value) were used for interpretation, with largely varying results for the activation energy (175 and 290 kJ/mole). The estimated stress exponent was about 1, but increased to about 4 in load change experiments.

In the ANL compression creep tests [2,3] steady-state stresses were determined at constant deformation rates. A stress exponent of 4.8 resulted in the stress range of 96 to 184 MPa at 900 °C [2]. The stress exponent was found to be largely temperature-dependent and varied in the range of 1 to 8 [3].

There is a large difference in the parameter dependences of the creep rate derived at KfK [1] and ANL [3]. Therefore no general recommendation could be given for the ITER Blanket Materials Data Base. Two causes of the discrepancy are imaginable: (1) an increase in the stress exponent with the load, (2) a change in the creep mechanisms during the testing period and with increasing temperature, respectively. Whereas initially grain boundary processes might be determinant, processes taking place in the lattice might dominate at higher deformation.

Use of the creep data applicable to lower load and lower deformation seems to be more reasonable in considerations of the mechanical interaction with the metallic cladding. The 100-hour values of creep rate can be expressed with sufficient accuracy by the formula

$$\dot{\varepsilon} = 50 \, \sigma \exp(-180/RT) \exp(29P), \; 1/h$$

$[\sigma] = MPa, [T] = K, P = porosity.$

It can be assumed that for $\dot{\varepsilon} \leqq 10\text{-}6/h$ at 10 MPa compressive stress, breeding materials can be considered as virtually rigid. The corresponding temperature limits were found at about 650 °C for 90 % dense Li_4SiO_4 and between 500 and 550 °C for the 78 % dense material.

References

1. H. ZIMMERMANN
    Mechanische Eigenschaften von Lithiumsilikaten für Fusionsreaktor-Brutblankets.
    KfK 4528 (1989)

2. K. BÄR, C.Y. CHU, J.P. SINGH, K.C. GORETTA, J.L. ROUTBORT, M.C. BILLONE, R.B. POEP-PEL
    Mechanical Properties and Deformation of Polycrystalline Lithium Orthosilicate.
    Int. Symp. Fusion Nucl. Technol., Tokyo, April 10 - 15, 1988

3. M.C. BILLONE, W.T. GRAYHACK
    Summary of Mechanical Properties Data and Correlations for Li2O, Li4SiO4, LiAlO2, and Be.
    ANL/FPP/TM-218 (1988)

Table 4.2.2.1: Elastic properties of Li_4SiO_4 ANL [2], (upper section) and KfK measurements (lower section).

Porosity %	E GPa	ν
32	38.2	0.23
23	57.1	0.24
7	103.2	0.24
4	94.9	
2	82.8	
30	42	
22	38	
10	79	0.25
10	77	0.25
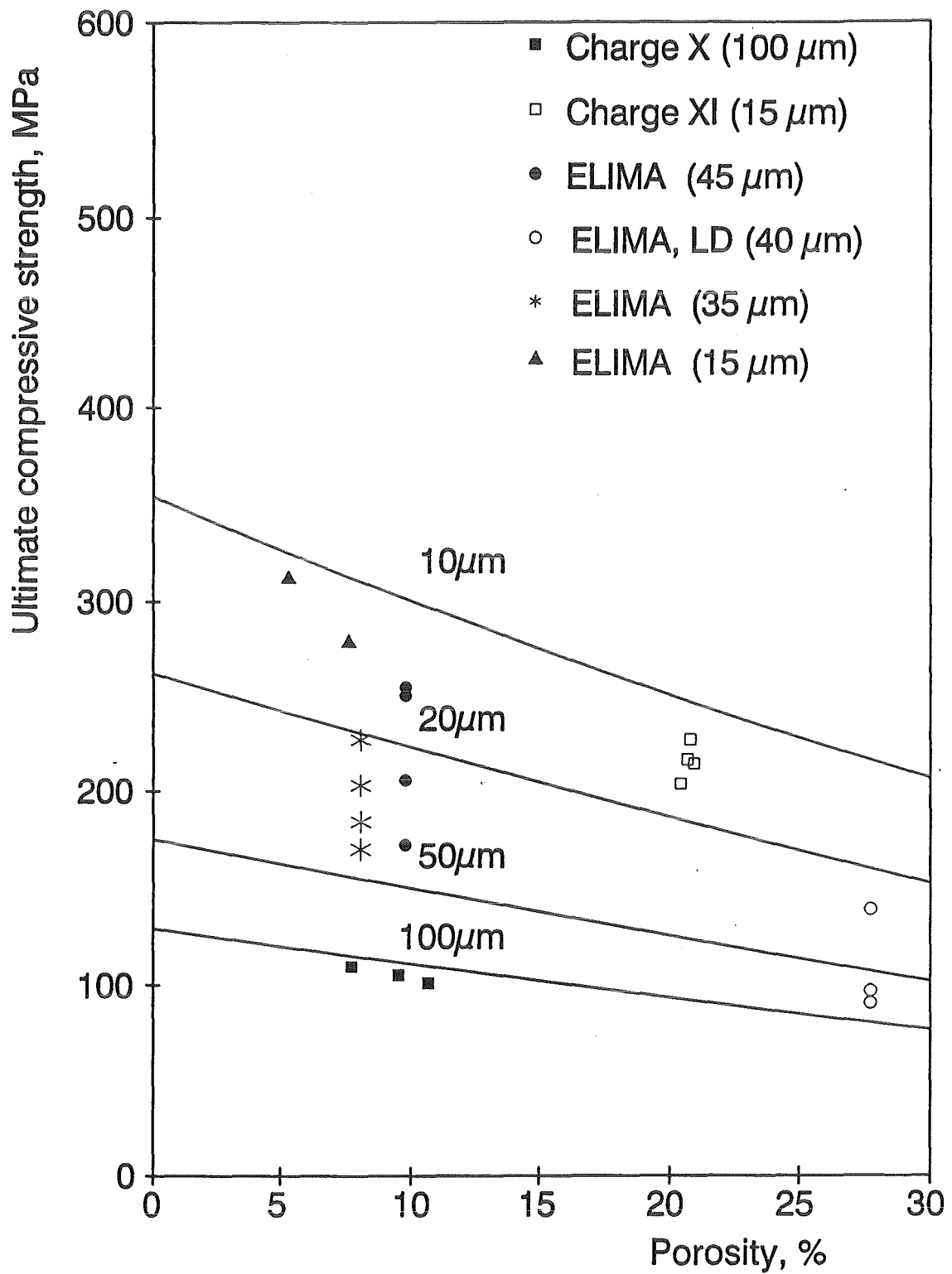
Fig. 4.2.2.1 : Ultimate compressive strength of Li_4SiO_4 with different mean grain size versus porosity.
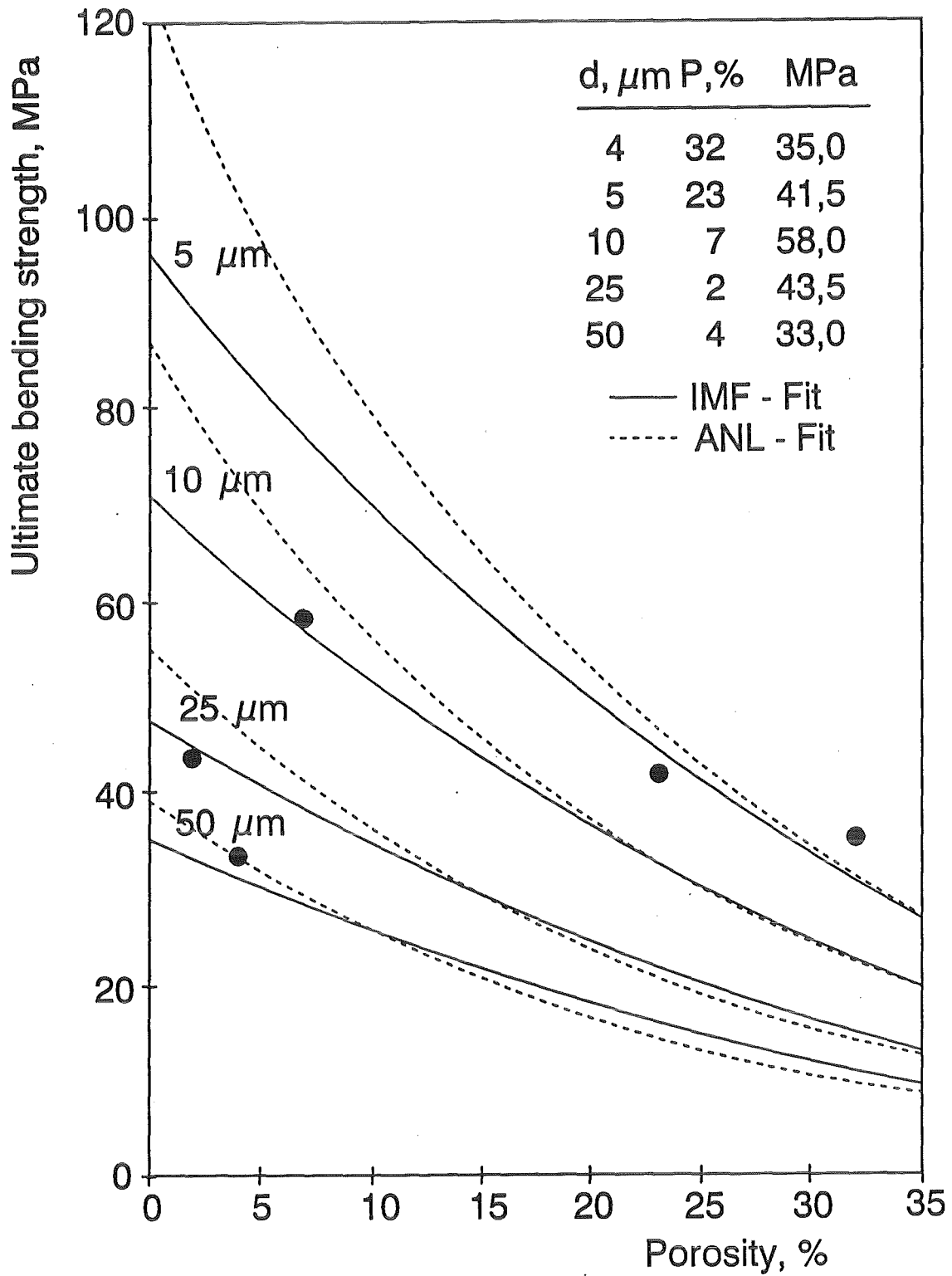
Fig. 4.2.2.2: Ultimate bending strength of Li_4SiO_4 with different mean grain size versus porosity.

4.2.3 Compatibility with structural materials (W. Dienst, P. Hofmann)

The thermodynamic stability of the oxides considered as candidate tritium breeder materials, such as Li_2O, $LiAlO_2$, Li_2SiO_3, Li_4SiO_4 and Li_2ZrO_3, determines their chemical reactivity with respect to the cladding material in the blanket. The free enthalpies of formation of theses oxides are considerably lower than the enthalpy of oxide formation of the cladding material constituents such as Cr and Fe. Therefore, a direct reaction of the pure oxide breeder materials with the cladding is thermodynamically not possible. Secondary effects should be important for the capability of the breeder materials to cause interactions, e.g., the presence of lithium hydroxide or lithium carbonate as impurities introduced during fabrication or resulting from the oxygen or moisture content (oxygen and hydrogen partial pressure) of the environmental atmosphere.

To determine the reaction behavior of the potential breeder materials and their dependence on temperature, time, and environmental conditions, compatibility experiments in closed stainless steel capsules have been performed at KfK [1,2]. To find out if the chemical interactions depend on the LiOH formation or not experiments with H_2O and NiO (oxygen source) were performed. H_2O will provide moisture and NiO will simulate an oxygen potential in the system.

The cladding materials mainly investigated were the austenitic stainless steel AISI 316 (17 % Cr, 13 % Ni, 2 % Mo) in solution-annealed condition, and the martensitic-ferritic Cr steel 1.4914 (0.2 % C, 11 % Cr, 0.5% Mo) quenched and aged for 2 h at 700 °C. Steel capsules were filled with pressed powders of Li_2O, Li_4SiO_4 and Li_2SiO_3, and small additions of H_2O or NiO, mostly 1 mol% NiO per 1 mol Li_2O. The annealing temperatures were 500, 600, 700, 800 °C in the first series [1], and 800, 900, 1000 °C in a second series [2]. The annealing periods were in the range from 25 to 500 h. At the higher annealing temperatures $\geqq$ 800 °C, two nickel-base alloys Hastelloy X and Inconel 625 were included in the experiment.

Reaction rates are determined by measuring the depth of visible penetration of the reaction into the capsule wall and/or the thickness of reaction product layers between breeder and capsule material. The extent of reaction caused by Li_4SiO_4 and Li_2SiO_3 was much smaller than that of Li_2O. Because the formation of oxide scale and internal penetration could be described by a parabolic function $x^2 = k \cdot t$ (x = reaction layer thickness, t = reaction time, k = the rate constant), k can be plotted versus $1/T$. The extent of cladding attack caused by the various breeder materials is represented in Fig. 4.2.3.1.

The extent of cladding attack caused by the NiO impurity addition was generally comparable to that caused by the H_2O addition, even in the presence of Li_2O. Accordingly, the formation of LiOH does not appear to play the decisive role, but the presence of reactive oxygen introduced by H_2O or NiO seems to be the controlling factor. With respect to the aggressive behavior of the various breeding materials the tendency to form LiOH is not re-

sponsible for the differences, but rather the thermodynamic stability of each oxide with re-spect to the formation of lithium chromate by reaction with the cladding material.

Cladding attack on the martensitic-ferritic Cr-steel 1.4914 containing only about 11 % Cr was in most cases not much stronger than the attack on the austenitic Cr-Ni steel AISI 316 containing about 17 % Cr. It seems that during the formation of an oxide layer with poor protective properties, fast Cr transport along the grain boundaries of the initially finely grained 1.4914 martensitic structure is comparably effective in delaying the cladding attack as the higher Cr content in the more coarsely grained austenitic steel. However, this effect is offset by the coarser microstructure of 1.4914 found at temperatures > 700 °C and for long annealing times. But even after 500 h at 800 °C Li_4SiO_4 and Li_2SiO_3 did not produce more cladding attack on 1.4914 than on type 316 stainless steel.

It appears that the depths of cladding attack due to Li_4SiO_4 and Li_2SiO_3 (with NiO added in each case) are closer to each other at very high temperatures than had been expected on the basis of results obtained earlier below 800 °C [1]. This is partly due to an exclusive NiO attack, especially if Li_2SiO_3 is involved. But in any case it gave reason for considering Li_4SiO_4 to be so harmless that its application in operation above 800 °C must not be excluded. In particular Li_4SiO_4 does not exhibit an increased cladding attack at very high temperatures as Li_2O (in good agreement with results from ref. [3]).

All the results obtained for AISI 316, Hastelloy X and Inconel 625 are presented in Fig. 4.2.3.1 in the scatter bands above 800 °C; some minor overlapping occurs between Li_4SiO_4 and Li_2SiO_3. This allows the conclusion that from a technical point of view there is no major difference in the compatibility behavior of AISI 316 and the Ni-base alloys.

All the compatibility tests with uncontrolled impurities and, on the other hand, with con-trolled additions of LiOH or NiO to the breeder materials gave the impression that 1 mol% per mol of Li_2O content is a conservative choice to cover the relevant influence of oxygen releasing impurities. Accordingly the following correlation for the cladding penetration depth with Li_4SiO_4 is estimated from Fig. 4.2.3.1:

$$x^2 = 1 \times 10^5 \, \mu m^2/h \cdot \exp(-100 \, kJ \cdot mol^{-1}/RT) \cdot t$$

Of course, these results are not relevant to the conditions in a blanket gas purging system, where the oxidation potential will be governed by a low partial pressure of water vapour, which is mainly due to the required release of $(H,T)_2O$ from the oxide breeder materials. Therefore a new test series has been started with Li_4SiO_4, Li_2SiO_3 and Li_2O/AISI 316 reaction couples in flowing argon with constant H_2O partial pressures of 10 and 100 Pa. The anneal-

ing temperatures were 600, 700, 800 and 900 °C for annealing periods in the range of 24 to 1000 h.

The results obtained up to now appear suprising, because the reaction rates were much higher than in the preceding capsule tests with lithium silicates, but even lower with Li_2O (Fig. 4.2.3.2) except at 900 °C. The experiment and the evaluation work has not yet finished, and therefore the temperature dependence has still to be analyzed. Preliminarily, the following correlation for the reaction zone growth (x = zone thickness) can be given for Li_4SiO_4 at 10 Pa H_2O as a first approximation, which is still adjusted to the above-mentioned temperature dependence of the capsule test results:

$$x^2 = 4 \times 10^5 \, \mu m^2/h \cdot exp \, (- \, 100 \, kJ \, mol^{-1}/RT) \cdot t$$

The increase of x^2 with the H_2O partial pressure was moderate, in the range of 2 to 4 x at 100 Pa. It will be tried to proceed to still lower H_2O partial pressure, down to about 1 Pa.

These recent results show that Li_4SiO_4 could be the most aggressive oxide breeder material under operation atmosphere conditions. The reaction rate given by the above formula comes up to the scattering band for Li_2O in Fig. 4.2.3.1, which means that the cladding attack could become critical above about 800 °C. The enhanced cladding attack with Li_4SiO_4 at slower oxygen supply, compared to the capsule tests, could be due to a change from sequent cladding oxidation and Li_2O transfer to a simultaneous reaction. The latter maybe promotes the formation of multinary, particularly multiphase reaction products with increased oxygen permeability. On the other hand, the reaction with pure Li_2O breeder material always seems to form a lithium chromate and/or ferrate layer, which is even less permeable at slower oxygen supply.

References

1. P. HOFMANN, W. DIENST
    Chemical compatibility between lithium-based oxide ceramics and stainless steel.
    J. Nucl. Mater. 141-143 (1986) 289-293

2. P. HOFMANN, W. DIENST
    Compatibility studies of metallic materials with lithium-based oxides.
    J. Nucl. Mater. 155-157 (1988) 485-490

3.   L. YANG, R. MEDICO, W. BAUGH, K. SCHULTZ
      Irradiation study of lihtium compound samples for tritium breeding application.
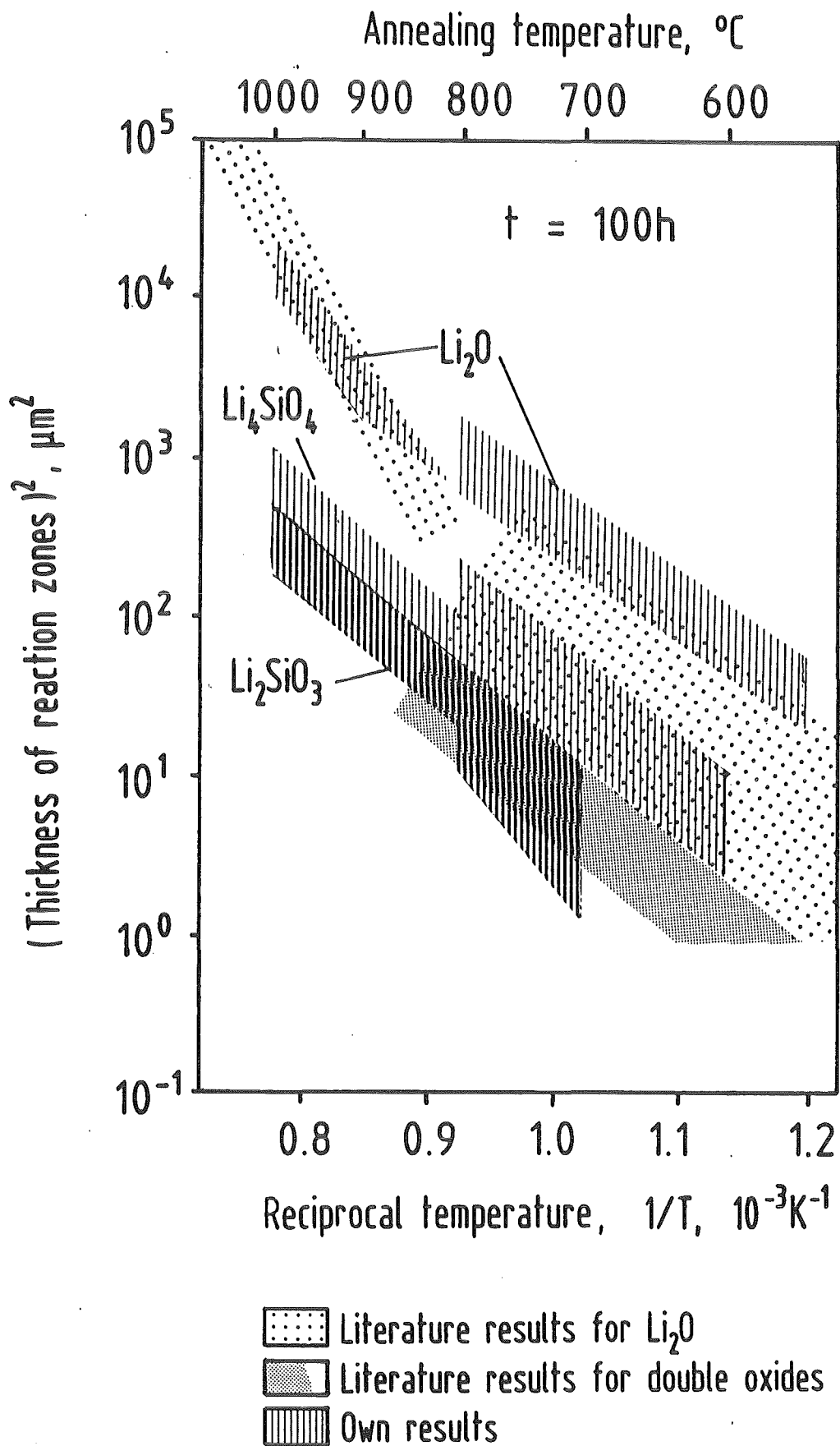   J. Nucl. Mater. 103-104 (1981) 585-589. ,

Fig. 4.2.3.1 : Chemical reaction of Li-based oxide compounds with AISI 316, Hastelloy X and Inconel 625, normalized to a reaction time of 100 h.
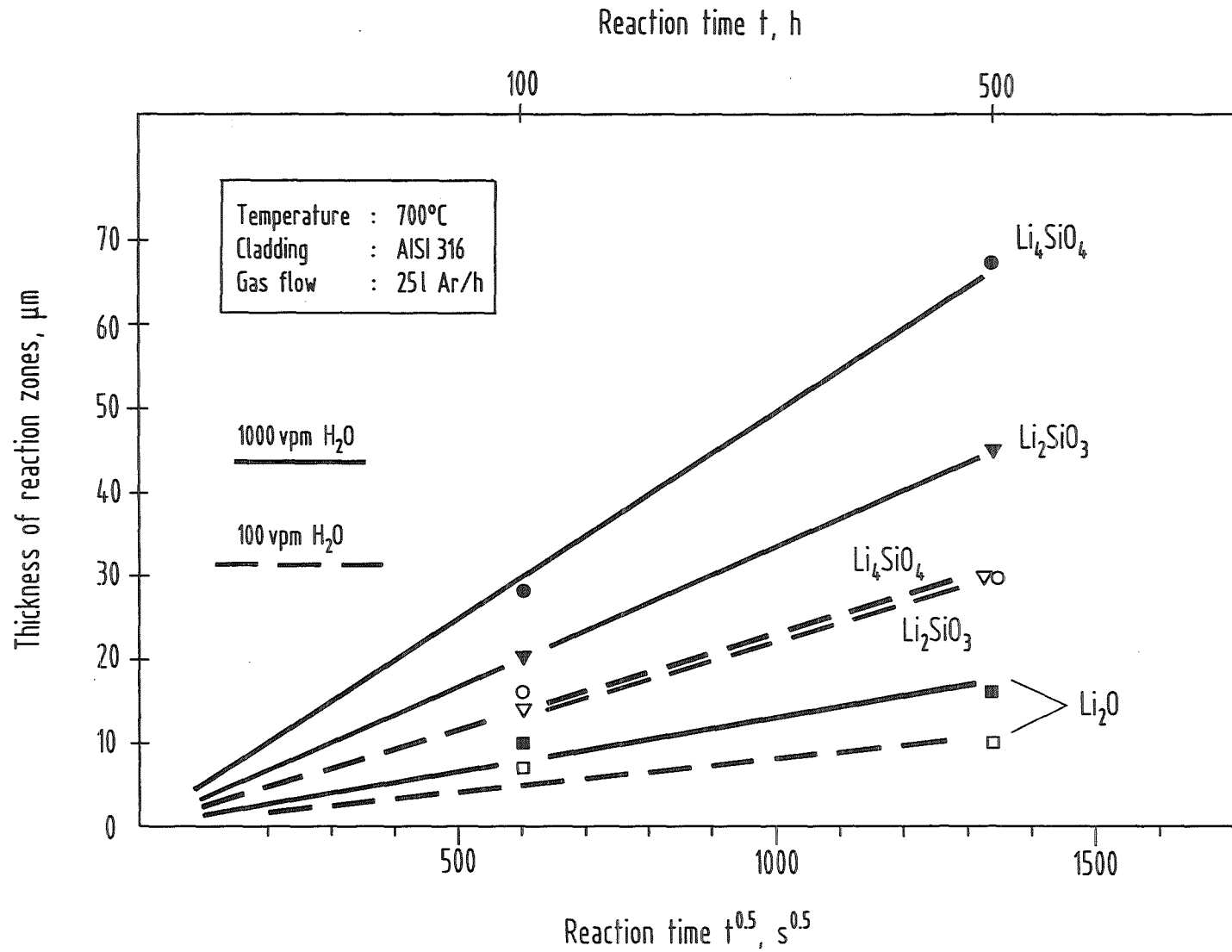
Fig. 4.2.3.2 : Chemical reaction of Li-based oxide compounds with stainless steel AISI 316 in dependence on the H_2O partial pressure.

4.2.4. Thermal stability of and solubility of tritium in lithium orthosilicate (R.D. Penzhorn)

Lithium ceramic breeding materials for fusion reactors exhibit different thermochemical properties which need to be determined and evaluated for the design of a blanket.

4.2.4.1. Equilibrium evaporation of lithium silicates

Detailed knowledge of the thermochemistry of candidate tritium breeder ceramics is important because it provides information on the oxygen activity of the lithium compounds, which controls the T_2O/T_2 ratio of tritium released from a breeding ceramic, and on the rate of vaporization, which determines the maximum temperature of operation of a blanket.

Lithium silicates, compared with other lithium breeders of similar lithium density, show a fairly high thermal stability. Of these, Li_4SiO_4 is particularly interesting because of its high lithium density and the rapid diffusion of tritium in this compound. Thermochemical properties of the silicates were investigated by mass spectrometric analysis of Knudsen effusates; partial pressures were obtained by analysis of the vapor effusing from platinum Knudsen cells. The measured ion intensities, I_i, were converted to partial pressures p_i of species i using the equation

$$p_i = K (I_i, T/\sigma_i, \gamma_i, \chi_i),$$

where K is a calibration constant of the instrument, σ_i is the ionization cross section of atom or molecule i, γ_i is the electron multiplier gain and χ_i is the atom fraction of the measured isotope.

The mass spectrometrically determined vapor pressures of Li and O_2 over Li_2SiO_3 and Li_4SiO_4 below and above the melting points of the meta and orthosilicates (1474 and 1528 K respectively) are shown over a wide range of temperatures in Fig. 4.2.4.1. It is seen that the vapor pressures of Li and O_2 over both silicates are the predominant species. The other species comprised gaseous lithium oxides LiO, Li_2O, and Li_3O and Li_2SiO_3 over liquid Li_2SiO_3 and LiO, Li_2O, and Li_3O over solid and/or liquid Li_4SiO_4.

Equilibrium constants, K_{eq}, obtained from partial pressures were used to calculate reaction enthalpies employing known Gibbs free energy functions. The thermal decomposition processes derived from the data of solid and liquid Li_2SiO_3 and of solid and liquid Li_4SiO_4 are summarized in Table 4.2.4.1 together with the corresponding standard reaction enthalpies.

Using the partial pressures of oxygen measured over solid Li_2SiO_3 and solid Li_4SiO_4 the T_2O/T_2 ratio attained under equilibrium conditions was estimated. For the calculations the equilibrium
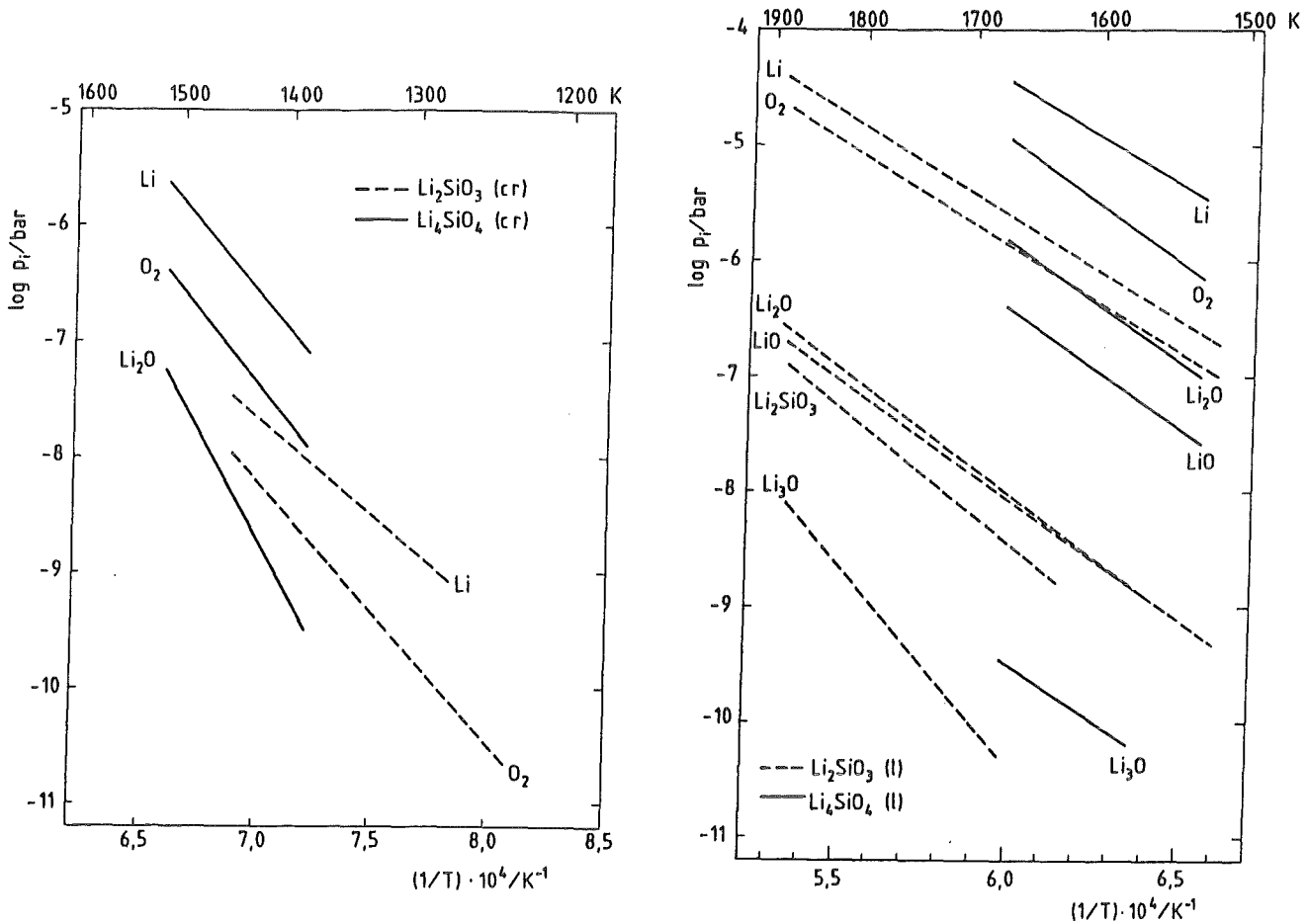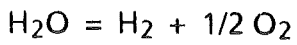
$$H_2O = H_2 + 1/2\,O_2 \qquad\qquad (1)$$

Fig.4.2.4.1. Partial pressures of atoms and molecules over solid and liquid Li_2SiO_3 and Li_4SiO_4

was used instead of the corresponding reaction with tritium, because the isotope effect is small compared to the uncertainty of the estimate. The temperature dependence for the H_2O/H_2 ratio is given by

$$\log p_{H2O}/p_{H2} = A/T + B,$$

the coefficients A and B having values of 1588 and 0.979 for Li_2SiO_3 and 623 and 2.05 for Li_4SiO_4 respectively. A simple calculation shows that at the temperatures expected to be attained in an actual blanket tritium will mainly exist as T_2O if quasi-equilibrium conditions prevail.

4.2.4.2. Free evaporation of lithium orthosilicate

The maximum sublimation rates of vapor species emitted from lithium orthosilicate in a blanket at elevated temperatures can be obtained from Knudsen effusion equilibrium data [1-3]. This rate will only be attained if the number of collisions between the gas particles and the surface of the lithium ceramics is sufficient for establishing an equilibrium. The minimum sublimation rates, on the other hand, are given by the Langmuir free evaporation. Since neither one is expected to be reached in an actual blanket and only Knudsen effusion equilibrium data have been reported in the literature a free evaporation study (collision-free condition) of lithium orthosilicate was carried out [4].

Table 4.2.4.1. Standard reaction enthalpies for various equilibria obtained from partial pressure measurements with Li_2SiO_3 and Li_4SiO_4.

Reaction	$\Delta H^o_{298,r}$ * [kJ/mol]
solid Li_2SiO_3	
$Li_2SiO_3(cr) = 2Li(g) + 1/2O_2(cr) + SiO_2(cr)$	1008.0 ± 4.1
$Li_2SiO_3(cr) = Li_2O(g) + SiO_2(cr)$	540.4
$Li_2O(g) = 2Li(g) + 1/2O_2(g)$	453.0
liquid Li_2SiO_3	
$Li_2SiO_3(l) = 2Li(g) + 1/2O_2(g) + [SiO_2]^{**}$	984.6 ± 5.5
$Li_2SiO_3(l) = Li_2O(g) + [SiO_2]$	531.6 ± 4.8
$Li_2O(g) = 2Li(g) + 1/2O_2(g)$	421.1 ± 1.5
$LiO(g) = Li(g) + 1/2O_2(g)$	66.9 ± 3.6
solid Li_4SiO_4	
$Li_4SiO_4(cr) = 2Li(g) + 1/2O_2(g) + Li_2SiO_3(cr)$	960.70 ± 2.38
$Li_4SiO_4(cr) = Li_2O(g) + Li_2SiO_3(cr)$	520.43 ± 2.69
$Li_2O(g) = 2Li(g) + 1/2O_2(g)$	440.23 ± 1.44
$Li_2O(g) = LiO(g) + Li(g)$	360.61 ± 0.84
liquid Li_4SiO_4	
$Li_4SiO_4(l) = 2Li(g) + 1/2O_2(g) + Li_2SiO_3(l)$	946.34 ± 0.73
$Li_4SiO_4(l) = Li_2O(g) + Li_2SiO_3(l)$	510.87 ± 2.51
$Li_2O(g) = 2Li(g) + 1/2O_2(g)$	435.38 ± 2.15
$Li_2O(g) = LiO(g) + Li(g)$	361.91 ± 0.74

* The erros given are standard deviations
** $[SiO_2]$ = unknown state of SiO_2 in the molten Li_2SiO_3 (l).

For the free evaporation experiments a polycrystalline, flat and circular surface of a solidified melt of lithium orthosilicate, which simulates the pebbles manufactured by solidification of liquid droplets, was used as a source. Neutral particles emitted from the source were analyzed mass spectrometrically.

A comparison between data averaged over several Langmuir evaporation runs and Knudsen effusion results is shown in Fig. 4.2.4.2.
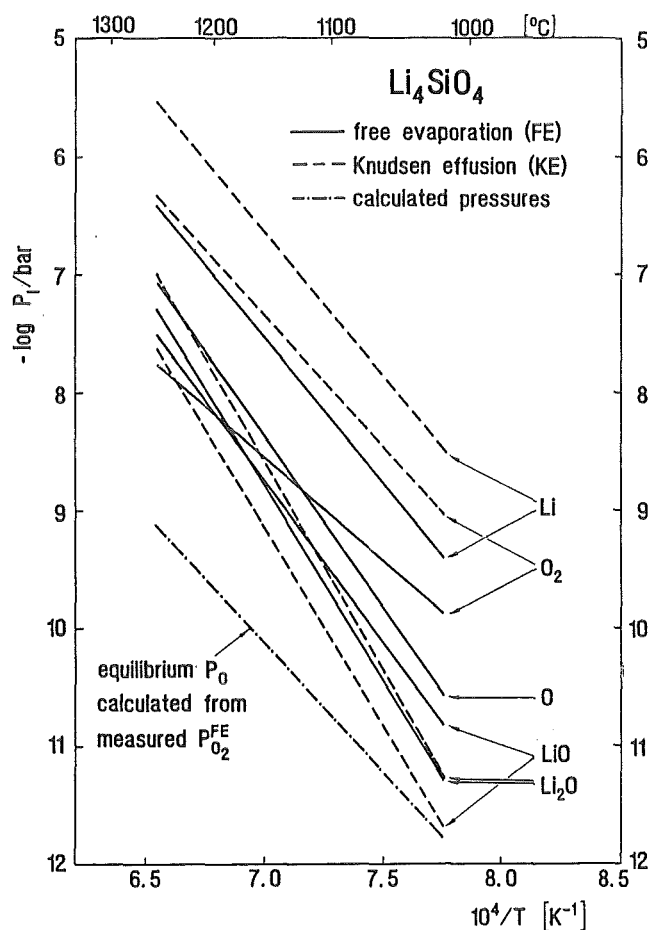
Fig. 4.2.4.2.
Results of free
evaporation and
Knudsen effusion
runs

The results show that

- the lithium pressures in free evaporation are almost an order of magnitude lower than the equilibrium lithium pressures

- the pressures of atomic oxygen in free evaporation are much higher than those calculated from the O_2 pressures measured in free evaporation experiments

- the O_2 pressures measured in free evaporation are considerably lower than those required from oxygen mass balance.

From the data in Fig. 4.2.4.2. the equilibrium constants K_1 and K_2 for the Langmuir evaporation and and the Knudsen effusion for the reactions

$$Li_4SiO_4 \text{ (cr)} = 2 \, Li \text{ (g)} + O \text{ (g)} + Li_2SiO_3 \text{ (cr)} \qquad (2)$$

$$Li_2O \text{ (g)} = LiO \text{ (g)} + Li \text{ (g)} \qquad (3)$$

were evaluated and free energy changes ΔG° were calculated using the expression

$$\Delta G^\circ = - RT \ln K$$

Since the relative differences in ΔG° between Knudsen effusion and free evaporation data were found to be of only a few percent, it is concluded that Li, O, LiO, and Li_2O equilibrate at the surface prior to desorption. In contrast to this, the O_2 molecules in free evaporation are not in equilibriuum with atomic oxygen. In reaction (2) the low evaporation of Li is balanced by a high pressure of atomic oxygen. Similarly, in reaction (3) LiO and Li_2O adjust, by equilibration, to the lower lithium pressure as compared to that obtained by Knudsen effusion. Extrapolation of the O pressures observed in free evaporation to the range of operating temperatures of a reactor blanket yields oxygen activities comparable to those calculated from Knudsen effusion results. Therefore, an increased reactivity of oxygen with metal surfaces in the blanket is not anticipated in this temperature range.

For a freely evaporating gas species i the pressure obtained from free evaporation (FE) studies are related to those from Knudsen effusion (KE) measurements by the evaporation coefficient α_i according to

$$\alpha_i = p_i^{FE}/p_i^{KE}$$

For lithium the evaporation coefficient was found to be 0.13 and 0.12 at 1528 and 1289 K, respectively (the accuracy of the data do not allow to deduce a temperature dependence). From this result and the assumption that free evaporation predominates in a reactor blanket it was concluded that the temperature at which the total lithium pressure exceeds 10^{-2} Pa is higher than 1120 °C, the value obtained from Knudsen effusion studies [2].

4.2.4.3. Solubility of hydrogen in lithium silicates

The tritium inventory of the blanket is determined to a large extent by the adsorption on and absorption in lithium ceramics of tritium water and by the solubility of tritium gas in the material.

The solubility of hydrogen in lithium silicates was measured employing a volumetric and a tracer technique [5]. Lithium silicate pellets were pretreated by repeated loading/deloading cycles at elevated temperatures until the concentration of residual impurities observed in the released hydrogen was negligible. In an actual run, pellets were equili-

brated with hydrogen at constant temperatures between 450 and 550 °C and pressures between 470 and 550 mbar over a period of about a week. The solubility of hydrogen was then obtained from the isothermal gas release over an analogous period of time. The tracer experiments were carried out with tritiated hydrogen. The solubility was estimated from the tritium content in the solid as determined by liquid scintillation counting. For lithium metasilicate the solubility was found to increase from 2×10^{-5} to 4×10^{-5} $mol_H/mol_{Li2SiO3}$ at 450 and 550 °C, respectively. The solubility of hydrogen in lithium orthosilicate at 550 °C was found to increase from 1×10^{-5} up to 12×10^{-5} $mol_H/mol_{Li4SiO4}$ when the hydrogen pressure was increased from 550 to 1000 mbar [6].

References

1. R.-D.PENZHORN, H.R.IHLE, P.SCHUSTER, K.ZMBOV, The Evaporation Process of Solid Lithium Metasilicate, J. Nucl. Materials **155-157**, 471 (1989).

2. H.R.IHLE, R.-D.PENZHORN, P.SCHUSTER, The Thermochemistry of Lithium Silicates in View of their Use as Breeder Materials, Fusion Eng. Design, **8**, 393 (1989).

3. R.-D.PENZHORN, H.R.IHLE, P.SCHUSTER, H.WEDEMEYER, Thermochemical Comparison of Lithium Orthosilicate Pebbles Manufactured by Two Different Procedures, Fusion Eng. and Design, **12**, 493 (1990).

4. R.-D.PENZHORN, H.R.IHLE, S.HUBER, P.SCHUSTER, Free Evaporation from Lithium Orthosilicate Surfaces, 16th SOFT, London (1990).

5. M.GLUGLA, K.H.SIMON, R.-D.PENZHORN The Solubility of Hydrogen in Lithium Metasilicate, J.Nucl.Materials **155-157**, 513 (1988).

6. M.GLUGLA, R.-D.PENZHORN unpublished results.

4.3 Li₄SiO₄ Pebble Development

4.3.1 Pebbles fabricated by melting (G.Schumacher)

4.3.1.1 Introduction

The Karlsruhe helium cooled ceramic breeder design is based on self supporting canisters containing lithium orthosilicate pebbles of 0.35-0.6 mm diameter in the gap between the cooled beryllium plates that serve as a neutron multiplier[1]. Helium sweep gas flows through the gap and carries away the released tritium.

Ceramic breeding material was chosen because of its good compatibility with other materials at operating temperatures in the reactor blanket[2]. Among the lithium ceramics the orthosilicate has excellent tritium release behaviour. Small pebbles are favoured against pellets because small pebbles have a better thermal stress resistance.

So far, production by spraying liquid material has been proven a suitable way to fabricate pebbles. This method is employed by Schott Glaswerke, Mainz, Germany, a company able to produce large pebble quantities. All pebbles examined during this work are made by Schott. As compared to pebbles prepared by granulation and sintering, pebbles produced from the melt are closer to the spherical shape, have a smoother surface and a higher density. The only drawback of the production method is that it requires quenching from melting temperature. Therefore, some of the pebbles may contain cracks and stresses that lower their mechanical stability. An important task of this work is is therefore to optimize the structure in a way that improves the mechanical properties of the pebbles produced from the melt. Two types of tests are carried out to examine the mechanical properties, one determines the compressive force a single pebble can sustain before it breaks, the other is a thermal cycling test that simulates the influence of mechanical and thermal stresses that are imposed on the pebble bed in the canister of a fusion reactor blanket.These tests are described in section 4.3.4.

Improvement of mechanical properties requires to examine the microstructure and chemical composition of the material and to look for relations between structure and mechanical stability. It was mentioned earlier that annealing and recrystallization of the pebbles above a temperature of 1024°C could lead to healing of microcracks if the orthosilicate contains at least a slight surplus of silicon to

the stoichiometric composition [3]. More detailed work has been done since then and and is reported here.

4.3.1.2 Density

Measurement of density by pycnometry yielded a value of 98% of the theoretical density for the pebbles. The pebble bed density was measured employing a cylindrical container of 16 mm inner diameter and a volume of 5.7 cm³. This container was also used to conduct the manual thermocycling tests [3]. The container looks like a bottle with a neck of 4 mm inner diameter. This allows an exact definition of the volume. After filling the container gets vibrated to ensure the maximal bed density is attained. Depending on the batch, bed densities between 1.41 and 1.49 g/cm³ are measured.

4.3.1.3 Microstructure

The structure of the lithium orthosilicate pebbles depends on the chemical composition. The section of the Li-Si-O phase diagram in the neigbourhood of the stoichiometric orthosilicate [4,5] is shown in Fig.4.3.1.1. It reveals that the stoichiometric composition solidifies as a single phase, whilst a composition with a slight surplus of silica solidifies with two phases. One phase is orthosilicate, the other corresponds to the solid line that leeds down to the eutectic composition on the silica rich side. Rapid cooling, for instance, of a composition indicated by the dashed line would produce a structure characterized by orthosilicate crystals growing in a silica rich glassy phase. This behaviour can be used to influence the structure of the material.

Pebbles produced by spraying liquid material of different compositions exhibit microstructures as they are expected fom the above discussion of the phase diagram. Pebbles with a composition close to the stoichiometric composition of orthosilicate show large areas with different structures after quenching from the melt during production. Part of the structure looks monophasic and almost completely crystallised, part has a dentritic structure as illustrated by scanning electron microscopy (SEM) in Fig.4.3.1.2. Grains of about 10 µm diameter and up to 50 µm length are visible. The grains tend to grow into the same direction within the large areas.
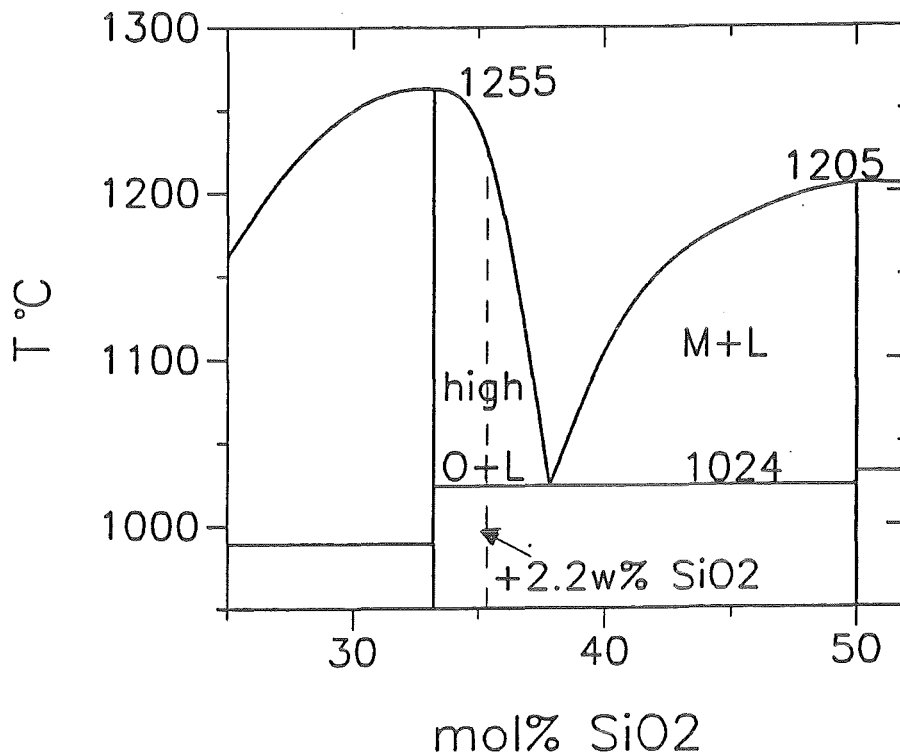
Fig.4.3.1.1: Part of the Li₂O/SiO₂-phase diagram [4,5]

Pebbles with a surplus of 2.2 w% silica to the stoichiometric composition have a dentritic structure with grains of up to 5 μm diameter and 15 μm length. The dentritic structure spreads out over the whole cross section of the pebble as shown on the right of Fig.4.3.1.2. This structure is an indication of a subcooled liquid. It reveals from the silicon rich part of the phase diagram in Fig.4.3.1.1 that some condition belonging to a temperature above 1024°C was frozen, in which both, orthosilicate crystals and a silicon rich liquid, existed together. Therefore, the pebbles with a surplus of 2.2 w% silica have a glass cemented grain structure. This is well illustrated in the lower right part of Fig.4.3.1.2.

4.3.1.4 Thermal treatment

As fabricated pebbles have internal stresses because of the rapid quenching from melting temperature during the production process. The pebbles may also contain cracks because of this process. Most of the cracks observed with ceramographic analysis are microcracks that develop along grain boundaries during quench-

ing. Microcracks could be healed when pebbles with 2.2 % surplus of silica are heated above 1024°C, the eutectic melting point of the glassy phase that remained because of the fast cooling of the molten droplets.

It was found in a series of annealing experiments that heating the pebbles at 1030°C for 5 min gives the best results. The SEM of the microstructure in Fig.4.3.1.3 shows grain growth in stoichiometric and silicon rich orthosilicate pebbles. Grains in stoichiometric material are very large and microcracks are still visible along the grain boundaries at high magnification, Fig.4.3.1.3, left. Grains in the hyperstoichiometric material are 20-40 μm big, Fig.4.3.1.3, right. The second phase which precipitated in the grain boundaries heals microcracks and prevents the scatter of mechanical properties. This benificial behaviour could not be observed when alumina was added as a further component besides silica. Addition of tellurium, however, did not hinder the healing of microcracks but furthermore supported uniform crystalization and improved the mechanical stability (see section 4.3.4.2).

As expected, pebbles with a surplus of silicon started to stick together at 1030°C after already 1 min because of liquification of the second phase, while pebbles from stoichiometric orthosilicate showed no interaction. From looking at the surface after heat treatment it is obvious that some molten material appeared at the surface of the silicon rich pebbles during heating, Fig.4.3.1.4. A special furnace build by HITEC-Materials, Karlsruhe was employed to prevent pebbles from sticking together during thermal treatment. It is a tube furnace with rotating tube and rocking tube axis. An alumina crucible that is placed in the centre of the furnace tube contains the pebbles together with zirconia spheres of 2mm and alumina spheres of 4mm size that force the pebbles to move when the crucible rotates and rocks. A thermocouple inside the crucible allows exact temperature control.

Internal stress in the pebbles can be released already by annealing above 700°C and subsequent cooling to room temperature with 100°C/h.

It is known that lithium orthosilicate easily takes up moisture fom air [3]. The weight of pebbles produced from the melt increases by 0.1 % after 2 days of exposure already. Saturation is reached after 40 days at about 0.5 wt%. Therefore, if pebbles were exposed to moisture air before, the heating rate during annealing has to be kept below 50°C/h to prevent build up of high water vapour pressure inside the pebbles until a temperature of 300°C is reached. Otherwise microcracks could develop and cause scatter in mechanical stability.
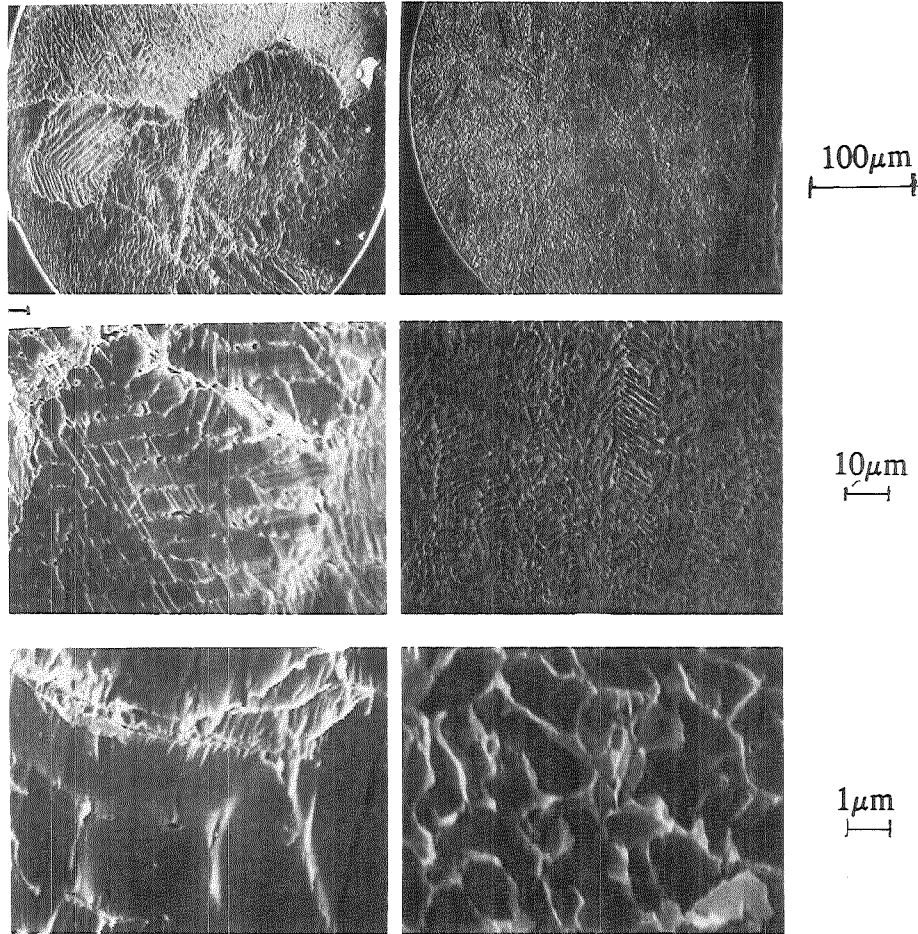
Fig. 4.3.1.2   SEM of a polished and etched cross section of lithium orthosilicate pebbles as produced by Glaswerke Schott, Mainz. Left: Li$_4$SiO$_4$, right: Li$_4$SiO$_4$ + 2.2 w% SiO$_2$
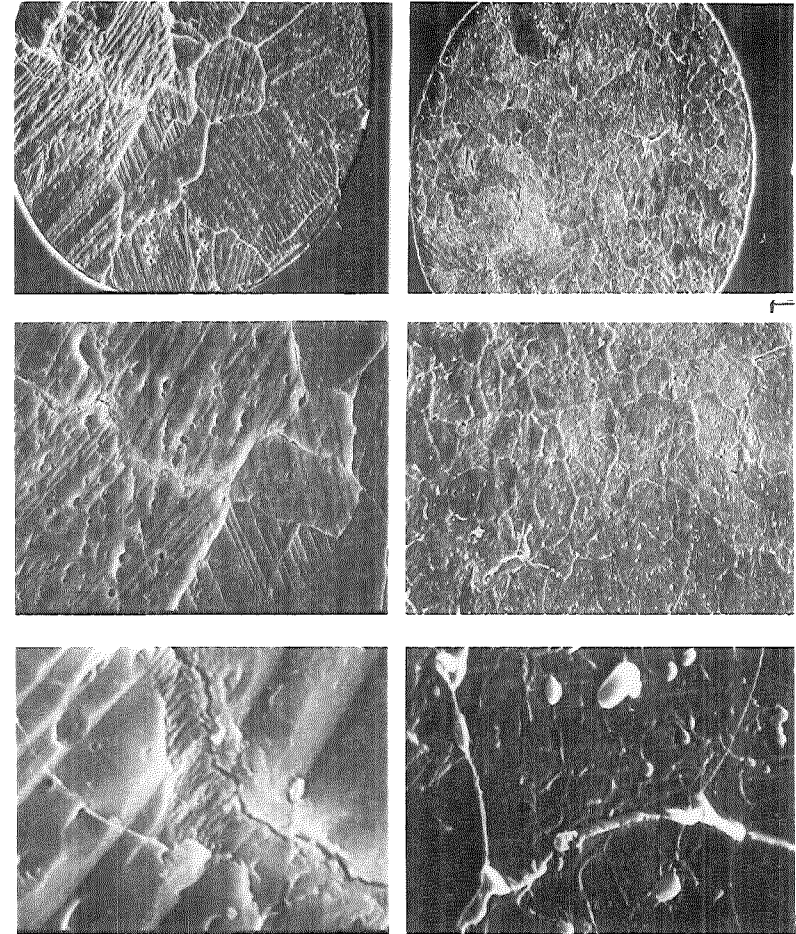
Fig. 4.3.1.3   SEM of specimens of Fig. 4.3.1.2 after annealing 5 min at 1030 °C. Left: Li$_4$SiO$_4$, right: Li$_4$SiO$_4$ + 2.2 w% SiO$_2$
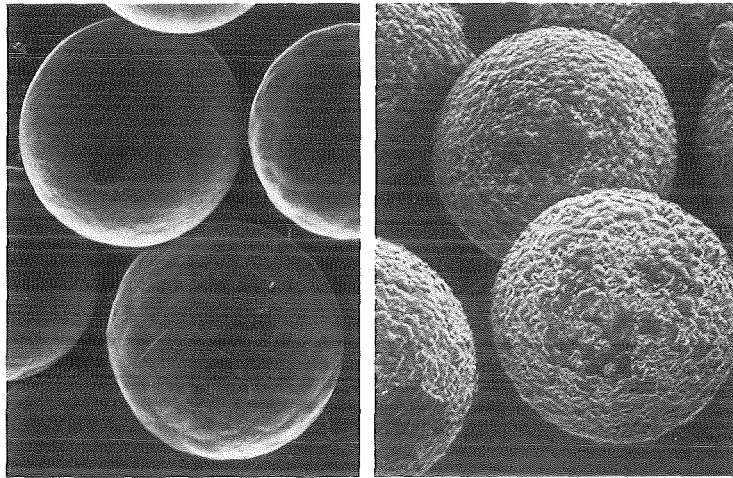
Fig.4.3.1.4   Surface of stoichiometric (left) and silicon rich (right) pebbles after annealing 5 min at 1030°C

4.3.1.5 Conclusions

Lithium orthosilicate pebbles produced by spray of liquid droplets have almost sperical shape, a smooth surface and high density. Because of these properties the pebble bed reaches a density of 1.41-1.49 g/cm3 that satisfies the design requirements. Annealing of pebbles above 1024°C for a short time leads to healing of microcracks and crystalization if the orthosilicate is hyperstoichiometric in silica. Addition of alumina has a negative influence while tellurium reduced crack formation during fabrication and supported crystallization.

References

1.   M. DALLE DONNE, U. FISCHER, M. KUECHLE, G. SCHUMACHER, G. SORDON, E. BOJARSKI, P. NORAJITRA, H. REISER, H.D. BASCHEK, E. BOGUSCH,   "Pebble Bed Canister: The Karlsruhe Ceramic Breeder Blanket Design for the EuropeanTorus", J. Fus. Techn. 14 (1988) 1357

2.   P. HOFMANN, W. DIENST, "Chemical Interactions of Beryllium with Lithium Based Oxides and Stainless Steel", J. Nucl. Mater. 171 (1990) 203

3.   G. SCHUMACHER, M. DALLE DONNE, S. DORNER, "Properties of Lithium Orthosilicate Spheres", J. Nucl. Mater. 155-157 (1988) 451

4.   C. KRACEK, " The Binary System Li2O-SiO2", J. Phys. Chem. 34/12 (1930) 2341

5.   H. SKOKAN, Kernforschungszentrum Karlsruhe, Germany, IMF, personal comunication

4.3.2   Sintered pebbles (E. Günther, H. Wedemeyer)

Sintered pebbles of lithium orthosilicate were developed to be fabricated by a powder metallurgical agglomeration process from sinterable orthosilicate powders to meet the specifications of the Karlsruher pebble bed concent. The overall process was developed in two steps:
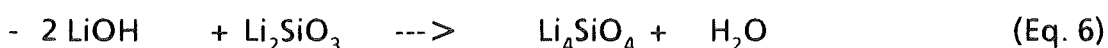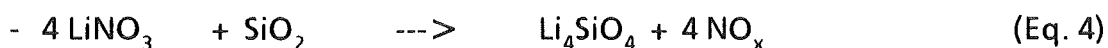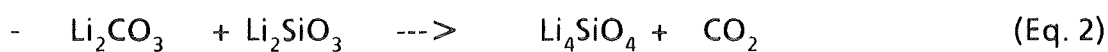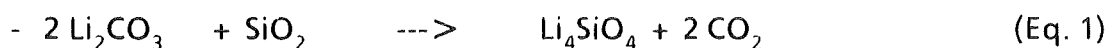
- fabrication of sinterable lithium orthosilicate powders,
- fabrication of sintered pebbles.

Specification of the Materials

The main topics of the specification are given by physical demands of the pebble bed design and the results of neutron irradiation experiments concerning the tritium release behaviour. From this, the diameter of the pebbles is specificated to be 0.500 ± 0.060 mm, the material density to be > 90 % th.d. and the tap density to be > 1.30 g/cm^3. As a result from irradiation experiments, the chemical impurities should be as low as possible. Especially carbon impurities, mainly given in form of lithium carbonate (Li_2CO_3), are specificated to be less than 0.3 wt%. Moreover, the sodium impurities should be less than 0.02 wt%. A specification of the mechanical stability of the pebbles is given by a thermo-mechanical cycling test, where the part of fractured pebbles after ten cycles between 600 and 60 °C in a metallic cylinder should be less than 2% and the pebbles should be dust free.

Fabrication of Sinterable Powders

Lithium orthosilicate can be prepared by different chemical reactions:

- $2 Li_2CO_3 + SiO_2 \longrightarrow Li_4SiO_4 + 2 CO_2$ (Eq. 1)
- $Li_2CO_3 + Li_2SiO_3 \longrightarrow Li_4SiO_4 + CO_2$ (Eq. 2)
- $2 Li_2O_2 + SiO_2 \longrightarrow Li_4SiO_4 + O_2$ (Eq. 3)
- $4 LiNO_3 + SiO_2 \longrightarrow Li_4SiO_4 + 4 NO_x$ (Eq. 4)
- $4 LiOH + SiO_2 \longrightarrow Li_4SiO_4 + 2 H_2O$ (Eq. 5)
- $2 LiOH + Li_2SiO_3 \longrightarrow Li_4SiO_4 + H_2O$ (Eq. 6)

The reactions of lithium carbonate and silica (Eq. 1) or lithium metasilicate (Eq. 2) were found to be possible at temperatures above 600 °C. The powder preparation from those reactions were successfully developed [1]. Sinterable powders were obtained from spray-dried

aqueous suspensions after calcination at 750 to 800 °C. The main disatvantage of this simple process is given with the necessary high temperature of 1100 to 1150 °C during sintering to minimize the carbon impurities. The lithium peroxide (Li_2O_2) reaction (Eq. 3) leads to a very pure orthosilicate powder [1, 2]. But the densification of such powders during sintering is difficult due to high amounts of adsorbed oxygen up to high temperatures, resulting in larger amounts of closed porosity. The same disadvantages were observed with the reaction of lithium salts (i.e. $LiNO_3$) and silica (Eq. 4). The gaseous reaction products (i.e. NO_2) tend to adsorb at the powder particles resulting in impurities and closed porosity. Pure orthosilicate was obtained from the reactions of lithium hydroxide (LiOH) and silica (Eq. 5) or metasilicate (Eq. 6). But, as the hydroxide melts at 450 °C, at a temperature below the reaction temperature of about 600 °C, no finely dispersed powder could be achieved. An organic precursor material is obtained if lithium hydroxide and silica is reacted as a suspension in n-type alcohols (CH_3OH, C_2H_5OH, ...). Calcination of the spray-dried powders immediately leads to an orthosilicate powder with only traces of lithium carbonate, hydroxide and metasilicate [3 to 9] . The process leads to pure, very fine dispersed and sinterable orthosilicate powders as pointed out below and can easily be scaled-up to an industrial production [10].

Following the scheme of powder fabrication, given in figure 4.3.2.1, lithium hydroxide and amorphous silica ("Aerosil") are reacted in stoichiometric amounts as a suspension in methanol. Within this "Methanol Process" an organic compound is formed, which contains lithium and silicon in desired stoichiometric amount. This organic phase is isolated by spray-drying and the powders obtained furthermore used as a precursor for the following steps of powder processing (figure 4.3.2.2). Calcination of this powder at a temperature of about 700 °C than leads to a very fine and sinterable material, which can be easily pressed into any shape without further binding agents and densified by sintering in air at a temperature of about 1030 °C up to 93 %th.d. The obtained materials are characterized by chemical analysis and X-ray diffraction measurement. As a result, the materials are monophase orthosilicate, sometimes with traces of metasilicate and/or lithium carbonate. The amount of further chemical impurities depends only on the level of impurities of the starting materials.

A special advantage of this "Methanol Process" is given by the possibility to modify the mixture of the starting materials, i.e. to fabricate different types of doped orthosilicates. Concerning the alumina doped lithium orthosilicates, solid solutions in the form of $Li_{4-3x}Al_xSiO_4$ might be of some interest [11 to 13].

The industrial application of the "Methanol Process" was tested in a scaling-up experiment whereas a batch of 70 kg lithium orthosilicate powder was produced under industrial conditions [6, 10]. It was shown that the formation of the organic compound in methanol (Fa. ROTH, Karlsruhe) and spray-drying of the suspension is possible in larger batches; the technique of spray-drying of organic suspensions (Fa. NIRO, Copenhagen) is also well estab-

lished. The calcination process was carried out in a vortex-type facility (CONVEX drying system, Fa. BUSS, Pratteln, Switzerland) without any further complications. The orthosilicate powders should be stored under dry conditions to prevent decomposition by hydrolysis in moistured air and pick-up of carbon dioxide, which leads to the formation of lithium hydroxide and lithium carbonate.

Fabrication of Sintered Pebbles

To meet the specifications, especially for the demanded tap density, the material density and the spherical shape of the pebbles have to be optimized as pointed-out in figure 4.3.2.3. The tap density is plotted as a function of the material density and a packing factor F which may describe the quality of the geometrical shape of the pebbles, resulting in increasing values of F with increasing sphericity, as the highest tap density is achieved with uniform spheres. Such uniform spheres are normally fabricated by grinding methods but up to now, there is no experience in grinding of spheres with less than 1 mm in diameter. The spherical shape has to be obtained within the sintering process, whereas sintering in a fluidized-bed leads to sufficient results.

Following the fabrication scheme of the pebbles, given in figure 4.3.2.4, the calcinated powders are suspended in methanol, mixed with binding agents (i.e. "Avicel" and/or polysaccharose) in amounts of 2-3 wt.%, and after homogenization of the mixture the powders are isolated by spray-drying. Homogenization of the mixture under wet conditions was shown to be necessary as dry-mixing mostly resulted in inhomogeneous distribution of the small amounts of binding agents. Alcohol (methanol) is used for this suspension to prevent hydrolytic effects of the silicate powders. Spherical pebbles of these powders are obtained by a special powder metallurgical process: The powders are wetted with small amounts of water, passed through a sieve, the obtained sticks are broken by shaking, and the primary granules (figure 4.3.2.5) are then rounded-up on a rotating disk. The advantage of the extrusion step is the slight pre-densification of the primary granules. Granulation of the powders on rotating disks or under fluidized conditions as usual were shown to be not sufficient, as the spray-dried powders exhibit extraordinary gliding properties which prevent the growing-up of larger agglomerates. In the following fabrication steps the pebbles are dried, dewaxed, and pre-sintered at temperatures of up to 900 °C, and lastly sintered in a fluidized-bed at 1030 °C for two hours and cleaned from dust (figure 4.3.2.6) [9]. The first step of the sintering process is carried out in a usual resistance furnace with the granules placed in an alumina crucible to prevent destroying of the granules which might happen under fluidized-bed conditions [14, 15]. Otherwise, sintering in a fluidized-bed as the second step leads to the spherical shape of the granules. The obtained pebbles are characterized by chemical analysis, metallographic examination, and X-ray diffraction measurement.

Depending on the powder preparation, the materials are nearly monophasic. A typical result of the chemical analysis is given in table 4.3.2.1.

The observed grain-sizes are normally in the range of 10 to 30 µm, but with a strongly controlled temperature-time-program during sintering grain-sizes of less than 10 µm can be achieved [16]. Lithium orthosilicate tends to strong grain-growth during sintering especially at temperatures above 1024 °C, when substoichiometric orthosilicate eutectoidally decomposes in high-orthosilicate and liquid, from which liquid sintering may occur (figure 4.3.2.7).

The powder metallurgical agglomeration is a typical batch-type process. Scaling-up of this process to an industrial production is given with a nearly continuously working facility (NICA-System), developed Fa. LUJUS-MEDICAL AB in Göteborg, Sweden, whereas the different steps of powder processing, extruding into sticks and agglomeration is fitted to a uniform equipment.

References

1.   D. VOLLATH, H. WEDEMEYER, and E. GÜNTHER, "Improved Methods for Fabrication of Lithium Silicates," Proc. 1st Conf. Fusion Reactor Materials, Tokyo, Japan, June 3-6, 1984; Nucl. Mater. 133/134, 221 (1985).

2.   D. VOLLATH, H. WEDEMEYER, and E. GÜNTHER, "Verfahren zur Herstellung von Sinterfähigem Pulver aus Lithiumorthosilikat Li_4SiO_4 und dessen Verwendung, "Ger. Patent No. DE-PS 34 15 326 C2 (1988).

3.   H. WEDEMEYER and D. VOLLATH, "Fabrication of Lithium Containing Ceramic as Breeder Materials for Fusion Reactors," Proc. VII. German-Jugoslav-Meeting on Material Science," Bad Herrenalb, Germany, April 1985;
G. ONDRACEK and O. VÖHRINGER (Ed.), "Contemporary Inorganic Materials: Progress in Ceramics, Metals and Composites," KFA-JÜLICH GmbH (1986).

4.   D. VOLLATH and H. WEDEMEYER, "Preparation of the Lithium Silicates Series from Li_2SiO_3 to Li_8SiO_6 in Alcoholic Media," Proc. 2nd Conf. Fusion Reactor Materials, Chicago, USA, April 13-17 1986; J. Nucl. Mater. 141/143, 334 (1988).

5.   D. VOLLATH and H. WEDEMEYER, "Techniques for Synthesizing Lithium Silicates and Lithium Aluminates," Amer. Ceram. Soc. Meeting, Pittsburg, USA, April 26-30, 1987; Advances in Ceramics 25, 93 (1989).

6.   D. VOLLATH, H. WEDEMEYER, and E. GÜNTHER, "Herstellung Sinterfähiger Pulver für Binäre und Multinäre Keramische Oxidwerkstoffe," Ger. Patent No. P 37 25 740.4 (1987).

7.   H. WEDEMEYER and D. VOLLATH, "Synthesis of Binary or Multinary Oxide Ceramics in Methanol Suspensions," Amer. Ceram. Soc. Meeting, Indianapolis, USA, April 23-27, 1989; Powder Metallurgy International 22, 33 (1990).

8.   H. WEDEMEYER and H.-J. RITZHAUPT-KLEISSL, "Lithiumkeramik für Fusionsreaktoren: Herstellung und Charakterisierung," Proc. Jahrestagung Kerntechnik, Nürnberg, Germany, May 15-17, 1990, p. 577, INFORUM (1990).

9.   H. WEDEMEYER and E. GÜNTHER, "Fabrication of Powders and Sintered Spheres of Lithium Ceramics as Breeder Materials in Nuclear Fusion," The First European East-West Symp. on Materials and Processes, Helsinki, Finland, June 10-18, 1990; J. Materials and Product Technology (in press).

10.   D. VOLLATH, H. WEDEMEYER, E. GÜNTHER, and H. ELBEL, "Semi-Industrial Proction of Li_4SiO_4 Powder and Pebbles," 1st Symp. Fusion Nuclear Technology, Tokyo, Japan, April 10-19, 1989; Fusion Eng. Design 8/10, 1 (1989).

11.   A. SKOKAN, D. VOLLATH, H. WEDEMEYER, E. GÜNTHER, and H. WERLE, "Preparation, Phase Relationships and First Irradiation Results of Lithium Orthosilicate Doped wit Al^{3+}- and P^{5+}-Ions," 15th Symp. Fusion Technology, Utrecht, The Netherlands, September 19-23, 1988; Vol. 2, p. 1025, North-Holland (1989).

12.   D. VOLLATH, H. WEDEMEYER, H. ZIMMERMANN, and H. WERLE, "Doped Lithium Orthosilicates, Preparation and Properties," 4th Conf. Fusion Reactor Materials, Kyoto, Japan, December 4-8, 1989; J. Nucl. Mater. 174, 86 (1990).

13.   D. VOLLATH and H. WEDEMEYER, "The Use of Solid Solutions of the System Lithium Orthosilicate - Eucryptite as Breeder Materials," Amer. Ceram. Soc. Meeting, Indianapolis, USA, April 23-27, 1989; Advances in Ceramics 27, 3 (1990).

14.   D. VOLLATH and B. DÖRZAPF, "Hochtemperaturfließbett für Agglomerierende Schüttgüter," Ger. Patent No. G 89 02 839.2 (Jan. 1989).

15.   E. GÜNTHER and D. VOLLATH, "Hochtemperaturfließbett für Nicht-Agglomerierende Schüttgüter," Ger. Patent No. G 89 02 838.4 (1989).

16.   H. WEDEMEYER, H.-J. RITZHAUPT-KLEISSL, E. GÜNTHER, and H. WERLE, "Fabrication of Grain-Size Controlled Lithium Orthosilicate," Proc. 16th Symp. Fusion Technology London, UK, September 3-7, 1990 (in press).

Table 4.3.2.1:   Chemical analysis of Li_4SiO_4 (ALICE-3-type material)

Li :	22.43 ± 0.29	wt.%	Fe :	0.028 ± 0.001	wt.%
Si :	23.13 ± 0.10	wt.%	Cr :	0.0073 ± 0.0002	wt.%
			Mn:	0.0002 ± 0.0001	wt.%
			Ni :	0.0047 ± 0.0002	wt.%
			Co : <0.0003		wt.%
			Ti :	0,0021 ± 0.0001	wt.%
			Zr :	0,073 ± 0.013	wt.%
			Cu :	0.0008 ± 0.0001	wt.%
			Zn :	0.0014 ± 0.0001	wt.%
			Al :	0.052 ± 0.001	wt.%
			Ca :	0,018 ± 0.002	wt.%
			Na:	0.011 ± 0.001	wt.%
			K :	0.0003 ± 0.0001	wt.%
			C :	0.078 ± 0.003	wt.%
			S :	0.065 ± 0.020	wt.%
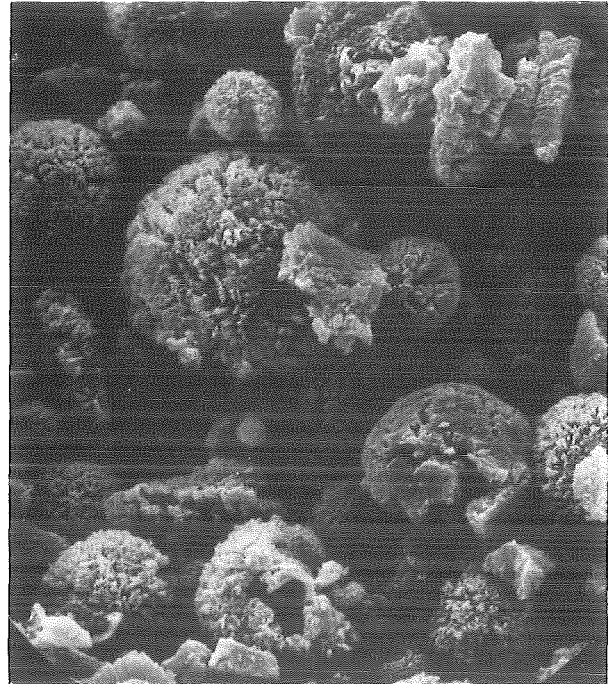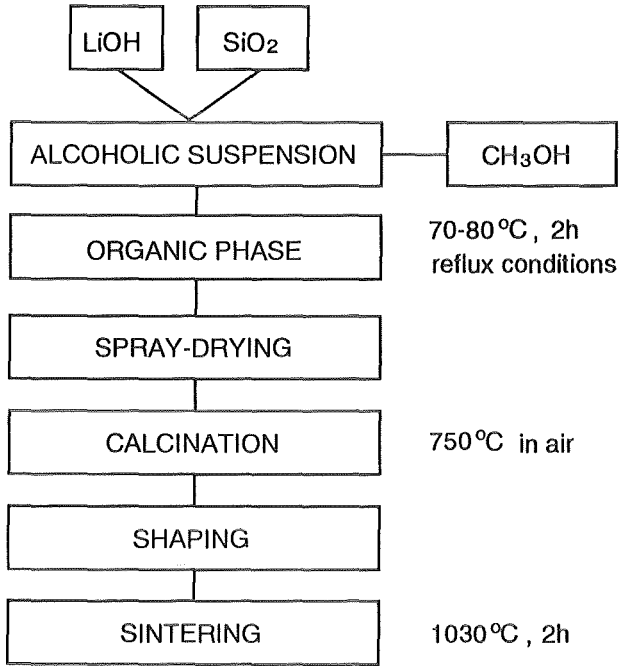
Fig. 4.3.2.1: Scheme of powder fabrication for Li₄SiO₄

Fig. 4.3.2.2: Spray-dried powder of Li₄SiO₄ (organic phase)

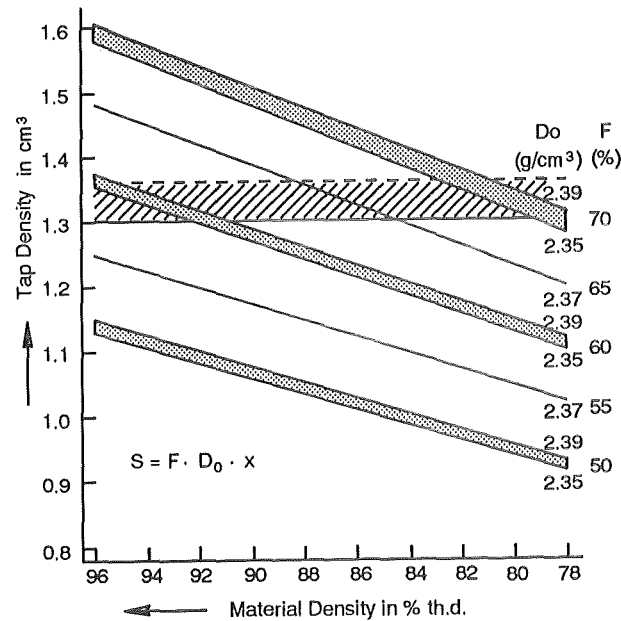Fig. 4.3.2.3: Tap density vs. material density and packing factor

for Li_4SiO_4 pebbles (S = tap density in g/cm^3,

F = packing factor in %, D_o = theoretical density

in g/cm^3, x = matrial density in % th.d.)
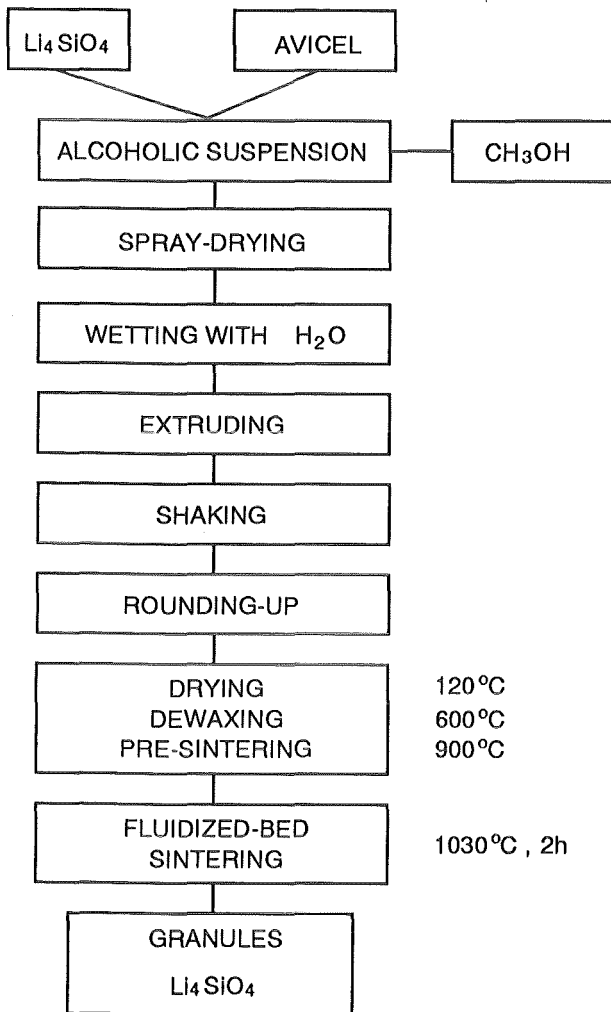
Fig. 4.3.2.4: Scheme of pebble fabrication
for Li_4SiO_4
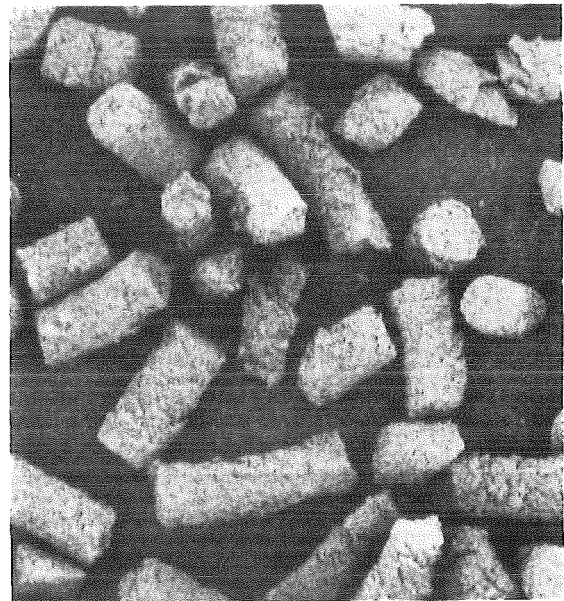

Fig. 4.3.2.5: Primary granules of
Li_4SiO_4
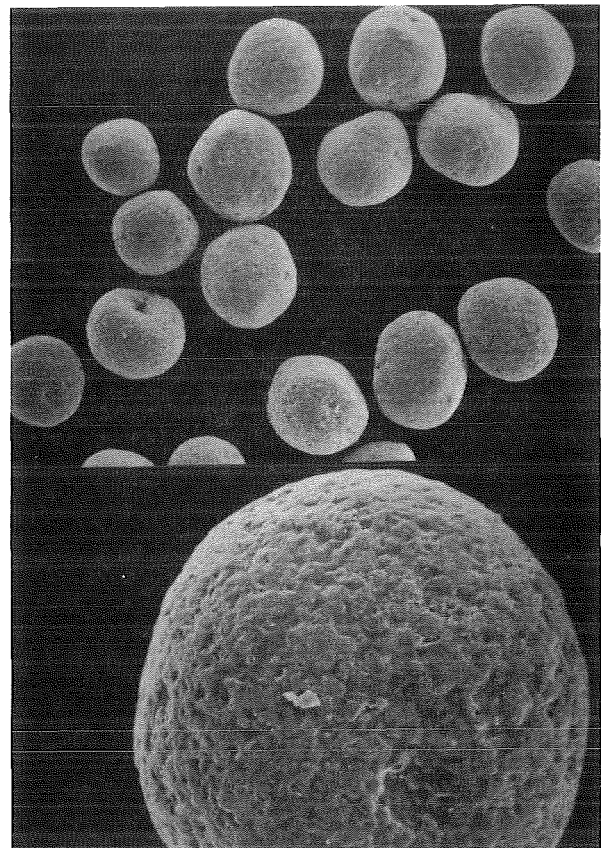

Fig. 4.3.2.6: Sintered pebbles of Li_4SiO_4

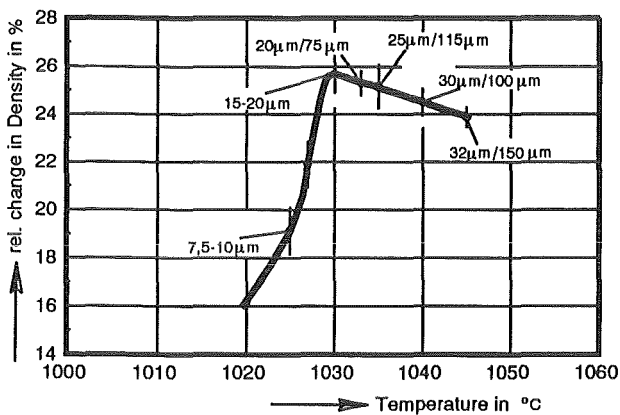Fig. 4.3.2.7: Densification and grain-growth of
Li_4SiO_4 during sintering (heating
rate 5 °C/min, time of sintering 5 hours)

4.3.3.   Pebble characterization and chemical analysis

4.3.3.1   Pebble charaterization (R. Knitter)

The methods, which were used to characterize the Li_4SiO_4 pebbles for the irradiation experiments fabricated by sintering or melting, are described and the results are summarized below. The measured densities of the samples are listed in table 4.3.3.1.

Determination of the Tap Density

The tap density of the bulk material was measured in a tap machine according to DIN 53194. The examined orthosilicate sintered sample with particle sizes ranging from 315 to 630 µm yielded a tap density of about 1.35 g/cm^3. For the molten pebbles a tap density of about 1.43 g/cm^3 was measured.

X-ray Powder Diffractometry

The powder diffractometry was carried out in a diffractometer with Bragg-Brentano geometry using Cu-Kα radiation. The lower limit for the identification of crystalline phases amounts to about 5 wt%.
In the lithium orthosilicate sintered pebbles small amounts of lithium metasilicate (Li_2SiO_3) could be detected, which may be due to lithium losses during sintering, whereas in the molten pebbles a very small amount of a phase is observed, possibly containing SiO_2, which could not be identified so far.

Mercury Intrusion Porosimetry

Mercury intrusion porosimetry was performed in order to determine the geometric density as well as the amount and size distribution of open pores down to a minimum pore diameter. For the density determination, the volume of the mercury displaced by the immersed body is measured, whereas for the measurement of pore size distribution the volume of mercury penetrating the open pores under increasing pressure is determinded as a function of that pressure. The relationship between the geometry of the open pores and the mercury pressure is established by the Washburn equation assuming that the channels of the open porosity can be approximated by cylindrical capillaries [1] . In the equipment used the model yields a lower limit of 3.5 nm for the detectable capillary diameter. The measured densities of the sintered and molten pebbles were 2.05 and 2.29 g/cm^3, respectively (table 4.3.3.1).

Helium Pycnometry

With helium as a penetrating medium it is possible to get access to the total volume of the open pores, including those fractions, which are not penetrable by the non-wetting mercury. The measurement yields the density of the sample including only the closed porosity. The difference between measured and theoretical density gives in this case the closed porosity. The measured densities of the sintered and molten pebbles were 2.39 and 2.40 g/cm^3, respectively (table 4.3.3.1).

Measurement of the Specific Surface Area

One method for the determination of the specific surface area is based on the theory developed by Brunauer, Emmett and Teller on the adsorption of nitrogen at its boiling point and the measurement of the adsorbed nitrogen volume [2, 3] . The same method using krypton as the adsorbed medium is also sensitive to surface areas below 1 m^2/g, which is the limit of detection for nitrogen. The specific surface area of the sintered and molten pebbles were 1.5 and 1.3 m^2/g, respectively.

Optical and Scanning Electron Microscopy

In order to oberserve the structure of the pebbles etched micro-sections and the as prepared pebbles were examined under optical microscope and SEM including EDX. The mean grain diameter of the lithium orthosilicate sintered pebbles is about 20 μm. Some small round inclusions, possibly lithium metasilicate, are observed at the grain boundaries and sometimes also in the grains, indicating the existence of a partial melting at 1024 °C during sintering. Amount the molten pebbles there is a small amount of hollow speres. Some cracks could be observed in this material, which may be due to thermal stresses during cooling. No foreign phase could be detected by microscope.

Table 4.3.3.1:   Density of the Li_4SiO_4 pebbles

| | pebbles fabricated by | |
	sintering	melting
Hg-Porosimetry		
D [g/cm3]	2.05	2.29
D [%TD]	85.8	95.4
P_{open} [%]	14.2	3.6
P_{closed}[%]	--	1.4
He-Pyknometry		
D [g/cm3]	2.39	2.40
D [%TD]	100	100.0
P_{closed} [%]	--	--

4.3.3.2   Pebbles chemical analysis (C. Adelhelm)

The composition of Li_4SiO_4 in form of sintered or molten pebbles and as starting powder material is determined by chemical analysis. The analysis of the main compounds like Si, Li require an analytical methode of high accuracy and precision. Determining impurities emphasis is laid on low detection limits resp. sensitive methods. Samples or pebbles with a particle size greater than 2 mm are crushed and stored under a protective atmosphere because the increased surface absorbes moisture and CO_2. The different analytical methods are described below:

Silicon

In silicate analysis X-ray flucrescence spectrometry (RFA) provides a reliable methode for determining elements heavier than fluoride and more than 0,1 % by weight [4]. 300 mg of the sample is fused with 8 g of sodium or lithiumtetraborate and casted into a solid bead. Reference beads are fused with known amounts of element oxides reconstituting the sample. Beside the time-consuming gravimetric silicon analysis the RFA-method reveals the best repeatability. Amounts of 20 to 30 % Si by weight can be analysed in the limits of 0,05 to 0,1

% by weight. As the concentration of the metallic impurities lies usually below the detection limit the RFA-method is only used for silicon analysis.

Lithium and metallic impurities

A mixture of hydrofluoric, nitric and perchloric acid is used to decompose the silicate and to evaporate subsequently silicontetrafluoride [5]. The remaining elements are kept in solution by hydrochloric and hydrofluoric acid. The lithium, sodium and potassium content is measured by atomic absorption spectrometry (AAS) and the other elements as listed in table 4.3.3.2 by inductive coupled plasma spectrometry (ICP-OES). Lithium determination by AAS yields a repeatability standard deviation of 0,3 % for a concentration range of 15 to 25 % by weight. The detection limits in table 4.3.3.2 are referred to a sample concentration of 50 mg per ml solution.

Water

Most silicates contain water in form of absorbed moisture or as hydroxyl groups. In a silica tube furnace 0,5 to 1,0 g of a sample is heated at 650 °C under dried, streaming nitrogen carrying the evolved water into the Karl-Fischer reagent. The water content is titrated coulometrically. This method is specific for water analysis [6].

Carbon dioxide, total carbon

Also under streaming nitrogen or argon, purified by passage through soda lime tubes, carbon dioxide is liberated with phosphoric acid or by heating in a furnace at 1200 °C and carried into a coulometric cell, where it lowers the pH. Back-titration takes place by electrolytically generated hydroxide ions.

Combustion in a stream of oxygen using a high-frequency induction furnace records total carbon, the carbonate and non-carbonate carbon. The liberated carbondioxide is determined by infrared measurement. Both methods are calibrated by known amounts of lithiumcarbonate.

**Table 4.3.3.2   Detection limits of impurities in lithiumsilicate**

element	detection limit $[\mu g/g]$	element	detection limit $[\mu g/g]$
Al	5	Na	1
Ca	3	Ni	3
Co	2	Ti	1
Cr	4	W	25
Cu	2	Zu	2
Fe	4	Zr	1
K	2	C_{total}	50
Mn	0,5	CO_2	50
Mo	20	H_2O	50

References

1.   E. W. WASHBURN, "Note on a Method of Determining the Distribution of Pore Sizes in a Porous Material," Proc. Nat. Acad. Sci. U.S.A. 7, 115 (1921)

2.   S. BRUNAUER, P. H. EMMETT and E. TELLER, "Adsorption of Gases in Multimolecular Layers," J. Am. Chem. Soc. 60, 309 (1938)

3.   S.J. GREGG and K. S. W. SING, "Adsorption, Surface Area and Porosity," Academic Press, London (1967)

4.   C.O. INGAMELS, "Lithiummetaborate flux in silicate analysis", Anal. Chim. Acta, 52, 323-334 (1970)

5.   P.G. JEFFREY, D. HUTCHISON, Eds., "Chemical methods of rock analysis", 3rd Edition, Pergamon Press 43 ff. (1983)

6.   A. FARZANEH, G. TROLL, " Quantitative Hydroxyl- und H_2O-Bestimmungsmethode für Minerale, Gesteine und andere Festkörper", Fresenius z. Anal. Chem. 287, 43-45 (1977)
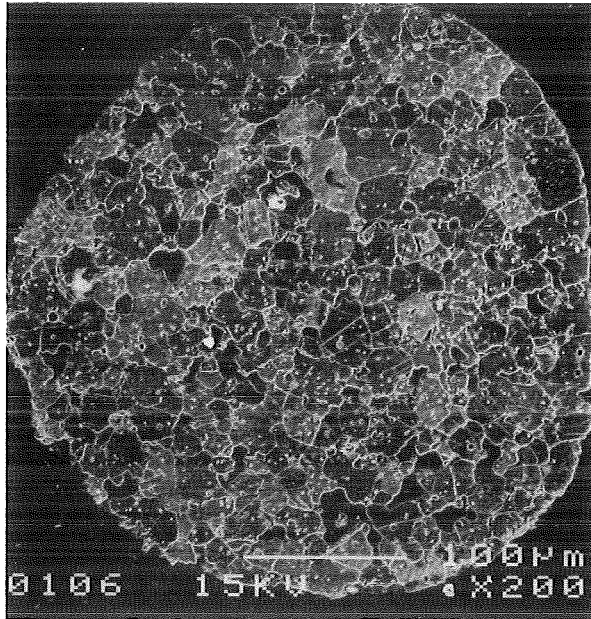
Fig. **4.3.3.1:** SEM micrograph of the polished and etched surface of a sintered lithium orthosilicate pebble.
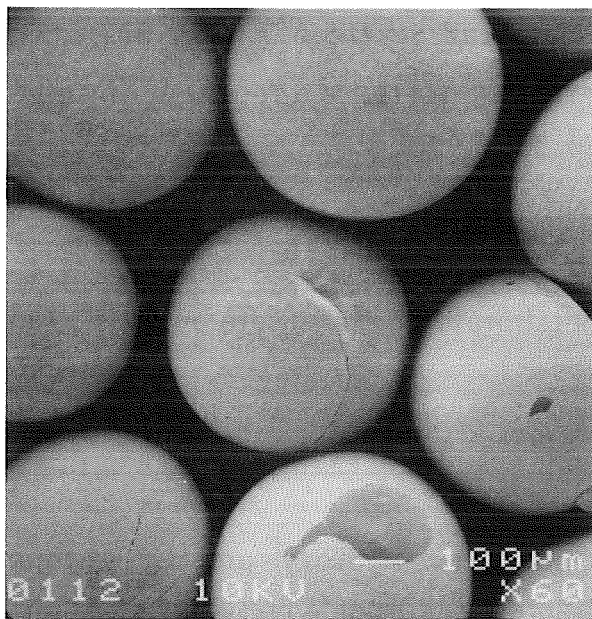
Fig. 4.3.3.2: SEM micrograph of molten lithium orthosilicate pebbles.

4.3.4 Mechanical and thermal cycle tests on the pebbles (G. Schumacher)

4.3.4.1 Introduction

Lithium orthosilicate pebbles are exposed to mechanical stresses in the blanket canisters during the thermal cycles of the reactor. They must sustain the pressure exerted by the canister wall when its temperature drops to a lower value. Therefore, it is important to examine the mechanical stability under mechanical and thermal stresses. Two types of tests are done, one is a simple pressure test, the other simulates the conditions in a blanket canister during thermocycling.

The pressure test is conducted by exposing single pebbles to a continuously increasing weight load until the pebble breaks. In the thermocycling test, a container that is filled with pebbles is heated to 600°C and, after equilibration of temperature inside the pebble bed, quenched in water. The amount of broken pebbles serves as a measure of the ability of the pebbles to withstand the stresses during thermocycling. It is important that broken particles don't crumble into fine powder that could impede the flow of helium through the pebble bed.

4.3.4.2 Pressure tests

First a simple test is applied to the pebbles. A continuously increasing weight load is imposed by a piston to a single pebble until it breaks. The load is made by a water container that gradually fills with water. The pebble is placed on a balance that measures the load, Fig.4.3.4.1. The load, at which the pebbles break, averaged through 10 tests, is called the fracture load. Sufficient mechanical stability can be assumed for fracture loads above 5 N. When pebbles break below 4 N, it can be assumed that cracks are the reason. Standard values for the fracture load are 5-10 N for pebbles consisting of lithium orthosilicate with addition of 2.2 w% silicon oxide after annealing at 1030°C for 5 minutes. Before annealing about 2 pebbles out of 10 break below 4 N because of cracks. Standard fracture loads of pebbles consisting of an orthosilicate close to the stoichiometric composition are below 4 N and scatter down to 1 N. Typical values for the fracture load of pebbles of different composition before and after annealing are given in table 4.3.4.1. The table also shows the loads that the single pebbles of the respective batches can sustain during a series of ten tests until they break. It is obvious from table 4.3.4.1 that pure orthosilicate pebbles have much lower fracture loads.This is not influenced by annealing to a measurable extent. Scattering of values gets smaller
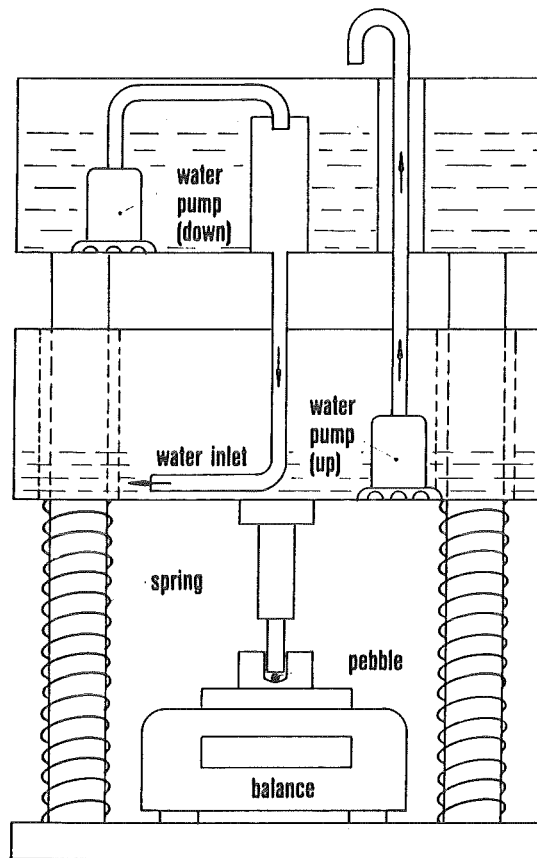
Fig.4.3.4.1: Apparatus for the pressure tests

for pebbles containing a surplus of 2.2 wt% of silica. This holds also for the pebbles that contain besides silica tellurium. Sintered pebbles (comp. 4.3.2) have much lower fracture loads than pebbles with a surplus of silica that are produced from the melt.

During the tests it was observed that pebbles exposed to room air improved mechanical properties dependent on the time of exposure. Fracture loads increased up to 30% after 3 weeks. This raises the question of the influence of temperature and dry inert gas atmosphere on the mechanical properties. Therefore, a series of tests was started, in which pebbles were first dried at different temperatures and then their fracture load was measured.

Tab.4.3.4.1: Fracture loads FL [N] and loads [N], at which single pebbles break. Pebbles are of pure orthosilicate and orthosilicate + additives

Sample/nr.	1	2	3	4	5	6	7	8	9	10	FL
pure, o	2.7	2.7	2.7	2.7	3.5	3.9	2.5	1.8	3.3	3.6	2.9
pure, d	1.6	5.4	3.6	2.5	0.6	0.2	3.0	3.2	4.3	3.8	2.8
+ silica, o	3.5	5.7	11	11	6.2	5.0	3.4	12	5.4	9.0	7.2
+ silica, d	7.0	4.8	8.5	9.8	6.9	10	6.3	9.0	7.0	7.9	7.7
+ silica,Te, o	12	13	7.0	6.0	8.0	12	13	11	11	13	10.6
+ silica,Te, d	5.0	11	9.5	12	10	10	10	8.9	11	11	9.8
sintered pebbles	4.4	3.6	4.9	6.9	4.4	4.7	4.3	5.0	4.6	3.6	4.6

o = original (as fabricated)   Addition of silica = 2.2wt%, of Te = 0.5wt%

d = annealed in rotating tube furnace

Nine drying temperatures from 200 to 1000°C in steps of 100°C were applied. With exception of the 200 and 300°C runs, pebbles were heated with a rate of 100°/h to the destination temperature, then kept there for 10 h and after this cooled again with 100°/h. Again, it was important to keep the heating rate for the first two steps below 50°C/h, to prevent crack formation because of too high internal water vapour pressure. Ten samples were taken after each step for measurement of the fracture load. The result of the series of drying tests is given in Fig.4.3.4.2.

It reveals fom the heating tests under dry atmosphere that the fracture loads of pebbles with additives of 2.2 wt% silica (89/3, 89/6) decrease until the water has been released at about 700°C. Then, the fracture load remains constant up to the maximal annealing temperature of 1000°C. Values for pure orthosilicate (89/4) and for those with an addition of only 1 wt% silica (89/5) are much lower but show the same tendency. Additions of alumina are of negative influence (89/5,
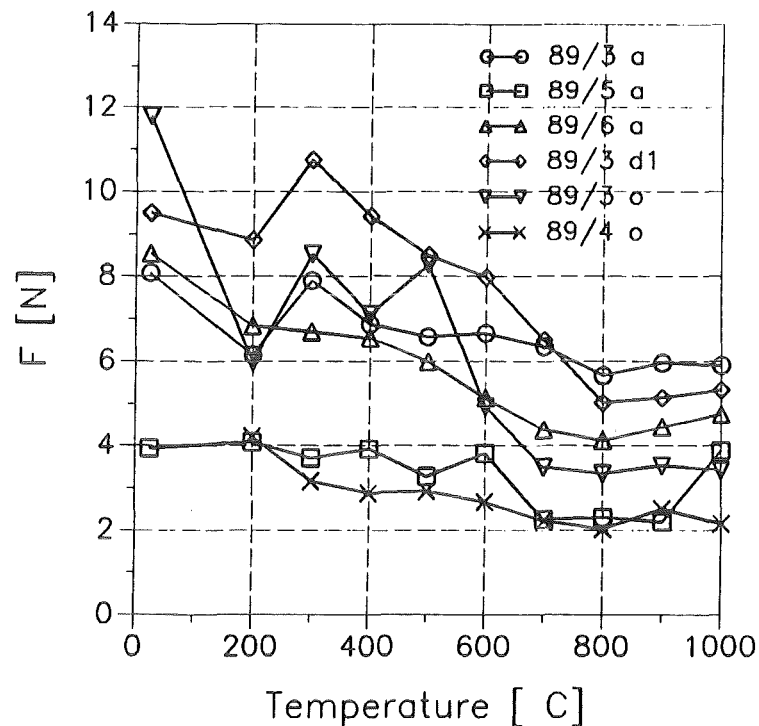
o = as fabricated

a = annealed at 1030°C for 5 min in stationary furnace

d1 = ann. at 1030°C for 5 min in rotating tube furnace

89/3 = Li_4SiO_4 + 2.2w% SiO_2 89/4 = Li_4SiO_4

89/5 = Li_4SiO_4 + 1w% SiO_2 + 0.3w% Al_2O_3

89/6 = Li_4SiO_4 + 2.2w% SiO_2 + 1w% Al_2O_3

Fig.4.3.4.2   Dependence of the fracture load of pebbles on the temperature of drying in inert gas atmosphere for different material compositions and heat treatment.

89/6). Samples (89/3a, 89/3d1) that were annealed at 1030°C for 5 min. after fabrication (see section 4.3.1.3) have better mechanical stability than those in the as fabricated condition (89/3o). This shows that annealing after fabrication is an important step in preparation of pebbles with good mechanical stability.

4.3.4.3 Thermocycling tests

The thermocycling test simulates the mechanical and thermal stresses that are imposed on the pebble bed in a blanket canister during reactor operation. Pebbles are filled in a container that is equipped with two thermocouples, one in the centre of the pebble bed, the other attached to the wall. The container is heated until the wall temperature is 600°C. At this time the temperature in the centre of the bed is between 530 and 600°C. Then the container is moved out of the furnace and quenched in water until the wall temperature drops to 50 - 100°C. This is the moment at which stress is imposed to the pebble bed, because its centre is still at a temperature above 500°C.

The first thermocycling tests were done manually using a cylindrical container of 15 mm inner diameter heated in an HF-induction coil and dropped into a water bucket below the coil [1]. Now, an hydraulic automat is used to move the container from a furnace to the water bath and back when the desired temperatures are reached, Fig.4.3.4.3. The container used with this equipment is flat and thus closer to the blanket canister geometry.
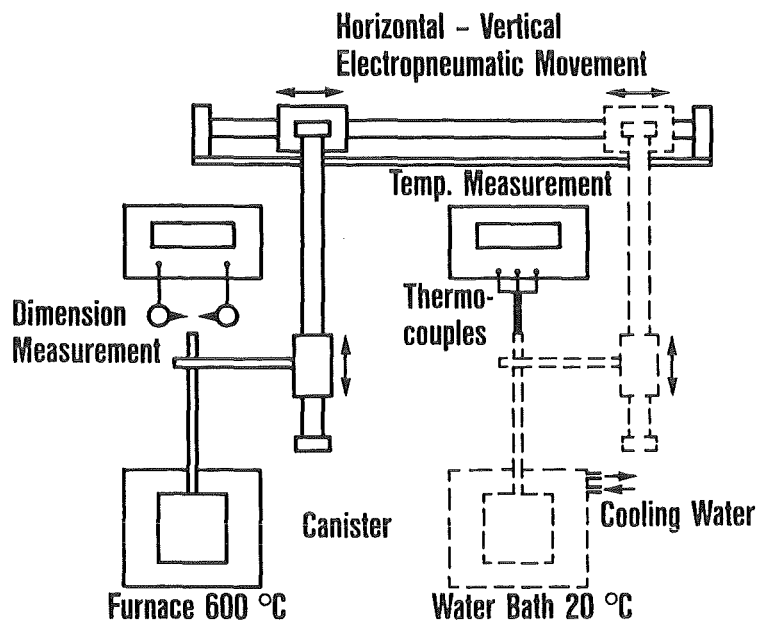

Fig.4.3.4.3: Apparatus for the thermal cycle test

A typical temperature profile of the thermocycling test is given in Fig.4.3.4.4, that shows three cycles out of a series of ten. The w-line represents the temperature course of the canister wall, the b-line the temperature in the centre of the pebble bed. The striking difference between both curves is the minimum temperature that is reached during cycling. While the canister wall temperature drops down to 62°C, the bed centre temperature falls to 355 °C but about 3 min later only. The temperature difference increases to a maximum of 470°C when the container wall temperature reaches its lowest point during quenching. At that time the pebbles are under the highest pressure from the container wall. After the test the pebbles are sieved and the percentage of broken material is determined. This test certainly represents extreme conditions that may not occur in a fusion reactor blanket. Thus, conclusions drawn from the test results will be conservative ones. The former manual tests were still more severe with a maximum temperature difference of 520°C.
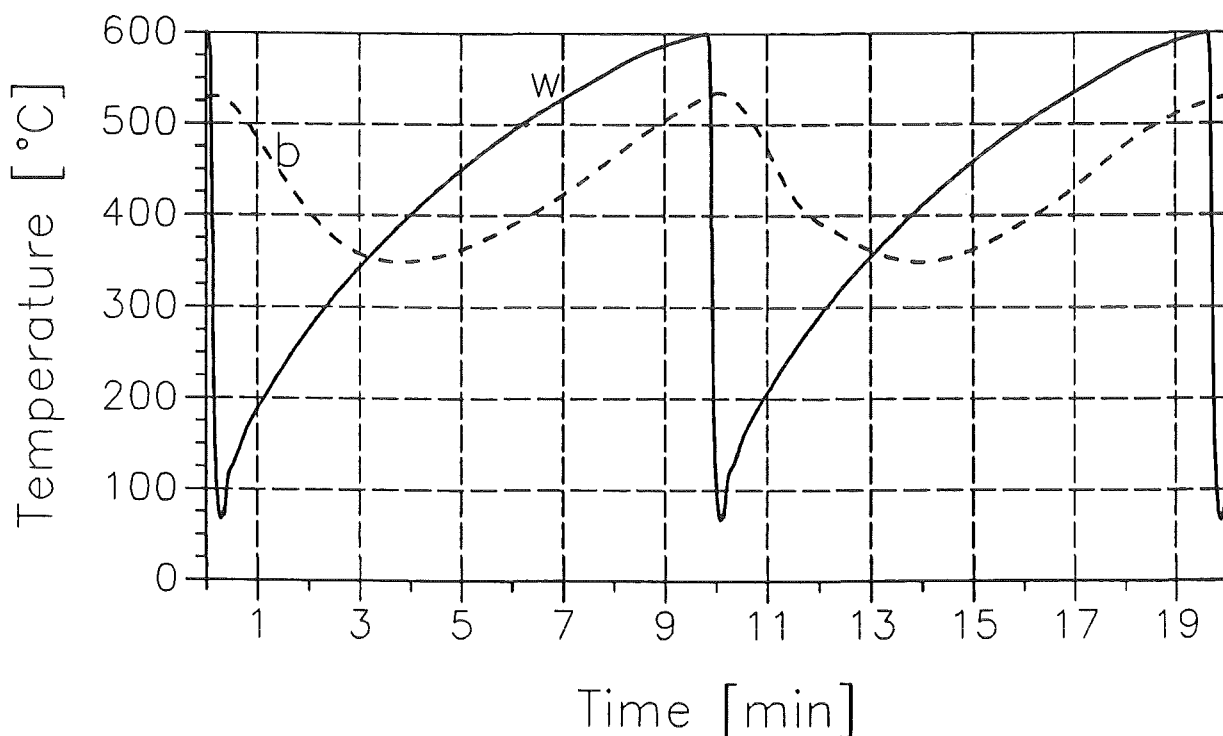

Fig.4.3.4.4: Temperature in container wall (w) and pebble bed (b) during thermocycling

Results of the mechanical and thermal stress simulation test are given in Tab.4.3.4.2. It shows, that the result of the test improves remarkably by optimised annealing only if Li4SiO4 has a surplus of 2.2% of SiO2. This is the effect of the already described process of healing microcracks. It is important, that the part of fine powder is kept low, because this could be moved by the sweep gas. By comparing the last two tests, it results that the more severe conditions of the manual tests produces a higher part of broken material. Tests with pebbles containing additives of silica and tellurium are not yet done. However, it can be assumed, that with high values in the fracture load good results for the thermocycling test can be expected. Sintered pebbles show a good performance, although their fracture loads are relatively low. This may be due to the absence of destructive microcracks in the sintered material.

Table 4.3.4.2: Results of the simulation of mechanical and thermal stress in a blanket canister.

Material	composit.	% broken	%fine*
86/1 o	+ 2.2 w% SiO2	11	0.02
86/1 a	dto	2	0.02
89/1 o	Li4SiO4	6	0.12
89/1 a	dto	10	0.05
90/1 d	+ 2.2 w% SiO2	1.4	negl.
90/1 d **	dto	0.05	negl.
sintered pebbles	Li4SiO4	1.4	negl.

* particles < 0.05 mm   ** test with the apparatus shown in Fig.4.3.4.3
                                        ($\Delta T = 470°C$)

o = as fabricated   other tests were performed manually ($\Delta T = 520°C$)

d = annealed in rotating tube furnace   a = annealed in stationary furnace

4.3.4.4 Conclusions

After thermal treatment the fracture load of the pebbles fabricated by melting is better than 5 N, which is considered to be high enough for pebbles to withstand the stress during temperature cycles in a fusion reactor blanket. In a second test, that simulates the stress conditions, it was found that only less than 1.5 % of the optimised pebbles, both fabricated by melting and by sintering, break even under conditions that seem to be more severe than during the blanket function.

A series of tests with pebbles of different composition treated in an optimised annealing process show that composition and thermal treatment are important factors for improving the mechanical properties of lithium orthosilicate pebbles fabricated by melting. A surplus of 2.2 % of silica to the stoichiometric composition allows to change the structure during thermal treatment in a way that a fine grained glass cemented structure without microcracks develops, which has optimal mechanical properties. Pebbles that contain 0.5 wt% tellurium, besides the silica addition, show the highest mechanical stability observed so far.

References

1. G. SCHUMACHER, M. DALLE DONNE, S. DORNER, "Properties of Lithium Orthosilicate Spheres", J.Nucl.Mater. 155-157 (1988) 451

4.4   Lithium Metazirconate (Li$_2$ZrO$_3$) Pebbles

4.4.1   Li$_2$ZrO$_3$ properties (W. Dienst, B. Schulz)

Mechanical strength data of Li$_2$ZrO$_3$ material are scarce in general. A parameter correlation was only given for the Young's modulus, based on measurements of the ultrasonic pulse velocity [1]. The version accepted for the ITER Blanket Materials Data Base is:

$$E = 203.35 (1 - P) (1 - 1.286 P)^2 [1 - 2.40 \times 10^{-4} (T - 293)]$$
$$[E] = GPa, P = \text{porosity} [T] = K$$

The poisson number was found to be about 0.2 [2,3].

Only single data have been given for the ultimate compressive (σ_c) and bending strength (σ_b).

$$\sigma_c = 396 \text{ MPa} (P = 20 \%, d = 0.8 \text{ } \mu m) [1]$$
$$\sigma_c = 230 \pm 31 \text{ MPa} (P = 20 \%, d \approx 2 \text{ } \mu m) [2,3]$$
$$\sigma_b = 65 \pm 15 \text{ MPa} (P = 20 \%, d \approx 2 \text{ } \mu m)$$
with no considerable decrease up to 600 °C [2,3]

First compressive creep measurements on Li$_2$ZrO$_3$ samples of 10 % porosity at 900 °C showed a creep rate level similar to that determined for Li$_4$SiO$_4$ [4].

The chemical compatibility of Li$_2$ZrO$_3$ with stainless steel cladding was only tested in few experiments. The penetration depth of the cladding attack was found to be < 10 μm after 1000 h at temperatures of 550 to 700 °C [5,6] and consequently is of minor importance in comparison with Li$_4$SiO$_4$. Li$_2$ZrO$_3$ was classed with the less reactive breeder materials, like LiAlO$_2$ and Li$_2$SiO$_3$, for which the following correlation for the cladding penetration x was considered [7]:

$$x^2 = 3 \times 10^4 \text{ } \mu m^2/h \cdot \exp (- 100 \text{ kJ mol}^{-1}/RT) \cdot t$$

Of course, this level of attack is technically insignificant. But the conditions concerning the oxygen supply in the capsule tests were not relevant to those in the gas purging system of a breeder blanket.

Thermal conductivity

The thermal conductivity of Li$_2$ZrO$_3$ is far away from giving a recommended function. Fig. 4.4.1.1 gives results of measurements at KfK and those published in literature [5,8]. It shows clearly that not only the absolute value but the temperature dependance itself is not clear.

Specific heat

Apart from the tabulated data in [9], two authors [2,8] measured specific heat of Li_2ZrO_3. The temperature dependence of c_p does not seem to be very large. The values given in [2,8,9] differ from each other in the same order than c_p varies with temperatures. This constant value of $c_p = 0.84$ J/g·K is recommended in the temperature range RT < T < 1000 K.

Thermal expansion

Data are available from work described in [8,10]. It follows for:

$$RT < T < 1075 \text{ K} \qquad \alpha = 10.0 \cdot 10^{-6} \text{ K}^{-1}$$

References

1. B. RASNEUR, Determination of mechanical characteristics of γ-$LiAlO_2$ and Li_2ZrO_3 materials for a fusion reactor blanket. 15th Symp. on Fusion Technology, Utrecht, 19-23 September 1988

2. P. KENNEDY, The preparation, characterization and properties of lithium oxide and lithium-meta-zirconate specimens irradiated in HFR Petten in the second and third EXOTIC experiments. Fusion Technology 1986, Proc. 14th Symp. Avignon, 8 - 12 September 1986, p. 1013

3. K. GILCHRIST, P. KENNEDY, S.D. PRESTON, SNL EXOTIC programme review 25/6/87. Workshop on Progress in Ceramic Tritium Breeding Materials Development, Petten, June 24-26, 1987

4. K. BÄR, C.Y. CHU, J.P. SINGH, K.C. GORETTA, J.L. ROUTBORT, M.C. BILLONE, R.B. POEPPEL, Mechanical Properties and Deformation of Polycrystalline Lithium Orthosilicate. Int. Symp. Fusion Nucl. Technol., Tokyo, April 10 - 15, 1988

5. P.A. FINN, T. KURASAWA, S. NASU, K. NODA, T. TAKAHASHI, H. TAKESHITA, T. TANIFUJI, H. WATANABE, Solid oxide compounds - properties necessary for fusion applications. Proc. 9th Symp. on Engineering Problems of Fusion Research, October 26-29, 1981, Chicago, Vol. II, p. 1200

6. P. HOFMANN, W. DIENST, Chemical compatibility between lithium-based oxide ceramics and stainless steel. J. Nucl. Mater. 141-143 (1986) 289-293

7. P. HOFMANN, W. DIENST, Compatibility studies of metallic materials with lithium-based oxides. J. Nucl. Mater. 155-157 (1988) 485-490

8. G.W. HOLLENBERG, D.E. BAKER, Thermal properties of Li-ceramics for Fusion applications, Hanford, HEDL-SA-2674FP (1982)

9. I. BARIN, O. KNACKE, Thermochemical data Properties of Inorganic Substances, Springer-Verlag Berlin 1973

10. A.J. FLIPOT, E. BRAUNS, P. DIELS, Preparation, Characterization and Properties of Li_2ZrO_3 fabricated form Li_2CO_3 and ZrO_2, Proc. 15th Symp. Fusion Technology, Utrecht, 19.-23.9.1988, 1009

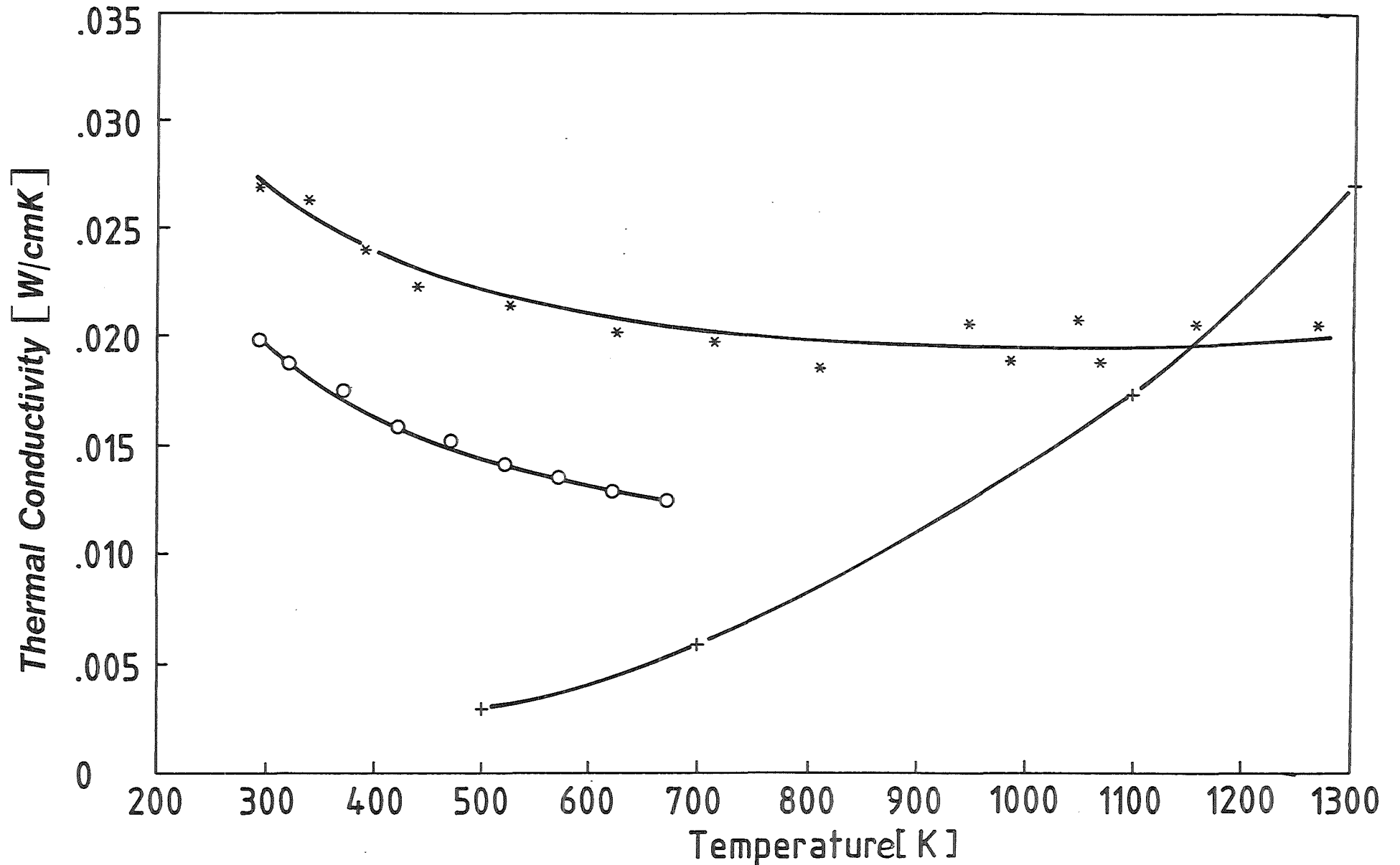Fig. 4.4.1.1: Thermal conductivity of Li₂ZrO₃; *** - KfK density 0.83 ρ_{th}; ooo [8]; + + + [5].

4.4.2 Li₂ZrO₃ pebble fabrication

4.4.2.1. Fabrication with the KfK method (E. Günther, H. Wedemeyer)

Sintered pebbles of lithium metazirconate were developed to be fabricated by a powder metallurgical agglomeration process from sinterable metazirconate powders to meet the specifications of the Karlsruher pebble bed concept, whereas the lithium metazirconate has to be seen as a back-up material to the lithium orthosilicate. The overall process was developed in two steps similar to the fabrication of the orthosilicate material (see Chapter 4.3.2):
- fabrication of sinterable lithium metazirconate powders,
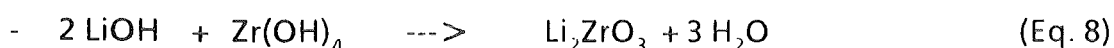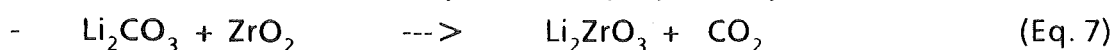- fabrication of sintered pebbles.

Specification of the Materials

The main topics of the specification are similar to that of the orthosilicate:
- diameter of the pebbles   : 0.500 ± 60 μm
- material density   :   ~ 90   % th.d.
- tap density   :   > 2.25   g/cm³
- carbon impurities   :   < 0.3   wt.%
- sodium impurities   :   < 0.02   wt.%
- fractures after thermocycling : < 2   %

Fabrication of Sinterable Powders

Lithium metazirconate mainly has been prepared by two different chemical reactions:

- $Li_2CO_3 + ZrO_2 \quad ---> \quad Li_2ZrO_3 + CO_2$ \hfill (Eq. 7)

- $2\,LiOH + Zr(OH)_4 \quad ---> \quad Li_2ZrO_3 + 3\,H_2O$ \hfill (Eq. 8)

Similar to the powder preparation of lithium orthosilicate (see Chapter 4.3.2) the reaction of lithium carbonate and zirconia (Eq. 7) leads after sintering to higher amounts of carbonate impurities and closed porosity due to adsorption of carbon dioxide. The reaction of lithium hydroxide and α-zirconium acid ($Zr(OH)_4$) has been successfully carried out suspended in stoichiometric amount in methanol.

Zirconium n-propoxide was used as the zirconium bearing starting material, hydrolized to α-zirconium acid in methanol by adding a small amount of water.

Following the scheme of powder preparation, given in figure 4.4.2.1, an organic compound is formed and isolated by spray-drying (figure 4.4.2.2). During calcination of this powder the organic phase is decomposed and zirconia is formed besides a small amount of lithium car-

bonate in a first step. Calcination at a temperature of about 700 °C then leads to pure metazirconate with traces of zirconia and lithium carbonate [1, 2].

Fabrication of Sintered Pebbles

The fabrication of sintered pebbles follows the same route as described in detail in chapter 4.3.2 with the fabrication of sintered orthosilicate pebbles. Again the pebbles are fabricated by a powder metallurgical process: The powders are wetted with small amounts of water, passed through a sieve, the obtained sticks are broken by shaking, and the primary granules are then rounded-up on a rotating disk. The granules are long-time sintered in a fluidized-bed at a temperature of about 1250 °C and cleaned from dust. The resulting pebbles are shown in figure 4.4.2.3 [2]. A small amount of lithium oxide is lost during sintering mainly at the surface of the pebbles from which the formation of some amounts of zirconia is observed at the X-ray pattern of the sintered pebbles. A typical result of chemical analysis of this material is given in table 4.4.2.1.

References

1.   D. VOLLATH and H. WEDEMEYER, "Process for the Preparation of Lithium Metazirconate," 4th Conf. Fusion Reactor Materials, Kyoto, Japan, December 4-8, 1989; J. Nucl. Mater. (1990) (in press).

2.   H. WEDEMEYER and E. GÜNTHER, "Fabrication of Powders and Sintered Spheres of Lithium Ceramics in Nuclear Fusion," The First European East-West Symp. on Material and Processes, Helsinki, Finland, June 10-18, 1990; J. Materials and Product Technology (in press).

Table 4.4.2.1: Chemical analysis of Li_2ZrO_3 pebbles (TRIDEX-type material)

Li : 8.65 ± 0.06 wt.%

Zr. : 55.34 ± 0.12 wt.%

Hf : 1.37 ± 0.02 wt.%

Si : 1.31 ± 0.04 wt.%

Fe : 0.15 ± 0.01 wt.%

Cr : 0.031 ± 0.002 wt.%

Ni : 0.019 ± 0.001 wt.%

Cu : 0.0013 ± 0.0005 wt.%

Co : 0.001 wt.%

Mn: 0.0021 ± 0.0001 wt.%

Al : 0.13 ± 0.01 wt.%

Mo: 0.009 wt.%
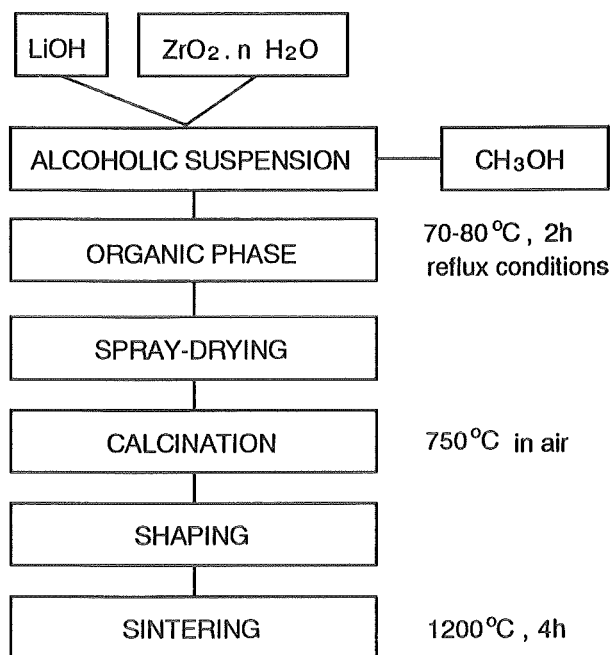
Na: 0.0004 wt.%

C : 0.083 ± 0.001 wt.%

Fig. 4.4.2.1: Scheme of powder fabrication for Li_2ZrO_3

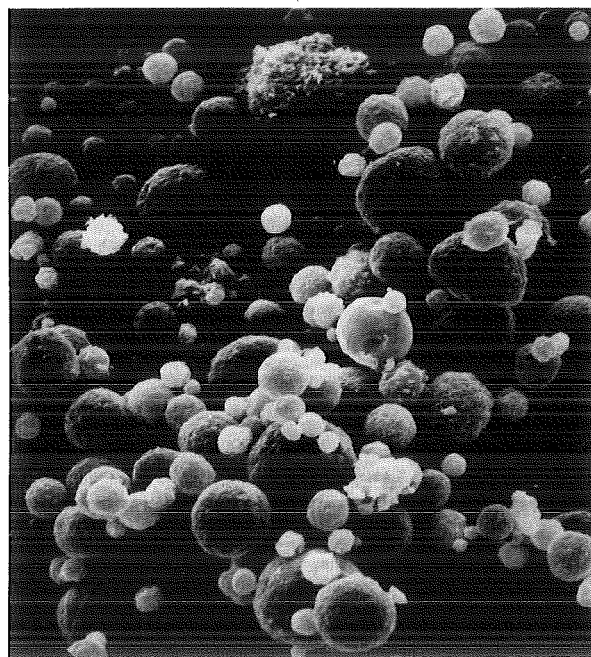Fig. 4.4.2.2: Spray-dried powder of Li_2ZrO_3 (organic phase)
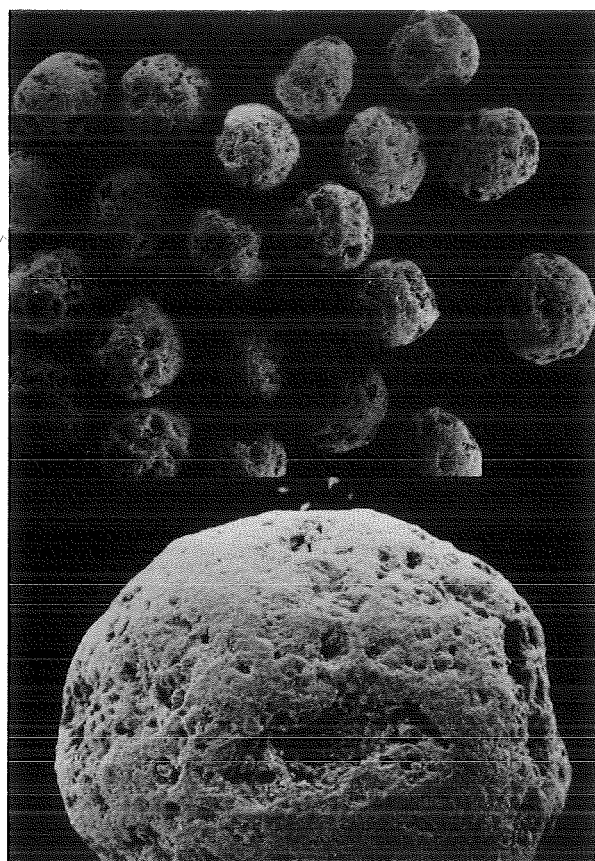

Fig. 4.4.2.3: Sintered pebbles of Li_2ZrO_3

4.4.2.2 Fabrication with the HITEC-method (G.Schumacher)

An examination of suitable production methods for lithium-metazirconate pebbles was conducted in co-operation with HITEC-Materials, Karlsruhe. It was agreed that melt spraying, like it is applied for lithium orthosilicate, could not be used, because of the high melting point of the material. It would require a crucible that could withstand lithium- metazirconate at temperatures above 1600°C. The following other methods were employed:

- flame spraying

- pelletizing and sintering

- flow-bed-spray-granulation and sintering

Flame spraying was abandoned after some tests, because this method was not able to produce pebbles of high density.

The last two methods that base on sintering after granulation require a sinterable powder. The as received powder with a grain size of about 60 µm was wet-milled in polyvenyl- alcohol. The powder slurry was spray- dried after milling. A powder of an average grain size of 4 µm was received after this procedure.

For the pelletizing process either a wax or polyvenyl-alcohol was added to the powder as a binder. With this material pebbles of a wide size range were received on a pelletizing mixer. It resulted after sintering and sieving that only 10% of the produced pebbles were within the desired 0.45 - 0.56 mm size range. Furthermore it was found that the majority of pebbles were fare off the spherical shape.

In preparation of the flow-bed-spray-granulation process the powder was dispersed in water containing wax that was provided by HOECHST, Augsburg, for this special application. The granulation process was conducted in the applications laboratory of ALPINE, Augsburg. This process can be controlled to provide pebbles within the desired diameter range. After the first step of optimisation 60% of the pebbles produced were within the range of 0.45 - 0.56 mm. After further optimisation the percentage can be increased to about 90%, which is common with the used apparatus. Sintering at 1200°C for 2 h resulted in a pebble density of 3.57 g/cm3. A rotating tube furnace was employed for sintering to prevent the pebbles form sticking together at 1200°C. Fig. 4.4.2.4 shows pebbles after sintering before sieving and separation of irregular shapes. The same pebbles after sieving and one run in a rotating tube separator are shown in Fig.

4.4.2.5. Fig. 4.4.2.6 illustrates how the grain structures of sintered pebbles look like. The grain size is within 10 - 40 μm. So far, the tests yielded that flow-bed-spray-granulation is a suitable method for producing pebbles.
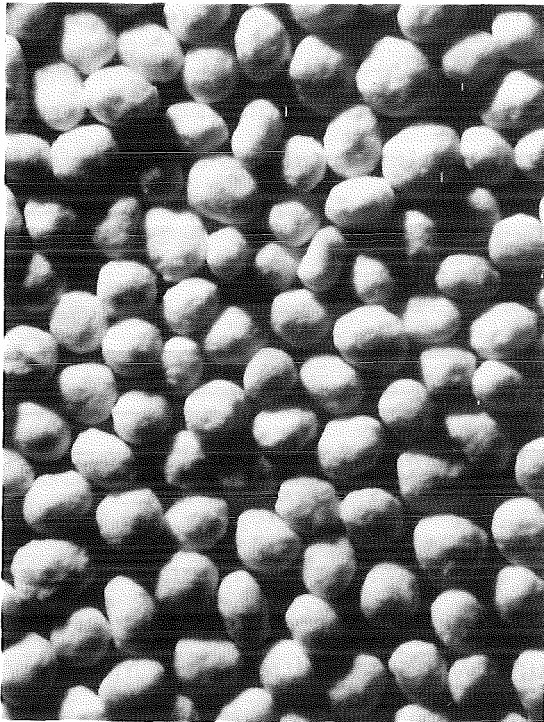

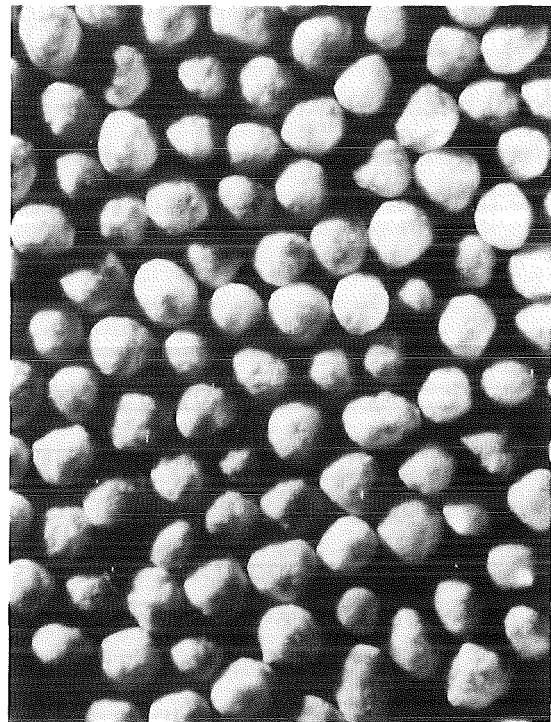Fig. 4.4.2.4: Pebbles as received after sintering

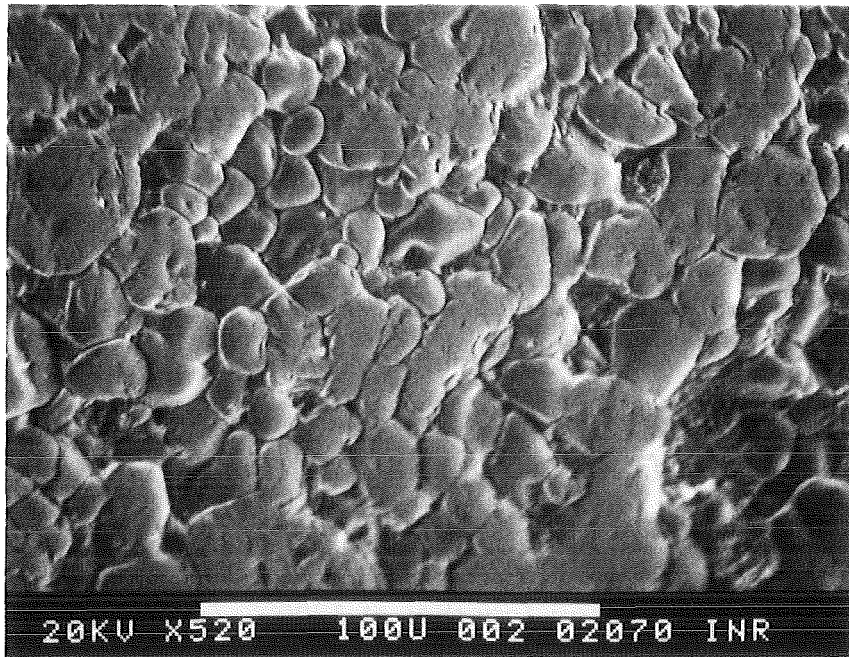Fig. 4.4.2.5: Pebbles of Fig. 4.4.2.4 after separation

Fig. 4.4.2.6: Grain structure of sintered pebbles

4.5 Technological Investigations

The design work for the Demo-blanket and for the test modules (s. Sections 2 and 3) has pointed out which are the main technological issues on which the R. and D. work has to be concentrated. Besides the development of the breeder material (Sections 4.2 and 4.3) other technological work is being performed at the Karlsruhe Nuclear Reactor Center (KfK). This section illustrates the technological work being performed at KfK. Four items appear to be very important as they may effect the blanket feasibility:

- effects of the periodic temperature variations on various blanket components,

- fist wall fabrication methods,

- development and testing of the brazing of the beryllium plates to the coolant tubes,

- measurements of the thermal conductivity of the bed of Li_4SiO_4 pebbles.

4.5.1 Thermal cycling tests: the HEBLO loop (H. Deckers, H. Reiser)

At the various stages of blanket development individual structural elements and original blanket assemblies have to undergo long term testing. Simulation of the loading due to the great number of thermal cycles during the service life of a fusion blanket is in the foreground of the investigations. To be able to perform such tests on small structural units a helium blanket test loop (HEBLO) is being erected at KfK. This loop will allow to perform two kind of experiments:

1) Thermal cycling tests involving parts which can be directly heated electrically. Typical examples include wall elements with brazed or welded cooling coils or channels. The thermal cycles can be generated in the test by variation of the heating power and/or the coolant flow through the coolant channels.

2) Tests on components or - preferably - on original blanket assemblies which cannot be directly heated electrically. The cyclic variation of the temperature in the test object and hence the thermal stresses must be generated here by quick variations of the cooling gas temperature.

The layout of the HEBLO loop is represented schematically in Fig 4.5.1. The loop consists of two parts:

The **main loop** accommodates as essential components the circulating compressor, the cooler, a filter, and a bypass line with control valve (H-V1) for adjusting the compressor output to a constant set value. A turbo compressor with gas bearing is used whose speed can be
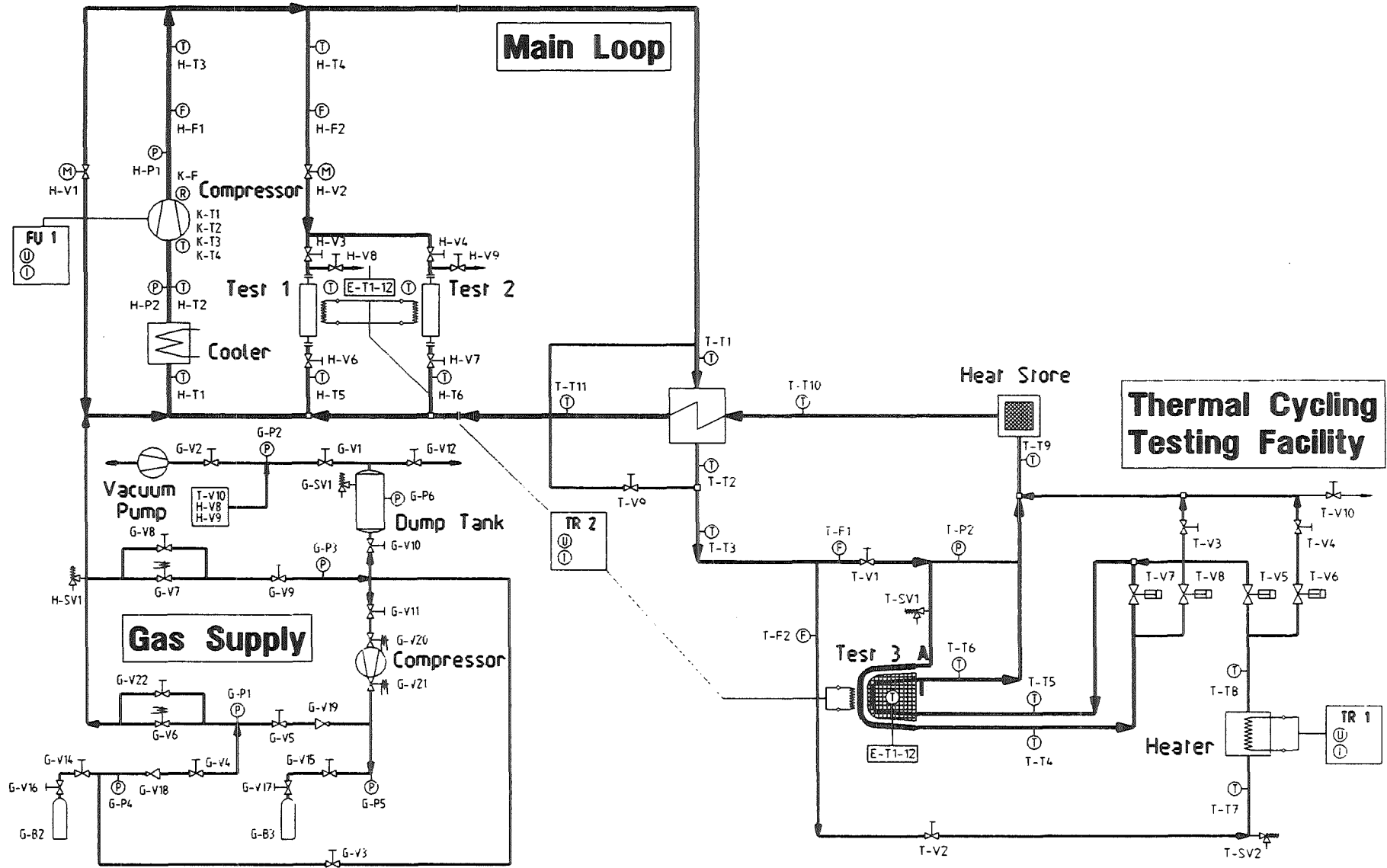
Fig. 4.5.1 Helium Blanket Loop.

continuously adapted to the conditions prevailing in the experiment by use of a transistor frequency transformer (FU-1).

The characteristic data of the helium system are:

- operating pressure   80 bar
- helium output of the compressor   100 m³/h, 0.33 kg/s
- pressure rise in the compressor   1.5 bar
- diameter of the pipework of the   65 mm
  main loop

In the main loop connections have been provided for two test sections where objects for testing can be operated which can be directly heated electrically (type 1 tests). The coolant flow can be controlled by means of a control valve (H-V2) installed in the common feed line. Heating of the objects to be tested is via a continuously controllable transformer (TR-2) of 30 kW maximum power.

Connected with the main circuit will be constructed a **testing facility** to be able to carry out **thermal cycling tests** on original blanket structures (type 2 tests). This facility will be designed such that an object can be tested which consists of a maximum of eight true size beryllium plates with cooling tubes and ceramic layers in-between. The object will be subjected to a maximum of 2×10^4 thermal cycles with temperatures ranging from about 280°C to 460°C. The stack of plates will be surrounded by an isothermally cooled canister. The ceramic pebble bed will be passed by a 1 bar purge gas flow.

The testing facility will be connected with the main loop via an intermediate heat exchanger where the cooling gas is brought to an elevated temperature level (approx. 260°C). The cooling gas volume is then divided into two streams, one of them flowing through the cooling tubes of the canister surrounding the beryllium plates. The canister can be electrically heated by means of the transformer TR-2. The other gas flow passes an electric heater (supplied by TR-1, maximum output 80 kW) and is heated there by 200 K at the maximum. The two branches subsequently join and end in the cooling coils of the beryllium plates.

To be able to generate the thermal cycles in the stack of plates the valves T-V7 and T-V5 are opened/shut in each cycle in such a way that the hot gas and the cold gas are alternately passed through the cooling coils of the beryllium plates. The respective other gas flow is returned directly to the intermediate heat exchanger by actuating the valves T-V8 and T-V6. To achieve special operating conditions it may become necessary also to vary the outputs of TR1 and/or TR2 in phase with the valves. Before they return to the intermediate heat exchanger, all gas flows pass a special temperature compensation line with a high heat capacity.

The HEBLO facility has been designed to operate permanently over extended periods of time because frequent disturbances of the regular cyclic mode of operation during shutdown and startup would exert an uncontrollable influence on the results. For this reason, a safety system has been provided which returns the facility into a safe condition in all conceivable accidents so that permanent direct supervision will not be necessary.

4.5.2   First wall fabrication methods (G. Reimann)

4.5.2.1 Walls with bored coolant channels

The plasma facing first wall of a fusion blanket is highly loaded thermally. It must be sufficiently cooled in order to avoid intolerably high thermal stresses. According to the reference concept for the helium-cooled solid blanket the coolant channels of the segment box with the first wall integrated will be fabricated by deep-hole boring followed by U-bending of the wall segments. Fig 4.5.2 shows a section of an outboard segment box with the first wall. The dimensions and contour of this wall were optimised by temperature and stress computations [1]. This implies for the fabrication that requirements must be met concerning the quality of the coolant channels in respect of the diameter of the borehole the distance from the outer edge of the wall and the pitch of the borings. It is one of the specifications for fabrication, e.g., that the thickness of the material between the coolant channels and the surface of the first wall does not exceed at any point by more than 0.5 mm the nominal value of 5.0 mm. With the dimensions of the demo blanket the maximum length of the coolant channels is 2.4 m. Discussions with manufacturers have revealed that, with this channel length, only boring from both sides will guarantee a sufficiently small eccentricity of the borings.

A specimen made of material 1.4404, roughly corresponding to AISI 316L, external dimensions 39.5 x 332 x 1200 mm, was ordered for use in first deep hole boring experiments. If borings in the desired quality are to be achieved, the specimen must be machined allround and care must be taken that the planar parallelity and angularity of the surfaces are maintained.

As the specimen had only half the length of the coolant channel the bores were drilled from one side. The borings were made on an NC controlled deep hole boring machine using the "boring and trepanning association technique". The boring tool is mounted on a borehole tubing. The lubricant for cooling is pressed through the annulus between the borehole tubing and the borehole wall. Besides cooling and lubrication of the cutter area, the lubricant ensures continuous removal of the shavings from the borehole through the interior of the borehole tubing.

He Cooling System 1   EB Welded   He Cooling System 2

850

Blanket
Canister

Li Ceramic Pebbles

Beryllium Plates

Cooling Tubes

Purge Gas Supply

Segment Box with First Wall

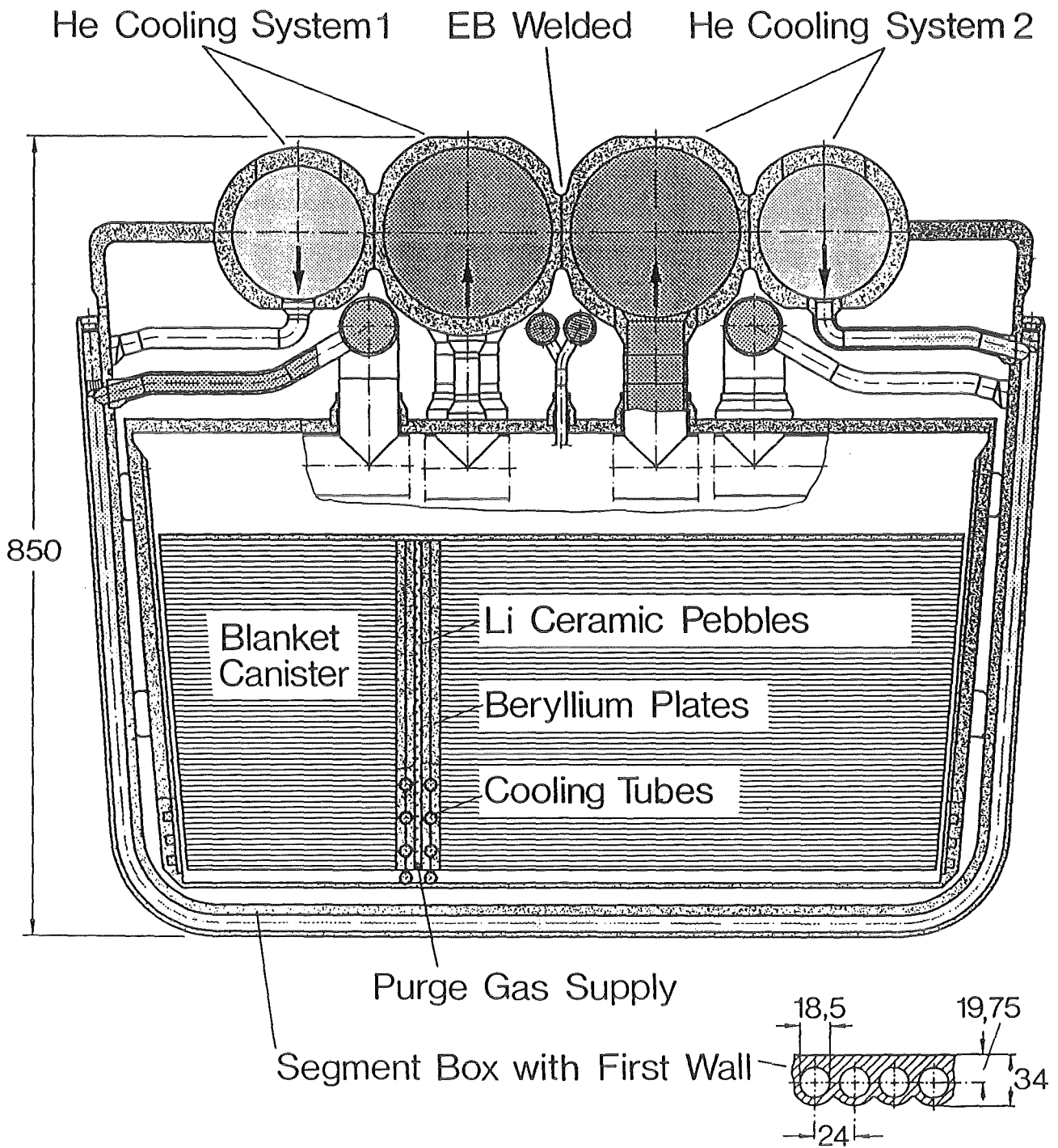18,5   19,75   34   24

Fig. 4.5.2   Radial-toroidal section of outboard blanket segment box.

A total of 12 bores, 18.5 mm in diameter, were drilled. The most favourable boring parameters were found in the first two borings and the machine was adjusted. A dimensional check of the completed specimen yielded that the quality of the other bores meets the specified requirements [2].

The outcome of this experiment is that deep hole boring offers a technique for fabrication of coolant channels of the first wall which, provided that specified measures are taken, allows the required tolerances to be met. It should be mentioned in addition that the technique is surprisingly favourable in terms of cost. The next reasonable step would be a deep hole boring test for the maximum coolant channel length of 2.4 m.

References

1.   P. NORAJITRA, unpublished, KfK, December 1989.

2.   K. MÜLLER, unpublished, KfK, September 1990.

4.5.2.2   Diffusion welded walls

An alternative to fabrication by deep hole boring of coolant channels of the first wall is considered to consist in milling grooves of any orientation into a plate and to surface weld this plate with a metal sheet covering it. The orientation of the channels can be adapted in an optimum manner to heat generation in the component.

Appropriate welding tests are being performed at MBB - now Deutsche Airbus - in Bremen with the objective of fabricating a diffusion welded component, 350 x 400 mm in size. The material selected is AISI 316L austenitic steel, i.e. the reference material for the first objects to be tested in the NET fusion machine.

In a series of 19 experiments in total, performed on small specimens of 40 mm diameter, the optimum welding parameters were determined. The parameters for diffusion welding are the surface condition of the parts to be bonded as well as the temperature, the pressure and the holding time during welding.

After they had been mechanically treated by planing or milling the specimen surfaces were subjected to an additional chemical treatment consisting in degreasing in an ultrasonic bath, pickling or nickel plating. Some specimens were left untreated. The welding tests in a high vacuum facility proceeded as follows: After evacuation the specimen area was induction heated to 950 °C to 1100 °C welding temperature and the interior of the facility was filled with argon. Then the specimens were loaded with a diffusion welding pressure of 6 N/mm^2 to 20 N/mm^2, holding time 4 to 72 hours. High pressures and temperatures reduce the holding time but, on the other hand, they may give rise to undesired changes in the material structure and to inadmissible deformations of the parts to be welded. The best results of welding were achieved for specimens with milled and pickled surfaces and the welding parameters of 950 °C temperature, 72 hours holding time and 6 N/mm^2 diffusion welding pressure. Upsetting of the specimens, overall thickness about 28 mm, amounted to $\leq$ 0.5 mm. Examinations performed after treatment of the specimens - i.e. examinations of the strength, metallographic examinations - have shown that diffusion welding causes volume diffusion accompanied by the intimate bonding of the parts whose strength is similar to that of the base material. Welding tests on the non-treated specimens yielded uneconomically long welding times and an excessive deformation of the material.

In the next step four pairs of plates, 240 mm in diameter, were diffusion welded in the same facility. The thicker plate was provided with grooved coolant channels, 10 x 10 mm in size, and testing channels having the same dimensions (Figure 4.5.3). The webs between the coolant and the testing channels differed in width; the minimum width was 5 mm. The first pair of plates were welded using the welding parameters determined from the small speci-

mens. However, it appeared that at the same welding pressure the welding temperature and time had to be increased to 1100 °C and 125 hours, respectively, in order to obtain a similarly good quality of the weld. The manufacturer gives as the reason that the surfaces to be bonded have become larger.

Post-test investigations including tightness tests have demonstrated that the bonding is good also around the narrow webs. The micrograph in Figure 4.5.4 shows a sector of the welded zone of a pair of plates with the grains growing beyond the welding plane. A grain which might be too coarse can be made finer by solution annealing of the machined part.

It is planned to diffusion weld the large prototype plates of 350 x 400 mm on an isostatic hot press in spring 1991. The welding parameters determined in the high vacuum facility can be transferred to that press. The isostatic hot press offers the possibility of welding plates up to 1.8 m x 1.2 m in size, with several plates piled up.

It is envisaged to subject the components to long-term thermal cycling tests in the HEBLO loop at a later date.
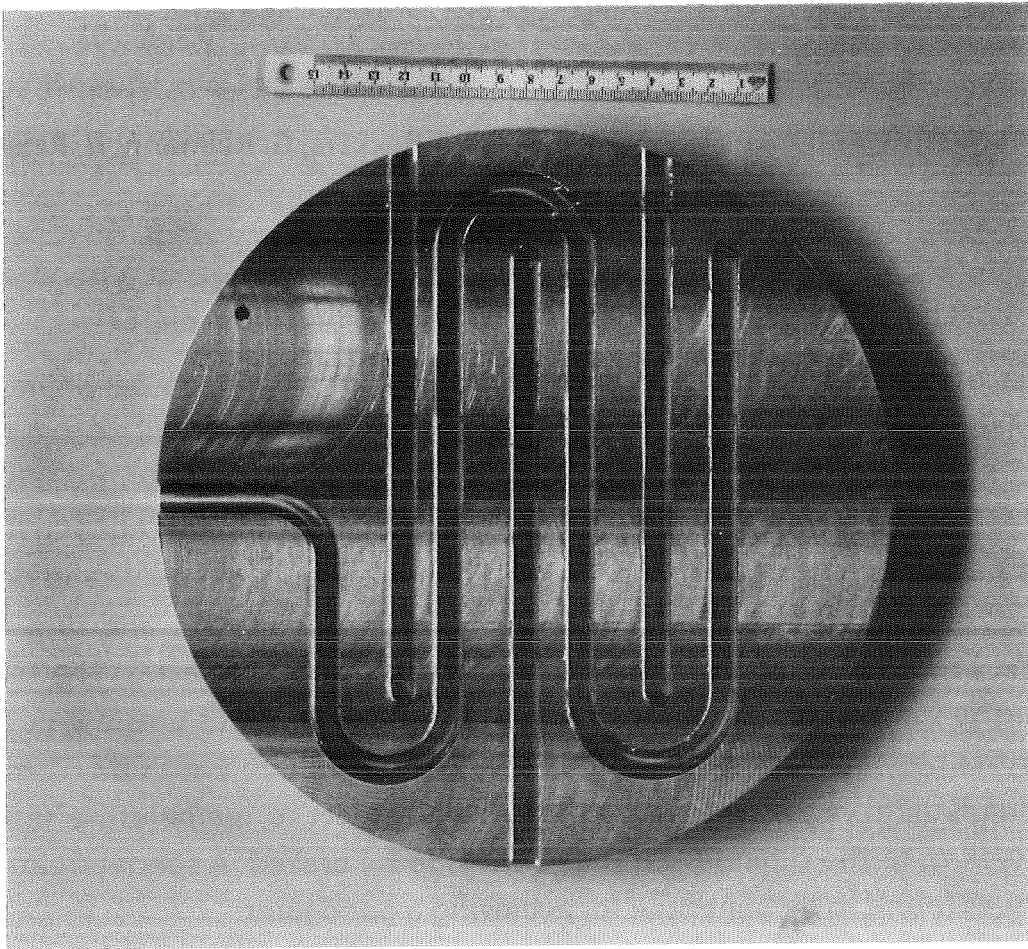
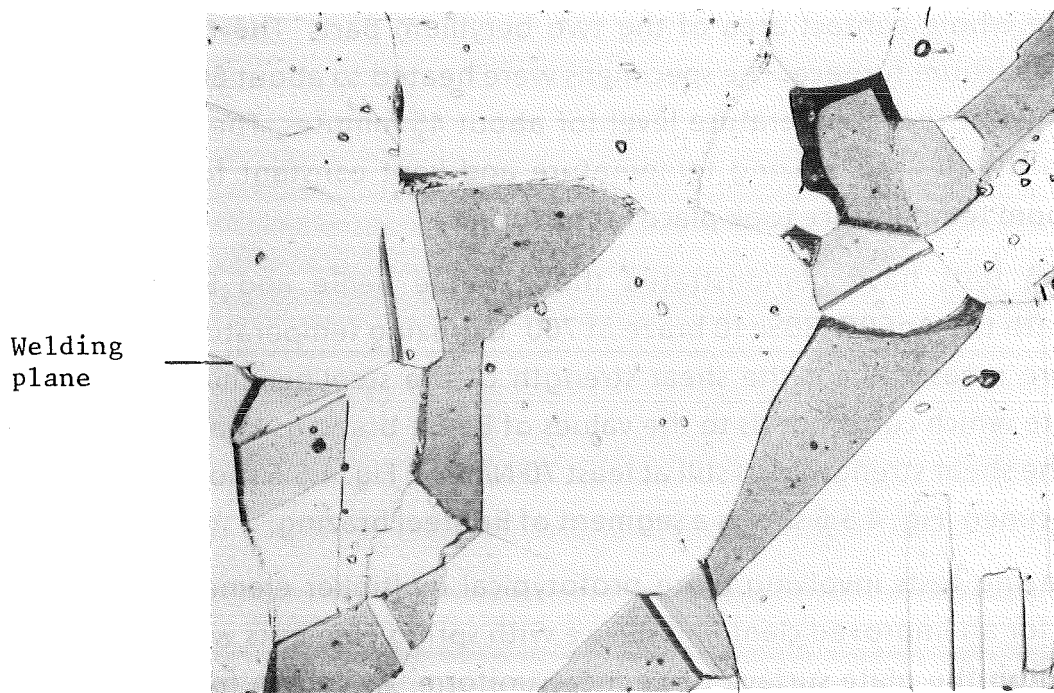Fig. 4.5.3 Plate with coolant and testing channels.

Welding
plane

Fig. 4.5.4 Welded zone in scale 200 : 1.

4.5.3 Beryllium-structural material brazing tests (H. Deckers, G. Reimann, H. Reiser)

Of special interest for the present blanket design is the realisation of a good and reliable thermal contact between the steel cooling tubes and the beryllium plates.

A first series of tests on the development of brazed joints between beryllium plates and 316L and Manet cooling pipes has already been completed at the W.C. Heraeus company, Hanau. In a first series of wetting tests a wide spectrum of silver brazes have been tested. The alloys selected have been Ag95Al5, Ag72Cu28, Ag66Cu29Sn5, and Ag60Cu30Sn10, both as foils and pastes. After completion of these preliminary tests the only candidates left for further investigations have been the ternary AgCuSn-brazes with 5 % and 10 % tin content. The foil type braze material proved to be superior to the braze pastes. The test also confirmed that the brazing temperature must be lowered as much as possible in order to reduce the brittle beryllide layers occurring at the braze-beryllium transition. This means that correspondingly high requirements are made with respect to temperature setting during brazing as well as to the cleanness of the surfaces to be brazed. A special treatment of the steel tubes was found to be beneficial for achieving a good joint.

With the two selected brazes tests were performed in which coolant tubes made of steel 316L were brazed to two beryllium segments, 100 x 40 x 10 mm in size each. The beryllium plates had been provided with semi-circular groves for accomodation of the tube and the brazing foils. Two 0.2 mm thick brazing foils each surrounded as semicircles the tube and covered the whole contact area of the two beryllium parts. The brazing tests were performed in a vacuum furnace. The specimens were heated to about 600 °C within 30 minutes and remained at that temperature level for about 45 minutes. Then the temperature was brought to the desired brazing temperature and kept constant for 30 minutes. Cooling down to room temperature took place in the furnace.

The brazing tests have demonstrated that reliable Be/Be and Be/steel brazes can be achieved with the Ag60Cu30Sn10 braze at 700 °C brazing temperature. Values of about 200 N/mm^2 were measured for the shear strength of the steel/beryllium compound at room temperature which corresponds to the values of Be/Be-brazings known from the literature. At 500 °C the shear strength was still at least 70 N/mm^2. Fig. 4.5.5 shows the micrograph of a brazed specimen. Fig. 4.5.6 shows a segment of Be/steel brazing.

Further brazing tests involving more prototypical multiplier elements are planned. They would call for an improved clamping device with spring elements which cause the pressure distribution on the plate surface to be more uniform. As known from Be/Be brazings, the shear strength might be capable of an increase to about 250 N/mm^2 by lowering the brazing temperature to less than 700 °C.
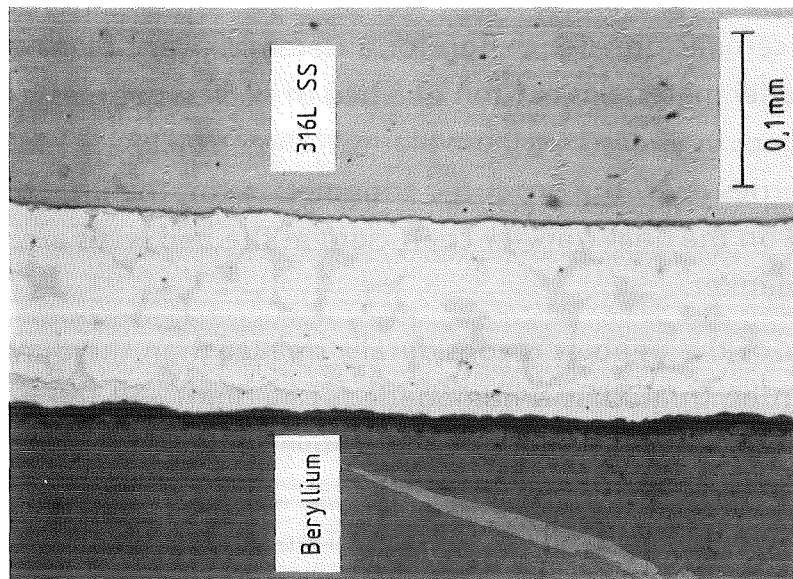
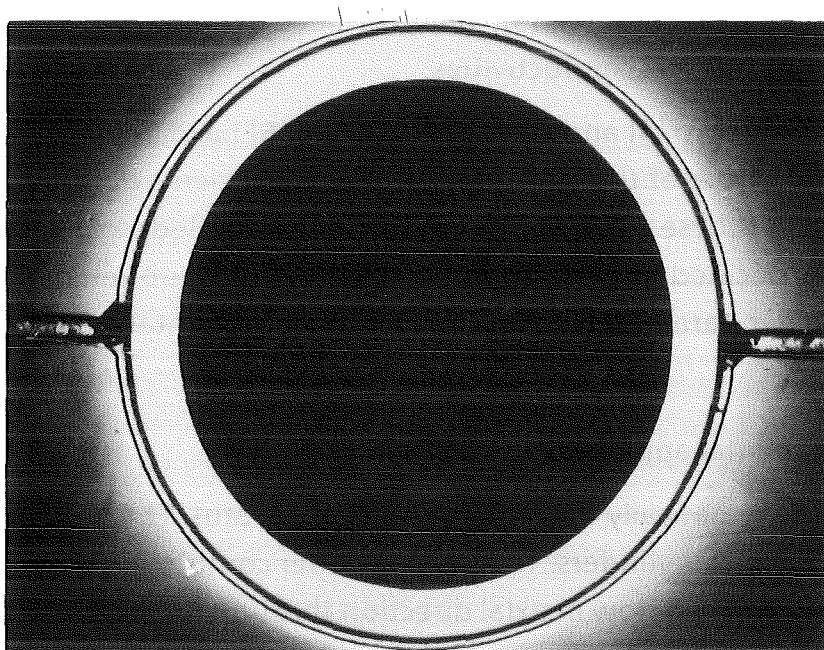Fig. 4.5.5 Micrograph of the brazing between beryllium and 316L stainless steel.

Fig. 4.5.6 Brazing of a 316L stainless steel tube to the two beryllium plates. The picture shows the beryllium / beryllium brazing as well.

4.5.4 Measurements of the effective thermal conductivity of the pebble bed
(M. Dalle Donne, G. Sordon)

The Karlsruhe ceramic breeder design for a Demo-relevant blanket is based on a concept where the breeder material is in form of a bed of Li_4SiO_4 pebbles. The pebble bed is placed in 6 mm wide gaps between beryllium plates. Helium at 0.08 - 0.1 MPa flows slowly through the bed and carries away the produced tritium. Data on the effective thermal conductivity of the bed and on the heat transfer coefficient at the bed walls are required for the proper design of the blanket.

If the diameter of the pebbles is considerally smaller than the dimensions of the bed, the pebble bed can be treated as a homogeneous medium and the heat transfer parameters can be reduced to two coefficients: the effective thermal conductivity of the bed and the heat transfer coefficient at the walls of the bed container. Various correlations for the two coefficients are available from the literature. Two models for the effective thermal conductivity have been considered in the frame of the present work, as they seem most relevant to the kind of bed we are proposing:

1. the model of Schlünder, Zehner and Bauer [1, 2] valid for beds of pebbles of any shape and size distribution, but with the same thermal conductivity of the solid, and

2. the model of Okazaki et al. [3], valid for beds of spherical pebbles with the same or two different thermal conductivities.

The models of Hennecke [4] and of Yagi and Kunii [5] have been used for comparison with the experimental values of the wall heat transfer coefficients obtained in the present investigation. The use of these correlations requires the knowledge of certain empirical parameters, thus it was decided to perform some experiments to obtain more precise information on the heat transfer parameters for the beds of particular interest for the present design.

4.5.4.1   Experimental apparatus

Fig. 4.5.7 shows schematically the experimental apparatus. The pebble bed is contained between two concentrical cylinders. The inner cylinder contains an electrically heated rod. The gas (helium or argon) can flow in axial direction through the bed.

The radial distribution of the temperature in the bed is measured in two axial positions in the central part of the test section, where the axial temperature gradients are negligible in comparison to the radial ones, by means of two banks of 32 thermecouples each, placed at various radii at four different azimuthal angles (Fig. 4.5.8). Furthermore the temperatures on the inner and outer cylinder surfaces are measured by thermocouples placed into the

walls. The temperature level of the bed has been varied by cooling the outer test section surface (Fig. 4.5.9) or by surrounding it by a thermal insulation of variable thickness.

The measurements were performed with flowing or stagnant helium or argon. The investigated beds were made of aluminum oxide (1, 2, 4 mm in diameter), of aluminum (2 mm diameter), steel (2 and 4 mm diameter) and lithium orthosilicate (0.5 mm diameter) pebbles. Binary mixtures of aluminum oxide pebbles of different diameters or of aluminum oxide either with aluminum or with steel pebbles were also investigated [6].

4.5.4.2 Experimental results

The results of all experiments are given in Ref. [6], here we will limit ourselves to show only those directly relevant to our blanket designs. Fig. 4.5.10 shows a typical radial temperature distribution in the bed of 0.5 mm Li_4SiO_4 pebbles in presence of stagnant helium, for a given axial position along the test section. Also shown are the measured temperatures at the inner cylinder surface ($R = R_1$) and at the outer cylinder surface ($R = R_2$). With a constant radial heat flux and bed thermal conductivity and with stagnant helium, the theory predicts a straight line in a semilogarithmic diagram temperature versus log R/R_2. Fig. 4.5.10 shows that the experimental points are correlated quite well by a straight line in such a diagram. This was always the case for all the tests with stagnant gas performed during this experiment [6]. The slope of the temperature curve allows to calculate the effective thermal conductivity of the bed. The difference between the measured temperature on the inner cylinder wall and the extrapolated temperature from the bed to the wall (Fig. 4.5.10) allows to calculate the heat transfer coefficient at the walls. This temperature difference is always smaller at the outer cylinder surface, so that the obtained heat transfer coefficients for the outer cylinder scattered considerally more than those for the inner cylinder and were not used for the correlation [6].

Fig. 4.5.11 shows the measured effective thermal conductivity of the bed formed of 0.5 mm Li_4SiO_4 pebbles in stagnant helium. At 400 °C the thermal conductivity is about 0.91 W/mK. The agreement with the predictions of Schlünder, Zehner and Bauer [1, 2] and Okazaki et al. [3] is reasonable.

Table 4.5.1 shows the measured heat transfer coefficients at the wall of the inner cylinder. In the case of direct contact between pebble bed and wall the heat transfer coefficient is about 0.45 W/cm2K. Experiments were also performed with a thin (0.1 mm) stainless steel wire gauze placed between the cylinder wall and the bed, because this was the solution adopted for the KfK blanket design for NET. In this case the scatter of the experimental data is larger. The value 0.1 W/cm2K is recommended.

Fig. 4.5.12 shows the thermal conductivity of mixtures of 0.5 mm beryllium and Li_4SiO_4 pebbles in stagnant helium for a bed porosity of 38 % and a temperature of 400 °C as a function of the beryllium volume fraction. These data have been calculated on the base of the experiments performed with beds made of mixtures of aluminum (as a simulation for the beryllium) and of aluminum oxide (for the Li_4SiO_4) pebbles and of a correlation for mixed beds suggested in Ref. [6]. For a mixed bed of beryllium and Li_4SiO_4 pebbles with a beryllium pebble fraction of 80 % (optimum from a neutronic point of view) the thermal conductivity increases to 3 W/mK.

Recently effective thermal conductivity measurements have been carried out for a bed of Li_4SiO_4 pebbles with diameters in the range 0.35 - 0.6 mm, which is the reference pebble bed for the Demo blanket design (see Chapter 2.1) [7]. The measured effective thermal conductivity data differ little from those of the bed with 0.5 mm Li_4SiO_4 pebbles.

References

1. P. ZEHNER, E.U. SCHLÜNDER, Wärmeleitfähigket von Schüttungen bei mäßigen Temperaturen, Chemie.-Ing.-Techn. 42, 14 (1970) 933.

2. R. BAUER, E.U. SCHLÜNDER, Effective radial thermal conductivity of packings in gas flow, Int. Chem. Eng. 18, 2 (1978) 181.

3. M. OKAZAKI, T. YAMASAKI, S. GOTOH and R. TOEI, Effective thermal conductivity for granular beds of various binary mixtures, J. Chem. Eng. Japan, 14, 3 (1981) 183.

4. F.W. HENNECKE, Über den Wandwiederstand beim Wärmetransport in Schüttungsrohren, Ph-D Thesis, University of Karlsruhe, Karlsruhe, Germany.

5. S. YAGI and D. KUNIL, Studies on heat transfer near wall surface in packed beds, A.I.Ch.E. Journal, 6, 1 (1960) 97.

6. G. SORDON, Über den Wärmetransport in Kugelschüttungen, Kernforschungszentrum Karlsruhe, report KfK-44 51, EUR 11391 DE (1988).

7. M. DALLE DONNE, A. GORAEIB, G. SORDON, Measurements of the effective thermal conductivity of a bed of Li_4SiO_4 pebbles of 0.35 - 0.6 mm diameter and of a mixed bed of Li_4SiO_4 and aluminum pebbles, to be published.

Table 4.5.1   Wall heat transfer coefficient (W/cm2K) for a bed of 0.5 mm Li$_4$SiO$_4$ pebbles and stagnant helium

Experiment	Li$_1$	Li$_2$	Li$_3$	Li$_4$	Li$_5$	Li$_6$	Li$_7$
with direct contact between pebbles and wall	0.53	0.42					
with the steel wire gauze at the wall			0.19	0.097	0.084	0.11	0.086

ELECTRIC SUPPLY

net
~

transformer

TEST SECTION

thermocouples

thermal insulator /
cooling tubes

heating rod

packed bed

gas outlet

GAS SUPPLY

T

gas

gasmeter

P

thermocouple wires

mV

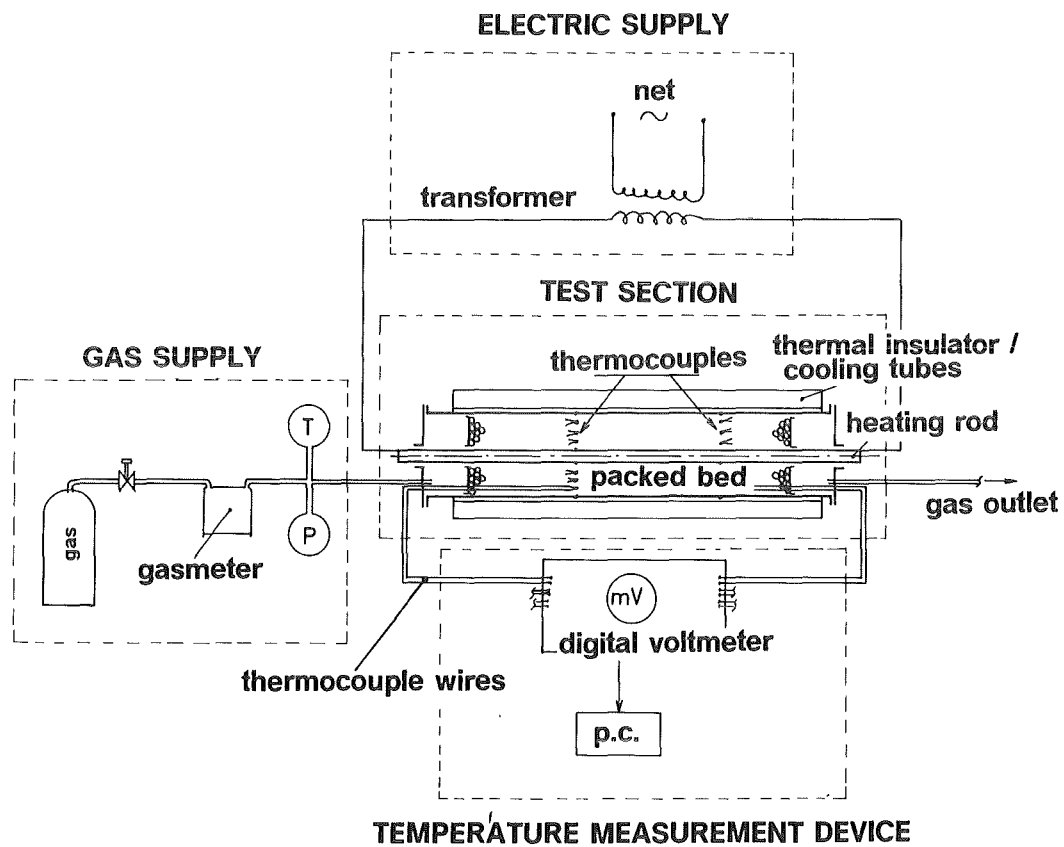digital voltmeter

p.c.

TEMPERATURE MEASUREMENT DEVICE

Fig. 4.5.7 Schematic representation of the experimental apparatus for the measurements of
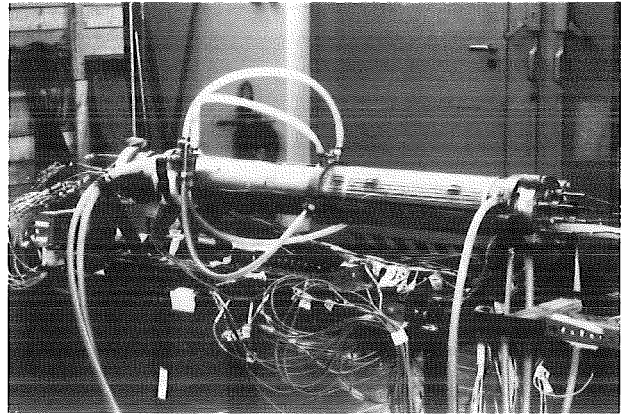the pebble bed effective thermal conductivity.
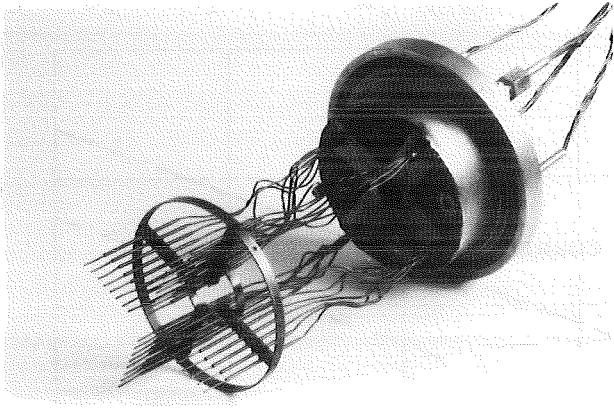
Fig. 4.5.8 View of a bank of 32 thermocouples for the measurement of the bed radial temperature distribution at an axial position of the test section.

Fig. 4.5.9 Outside view of test section showing the water cooling tubes of the outer cylinder.

EXP. N. LI.7
$R_1 = 0.8$ cm
$R_2 = 5.1$ cm
Li_4SiO_4 / He
$d_p = 0.5$ mm
$G = 0$ g/cm²s
z/DI = 1.9
RMS = 4.2 K

$k_e = 0.904$ W/m K

$\alpha_1 = 861 W/m^2 K$

Fig. 4.5.10   Radial temperature distribution in the bed.

— 221 —

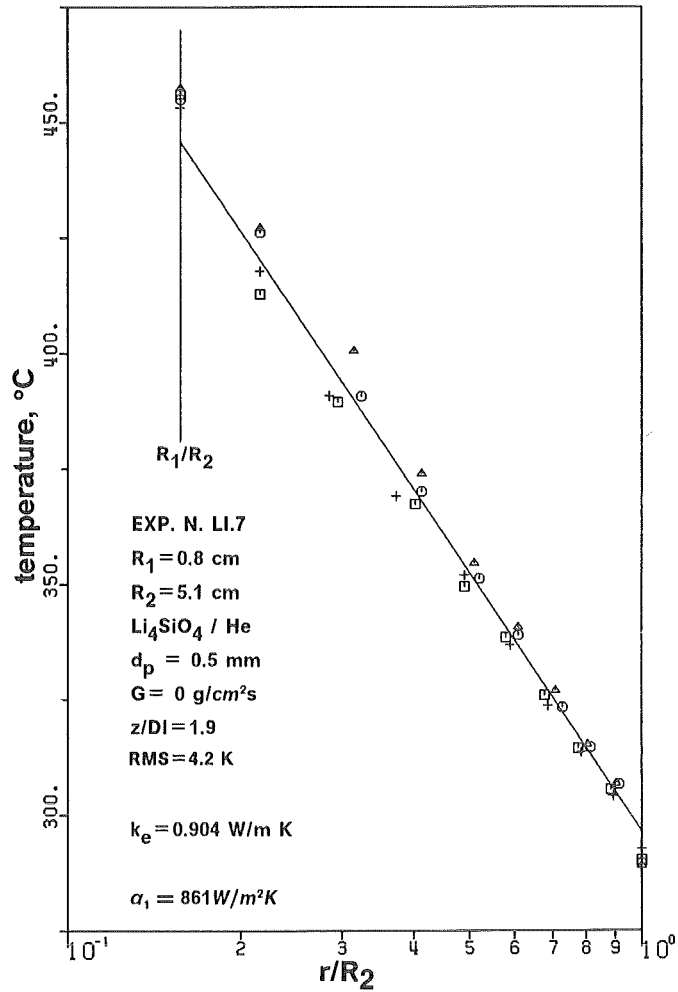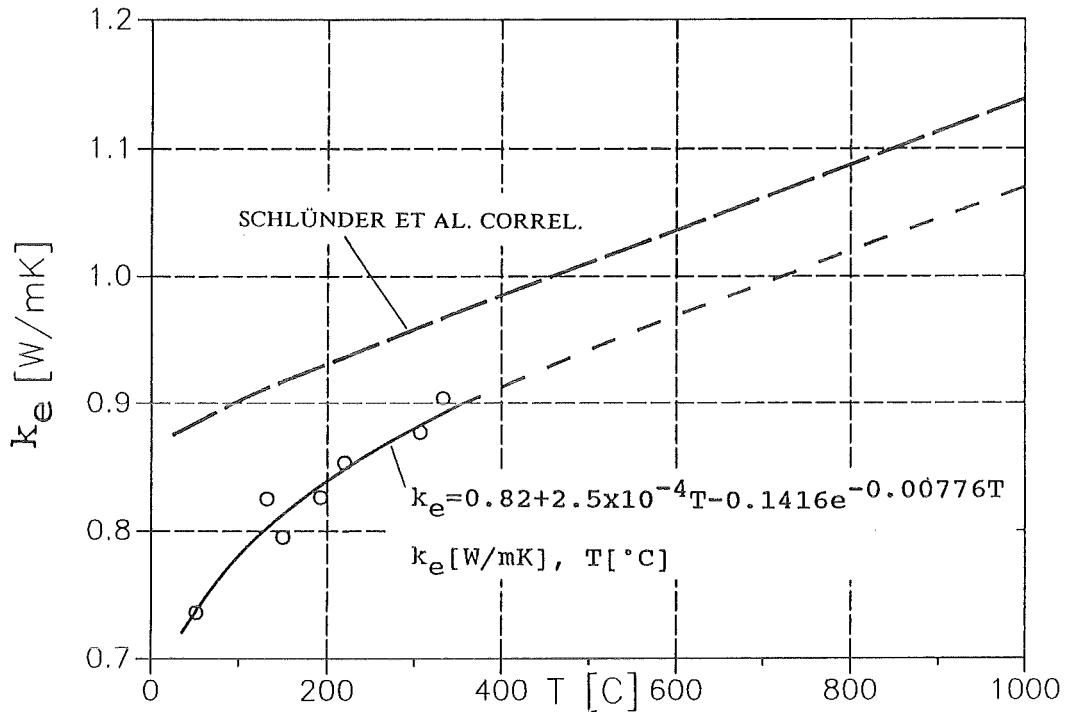Fig. 4.5.11   Effective thermal conductivity of the bed of 0.5 mm Li₄SiO₄ pebbles and stagnant helium.

In the graph:

SCHLÜNDER ET AL. CORREL.

$$k_e = 0.82 + 2.5 \times 10^{-4}T - 0.1416e^{-0.00776T}$$

$$k_e [W/mK], \quad T[°C]$$

Be + Li₄SiO₄ / He

$d_p = 0.5$ mm

$\psi = 0.38, \quad T = 400$ °C
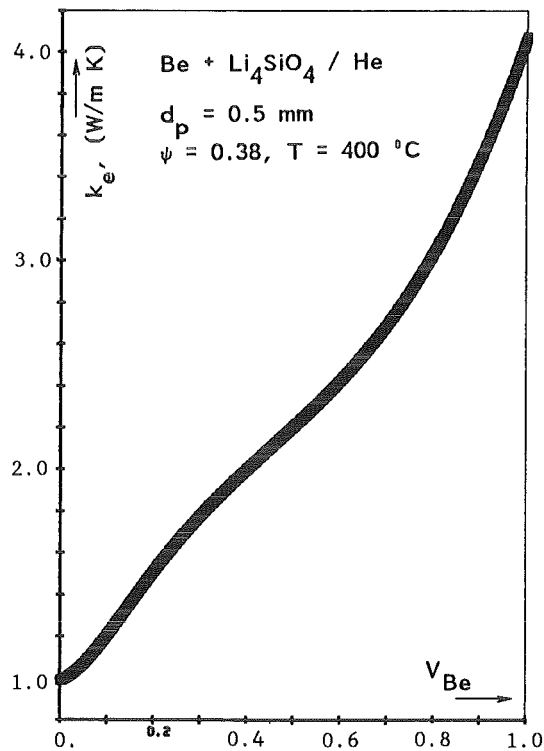
Fig. 4.5.12   Effective thermal conductivity of a mixture of 0.5 mm beryllium and Li₄SiO₄ pebbles in stagnant helium as function of beryllium volume fraction.

4.6 Irradiations and Tritium Release of Breeder Ceramics

4.6.1 Irradiations (H.E. Häfner)

Within the framework of breeder ceramic development KfK, in cooperation with EC partners, has initiated and performed since 1983 quite a number of irradiation experiments. Table 4.6.1 is a survey of the general programme and the goals pursued with the individual experiments. Furthermore KfK is participating in the joint European irradiation programme (EXOTIC, ALICE, SIBELIUS).

Table 4.6.1   Irradiation experiments and goals

Name of Experiment	Reactor	$LiAlO_2$	Li_2SiO_3	Li_4SiO_4	Li_6SiO_6	Li_2ZrO3	Li_2O	Experimental Goal *)	Status **)
MERLIN	FRJ 1/Jülich		X	X	X			A	compl.
DELICE 01/02	OSIRIS/Saclay		X	X				A, B	compl.
LISA 1/2	SILOE/Grenoble	X	X	X				A, C	compl.
LILA/LISA 3	SILOE/Grenoble	X		X		X		A, C	compl.
TRIDEX 1-6	FRJ 2/Jülich		X	X	X			A, C	compl.
ELIMA 1	KNKII/Karlsruhe		X	X				A, B	in pile
ELIMA 3	KNKII/Karlsruhe			X				A, B	rfi
COMPLIMENT									
DELICE 03	OSIRIS/Saclay	X	X	X		X	X	A,B,D	PIE
ELIMA 2	HFR/Petten	X	X	X		X	X	A,B,D	PIE

*)   Experimental goals
     A) Evaluate the mechanical and chemical integrity of the ceramic material
     B) Evaluate the tritium retention and release properties after irradiation
     C) Evaluate the tritium retention and release properties during irradiation
     D) Investigate if there is a different impact of neutron-dpas or t + a-dpas to the relevant properties

**)   Status
     compl.: irradiation and PIE completed   rfi: ready for irradiation
     in pile: under irradiation   PIE: post irradiation examination started

At a first stage of the irradiation programme tentative shortterm irradiations were performed in simple rabbits installed in the FRJ-1 reactor (MERLIN) in Jülich. At the same time, irradiation experiments to be performed in the reactors OSIRIS, Saclay, and SILOE, Grenoble, were specified in an agreement of cooperation concluded with CEA, France. The main goals of the OSIRIS irradiations **DELICE 01 and 02** were to study irradiation effects on dimensional, structural and property changes and the tritium release behaviour to be investigated in post-irradiation examinations. Another KfK test series of in-situ tritium release from lithium ceramics, LISA, is performed at the SILOE reactor.

For the experiments DELICE in OSIRIS a so-called COLIBRI capsule has been modified (fig. 4.6.1). This is a double-walled capsule type test rig accommodating several specimen rods in six and four channels respectively, of a matrix in an inner capsule tube. The irradiation temperatures are adjusted via gas gaps and controlled by means of a gas mixture provided in the controlling gap between the inner and outer containments. The main data of the DELICE 01 and 02 experiments are given in table 4.6.2.

Table 4.6.2   **Design and operating data of the irradiation experiments DELICE 01 and 02 performed in the OSIRIS reactor/Saclay**

		DELICE 01	DELICE 02	
Material		Li_2SiO_3	Li_2SiO_3	Li_4SiO_4
Density	[% T.D.]	65/85	65/90	65/90
Pellet diameter	[mm]	4.94	4.94	4.94
Sample stack height	[mm]	45	45	45
State of pellets		dry/wet	dry	dry
Number of sample stacks		45	8	12
Edge temperature	[°C]	500/700	440/700	440/700
T production rate	[$10^{13}cm^{-3}s^{-1}$]	0.8-7.7	2.1-8.1	2.1-11.3
Heat generation	[W/cm^3]	6-59	16-62	16-87
Linear rod power	[W/cm]	1.2-11.3	3.1-11.9	3.1-16.7
Irradiation time	[d]	26 (1985)	26 (1986)	26 (1986)

For the **LISA experiments** with continuous measurement of tritium release the socalled CHOUCA rig has been modified in Grenoble. This test rig contains six sample stacks, three each at two levels, which can operate at different temperatures (fig. 4.6.2). The specimen temperatures can range from 400 to 700 °C. The actual values can be adjusted by a gas gap and controlled by electrical heating. Following the LISA 1 and 2 experiments for which KfK

had been responsible, LILA/LISA 3 was carried out as a joint experiment in cooperation with the CEA.

Also in Jülich an irradiation rig has been developed for the continous in-pile measurement of the tritium released from breeder ceramic specimens; it will be installed in the FRJ-2 reactor (DIDO). This rig can be used by KfK too. Figure 4.6.3 is a schematic layout of the Jülich "Tritium Recovery Irradiation DIDO experiment" **TRIDEX**. Each test module accomodates three separately heatable and sweepable specimen capsules with three specimen columns each of approx. 8.5 mm diameter and 50 mm height.

In the **COMPLIMENT** irradiation experiment different ceramic blanket candidate materials were irradiated in parallel in the HFR reactor in Petten/Netherlands and in the OSIRIS reactor in Saclay. The objectives of these irradiations are (1) to compare the radiation damage caused in a single lithium ceramic compound by fast neutron scattering with the damage caused by the α- and T-particles from the $^6Li(n,\alpha)$T-reaction, and (2) to compare the radiation damage and the irradiation behaviour of various lithium ceramics in an identical test environment.

The two test groups of COMPLIMENT, named

DELICE 03 in OSIRIS / Saclay and **ELIMA 2** in HFR / Petten

comprise 72 sample rods supplied by the five partners

- CEA, Saclay / France $\quad\quad\quad$ ($LiAlO_2$)

- ENEA, Casaccia / Italy $\quad\quad$ ($LiAlO_2$)

- UKAEA, Springfields / UK $\quad$ (Li_2O, Li_2ZrO_3)

- CEN, Mol / Belgium $\quad\quad\quad$ (Li_2SiO_3, Li_2ZrO_3)

- KfK, Karlsruhe / Germany $\quad$ (Li_2SiO_3, Li_4SiO_4)

The experiment relating to 72 samples in total contains 4 matrices with 18 samples. The matrices are devoted to different best conditions in temperature and neutron flux. The whole test scheme according to these definitions is demonstrated in table 4.6.3 where every single sample is identified.

All the ceramic materials differing in type and origin and having the form of pellets or small spheres are enclosed in rods of identical design, 6 mm in outside diameter and 100 mm in total length. All the sample rods were clad at KfK under uniform conditions. As demonstrated, in fig. 4.6.4, the breeder material fills about half of the rod length while the remaining volume constitutes a gas plenum. The cladding tube and end caps are made of 1.4970 grade stainless steel.

Table 4.6.3 Test scheme and identification of sample rods COMPLIMENT in the comparative experiment

	ELIMA 2 / HFR-Petten		DELICE 03 / OSIRIS-Saclay		Sum of samples
	Matrix I 400 - 450 °C	Matrix II 650 - 700 °C	Matrix III 400 - 450 °C	Matrix IV 650 - 700 °C	
CEA, Saclay	$LiAlO_2$ 78 %*) P 139**) $LiAlO_2$ 78 % P 140 $LiAlO_2$ 62 % P 141 $LiAlO_2$ 84 % P 142	$LiAlO_2$ 78 % P 143 $LiAlO_2$ 78 % P 144 $LiAlO_2$ 62 % P 145 $LiAlO_2$ 84 % P 146	$LiAlO_2$ 78 % P 147 $LiAlO_2$ 78 % P 148 $LiAlO_2$ 62 % P 149 $LiAlO_2$ 84 % P 150	$LiAlO_2$ 78 % P 151 $LiAlO_2$ 78 % P 152 $LiAlO_2$ 62 % P 153 $LiAlO_2$ 84 % P 154	16
ENEA, Casaccia	$LiAlO_2$ 80 % P 117 $LiAlO_2$ 80 % P 118 $LiAlO_2$ 80 % P 119	$LiAlO_2$ 80 % P 120 $LiAlO_2$ 80 % P 121 $LiAlO_2$ 80 % P 122	$LiAlO_2$ 80 % P 155 $LiAlO_2$ 80 % P 156 $LiAlO_2$ 80 % P 157	$LiAlO_2$ 80 % P 158 $LiAlO_2$ 80 % P 159 $LiAlO_2$ 80 % P 160	12
UKAEA, Springfield	Li_2O 83 % P 131 Li_2O 79 % P 132 Li_2ZrO_3 80 % P 123 Li_2ZrO_3 80 % P 124	Li_2O 80 % P 133 Li_2O 82 % P 134 Li_2ZrO_3 80 % P 125 Li_2ZrO_3 80 % P 126	Li_2O 79 % P 135 Li_2O 81 % P 136 Li_2ZrO_3 80 % P 127 Li_2ZrO_3 80 % P 128	Li_2O 82 % P 137 Li_2O 82 % P 138 Li_2ZrO_3 80 % P 129 Li_2ZrO_3 80 % P 130	8 8
CEN, Mol	Li_2SiO_3 82 % P 161 Li_2SiO_3 82% P 163 Li_2SiO_3 75% P 165	Li_2SiO_3 82 % P 162 Li_2SiO_3 75% P 166 Li_2ZrO_3 80% P 164	Li_2SiO_3 82 % P 167 Li_2SiO_3 82% P 169 Li_2SiO_3 75% P 171	Li_2SiO_3 82 % P 168 Li_2SiO_3 75% P 172 Li_2ZrO_3 80% P 170	10 2
KfK, Karlsruhe	Li_4SiO_4 98 % MS 173 Li_4SiO_4 85 % SS 113 Li_4SiO_4 90 % P 109 Li_2SiO_3 90 % P 101	Li_4SiO_4 98 % MS 174 Li_4SiO_4 85 % SS 114 Li_4SiO_4 90 % P 110 Li_2SiO_3 90 % P 102	Li_4SiO_4 98 % MS 175 Li_4SiO_4 85 % SS 115 Li_4SiO_4 90 % P 111 Li_2SiO_3 90 % P 103	Li_4SiO_4 98 % MS 176 Li_4SiO_4 85 % SS 116 Li_4SiO_4 90 % P 112 Li_2SiO_3 90 % P 104	4 4 4 4
Sum	18	18	18	18	72

*) % Theoretical Density
**) KfK Rod Number

P = Sintered Pellets
MS = Molten Spheres
SS = Sintered Spheres

This means that the same groups of specimens containing 36 specimens each were irradiated in DELICE 03 and ELIMA 2. A DELICE capsule which has already been briefly described was used for irradiation in the thermal neutron flux of the OSIRIS reactor. The test rig for irradiation of the ELIMA 2 experiment with cadmium as the screen in the HFR reactor is shown in fig. 4.6.5. At four levels nine specimen rods each are arranged in a matrix. Protection against thermal neutrons is largely provided by a cadmium screen. The temperatures are set and controlled, respectively, via gas gaps.

Fig. 4.6.6 shows in a direct comparison the configuration of the breeder columns in the two irradiation experiments as well as the axial plots of the neutron fluxes in the OSIRIS reactor and in HFR. The irradiation data are given in table 4.6.4.

Table 4.6.4   Irradiation data of the COMPLIMENT comparative experiment

	ELIMA 2	DELICE 03
Test reactor Neutron flux	HFR / Petten Cd-screened	OSIRIS / Saclay thermal
Beginning of irradiation End of irradiation	April 1988 January 1989	October 1988 February 1988
Full power days [FPD]	178	77
Temperature, matrices I + III Temperature, matrices II + IV	400 to 450 °C 650 to 750 °C	
Lithium burnup	~ 0.25 %	~ 1 %
Radiation damage . by fast neutrons . by (α + t) particles . total	1.6 dpa 0.2 dpa 1.8 dpa	1.1 dpa 0.7 dpa 1.8 dpa

The experiments **ELIMA 1** and **ELIMA 3** in table 4.6.1 are irradiations in the fast neutron flux of the Karlsruhe breeder reactor KNK II. The first experiment, ELIMA 1, will attain the envisaged service life of 100 FPD in late 1990. At that time the experiment ELIMA 3 is scheduled to start in the KNK II reactor. It will involve rather large amounts of lithium-orthosilicate specimens specifically for measurement of their properties. The ELIMA 2 experiment, originally planned for execution at KNK II, was performed as stated previously within the COMPLIMENT experiment at HFR, Petten. The essential data of the two KNK II irradiations have been entered in table 4.6.5.

All the irradiation experiments described and listed in table 4.6.1 were prompted during the last years by KfK and have been financed by that company. The tests envisaged for the future will be performed in a collaborative effort with the European partners; see chapter 5, R&D programme prior to tests in NET/ITER.

Table 4.6.5   Design and data of operation of the KNK-II experiments ELIMA 1 and ELIMA 3

		ELIMA 1		ELIMA 3		
Material		Li_2SiO_3 Pellets	Li_4SiO_4 Pellets	Li_4SiO_4 Pellets	Li_4SiO_4 MS	Li_4SiO_4 SS
Density	[% T.D.]	65/90	65/90	92...95	95...98	85...90
Pellet diameter	[mm]	4.84	4.84	10/12.7	25 *)	25 *)
Sample stack height	[mm]	40	40	72	150	150
Number of sample capsules		12	12	4	3	1
Total heat generation	[W/cm^3]	5.8/8.2	7.0/10.0	3...4,5	1.8...2.8	2.3
Tritium production rate	[10^{13} atoms/cm^{3}s]	0.50/0.65	0.65/0.89	0,3...0,45	0.2...0.3	0.22
Irradiation time	[FPD]	ca. 100		ca. 170		
Damage rate by neutrons	[dpa]	ca. 1		ca. 2		
Damage rate by t + α	[dpa]	up to 1		up to 1		

MS = Molten Spheres, SS = Sintered Spheres   *)   pebble bed diameter

References:

1   K.R. KUMMERER, H. ELBEL, H.E. HÄFNER, Ceramic Breeder materials for Fusion Reactor Concept Irradiation Conditions and Experimental Program ENC '86, Genf, June 1986.

2   H.E. HÄFNER, K. HECKERT, K.-D. PHILIPP, Fusion Technology Programme Semi-annual Report April-September 1989, KfK Report 4677.

3   K.R. KUMMERER, H.-J. RITZHAUPT-KLEISSL, Comparative Irradiation of Different Lithium Ceramics, 4th International Conference on Fusion Reactor Materials, ICFRM-4, December 1989, Kyoto, Japan.

4   K.R. KUMMERER, L. DÖRR, Comparison of Lithium Ceramics in the COMPLIMENT Irradiation Experiment, 16th Soft-Conference, London, 1990.

5   E. BOJARSKY, H. ELBEL, H.E. HÄFNER, H. WERLE, Fusion Technology Programme, Semi-annual Report October 1985 - March 1986, KfK Report 4076.
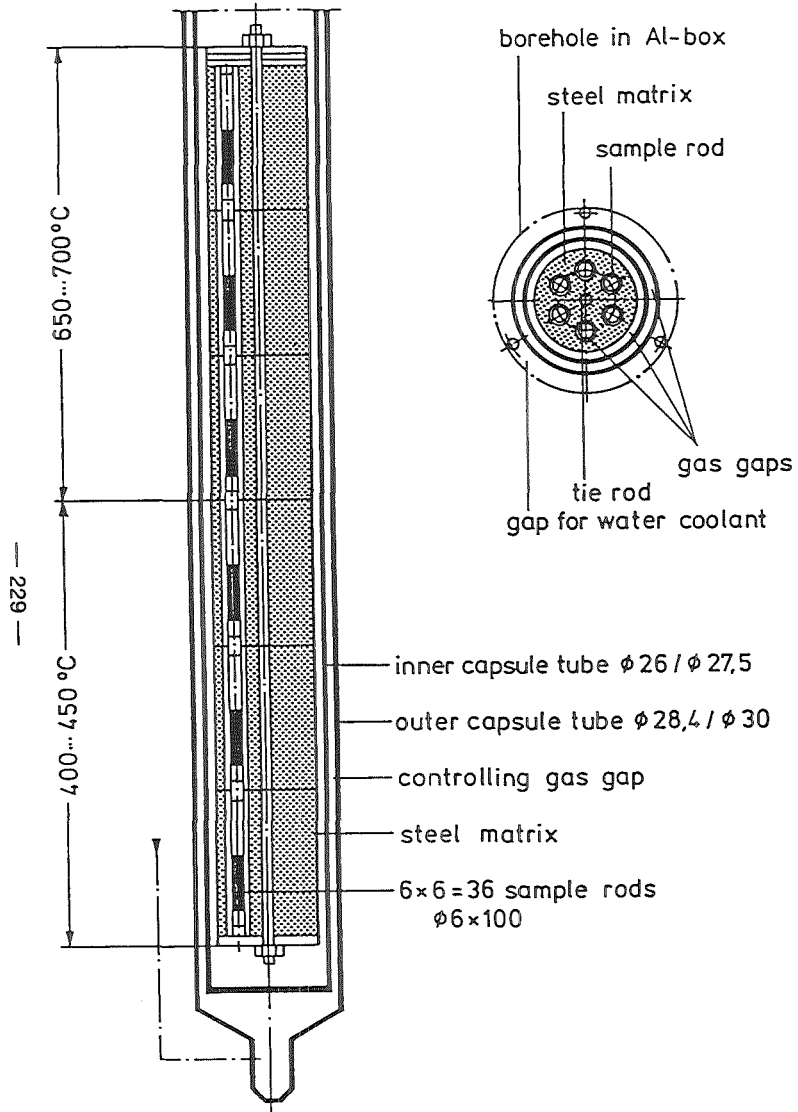
borehole in Al-box

steel matrix

sample rod

gas gaps

tie rod
gap for water coolant

inner capsule tube $\phi\,26\,/\,\phi\,27{,}5$

outer capsule tube $\phi\,28{,}4\,/\,\phi\,30$

controlling gas gap

steel matrix

$6\times6=36$ sample rods
$\phi\,6\times100$

$650\cdots700°C$

$400\cdots450°C$

Fig. 4.6.1   Scheme of DELICE capsule

$\varnothing\,14{,}5$

coolant watergap

SPND

additional heater

graphite block $\varnothing$ 55

thermocouple

CHOUCA-furnace $\varnothing$ 56/68

purge gas gaps

breeder material column
$\varnothing\,8\times80$

Fig. 4.6.2   Scheme of LISA capsule

3 modules in one rig ×3 = 9 capsules ×3 = 27 columns
a 4th module in a separate rig = 3 capsules ×3 = 9 columns
max. 36 columns

each module with 3
separately sweeped
and heated
capsules

thermocouples

coax sweep
gas line

φ54

150

φ32

heater

50
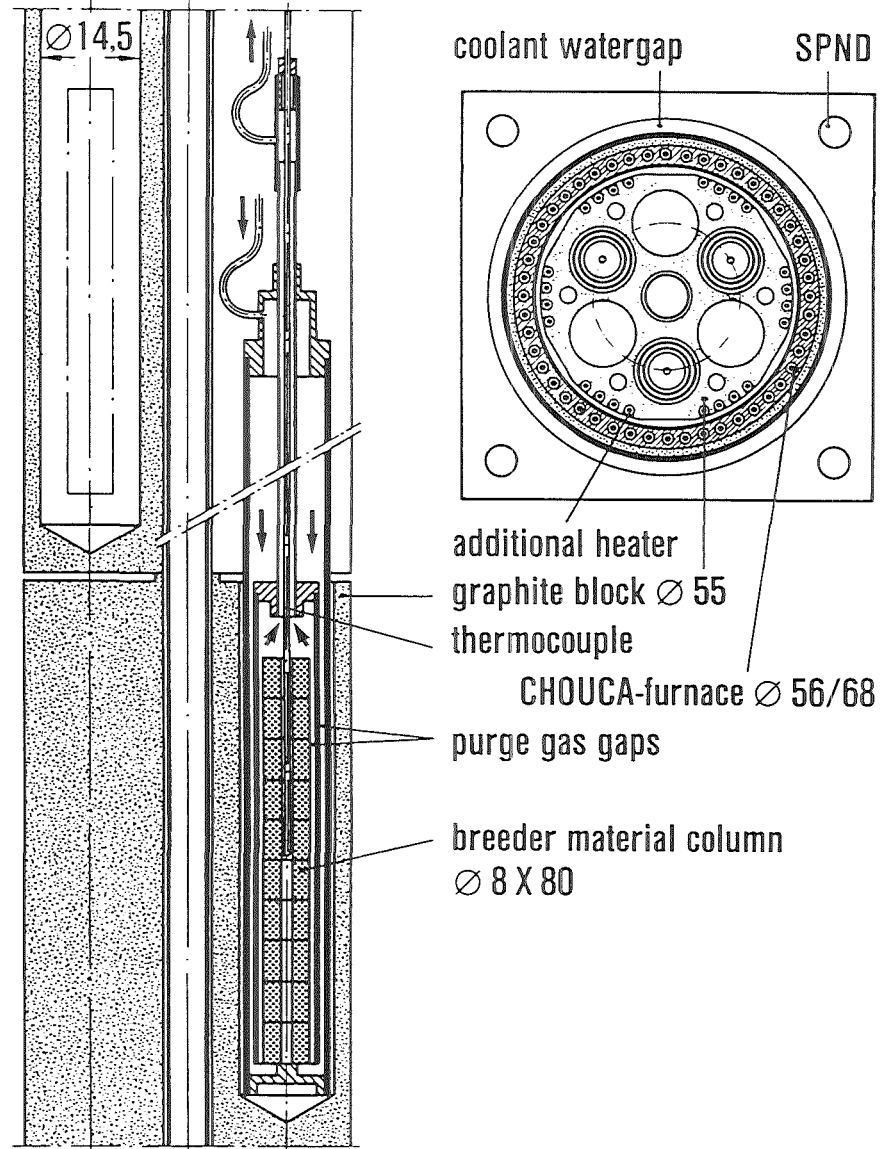
each capsule
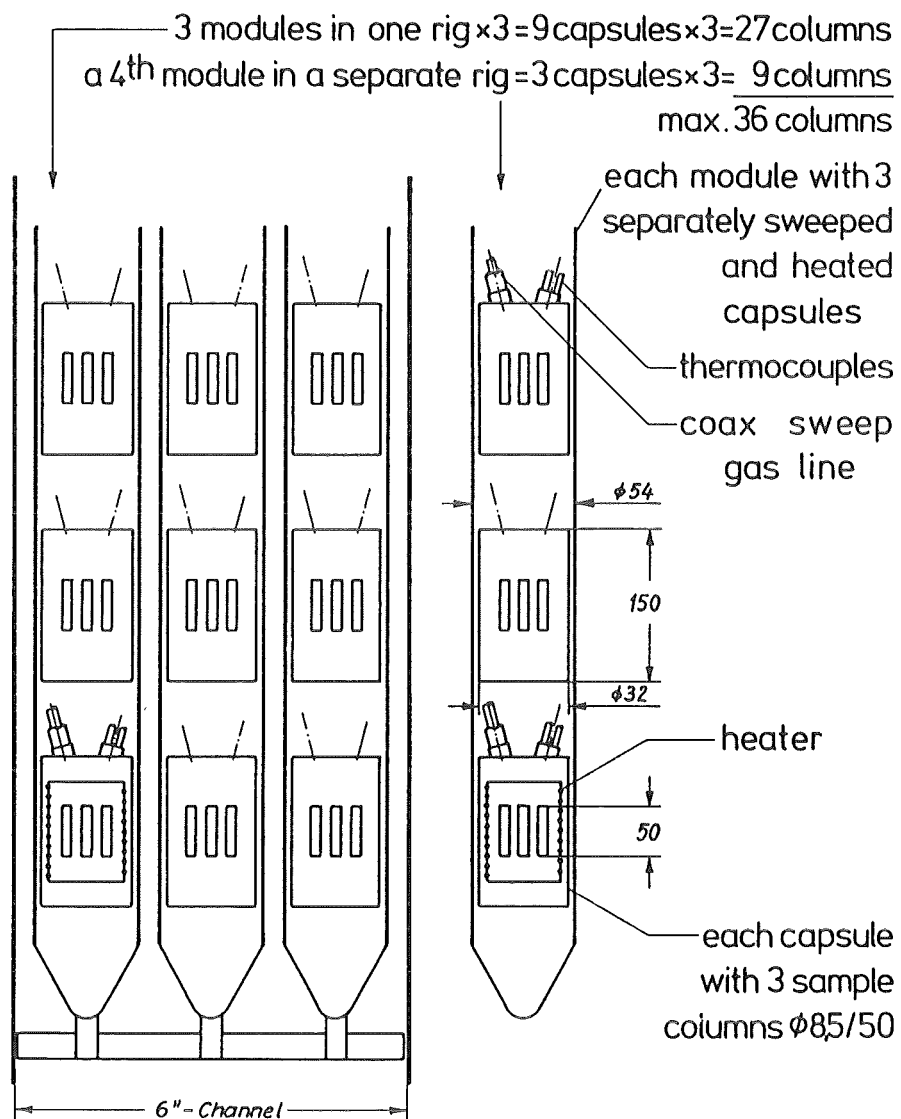with 3 sample
columns φ85/50

6"- Channel

Fig. 4.6.3   Scheme of TRIDEX rig
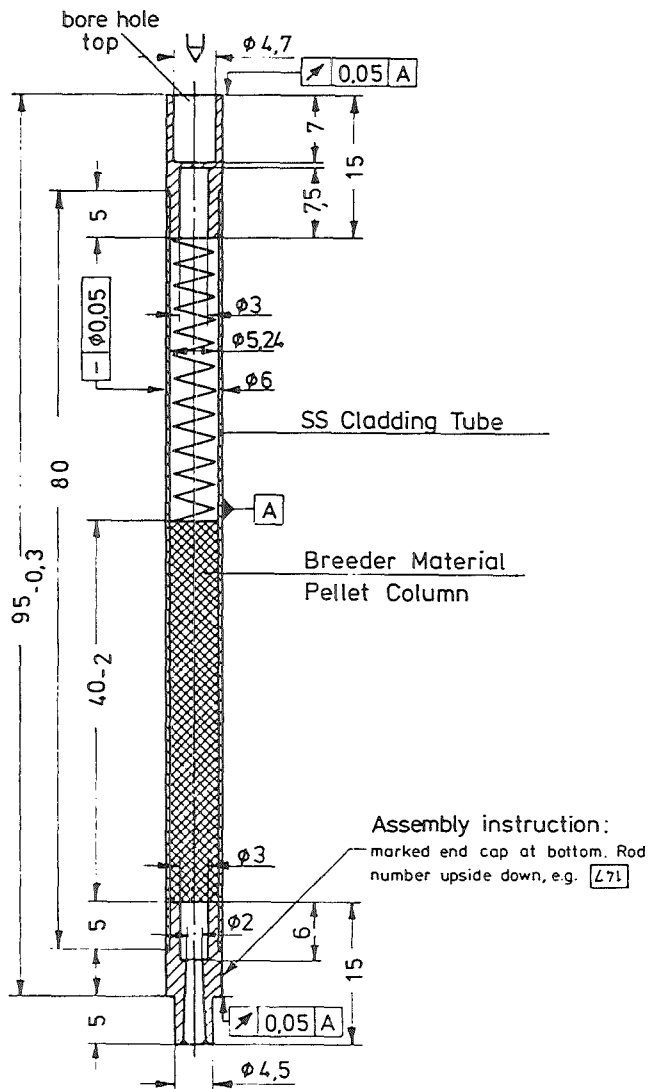
Fig. 4.6.4   Sample Rod for the COMPLIMENT
              Irradiation Experiment
              - Pellet Concept -
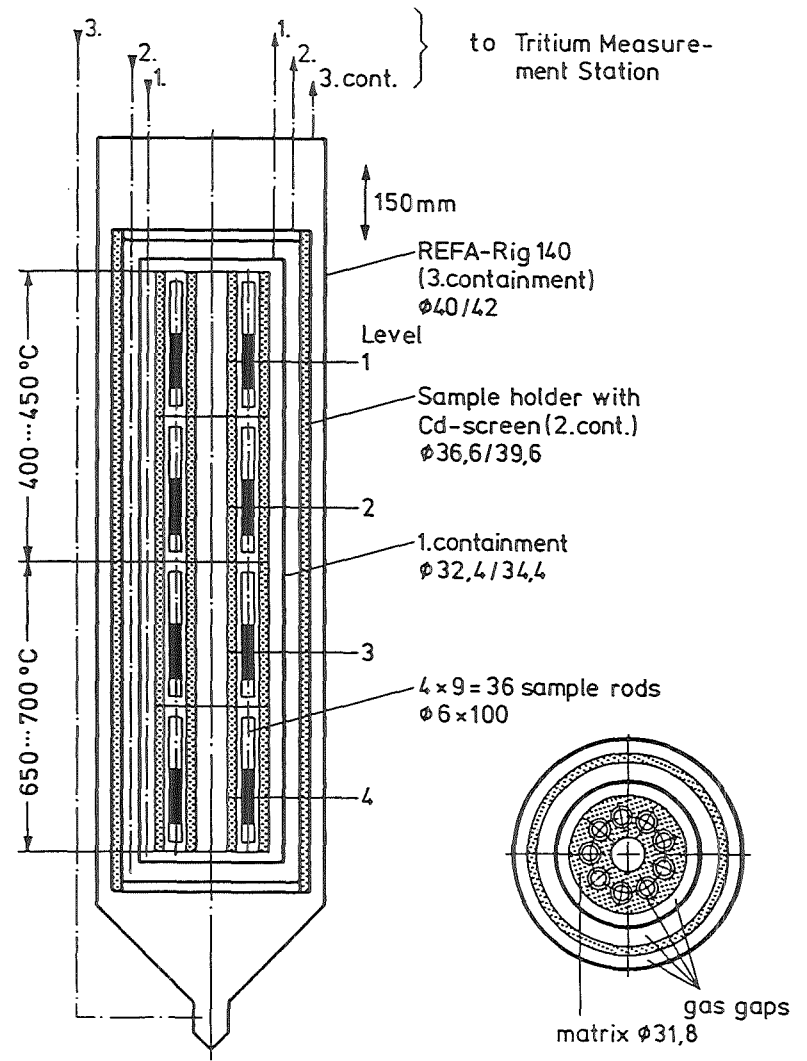
bore hole
top
⌀4,7
⌀0,05 A
7
15
7,5
5
⌀0,05
⌀3
⌀5,24
⌀6
SS Cladding Tube
80
A
Breeder Material
Pellet Column
40-2
95-0,3
Assembly instruction:
- marked end cap at bottom. Rod
  number upside down, e.g. ⌊71⌉
⌀3
5
⌀2
6
15
5
⌀0,05 A
⌀4,5

Fig. 4.6.5   Scheme of ELIMA 2 test rig

to Tritium Measure-
ment Station
3.
2.
1.
2.
1.
3.cont.
150mm
REFA-Rig 140
(3.containment)
⌀40/42
Level
Sample holder with
Cd-screen (2.cont.)
⌀36,6/39,6
1.containment
⌀32,4/34,4
4×9=36 sample rods
⌀6×100
400...450°C
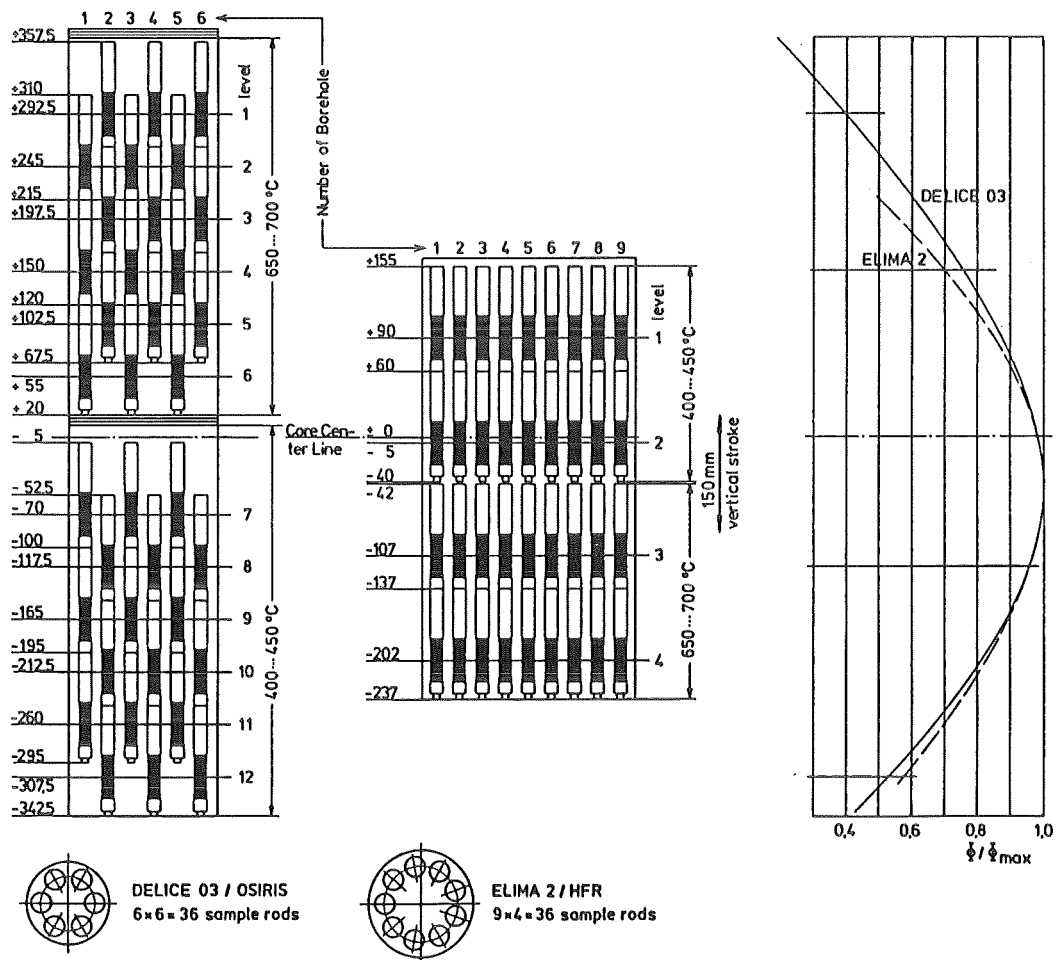650...700°C
1
2
3
4
gas gaps
matrix ⌀31,8

Fig. 4.6.6   Arrangement of the Samples in the COMPLIMENT
               Comparative Irradiation Experiment

4.6.2 Test samples preparation (H. Wedemeyer)

Irradiation test samples of various shapes were prepared by the fabrication methods pointed-out in chapter 4.3.2 for lithium orthosilicate and in chapter 4.4.2 for lithium metazirconate. Different methods were used for the preparation of the sintered orthosilicate specimen due to the progress in fabrication development. In table 4.6.2.1 to 4.6.2.4 the different irradiation tests are summarized and the various materials and preparation methods are pointed-out.

Table 4.6.2.1: Li_4SiO_4 test samples for helium purged test pins

Reactor Experiment Start of Irrad.	Shape of Samples	Material Density in %th.d.	Pellet/Pebble Dimension in mm	Number of Test Pins	Type of Fabrication
JRR-2 / Japan VOM-23H 1986	pebbles	85-90	4	1	CO_3
SILOE / Grenoble LISA-1 Oct./1985	pellets	90	8x8	1	CO_3
LISA-2 Nov./1986	pellets pebbles pebbles	90 85-90 98	8x8 0.5 0.5	1 1 1	CO_3 CO_3 Schott
LILA/LISA-3 June/1989	pellets pellets	90 85-90	8x8 8x8	1 1	ALC ALC (Al-doped)
SIBELIUS June/1990	disks pebbles	90 98	1.5x8 0.5	1 1	ALC Schott
CORELLI-1 May/1991	pebbles pebbles	85-90 98	0.5 0.5	1 1	ALC Schott
HFR / Petten EXOTIC-5 July/1989	pebbles	80	0.5	1	ALC
EXOTIC-6 May/1991	pebbles	98	0.5	1	Schott
DIDO / Jülich TRIDEX-1 March/1989	pellets	90	8x8	1	CO_3
TRIDEX-2 Sept./1988	pellets	90	8x8	2	CO_3
TRIDEX-3 Nov./1988	pellets	90	8x8	1	ALC
TRIDEX-4 April/1990	pellets pebbles pebbles	90 85-90 98	8x8 0.5 0.5	1 1 1	CO_3 (HIP) ALC Schott
TRIDEX-5 April/1990	pebbles	98	0.5	1	Schott

Type of Fabrication (materials prepared by KfK unless otherwise indicated):
CO_3 : Li_4SiO_4 powder prepared by the reaction Li_2CO_3 + Li_2SiO_3 → Li_4SiO_4 + CO_2
CO_3 (HIP) : Pellets fabricated by hot-isostatic pressing (HIP) of powders from the " CO_3-Fabrication"
ALC : Li_4SiO_4 powder prepared by the reaction 4 LiOH + SiO_2 → Li_4SiO_4 + 2 H_2O in alcoholic suspension
Schott : Pebbles prepared from melt by Fa. SCHOTT, Mainz

Table 4.6.2.2: Li$_4$SiO$_4$ test samples for closed test test pins

Reactor Experiment Start of Irrad.	Shape of Samples	Material Density in %th.d.	Pellet/Pebble Dimension in mm	Number of Test Pins	Type of Fabrication
EBR-2/USA					
FUBR-1 B	pellets	90	9.5x10	1	NO$_3$
in BEATRIX-1	pellets	90	16.5x10	1	NO$_3$
May/1987	pebbles	85-90	1	1	NO$_3$
OSIRIS / Saclay					
DELICE-2	pellets	65	5x5	6	CO$_3$
March/1986	pellets	90	5x5	6	CO$_3$
DELICE-3	pellets	90	5x5	4	ALC
Dec./1988	pebbles	85	0.5	2	ALC
	pebbles	98	0.5	2	Schott
ALICE-3	pebbles	85-90	0.3-0.6	2	ALC
Nov./1990	pebbles	98	0.3-0.6	2	Schott
KNK-2/Karlsruhe					
ELIMA-1	pellets	65	5x5	3	CO$_3$
Jan./1991	pellets	90	5x5	3	CO$_3$
	disks	65	2x5	3	CO$_3$
	disks	90	2x5	3	CO$_3$
ELIMA-3	disks	90	3x12.7		ALC
to be irrad.	pellets	90	5x10	4	ALC
	pellets	90	10x10		ALC
	pebbles	85-90	0.5	1	ALC
	pebbles	98	0.5	3	Schott
HFR / Petten					
ELIMA-2	pellets	90	5x5	4	ALC
June/1988	pebbles	85-90	0.5	2	ALC
	pebbles	98	0.5	2	Schott

Type of Fabrication (materials prepared by KfK unless otherwise indicated):

CO$_3$: Li$_4$SiO$_4$ powder prepared by the reaction Li$_2$CO$_3$ + Li$_2$SiO$_3$ → Li$_4$SiO$_4$ + CO$_2$

NO$_3$: Li$_4$SiO$_4$ powder prepared by the reaction 4 LiNO$_3$ + SiO$_2$ → Li$_4$SiO$_4$ + 4 NO$_x$

ALC : Li$_4$SiO$_4$ powder prepared by the reaction 4 LiOH + SiO$_2$ → Li$_4$SiO$_4$ + 2 H$_2$O in alcoholic suspension

Schott : Pebbles prepared from melt by Fa. SCHOTT, Mainz

Table 4.6.2.3: Li_2ZrO_3 test samples for closed test test pins

Reactor Experiment Start of Irrad.	Shape of Samples	Material Density in % th.d.	Pellet/Pebble Dimension in mm	Number of Test Pins	Type of Fabrication
SILOE / Grenoble LILA/LISA-3 June/1989	pellets	85-90	8x8	1	ALC
HFR / Petten EXOTIC-6 May/1991	pebbles	85-90	0.5	1	HITEC
DIDO / Jülich TRIDEX-5 April/1990	pebbles pebbles	85-90 85-90	0.5 0.5	1 1	ALC HITEC
TRIDEX-6 Oct./1990	pebbles pebbles	85-90 85-90	0.5 0.5	1 1	ALC HITEC

Type of Fabrication

ALC: Li_4SiO_4 powder prepared by the reaction $4\,LiOH + SiO_2 \rightarrow Li_4SiO_4 + 2\,H_2O$ in alcoholic suspension (prepared by KfK).

HITEC : Pebbles prepared by a powder metallurgical agglomeration process from a mixture of Li_2CO_3 and ZrO_2 by Fa. HITEC, Karlsruhe.

Table 4.6.2.4: Li_2ZrO_3 test samples for closed test test pins

Reactor Experiment Start of Irrad.	Shape of Samples	Material Density in % th.d.	Pellet/Pebble Dimension in mm	Number of Test Pins	Type of Fabrication
OSIRIS / Saclay ALICE-3 Nov./1990	pebbles	85-90	0.3-0.6	1	HITEC

Type of Fabrication

HITEC : Pebbles prepared by a powder metallurgical agglomeration process from a mixture of Li_2CO_3 and ZrO_2 by Fa. HITEC, Karlsruhe.

4.6.3   Tritium release (H. Werle)

Tritium inventory is an important aspect in blanket design. For economical and safety reasons it should be small, i.e. tritium release should be fast. In agreement with the other EC partners, KfK concentrated on lithium silicates and metazirconate.

The main goal of the tritium release investigations is the determination of the tritium inventory in the blanket for representative conditions. In addition it is important to identify and model tritium release controlling processes.

Three different kinds of tritium release measurements are performed:

1.   Tritium annealing of low-activity samples irradiated in closed capsules at room temperature

2.   Tritium annealing of high-activity samples irradiated in closed capsules at elevated, blanket-relevant temperatures

3.   Purged inpile tests under blanket-relevant conditions.

Early tests [1] confirmed previous results [2], that tritium release from orthosilicate is much faster than from metasilicate. Therefore orthosilicate was chosen as reference and metazirconate as backup material for the KfK blanket.

Generally it is found that tritium release form ceramics depends on a large number of parameters (temperature, microstructure, impurities and handling of samples; purge gas chemistry). In addition, tritium release is, especially for orthosilicate, a very complex process involving generally a series of different reactions. Therefore still no verified model for orthosilicate tritium release is available which allows to predict blanket inventories and optimal tritium release parameters based on out-of-pile annealing results. Blanket inventory estimations still require purged inpile tests under relevant conditions.

4.6.3.1   Annealing tests

The "low"-activity (tritium activity $\leq$ 1 MBq) samples are dried under vacuum or by He purging at temperatures up to 900°C, inserted under He atmosphere into gas-tight Pt-or Al-capsules and irradiated for about 20 h at room temperature in a field of moderated neutrons at the KfK cyclotron. The Pt-capsules are punctured in the closed annealing chamber, whereas the samples of the Al-capsules have to be reloaded (in a glovebag under He) into

stainless steel capsules for annealing. During insertion into the annealing chamber these samples are at air for some minutes.

The "high"-activity (tritium activity up to 10^4 MBq) samples are normally irradiated in closed stainless steel capsules under He atmosphere and at elevated temperatures for one or several reactor cycles (1 cycle about 20 d) in the OSIRIS reactor at Saclay or the HFR reactor in Petten. The drying procedure (2 h, 300 °C, vacuum), applied before welding the capsules is certainly not sufficient to remove contaminations (H_2O, CO_2, etc.) adsorbed during storage after sintering. After irradiation the capsules are opened and the samples are handled under dry, inert atmosphere.

Because of the very different activites, the "low"- and "high"-activity samples are annealed in two different, but principally similar facilites. They are made completely of stainless steel and consist of the gas supply and purification, the sample and Zn-reductor chambers and the tritium monitors (a proportional counter for the "low"- and an ionization chamber for the "high"-activity samples). The Zn-reductor (heated to 385 °C) reduces any tritiated water to gas in order to transfer the tritium quantitatively to the monitors. During annealing the samples are purged with high-purity He, He + H_2 or He + H_2O mixtures. The sample temperature is controlled by a programmable heater.

In the "low"-activity facility there exists a bypass around the Zn-reductor. This allows to measure only the gaseous (HT) fraction of the released tritium, because tritium water is adsorbed on the lines to the monitor. In addition this facility is equipped with a second sample chamber made of copper to study the influence of sample environment.

Several metasilicate and metazirconate samples and a large number of orthosilicate samples were annealed. Generally, tritium release from orthosilicate and metazirconate is observed to be much faster than from metasilicate. The main results are discussed in the following [3 - 7].

Pre-irradiation sample drying

For metasilicate pre-irradiation drying has only a small, for orthosilicate and metazirconate it has a strong influence on the tritium release kinetics during annealing. Probably this is because tritium bulk diffusion in metasilicate is slow, whereas in orthosilicate and metazirconate it is fast and therefore tritium is exchanged with and released together with physi- and chemisorbed water at the grain surface. Recent tests [7] indicate that for orthosilicate another impurity (probably carbonate from fabrication and / or from storage at air), which can only be removed by very hard drying ($\geq$ 800 °C), has a strong retarding effect on tritium release and may well be responsible for the observed large scatter of inpile tritium residence times.

Sample heating procedures

Different procedures, single linear ramps (usually with 5 °C/min) and sequences of ramps or steps with increasing final temperature up to a maximum of about 850 °C are applied. The different procedures are useful to identify and determine the characteristic parameters of the release-controlling processes.

The ramp tests clearly demonstrate that generally for all materials investigated and especially for orthosilicate, tritium is released from a series of different desorption sites (each characterized by a desorption constant, an activation energy and a fractional tritium inventory) (Fig. 4.6.3.1). The sequence -of-ramp-tests indicate that all tritium is trapped in these sites (i.e. there seems to exist no common bulk diffusion inventory) (Fig. 4.6.3.1).

Sample characteristics

For metasilicate ($\leq$ 85 % theoretical density) tritium release was found to be only weakly dependent on sample size and density and for orthosilicate ($\geq$ 95 % theoretical density), tritium release is essentially independent of these parameters. For all materials investigated, tritium release is enhanced with decreasing grain size (Fig. 4.6.3.2). This observation indicates that the tritium is distributed within the grains. This is in contradiction with the conclusion drawn from the sequences-of-ramp-test. Annealing tests were also performed with orthosilicate samples doped with Al^{3+}, P^{5+} and Mg^{2+} [8, 9]. A unique interpretation concerning the effect on tritium release was not possible.

Specific activity

The order of the release processes is a very fundamental parameter, because it describes the dependance of the release rate on the tritium inventory. For ortho- and metasilicate it was observed that the tritium release kinetics of samples from the same charge, differing in the specific activity by more than two orders of magnitude, is equal, indicating first order processes (i.e. release rate proportional to inventory).

Purge gas

Tritium release is essentially independent of purge gas pressure and flowrate. It is enhanced by additions of H_2 or H_2O to the purge gas, wheras already small amounts of O_2 ($\approx$ 1 vpm) are very detrimental.

Sample environment

In agreement with the above mentioned detrimental effect of O_2 on tritium release, it is observed that tritium release is faster in the reducing atmosphere of a stainless steel sample chamber than in the neutral atmosphere of a copper chamber.

Tritium specifics

The type of released tritium species (water or gas) also depends strongly on the sample environment. Whereas in a copper chamber for He purge gas more than 80 % and for He + 1 % H_2 still more than 60 % of the tritium is in the water form, in the reducing atmosphere of a stainless steel chamber, for both types of purge gases, above about 400 °C, essentially all detected tritium is gaseous.

4.6.3.2 Purged inpile tests

Two series of tests are performed: the LISA experiments [1, 10, 11] together with CEA at the SILOE reactor in Grenoble and the TRIDEX experiments [12] together with KFA at the DIDO reactor in Jülich. These facilities are rather similar. The samples are contained in stainless steel capsules and surrouned by electrical heaters. Zn-reductors are used ot convert any tritium water to gas. The facilities allow systematic variations of sample temperature (between about 300 and 700 °C), purge gas composition and flow rate. Moreover, in the LISA tests the tritium production rate can be varied by moving the inpile test section. A few selected KfK samples are also being tested in the Common European inpile tests EXOTIC-5 and -6 [13], performed in Petten. Before irradiation the samples are generally dried under vacuum or by He purging at temperatures between 500 and 800 °C for several tens of hours.

As mentioned, already the first KfK inpile test [1] demonstrated that tritium release of orthosilicate is much faster than from metasilicate. Later tests therefore concentrated on orthosilicate, especially pebbles suited for the KfK blanket. Recently also metzirconate, which too has very favorable tritium release properties, has been studied.

The most important parameter determined in the inpile tests is the tritium inventrory as a function of sample temperature. Usually the inventory I is normalized by the production rate p to yield the residence time τ = I/p = I/r (at equilibrium p = r, r release rate). The concept of a residence time is only useful if τ is independent of p. This requires r ~ I, i.e. first order release processes. In this case blanket inventories can be predicted using (calculated) production rates.

Because of its importance, the question of the order of release reactions was studied in LISA-2 [10] and in the recently performed test LILA/LISA-3 [11] for ortho- and metasilicate, metazirconate and aluminate. The kinetics was observed to be independent of, and the inventories to be proportional to the production rate. This indicates, in accordance with the annealing results, that the controlling processes obey first order kinetics.

The inpile results concerning purge gas effects too are in agreement with annealing observations. Inpile tritium release was found to be independent of purge gas flow rate and pressure. It is enhanced by H_2 and H_2O additions to the purge gas and strongly retarded by O_2. For orthosilicate the residence time was found to vary according to $\tau \sim 1 / p_{H2}$ with the H_2 partial pressure. Because with He + 0.1 vol% H_2 reasonable residence times are observed for the most promising ceramics, this mixture has become the reference purge gas in most studies.

In an effort to improve material properties, especially mechanical stability, a large number of different orthosilicate samples, mainly pebbles, have been tested inpile. A huge scatter in the inpile residence times up to two orders of magnitude is observed. Although, because suitable sample were not available, our knowledge in this field is still poor, it is quite clear that this huge scatter is not due to variations in usually considered sample characteristics (dimensions, density, microstructure).

Inpile residence times with H_2 + 0.1 vol% H_2 purge gas for recently produced orthosilicate and metazirconate sinter granulate and orthosilicate spheres prepared from the melt (Schott) are shwon in Fig. 4.6.3.3. At 400 °C (minimum blanket temperature) the residence times of all new charges are less than those of the older charge Schott 86, hitherto considered as reference, and sufficiently small (< 1d) for blanket applications. The data for the Li_4SiO_4 pebble Schott 86 have been used to calculate the tritium inventory in the breeder ceramic of the Demo blanket.

4.6.3.3 Modeling

Experimental investigations were accompagnied by efforts to model tritium release. Bulk diffusion and a series of first and second order desorptions processes at the grain surface were considered. From comparisons of measured and model-predicted tritium release the following conclusions were drawn: Whereas tritium release from metasilicate is mainly controlled by (slow) bulk diffusion, that of metazirconate and especially that of orthosilicate is essentially controlled by desorption (diffusion fast). The desorption processes are first order. In orthosilicate tritium exists in three different staces at the grain surface: physisorbed HTO, lattice-chemisorbed OT and very strongly bonded contamination (carbonate)-

chemisorbed OT. Tritium release behaviour is strongly determined by the number of "carbonate" sites.

Predicted residence times using this model and annealing results of various orthosilicate samples are also shwon in Fig. 4.6.3.3. The fact that the measured inpile values are bonded by the two desorption processes (from lattice and from "carbonate" sites) indicates that the huge scatter of inpile data is caused by carbonate impurities.

4.6.3.4   Summary of status and future work

Status
- Tritium residence times of newer charges of orthosilicate and metazirconante samples are sufficently small for fusion reactor applications.

  The dependence of the residence time on the temperature and on the H_2 content of the purge gas has been determined inpile for these materials.

- There are indications that tritium release from orthosilicate is strongly determined by carbonate impurities.

Future work
- Specification of reference model for tritium relase from orthosilicate
- Irradiation effects on orthosilicate tritium release
- tritium release from Be

References

1.   H. WERLE, J.J. ABASSIN, M. BRIEC, R.G. CLEMMER, H. ELBEL, H.E. HÄFNER, M. MASSON, P. SCIERS AND H. WEDEMEYER, "The LISA-1 Experiment: In-Situ Tritium Release Investigations", J. Nucl. Mater. 141-143 (1986) 321

2.   D. BRÜNING, D. GUGGI, H.R. IHLE AND A. NEUBERT, "Diffusion of Tritium in, and Chemistry of, Lithium-Orthosilicate", 13th Symp. on Fusion Technol., Varese 1984, Paper IP36, Vol.I, p. 427

3.   W. BREITUNG, H. ELBEL, J. LEBKÜCHLER, G. SCHUMACHER AND H. WERLE, "Out-of-pile Tritium Extraction from Lithium Silicate", J. Nucl. Mater. 155-157 (1988) 507

4.   W. BREITUNG, M. BRIEC AND H. WERLE, "Tritium Release form Lithium Silicate", Fusion Eng. Design 8 (1989) 323

5. W. BREITUNG, H. WERLE, "Tritiuminventar in keramischen Blankets", KfK-Nachrichten Jg.21, 4/89, p. 265

6. W. BREITUNG AND H. WERLE, "Experiemtnal Evidence for Tritium Release Controlling Processes in Lithium Silicates", to be published in J. Nucl. Mater.

7. W. BREITUNG, H. ELBEL, H. WEDEMEYER, H. WERLE, "Tritium Release from Low- and High-Density Lithium Meta- and Orthosilicate (Irradiation DELICE 2)", 16th Symp. Fusion Technology (SOFT), London, 1990,

8. A SKOKAN, D. VOLLATH, H. WEDEMEYER, E. GÜNTHER, H. WERLE, "Preparation, Phase Relationships and First Irradiation Results of Lithium Orthosilicate Doped with Al3 + - and P5 + -Ions", in: Fusion Technology 1988, A.M. Van Ingen, A. Nijssen-Vis, H.T. Klippel (editors), Elsevier Science Publishers B.V., 1989, p. 1025

9. D. VOLLATH, H. WEDEMEYER, H. ZIMMERMANN AND H. WERLE, "Doped Lithium Orthosilicate: Preparation and Properties", J. Nucl. Mater. 174 (1990) 86

10. H. WERLE, W. BREITUNG, M. BRIEC, R.G. CLEMMER, H. ELBEL, H.E. HÄFNER, M. MASSON, G. SCHUMACHER AND H. WEDEMEYER, "The LISA-2 Experiment; In-Situ Tritium Release from Lithium Orthosilicate (Li_4SiO_4)", J. Nucl. Mater. 155-157 (1988) 538

11. M. BRIEC, J. KOPASZ, S. CASADIO, H. WERLE, "In-Pile Tritium Release from Lithium Ceramics and Influencing Surface Processes", 16th Symp. Fusion Technology (SOFT), London, 1990

12. W. KRUG, H.G. BAYS, H. JÜNEMANN, W. KRAUTHAUSEN, F. SCHMIDT, J. SEFERADIS, L. WEISE, H. WERLE, "Bestrahlung von keramischen Brutmaterialien für Fusionsreaktor-Blankets im FRJ-2", Jahrestagung Kerntechnik, Düsseldorf, 1989

13. H. KWAST, R. CONRAD, S.D. PRESTON, G. VERSTAPPEN, N. ROUX, S. CASADIO, H. WERLE AND J.D. ELEN, "Comparison of the Tritium Residence Times of Various Ceramic Breeder Materials Irradiated in EXOTIC Experiments 4 and 5", 16th Symp. Fusion Technology (SOFT), London, 1990
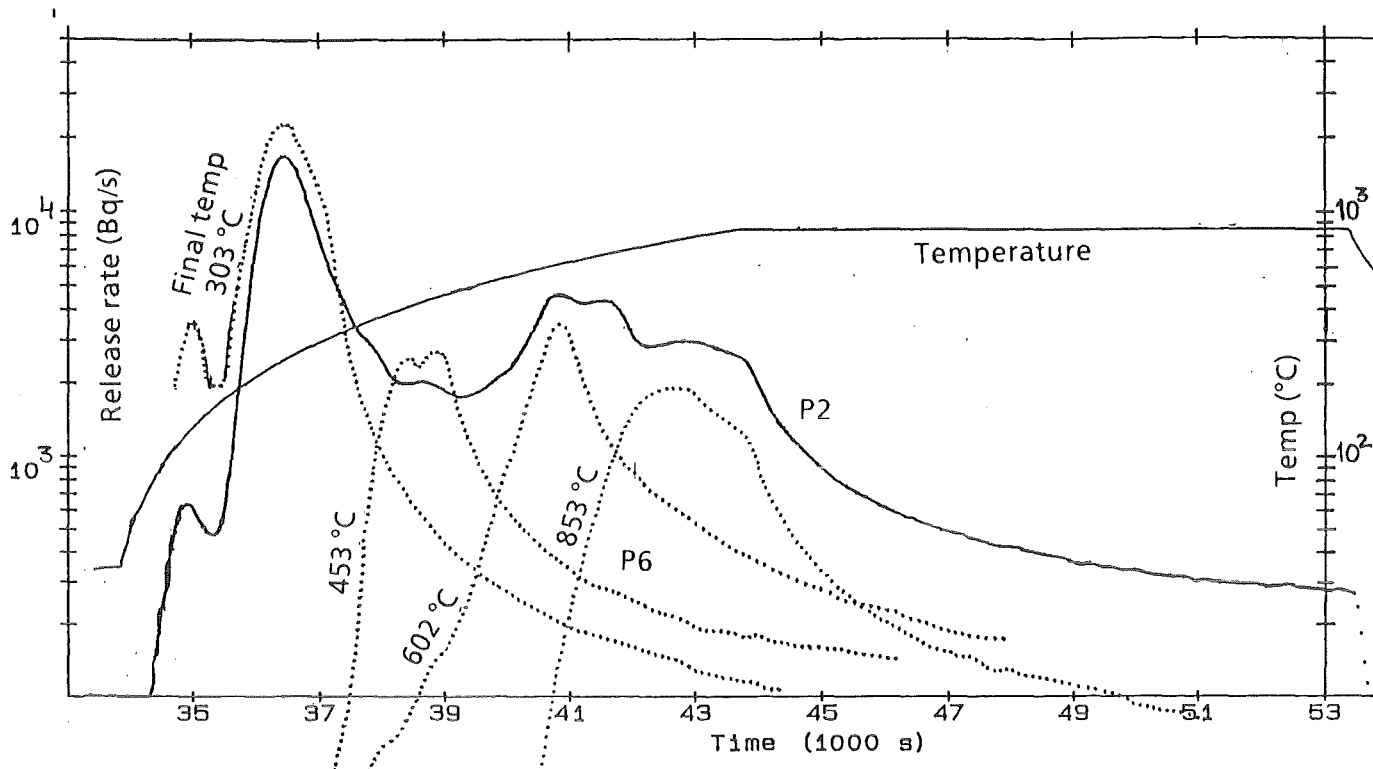
Fig. 4.6.3.1   Tritium release from low-density (65 %) orthosilicate of Delice 02
(pellet stack C1, irradiated at 700 °C) with He + 0.1 H_2 purge gas.
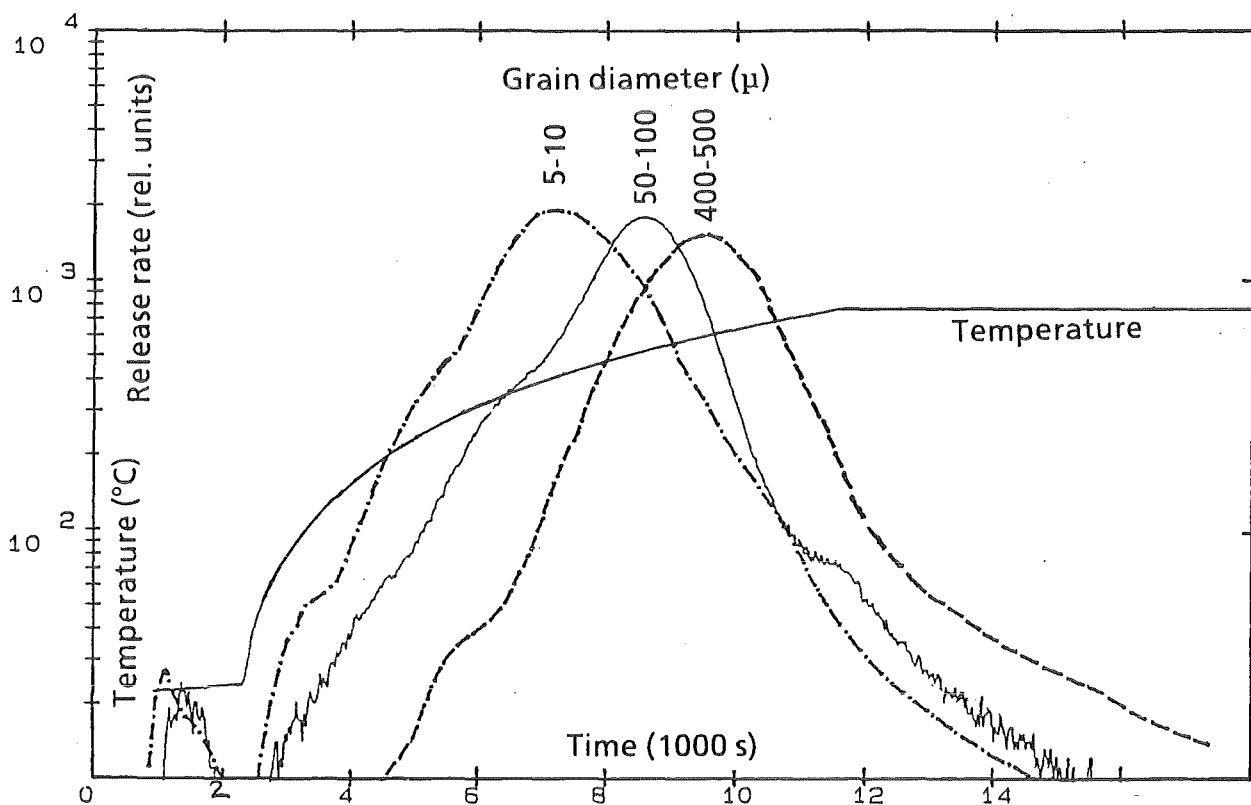Pellet P2 single 5 °C/min ramp, pellet P6 sequence of 5 °C/min
ramps.

Fig. 4.6.3.2   Tritium release from high-density orthosilicate samples with
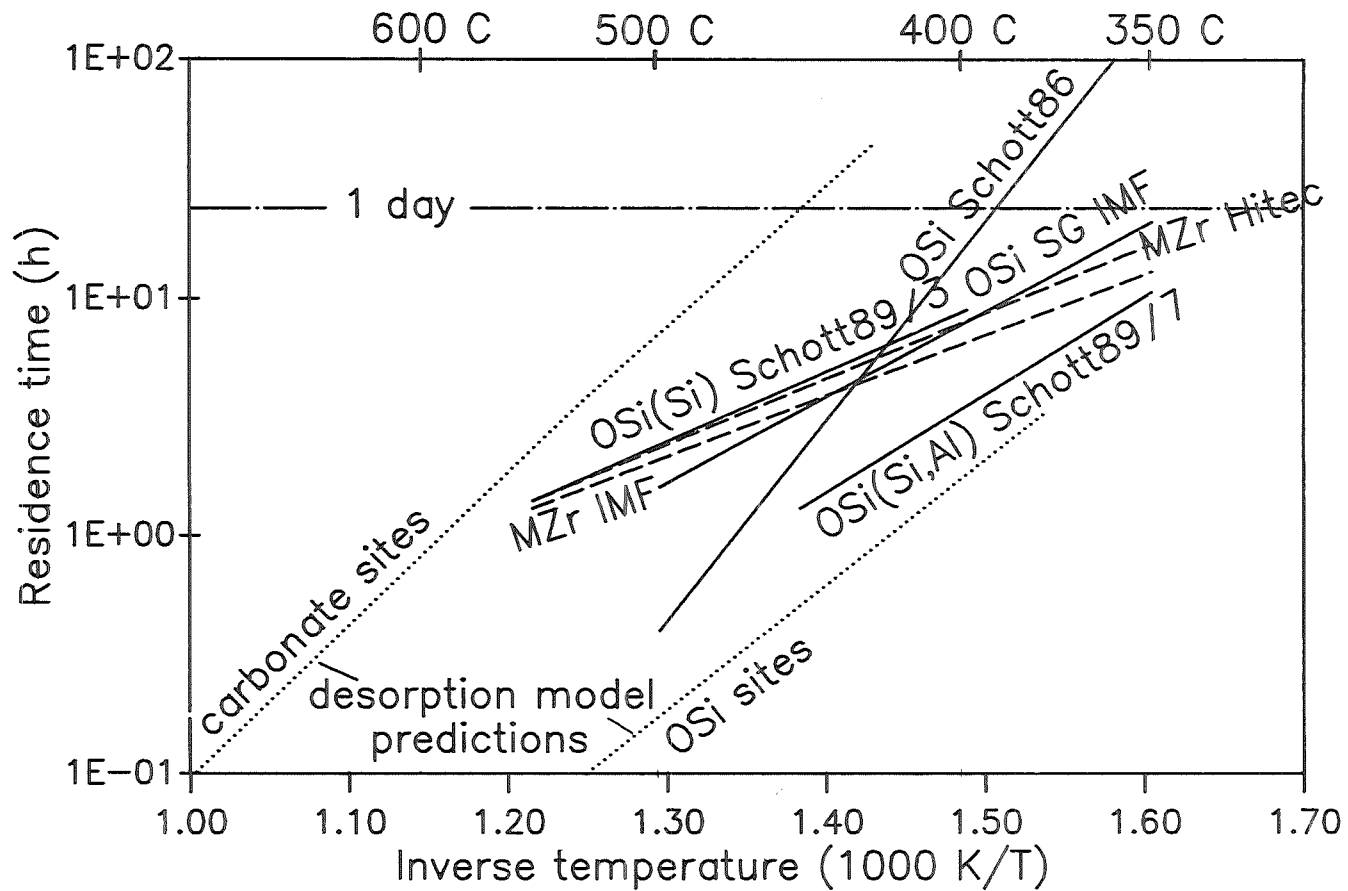different grain diameters for a 5 °C/min ramp and He purge gas.

Fig 4.6.3.3   Measured inpile residence times for recently produced metzirconate (MZr) and orthosilicate (OSi) and desorption model predictions for He + 0.1 % H_2 purge gas.

SG: sinter granulate   Schott: spheres prepared from melt

4.6.4 Post irradiation examinations (L. Dörr, P. Weimar, H. Werle)

4.6.4.1 Introduction

The solid breeder concept requires ceramic compounds with high lithium content, good tritium extraction characteristic at moderate temperatures, mechanical integrity, minor swelling and chemical compatibility with the containment. Measurement and comparison of the properties of various breeding ceramics irradiated at different temperatures and neutron fluences are carried out in the Fusion Ceramics Laboratory (FKL). The FKL is located in the Hot Cell Facility of KfK. It consists of four lead shielded boxes. An inert and dry atmosphere (N_2) is needed within the boxes to protect the ceramics from reactions with water vapor.

Oxygen and humidity content of the nitrogen gas is reduced by a closed gas processing loop to about 5 vol. ppm. Humidity is collected by a molecular sieve. Oxygen from leackage of the boxes is extracted by a heated zinc bed. In addition, tritium gas is removed by oxidation with copper oxide to tritiated water vapor which is collected by a molecular sieve.

Several operation modes of the box ventilation like closed circuit or once-through operation are possible: circulation of purified inert gas, ventilation with nitrogen from gas cylinders, exhausting of the box leackage and ventilation with air. A two step pressure gradient is maintained from the laboratory outside to the interior of the boxes at all operation modes to avoid contamination of the laboratory. Tritium activity of the atmosphere within the laboratory and the boxes is continously recorded. The Ceramic samples irradiated in closed metallic capsules are stored in the lead shielded box no. 1. (cif. Fig. 4.6.4.1).

The lead shielding (thickness 20 cm) reduces the radiation intensity from the neutron activated sample containers. Manipulators are used in the lead shielded boxes for handling purposes.

At first the capsules are inspected and photographed. The capsules are perforated in an evacuated vessel located in box no. 1 and a part of the expanding plenum gas is sampled in a gasometer. Dismantling of the sample rods is performed under inert-atmosphere of the cell. The samples are photographed and packed in new, un-irradiated capsules for storage and transportation. The tritium containing ceramic samples are less γ-active and can be handled in glove boxes. Capsules containing breeding ceramics are controlled with a γ-detector before transferring via pneumatic post into the unshielded glovebox no. 5. Weight and geometric dimensions of the samples are measured in glovebox no. 6.

Heating of the ceramic samples according to a special program (cif chap. 4.6.3) is used to evaluate the tritium release characteristics (box No. 5). The tritium activity is monitored by an ionization chamber. Purge gases with various percentages of H_2 or H_2O are used to optimize the tritium extraction characteristics. The reference purge gas consists of helium with 0.1 vol. % H_2. For determination of the tritium activity of the plenum gas the gasometer is connected to the ionization chamber and purged with the reference gas.

Irradiation induced swelling and open porosity changes of the samples are measured by mercury intrusion porosimetry (box no. 7). Swelling decreases the density which is determined from the volume of mercury displaced by the sample and the previously measured weight of the sample. The abundance and size distribution of the open pores are calculated from the volume of mercury penetrating the open pores as a function of the pressure applied. This technique was also used for unirradiated reference samples.

Changes of the thermal diffusivity of windows for HF heating and breeding ceramic pellets due to irradiation is measured by the laser flash apparatus located in box no. 4. A laser flash is absorbed on the front side of a black colored pellet and the time-dependent increase in the emission of infra-red light on the opposite side of the pellet is recorded. The thermal conductivity of beds of sintered and melt produced lithium orthosilicate (Li_4SiO_4) pebbles (mean diameter 0.5 mm) will be measured by the radial heat flow method in glovebox no. 8. Thermal cycling is applied to breeding ceramics to study thermomechanical properties.

Selected samples are transferred to the shielded metallographic unit located in the same building for further characterization. Photographs of fractured surfaces are taken by a scanning electron microscope. The elemental composition in the range from carbon to heavier elements is determined. The abundance and size distribution of grains and closed pores are explored by image analysis. In the frame of the European COMPLIMENT experiment (Comparison of Lithium Materials Damage Effects by Fast Neutrons and $^6Li(n,\alpha)T$ Reactions) Li_2O, $LiAlO_2$, Li_2ZrO_3, Li_2SiO_3, Li_4SiO_4 samples were irradiated in closed capsules at the reactors HFR-Petten and OSIRIS-Saclay, respectively. After irradiation the sample rods are transferred to the FKL at KfK.

4.6.4.2 Post irradiation examinations of Li-meta- and ortho-silicates

In the frame of the COMPLIMENT irradiation experiment (cif. Table 4.6.4. 2) different lithium containing ceramics were irradiated. Table 4.6.4.1 shows the irradiation conditions. As can be seen two different temperatures (400-450 °C and 650-750 °C) were chosen. According to the different irradiation times the Li-burnup was 0,25 at % and 1 at %, respectively. In the following some metallographic and fractographic images of the metallographic examinations of Li-ortho- and -metasilicates are shown. Fig. 4.6.4.2 illustrates the length changes of the breeder columns of different Li-ceramics. As can be seen only Li_2O and $LiAlO_2$ show a notable increase of the pellet stack length by swelling.

Fig. 4.6.4.3 depicts a metallographic cross section of Li-orthosilicate pellets (density: 90 % TD irradiated in HFR/Petten at 400-450 °C ELIMA 2, Matrix I, Tab. 4.6.4.2). The porosity is situated mainly at the corners of the grains. Fig. 4.6.4.4 shows a fractography of the same specimen. The trace of the fracture is intergranular. With higher magnifaction a second phase (Li_2ASiO_3, $LiCO_3$) can be observed at the surfaces of the grains. Fig.4.6.4.5 depicts a polished surface of a Li-metasilicate pellets with the same irradiation conditions (ELIMA 2, Matrix I). Here the pores are distributed uniformely across grains and interfaces. The fractography (Fig. 4.6.4.6) reveals an intragranular fracture. The next two figures show samples irradiated between 650-700 °C (ELIMA 2, Matrix II). Fig. 4.6.4.7 shows a cross section of Li-orthosilicate with two different magnifications. The comparison with the specimen irradiated at the lower temperature shows no difference in the microstructure. With higher magnification (500 x) a second phase can be seen at the grain boundaries. Fig. 4.6.4.8 illustrates a Li-meta-silicate irradiated at the same temperature region (650-700 °C). We see a relative dense unchanged microstructure with pores distributed uniformely over the cross section.

The grain size of both Li-silicates seems to be similar for the two different irradiation temperatures. In addition the grain size is similar to that of the as-fabricated specimen: i.e. no irradiation induced grain growth is observed.

4.6.4.3 Tritium release from Li-meta- and orthosilicate from the experiments DELICE 02 and COMPLIMENT

In section 4.6.3 tritium annealing tests and general conclusions drawn are discussed. Here a few results of DELICE 02 and COMPLIMENT are presented.

In DELICE 02 high- and low-density meta- and orthosolicate pellets have been irradiated in the thermal flux of the OSIRIS reactor (Table 4.6.1.2). Tritium residence times τ determined by dividing the annealed tritium inventory by the calculated tritium production rate are given in Table 4.6.4. 3.

Firstly it can be seen that tritium release from orthosilicate is remarkably faster (residence times smaller) than from metalisicate. Secondly, tritium release from orthosolicate is essentially independed of the density. The very weak dependence of orthosilicate tritium release from density is confirmed by Fig. 4.6.4.9, where tritium release curves during annealing with 5 °C/min for high- (OSiH) and low-density (OSiL) orthosilicate, irradiated at about 700 and 435 °C, respectively, are compared. The release curves for OSiH and OSiL are generally very similar and the maximum release is observed at about the same annealing temperaure ($\approx$ 700 °C). It should be mentioned that for OSiH an appreciable diametral swelling of 2.6 % (irradiated at 700 °C) and 1,2 % (irradiated at 435 °C) was observed.

Whereas generally and also in DELICE, orthosilicate has a much faster tritium release than metasilicate, very surprisingly, in COMPLIMENT-ELIMA-2 (Table 4.6.4.2), the KfK orthosilicate pellets (samples 109, 110) had a comparatively high inventory and slow tritium release (fig. 4.6.4.10) as the KfK metasilicate pellets (samples 101, 102).
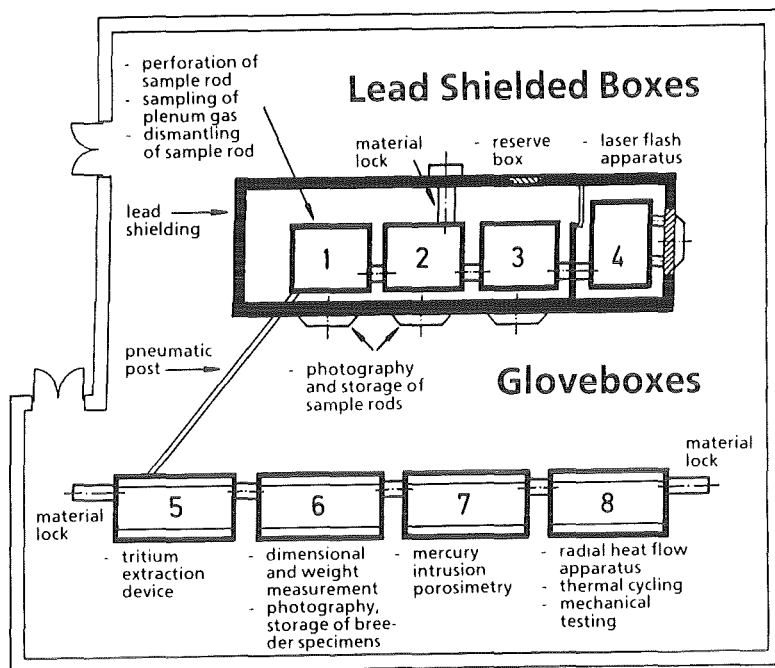
Fig. 4.6.4.1   Fusion ceramic laboratory (FKL)

	ELIMA 2	DELICE 03
Test reactor Neutron flux	HFR / Petten Cd-screened	OSIRIS / Saclay thermal
Begin of irradiation End of irradiation	April 1988 January 1989	October 1988 February 1988
Full power days [FPD]	178	77
Temperature, Matrix I + III Temperature, Matrix II + IV	400 to 450 °C 650 to 750 °C	
Lithium burnup	~ 0.25 %	~ 1 %
Radiation damage . by fast neutrons . by (α + t) particles . total	 1.6 dpa 0.2 dpa 1.8 dpa	 1.1 dpa 0.7 dpa 1.8 dpa

Table 4.6.4.1   Irradiation data of COMPLIMENT

	ELIMA 2 / HFR-Petten		DELICE 03 / OSIRIS-Saclay		Sum of samples
	Matrix I 400 - 450 °C	Matrix II 650 - 700 °C	Matrix III 400 - 450 °C	Matrix IV 650 - 700 °C	
CEA, Saclay	$LiAlO_2$ 78 %*) P 139**) $LiAlO_2$ 78 % P 140 $LiAlO_2$ 62 % P 141 $LiAlO_2$ 84 % P 142	$LiAlO_2$ 78 % P 143 $LiAlO_2$ 78 % P 144 $LiAlO_2$ 62 % P 145 $LiAlO_2$ 84 % P 146	$LiAlO_2$ 78 % P 147 $LiAlO_2$ 78 % P 148 $LiAlO_2$ 62 % P 149 $LiAlO_2$ 84 % P 150	$LiAlO_2$ 78 % P 151 $LiAlO_2$ 78 % P 152 $LiAlO_2$ 62 % P 153 $LiAlO_2$ 84 % P 154	16
ENEA, Casaccia	$LiAlO_2$ 80 % P 117 $LiAlO_2$ 80 % P 118 $LiAlO_2$ 80 % P 119	$LiAlO_2$ 80 % P 120 $LiAlO_2$ 80 % P 121 $LiAlO_2$ 80 % P 122	$LiAlO_2$ 80 % P 155 $LiAlO_2$ 80 % P 156 $LiAlO_2$ 80 % P 157	$LiAlO_2$ 80 % P 158 $LiAlO_2$ 80 % P 159 $LiAlO_2$ 80 % P 160	12
UKAEA, Springfield	Li_2O 83 % P 131 Li_2O 79 % P 132 Li_2ZrO_3 80 % P 123 Li_2ZrO_3 80 % P 124	Li_2O 80 % P 133 Li_2O 82 % P 134 Li_2ZrO_3 80 % P 125 Li_2ZrO_3 80 % P 126	Li_2O 79 % P 135 Li_2O 81 % P 136 Li_2ZrO_3 80 % P 127 Li_2ZrO_3 80 % P 128	Li_2O 82 % P 137 Li_2O 82 % P 138 Li_2ZrO_3 80 % P 129 Li_2ZrO_3 80 % P 130	8 8
CEN, Mol	Li_2SiO_3 82 % P 161 Li_2SiO_3 82% P 163 Li_2SiO_3 75% P 165	Li_2SiO_3 82 % P 162 Li_2SiO_3 75% P 166 Li_2ZrO_3 80% P 164	Li_2SiO_3 82 % P 167 Li_2SiO_3 82% P 169 Li_2SiO_3 75% P 171	Li_2SiO_3 82 % P 168 Li_2SiO_3 75% P 172 Li_2ZrO_3 80% P 170	10 2
KfK, Karlsruhe	Li_4SiO_4 98 % MS 173 Li_4SiO_4 85 % SS 113 Li_4SiO_4 90 % P 109 Li_2SiO_3 90 % P 101	Li_4SiO_4 98 % MS 174 Li_4SiO_4 85 % SS 114 Li_4SiO_4 90 % P 110 Li_2SiO_3 90 % P 102	Li_4SiO_4 98 % MS 175 Li_4SiO_4 85 % SS 115 Li_4SiO_4 90 % P 111 Li_2SiO_3 90 % P 103	Li_4SiO_4 98 % MS 176 Li_4SiO_4 85 % SS 116 Li_4SiO_4 90 % P 112 Li_2SiO_3 90 % P 104	4 4 4 4
Sum	18	18	18	18	72

*)   % Theoretical Density

**)   KfK Rod Number

P = Sintered Pellets
MS = Molten Spheres
SS = Sintered Spheres
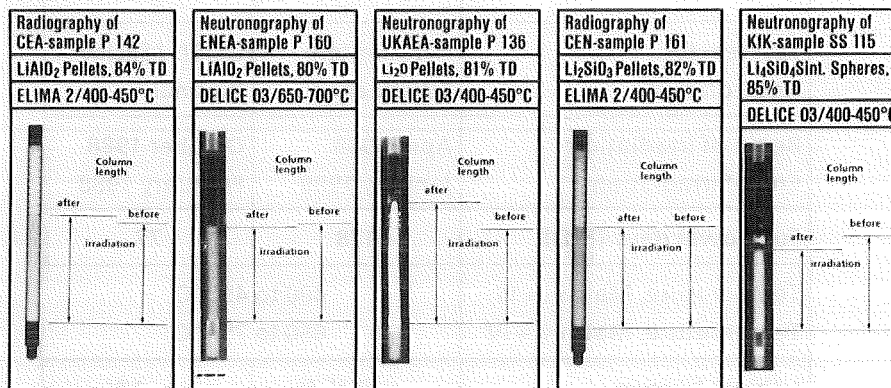
Table 4.6.4.2   The COMPLIMENT irradiation experiment

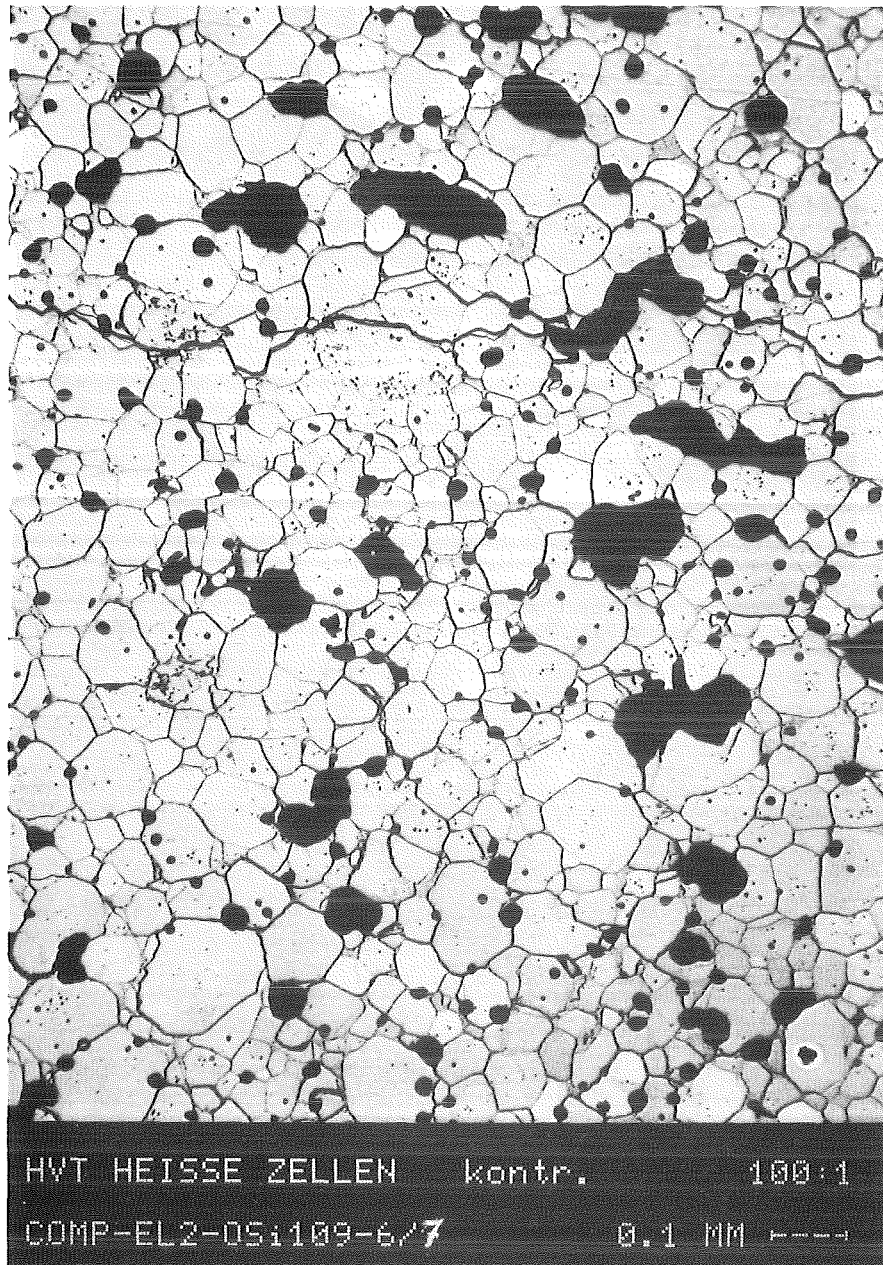Fig. 4.6.4.2   COMPLIMENT lenght change of Breeder colums

HVT HEISSE ZELLEN   kontr.   100:1
COMP-EL2-OSi109-6/7   0.1 MM ⊢——⊣

Fig. 4.6.4.3   Ceramographic section of Li$_4$SiO$_4$ sample P109 (cif. Table 2)
COMPLIMENT
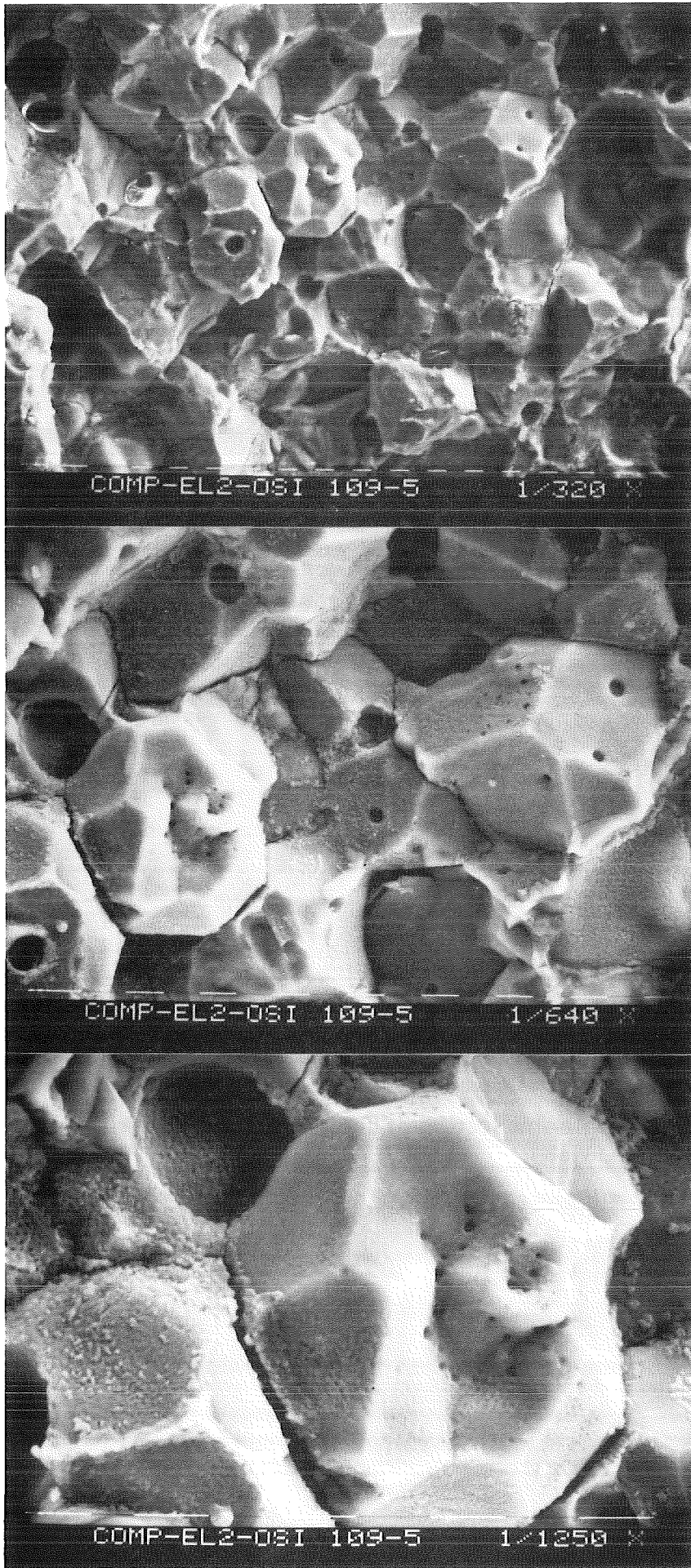
Fig. 4.6.4.4   same, fractography

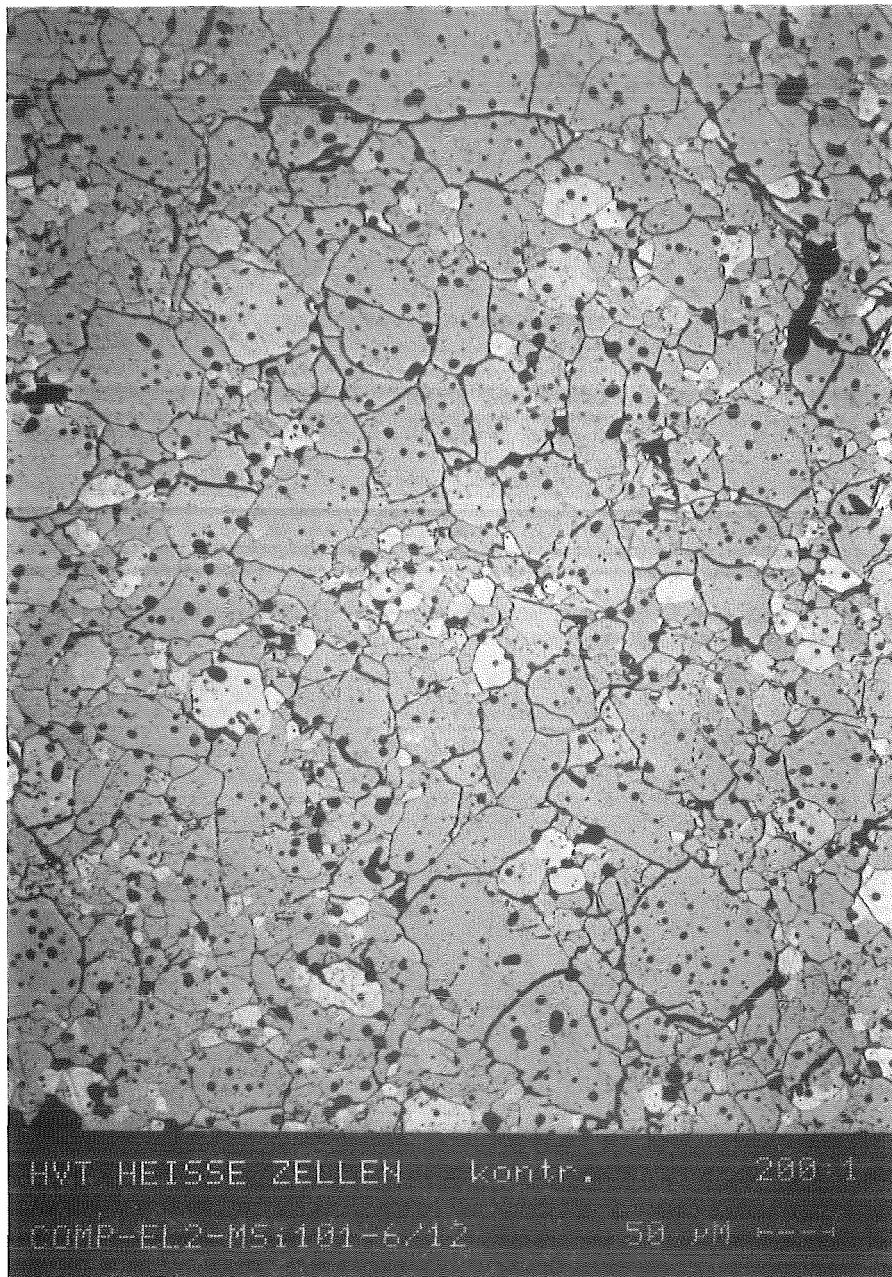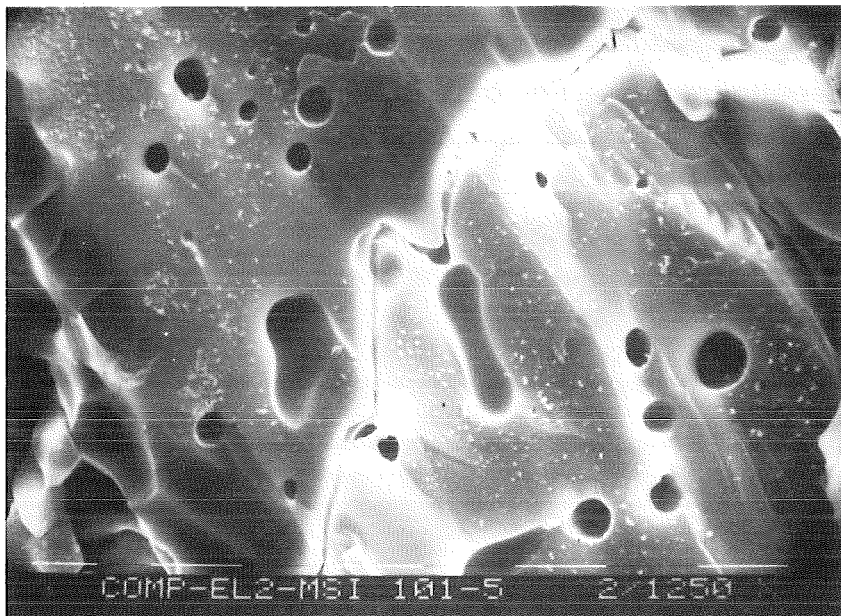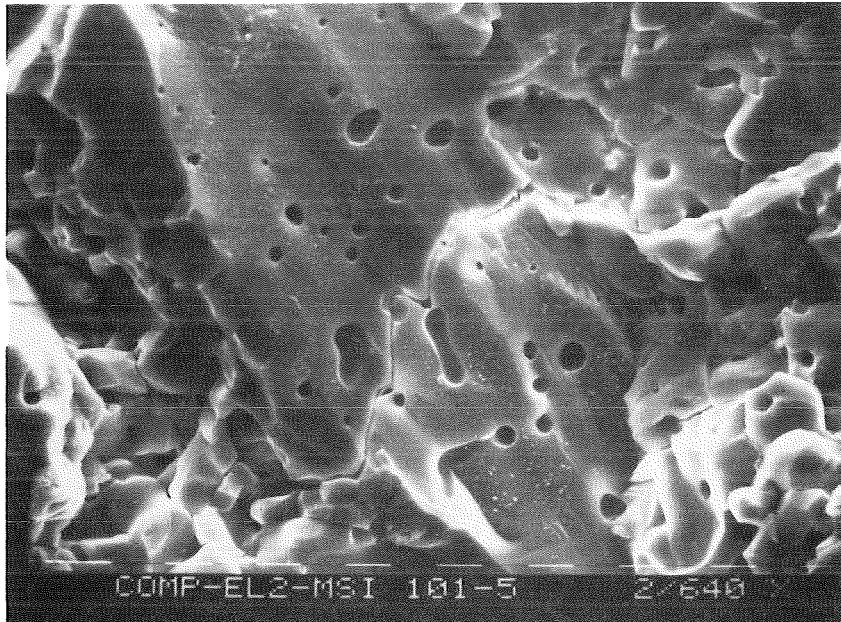Fig. 4.6.4.5   Ceramographic section of Li₂SiO₃ sample P 101 COMPLIMENT
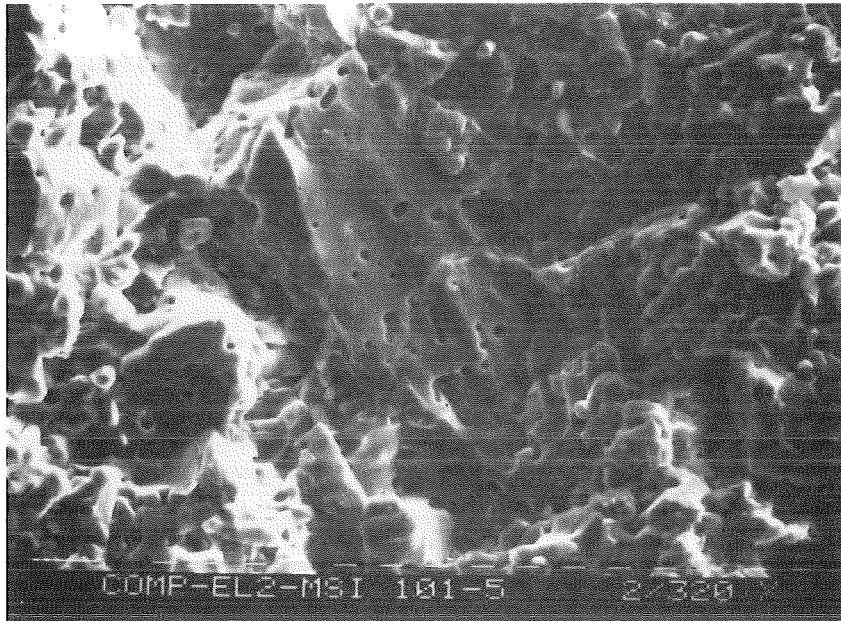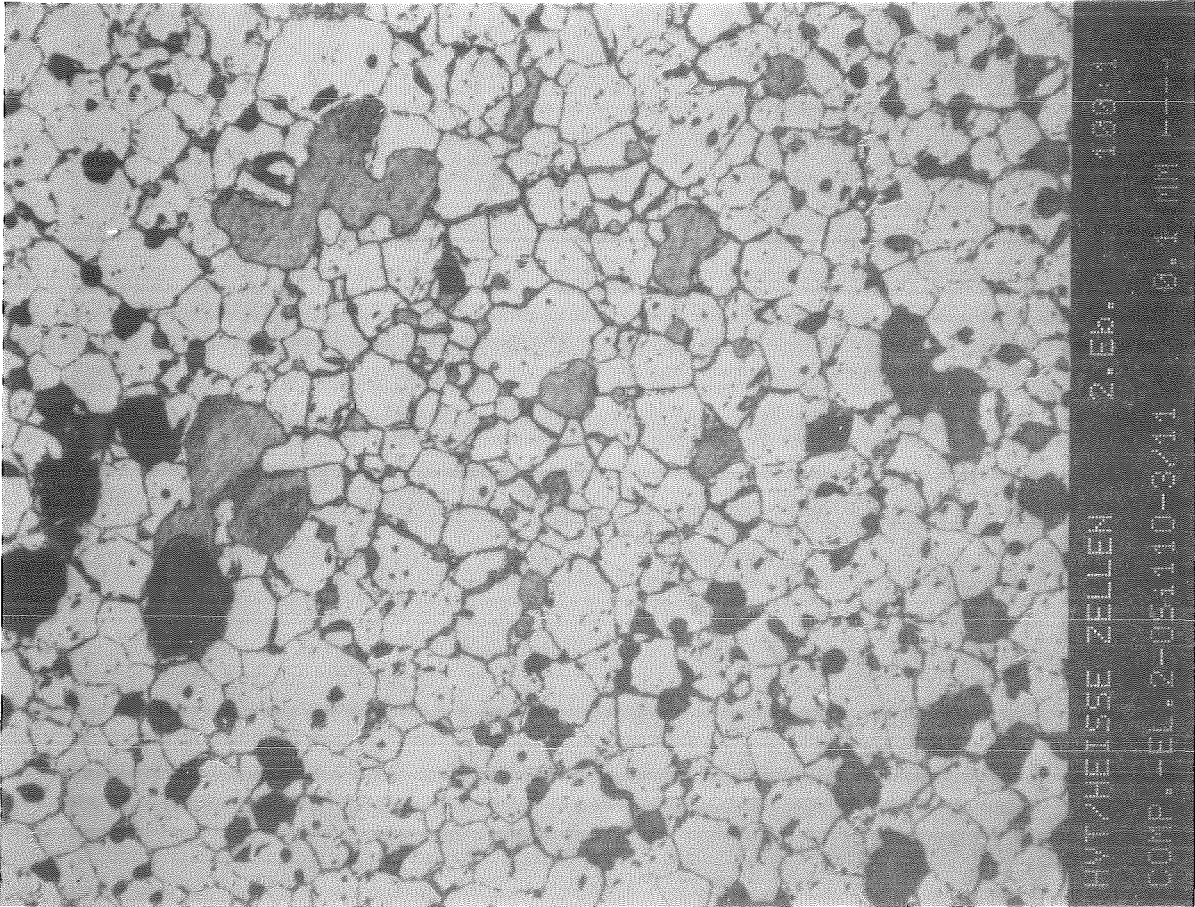
Fig. 4.6.4.6   same fractography

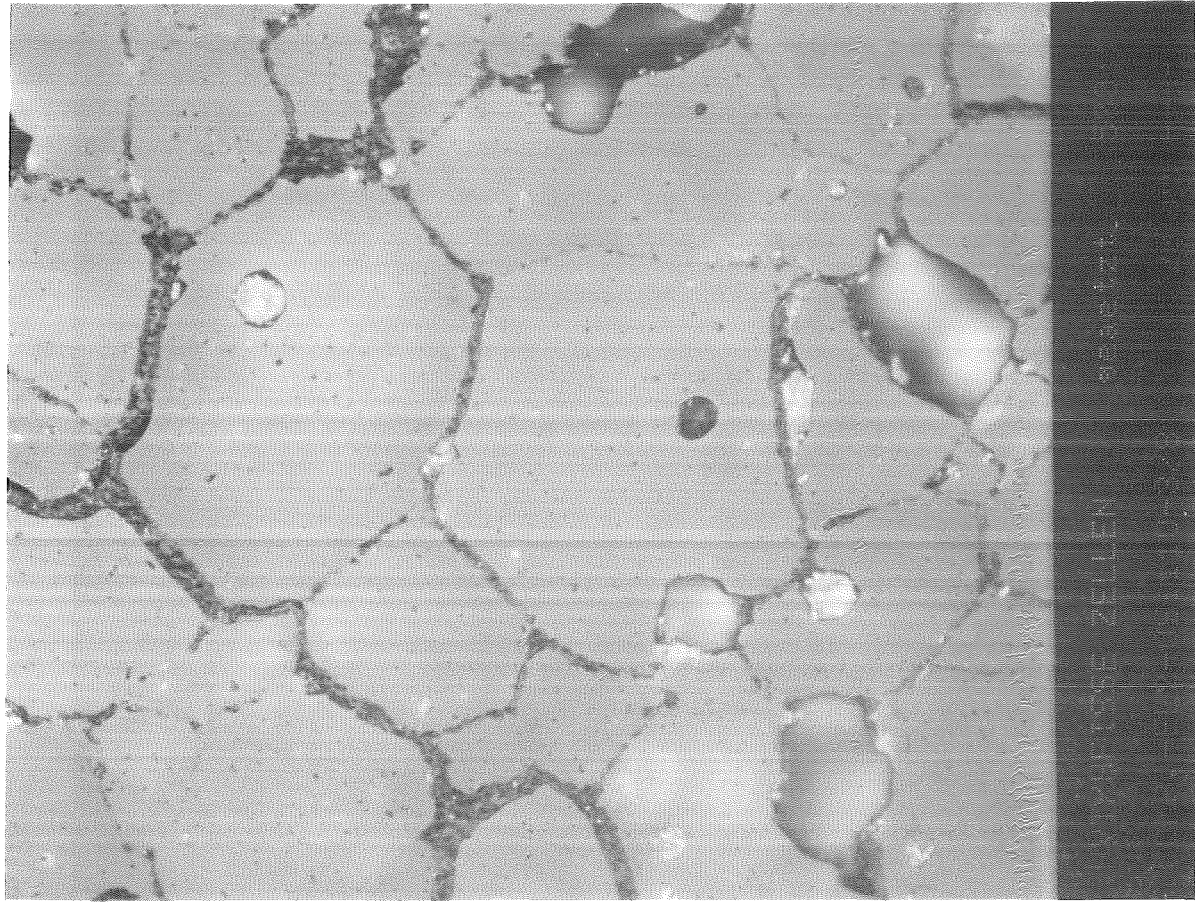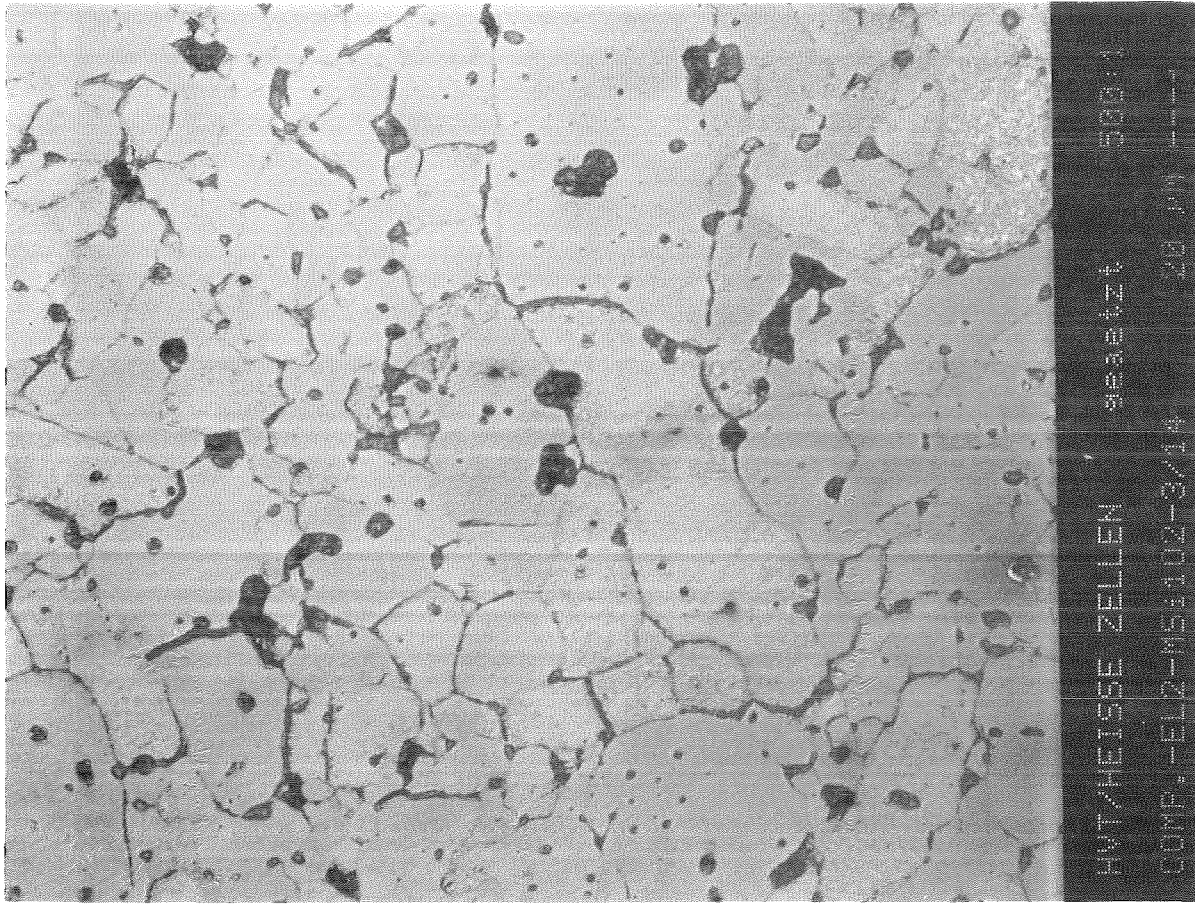Fig. 4.6.4.7   Ceramographic section of Li$_4$SiO$_4$ sample P 110 COMPLIMENT

Fig. 4.6.4.8   Ceramographic section of Li$_2$SiO$_3$ sample P 102 COMPLIMENT

Material	Sample No.	Irrad. Temp. °C	τ^*(h)
Orthosilicate 90 % T.D.	D1 D6	685-715 420-450	1,2 69
Orthosilicate 65 % T.D	C1 C6	685-715 420-450	2,5 64
Metasilicate 90 % T.D.	B1 B4	685-715 420-650	38 314

τ^* = $\dfrac{Inventory}{production\ rate}$

Table 4.6.4.3   Residence time τ for different Li-silicates of DELICE 02

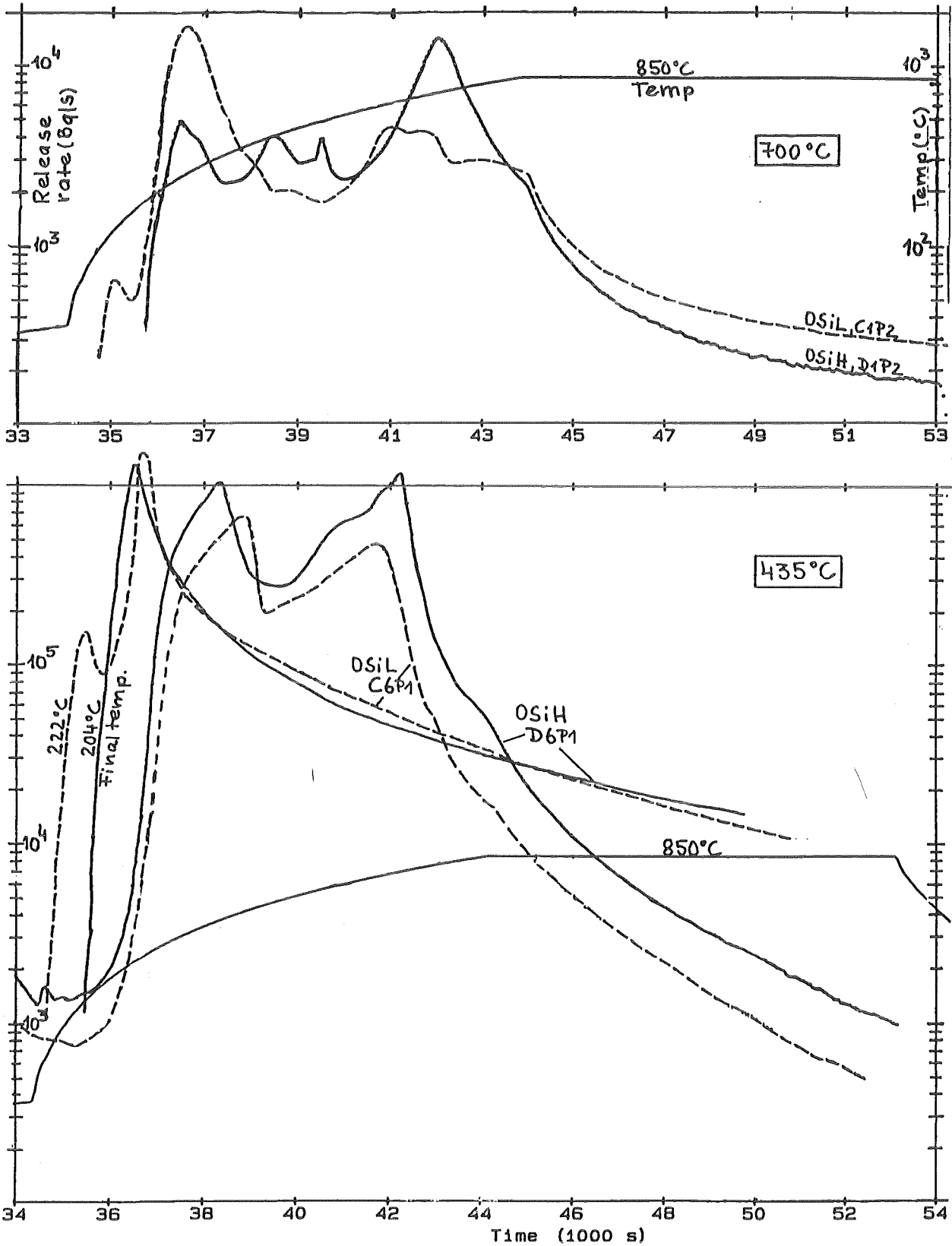Fig. 4.6.4.9   Comparison of tritium release from high (OSiH) and low (OSiL) density orthosilicate of DELICE 02 during annealing with 5 °C/min. and He + 0,1 % H₂ purge gas (TOP: Irradiation temperature 700 °C, Bottom: irradiation temperature 435 °C)
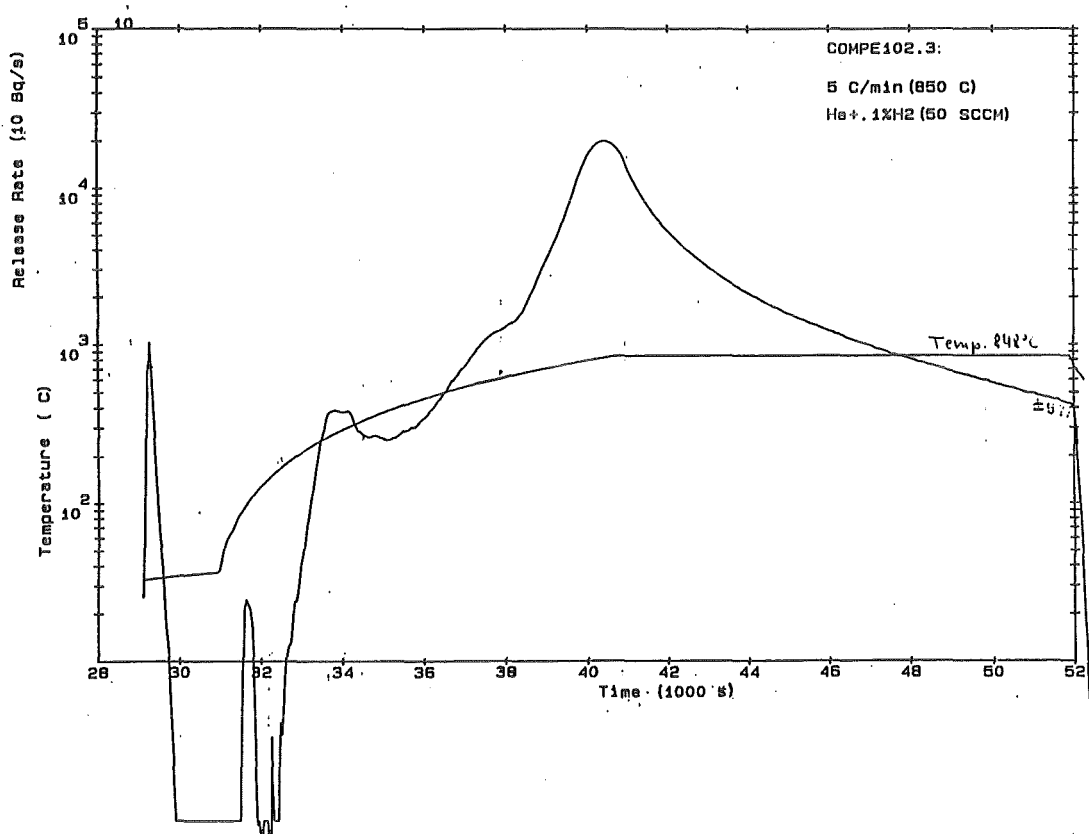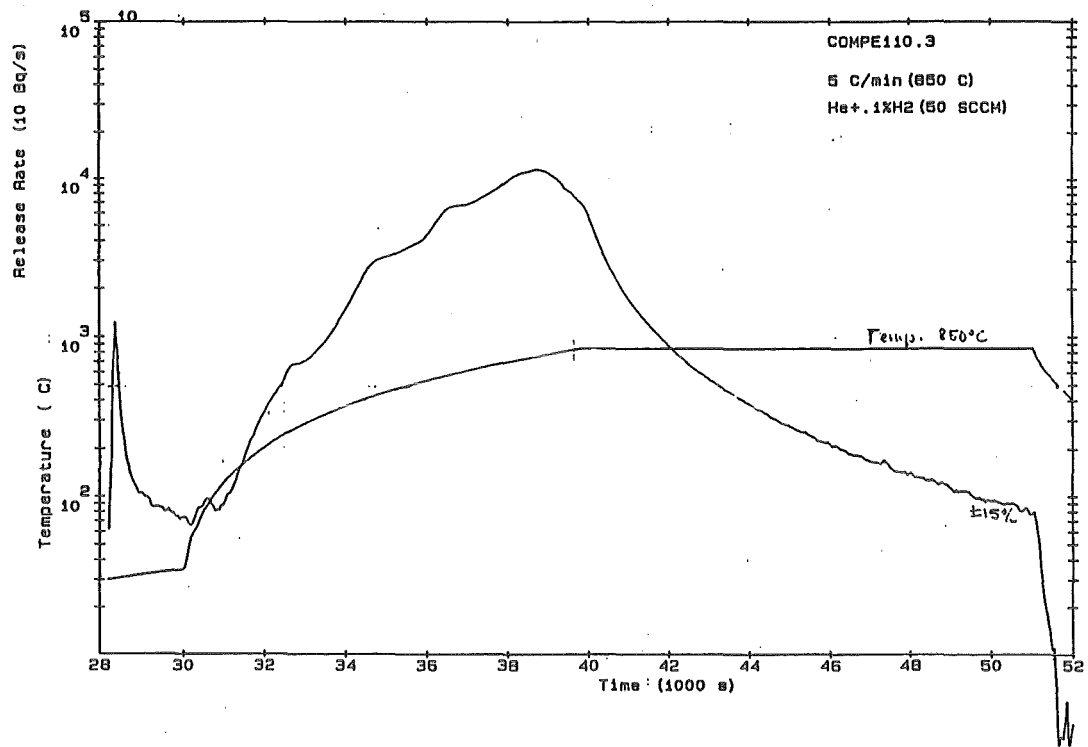
Fig. 4.6.4.10   Comparison of tritium release from ortho-(top) and metasilicate (bottom) of COMPLIMENT during annealing with 5 °C/min. and He + 0,1 % H₂ purge gas

4.7   Beryllium

4.7.1   Beryllium properties (M. Küchle)

4.7.1.1 Introduction

No material property measurements were made at KfK but the existing data were evaluated and best values were recommended for use in the EC-DEMO reactor blanket studies. This data base should not be used for engineering design of the blankets but only for the comparison of concepts.

A recommendation of beryllium properties is difficult because the measured properties are unique to a particular specimen /1/, batch to batch variations were observed and the properties depend on many parameters, including:

1.   fabrication process,
2.   grain size
3.   impurities
4.   direction of forces (longitudinal, transversal)
5.   temperature
6.   strain rate, load time
7.   porosity
8.   irradiation
9.   test procedure

The dependence on these parameters often is not separable and much more data would be needed for a real assessment than are presently available. Moreover, important changes in manufacturing beryllium powder product have improved the mechanical properties significantly since 1970 and a number of products with different material properties are on the market /2/. The bulk of information on irradiated material refers to products fabricated prior to this time, however. Materials favourable with respect to strength may not be so with respect to brittleness or irradiation resistance.

We assume that the best material available will be used for fusion applications and some improvements may be made in the future. Thus, we will not use the "minimum assured" values here but the best data. This refers to points 1 to 3 above. As regards orientation both values will be given if they are available and if significant differences exist. The temperature dependence will be given explicitly, low strain rate long load time data are generally more relevant to the fusion application. As was shown in /1/ and /17/ there is no advantage of using porous material, thus only high density material data will be reported. The impact of irradiation is the crucial issue and will be discussed in subsection 4.7.4.

Some compilations on data of unirradiated beryllium are available in the literature /1-8/, the basic reference here is /2/.

4.7.1.2. Physical and thermal properties

Atomic weight

Unirradiated beryllium consists to 100% of ^{9}Be with the atomic weight of 9.013 g/mol.

Density

The calculated density of pure beryllium is 1.8477 g/cm^3, the theoretical density of high purity block is

$$\rho = 1.855 \text{ g/cm}^3$$

The composition of this material is

BeO	C	Fe	Al	Si
%	ppm	ppm	ppm	ppm
0.9	200	250	70	60

Specific Heat

An equation for the specific heat is given in /2/, it refers to pure metal.

$$c_p = 2.353 + 0.632 \ 10^{-3} \ T + 0.107 \ 10^{-6} \ T^2 - 0.652 \ 10^5 \ T^{-2} \quad \text{(kJ/kg K)}$$

$$T(K) \qquad 300 < T < 1530K$$

Fig.4.7.1.1 shows the temperature dependence of c_p.

Melting Point

The same value is quoted in many references namely

$$T_m = 1283°C$$

Vapour Pressure

The vapour pressure of beryllium is very low. An equation is given in /2/. It reads

$$\log p = 6.186 + 1.454 \ 10^{-4} T - 16734 \, /T \ (\text{Atm})$$

T(K)

This corresponds to the following data:

T(°C)	700	800	900	1000
p(Pa)	$1.35 \ 10^{-6}$	$5.58 \ 10^{-5}$	$1.23 \ 10^{-3}$	$1.68 \ 10^{-2}$

Thermal Conductivity

There is a scattering of measured data, most referring to normal purity material. Fig. 4.7.1.2 shows a curve which is depicted from a graph of several curves given in /2/ the higher values were taken here.

Thermal conductivity will be reduced by porosity. It is recommended in /1/ to take this into account by a factor (1-p).

Electrical Resistivity

The curve given in /2/ is reproduced here as Fig. 4.7.1.3. The values agree to those given in /6/, slightly higher values are reported in /1/.

Thermal Expansion

Due to the anisotropy of the lattice structure the material expands differently in the directions parallel and normal to the pressing direction /2/. For the isotropic material the effect is negligible. In /7/ the following equation is proposed to describe the temperature dependence:

$$\alpha_m = 8.43 \ (1 + 1.36 10^{-3} T - 3.53 \ 10^{-7} T^2) \ 10^{-6} \ (K^{-1})$$

T(K)

It is illustrated in Fig.4.7.1.4 The values fall between two curves given in Fig.IV.1 of /1/.

4.7.1.3. Mechanical properties

Young's Modulus

In /7/ the following equation is proposed to describe the temperature and porosity dependence of beryllium:

$$E = 297 \exp (-3.5 \, p) \ (1 - 1.9 \ 10^{-4} (T - 293)) \ \text{GPa}$$

T(K)   p = vol. fraction of pores

In Fig. 4.7.1.5 E is plotted versus temperature with p as parameter. The room temperature value for zero porosity agrees well with data quoted elsewhere.

Poisson's Ratio

According to /2/ at low stress level in the elastic region Poisson's ratio is about 0.06-0.08. This is also quoted in /1/ and /6/. In /7/ a value of

$$v = 0.07$$

is recommended. This is also recommended here. In the plastic region the value increases to

$$v = 0.50$$

Yield Strength

Like other mechanical properties the yield strength of beryllium strongly depends on grain size and impurities. In a good approximation the yield strength $R_{p0.2}$ depends on the grain diameter d like /2/

$$R_{p0.2} \sim d^{-1/2}$$

For the fine-grain isopressed beryllium block which is assumed as the reference material here the temperature dependence of the yield strength is given in /2/. It is reproduced in Fig. 4.7.1.6. The directional dependence is small and can be neglected.

To better than 1% the curve of Fig. 4.7.1.6 can be described by the equation

$$R_{p0.2} = 370 - 0.302T + 10^{-4}(T-600)^2 \qquad \text{(MPa)}$$

T(°C)   0 < T < 500°C

Guaranteed minimum room temperatures tensile properties are given in /6/, with $R_{p0.2}$ for high purity material being 173 MPa compared to 398 MPa of Fig.6 which refers to an optimized material. According to the principles of this data base, which are explained in the introduction, the higher values are recommended here.

Ultimate Tensile Strength

For the ultimate tensile strength the situation is similar to the one for the yield strength. Again the data from /2/ are recommended and are reproduced in Fig. 4.7.1.6. They can be described by the equation:

$$R_m = 581 - 0.604\,T \quad (\text{MPa})$$

$$T\,(°C) \qquad 0 < T < 500°C$$

The guaranteed minimum room temperature value from /6/ is here 242 MPa compared to 569 MPa from Fig. 4.7.1.6.

Compressive Strength

The data base is not very complete but compressive strength is higher than tensile strength. As a conservative assumption the same values as for tensile strength can be used /2/.

Elongation

No difference between uniform and total elongation is made in the literature. Ductility of beryllium is low at room temperature and is directional dependent. This is because slip can only occur along basal planes and therefore the basal planes will have to be oriented parallel to the tensile axis if the material is to have any ductility /11/. For the high purity, fine grain isopressed material the directional dependence is small and room temperature elongation is 4% /2/. The elevatad temperature elongation of this material is shown in Fig. 4.7.1.7 /2/. At high strain rates (5×10^2 sec^{-1}) strain to failure is about one-half the value measured in static testing. A detailed strain rate dependence is not available.

It is important to realize that high values of tensile elongation can be obtained even at room temperature during the uniaxial extension of highly textured sheet, rod or tube but that under conditions of biaxial or triaxial strain rapid failure may occur /24/.

Fracture Toughness

Fracture toughness of beryllium products is low. K_{Ic} for high purity block was reported to be 50% higher than that of normal purity /2/. This is accompanied, however, with a reduction in yield strength. Fig. 4.7.1.8 shows the temperature dependence for normal purity beryllium /2/, no other more relevant data are available.

K_{Ic} is load rate dependent and a dynamic value should be used for the disruption conditions, but no relevant data are yet available.

Inpact Strength

Only limited data on the Charpy impact energy are available, they are summarized in /2/ and seem all to refer to room temperature. Values from 0.2 J to 10 J are reported, averaging at

2.6 J /2/. However, there is generally no correlation between ductility and tests such as fracture toughness or Charpy /2/.

References

1.   MCCARVILLE ET AL. Technical Issues for Beryllium Use in Fusion Blanket Applications, UCID-20319 (1985)

2.   N.P. PINTO, Chapter 16 "Properties" in "Beryllium Science and Technology" Vol.2, edited by D.R. Floyd and J.N. Lowe Plenum Press 1979

3.   H.H. HAUSNER (Editor) "Beryllium: Its Metallurgy and Properties", University of California Press Berkley (1965)

4.   G. CHEVEREAU, "Revue Bibliographique des Proprietes du Beryllium en vue de son utilisation dans la converture de Reacteurs a Fusion" CEA Note EMT / SERMA / BP / (1984) / 84 / N° 1639"T" / 3591-21-000

5.   HUI PIH "A Survey of Beryllium Technology and Nuclear Applications" ORNL-4421 (1969)

6.   J.M. DUPOUY "On the Use of Metallic Beryllium as Multiplier in the Breeding Blanket" NET/IN/84-59 (1984).

7.   M.C. BILLONE AND W.T. GRAYHACK "Summary of Mechanical Properties Data and Correlations for Li_2O, Li_4SiO_4, $LiAlO_2$ and Be" ANL/FPP/TM-218 (1988)

8.   M.A. ABDOU ET AL. Chapter VII, US-FED/INTOR, ICFW-82-17 (1982)
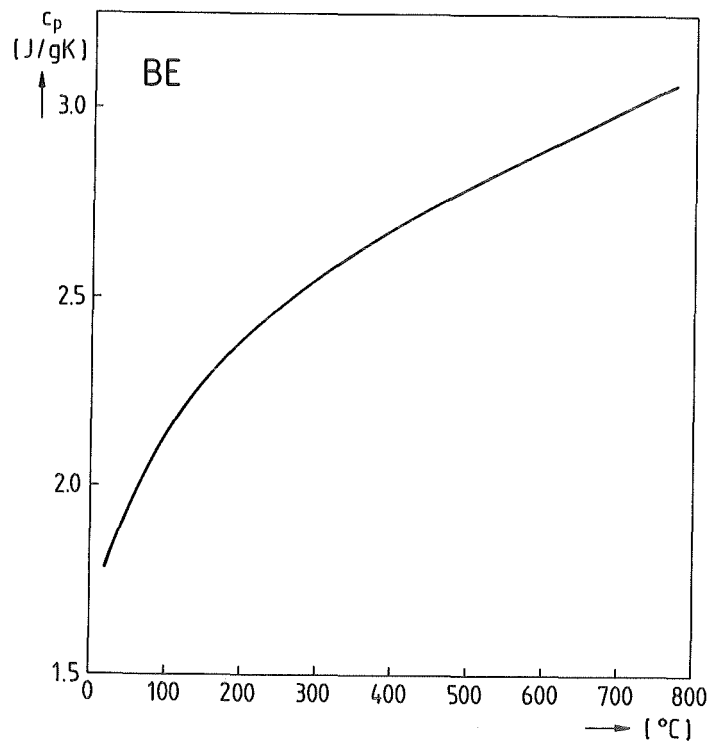
Fig. 4.7.1.1: Specific Heat

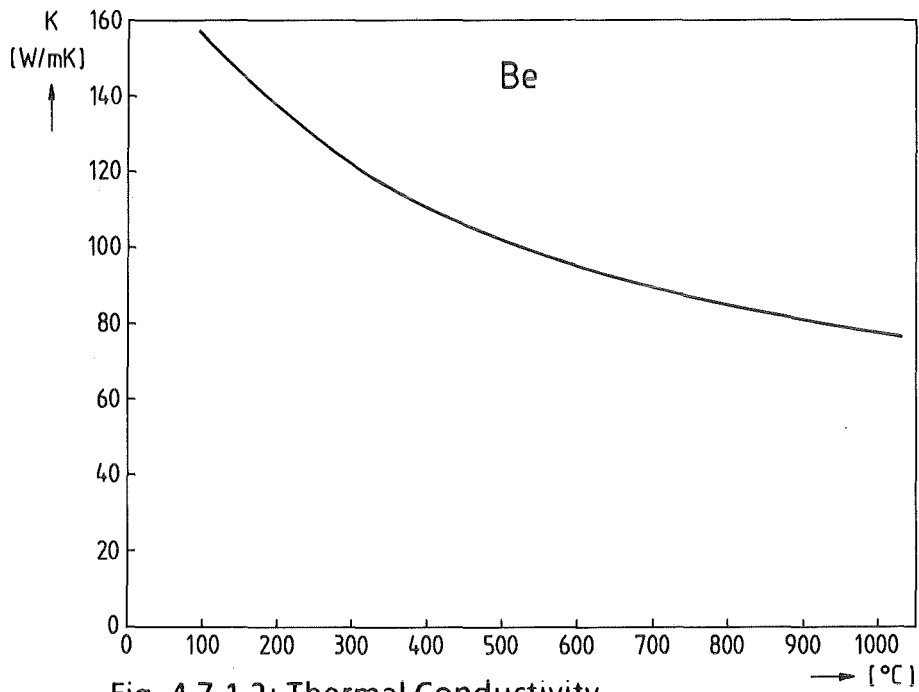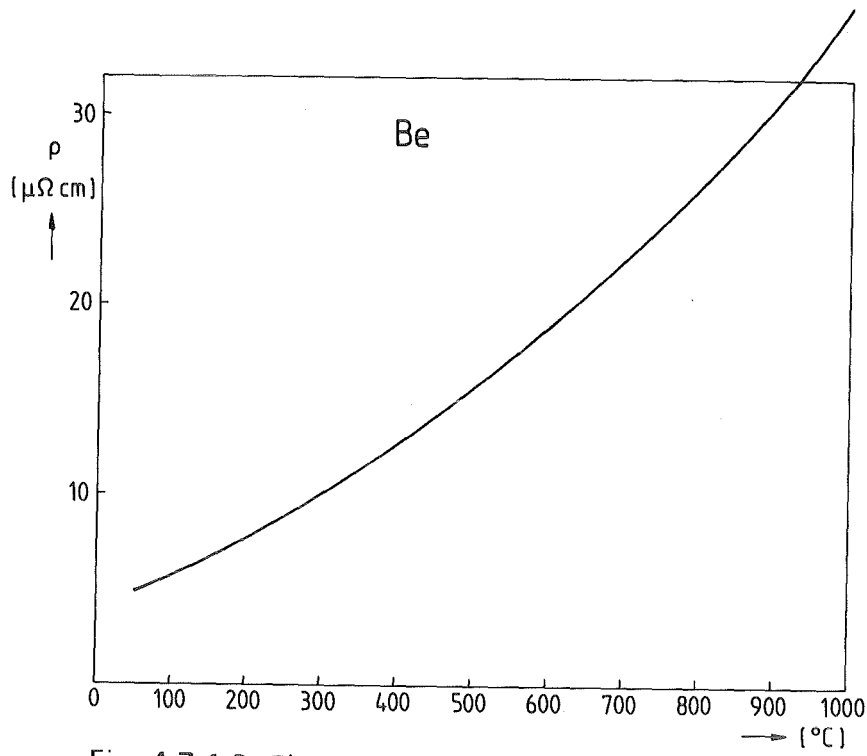Fig. 4.7.1.2: Thermal Conductivity
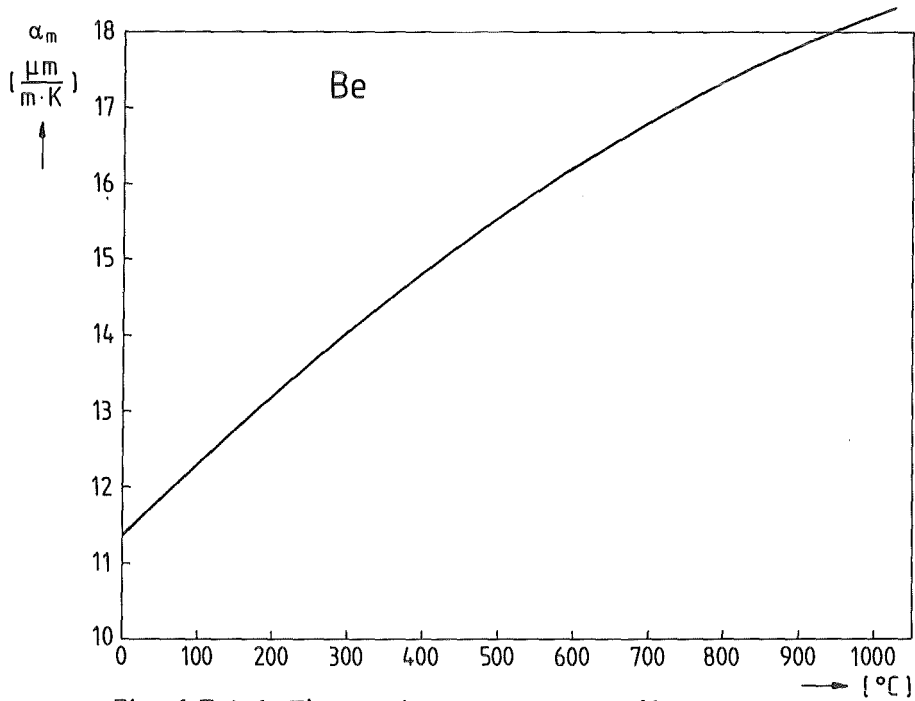
Fig. 4.7.1.3: Electrical Resistivity
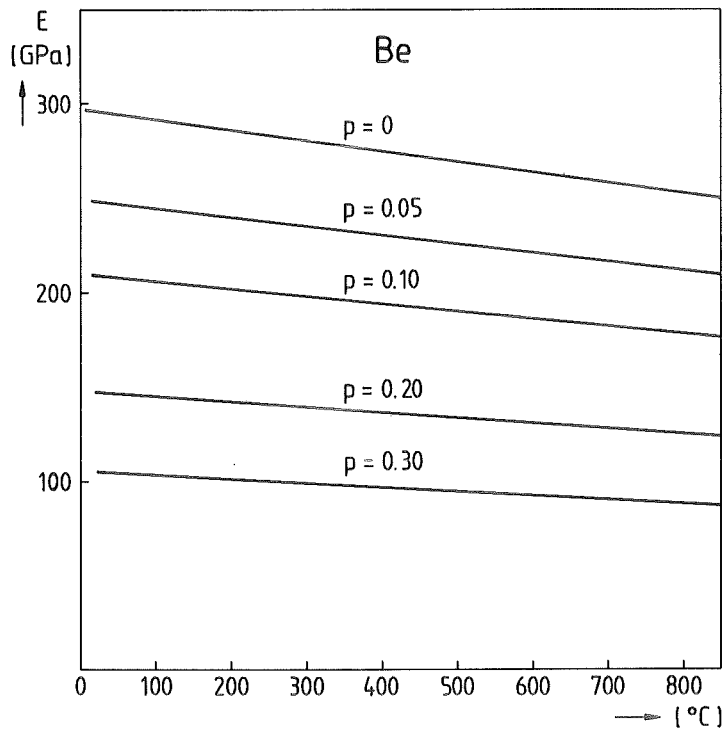

Fig. 4.7.1.4: Thermal Expansion Coefficient

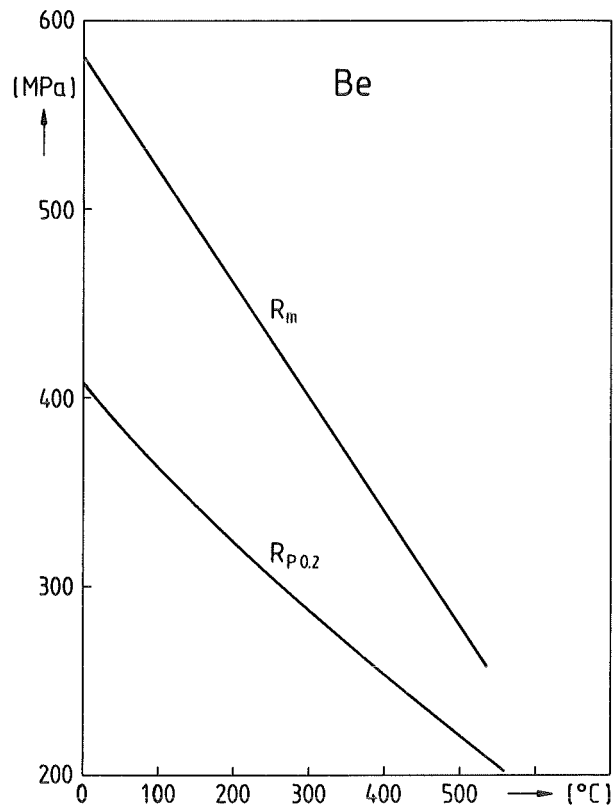Fig. 4.7.1.5: Young's Modulus,Porosity as
a Parameter

Fig. 4.7.1.6: Yield Strength $R_{p0.2}$
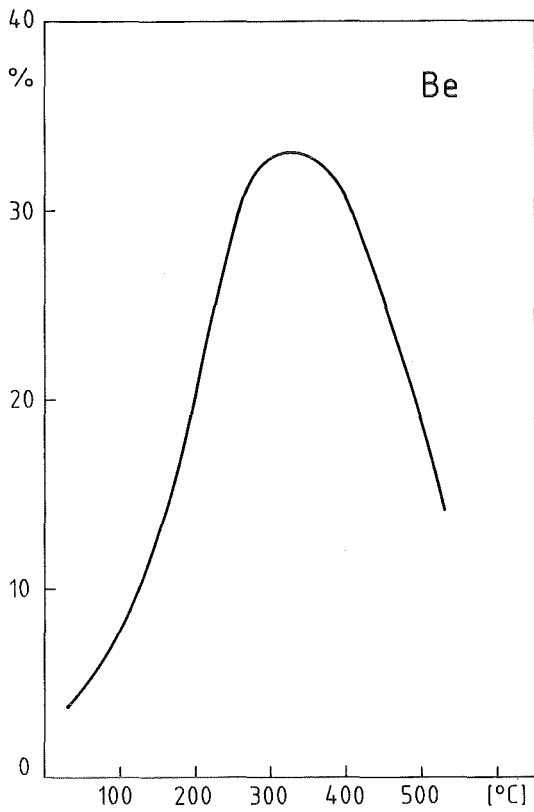and Ultimate Tensile
Strength R_m for fine-grain
Beryllium

Fig. 4.7.1.7: Elevated temperature
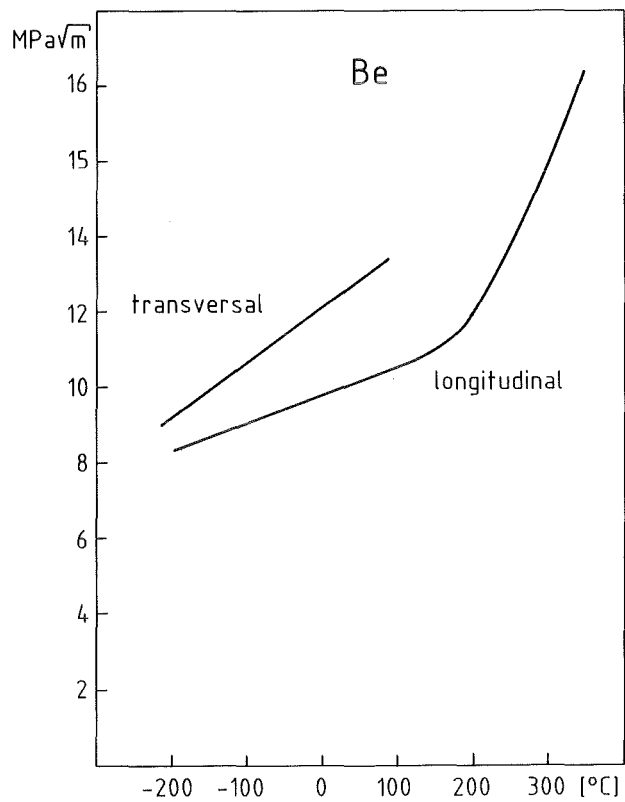elongation of fine grain
beryllium block

Fig. 4.7.1.8: Fracture Thoughness K_{Ic}

4.7.2 Out-of-pile compatibility with Li_4SiO_4 and structural materials (W. Dienst, P. Hofmann)

The chemical compatibility of Be with Li_4SiO_4, Li_2SiO_3 and stainless steel AISI 316 was investigated in the temperature range between 600 and 900 °C with annealing periods up to 1000 h [1]. Li_2SiO_3 and Li_4SiO_4 breeder pellets were used in the dried condition (2 h at 900 °C). The specimen configuration consisted of a stack of beryllium disks and Li_2SiO_3 or Li_4SiO_4 pellets in an annealing capsule made of stainless CrNi steel (AISI 316, 17 % Cr, 13 % Ni, 2 % Mo). The specimen stack was compressed by a hold-down spring. On the stack bottom beryllium was in contact with AISI 316 stainless steel so that also the compatibility of this material combination could be studied. After annealing the specimens were cut longitudinally and the two halves prepared metallographically. The depths of the reaction zones on the contact surfaces of the reaction couples were measured with an optical microscope. Some of the specimens were analyzed using an Auger microprobe analyzer and a scanning electron microscope (SEM).

No chemical interactions between Li_2SiO_3 and Be can be observed at 600 °C. The situation is probably similar for Li_4SiO_4 , but no experiments were performed at this temperature. At higher temperatures different types of reaction zones developed in the lithium silicates which can be broken down into uniform and locally restricted, but very deep attacks. Generally, the latter occur only after extended reaction periods and are more pronounced in the Be/Li_2SiO_3 system than in Be/Li_4SiO_4. At 650 °C, only localized chemical interactions can be observed even after 1000 h. Uniform continuous reaction zones along the Be/Li silicate contact surface can be observed at 750 °C and higher temperatures.

Reaction kinetics results of the Be/Li_4SiO_4 compatibility experiments are shown in Fig. 4.7.2.1. The figure shows the rate of uniform and of local, deep attack (the latter only at 750 °C) of the lithium silicate by Be as function of the square root of reaction time for temperatures between 600 and 900 °C. The chemical interactions can best be described by a parabolic rate law. In the temperature range of 650 to 750 °C, the test results cannot be correlated consistently for uniform attack. Therefore, they were combined into a scatter band. The uniform lithium silicate attack is approximately as fast on Li_2SiO_3 as it is on Li_4SiO_4, with maximum reaction zones of 25 µm thickness at 750 °C after 100 h annealing time. However, the localized very deep attack of the lihtium silicates in contact with beryllium determines the usability. The strong local attack of Li_2SiO_3 starts at about 700 °C, that of Li_4SiO_4 at about 750 °C, and the growth rates x^2/t are approximately one order of magnitude higher for Li_2SiO_3 compared to Li_4SiO_4.

Li_2SiO_3 and Li_4SiO_4 are thermodynamically unstable with respect to metallic beryllium; therefore, the described chemical interactions take place. The lithium silicates are reduced by beryllium while BeO is formed. The other main reaction products are Li_2BeSiO_4 and Li_xSi_y

[2]. The chemical composition of the lithium silicides Li_xSi_y depends on the system under consideration. The lithium silicides are partly liquid during reaction annealing and are the cause for the heavy local attacks of the lithium silicates. As any melting of the breeder material is not permissible under operating conditions, the maximum operating temperature of Li_2SiO_3 in contact with beryllium must be limited to 650 °C, that of Li_4SiO_4 to 700 °C.

At all temperature levels studied, particular grain boundary attack of beryllium took place at those points where the solid contact between beryllium and steel was not satisfactory. The reasons for that have not yet been clarified. They might lie in an attack via the gas phase by lithium and/or oxygen. Be-Li-O compounds might be formed. The maximum reaction depths in beryllium were 100 µm after 1000 h at 750 °C in the presence of Li_2SiO_3.

All the reaction rates determined on Be/Li_4SiO_4, Be/Li_2SiO_3, and also on Be/AISI 316 couples are presented in Fig. 4.7.2.2. Concerning the latter reaction system, beryllium diffuses into steel and reacts with nickel, forming a BeNi compound. Analyses with Auger microprobe showed substantial depletion in nickel of the steel matrix due to the formation of BeNi. The nickel depleted reaction zone is also visible on metallographic images.

Chemical interactions of beryllium with AISI 316 steel occur already at 600 °C. However, the reaction proceeds ony locally at that temperature level, and after 1000 h annealing time it attained a maximum depth of 25 µm. The results at 600 °C are comparable with data in the literature [3] according to which after 500, 1000 and 2000 h annealing time thicknesses of reaction layer of 13, 25 and 50 µm have been observed. At 650 °C the depth of attack after 1000 h is 50 µm at the maximum. Therefore, 600 °C should be considered as the safe maximum operating temperature at Be/stainless steel contact faces.

The conclusion concerning Be/AISI 316 compatibility was corroborated in experiments of the French partners [4], where similar reaction penetration depth was observed at 600 °C, but even deeper penetration (100 - 200 µm after 500 h) at 700 °C. It is particularly interesting that these experiments included reaction couples of beryllium with martensitic-ferritic steels (HT9, 1.4914). No reaction phenomena could be observed in such steels at 600 °C, and at 700 °C the reaction penetration depth in 1.4914 (30 µm after 500 h) was much smaller than in AISI 316 (see above) which could be due to the nickel content of AISI 316 (13 %).

For the ITER Blanket Materials Data Base [1,3,5], a linear time dependence has been considered for the penetration depth of the Be/AISI 316 reaction. The recommended correlation is:

$$x = 6.58 \times 10^4 \, \mu m/h \, exp \, (-1.29 \times 10^4/T) \, t$$
$$823 \leqq T \leqq 1173 \, K, \, 100 \leqq t \leqq 3000 \, h$$

References

[1]   P. HOFMANN, W. DIENST
       Chemical interactions of beryllium with lithium-based oxides and stainless steel.
       J. Nucl. Mater. 171 (1990) 203-214

[2]   O. GÖTZMANN
       Thermodynamics of ceramic breeder materials for fusion reactors.
       KfK 4567 (1989)

[3]   W. VICKERS, in:
       Proc. Int. Conf. on The Metallurgy of Beryllium, Institute of Metals Monograph and
       Report Series No. 28 (1961) p. 335.

[4]   T. FLAMENT, P. FAUVET, J. SANNIER
       Compatibility of stainless steel and lithiated ceramics with beryllium
       J. Nucl. Mater. 155-157 (1988) 496-499

[5]   M. BROC, T. FLAMENT, A. TERLAIN, J. SANNIER
       Compatibility problems in tritium breeding blankets
       J. Nucl. Mater. 179 - 181 (1991) 820 - 823
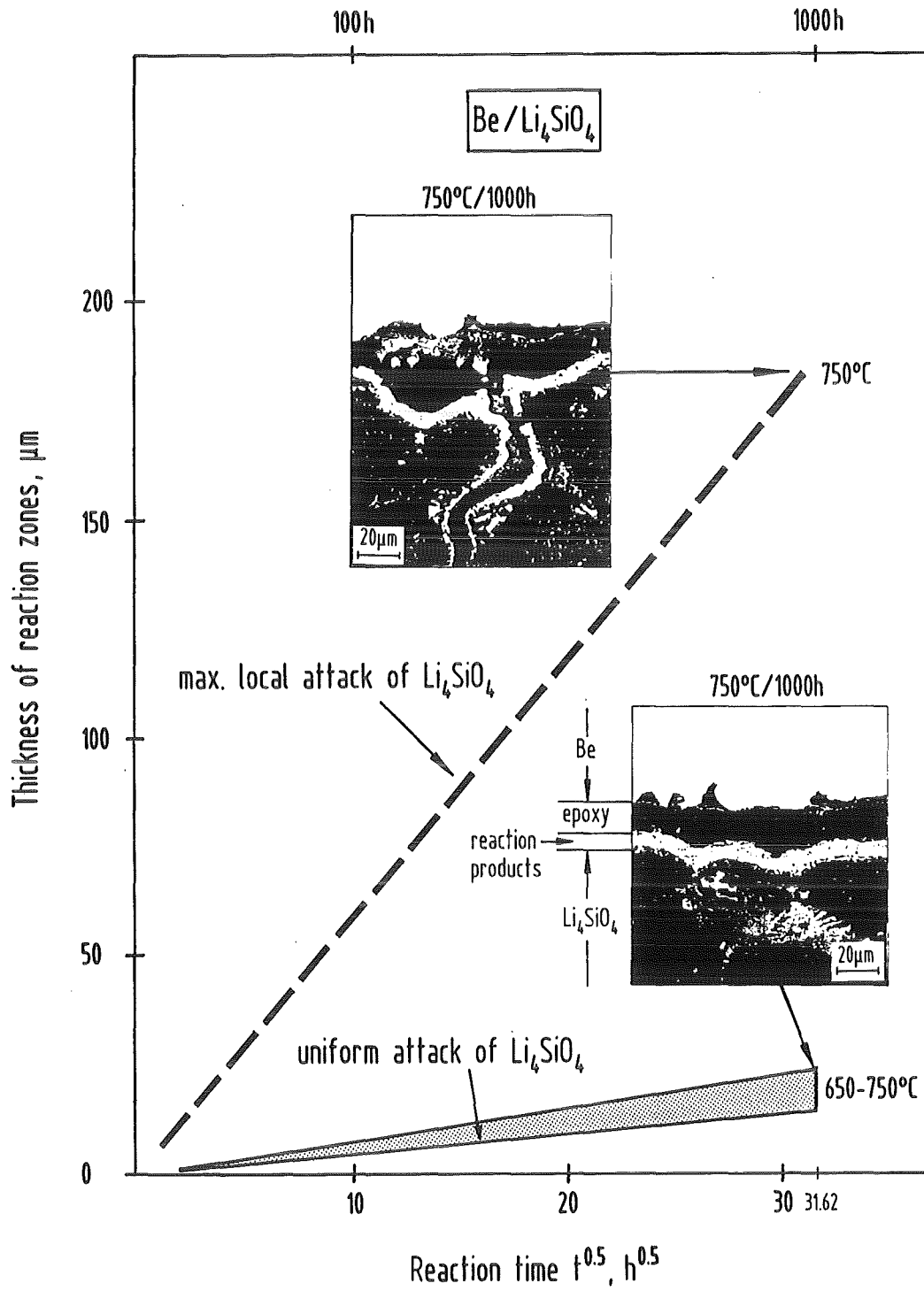
Fig. 4.7.2.1: Chemical interactions between Be and Li$_4$SiO$_4$.

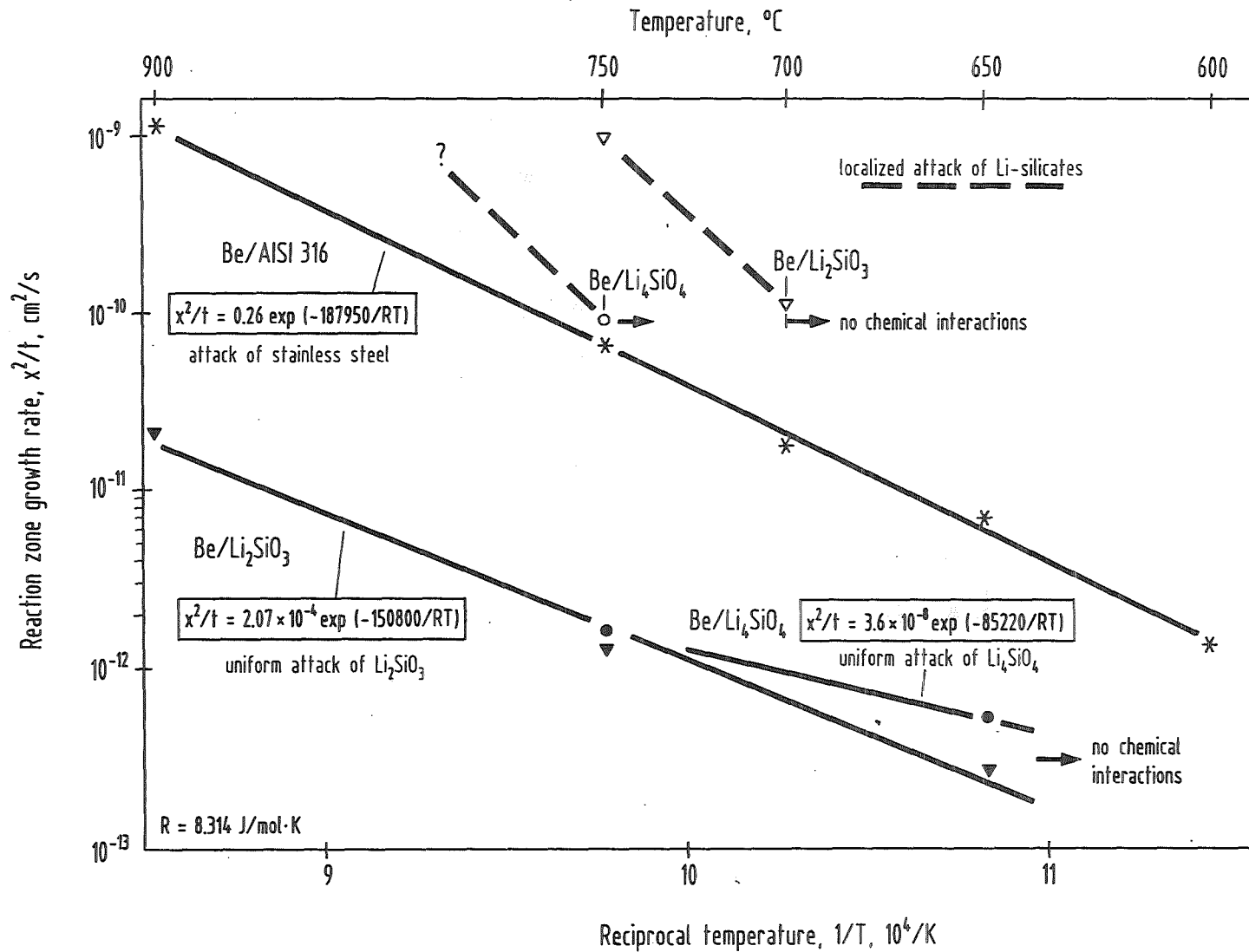**Fig. 4.7.2.2** : Reaction zone growth rates for the material couples Be/Li$_2$SiO$_3$, Be/Li$_4$SiO$_4$ and Be/AISI 316 stainless steel.

4.7.3 Inpile compatibility with Li$_4$SiO$_4$ and structural materials: SIBELIUS (H. Werle)

To address the inpile compatibility of Be with other blanket materials, the ECC-USA collaborative experiment SIBELIUS [1] has been performed in the SILOE reactor at Grenoble.

The primary objective is to assess the ceramic /Be/ steel compatability in a neutron environment. In addition, the influence of Be/ ceramic contact on ceramic tritium release as well as swelling, tritium release and He retention of Be is studied.

Four ceramics (LiAlO$_2$, Li$_4$SiO$_4$, Li$_2$ZrO$_3$ and Li$_2$O), two steels (316 L austenitic and 1.4914 martensitic) and three types of Be (Brush-Wellman: type B26, vacuum casting, <300 ppm BeO for compatibility tests; type O-50, hot pressed, 2800 ppm BeO and type S-65, hot pressed, 7000 ppm BeO for swelling and gas retention studies) are investigated. The Li$_4$SiO$_4$ samples (disks and spheres) were supplied by KfK.

Intimate contact is required for solid / solid interaction studies. Therefore samples with parallel surfaces and best achievable surfaces state are required. The ceramic specimens were characterized by CEA for density, chemical purity and microstructure. In addition, the surface state of all specimens were checked in microroughness tests. In order to evidence any irradiation effect on compatibility behavior, out-of-pile tests were performed by CEA in conditions identical to the SIBELIUS ones.

Eight capsules were irradiated (Fig. 4.7.3.1): five with stacks of flat disks of ceramic (1.5 mm), Be and steel (2 mm), including one with a shallow layer of Li$_4$SiO$_4$ spheres, two with ceramic only (LiAlO$_2$ and Li$_2$O), as reference to check Be influence on ceramic tritium release and one with Be only for swelling and gas retention studies.

All capsules, except that with Be only, were swept with He + 0.1 vol% H$_2$. The irradiation temperature was 550 °C, except for the capsule with Li$_4$SiO$_4$ spheres, which was at 450 °C. The thermal flux was 8 x 10^{13} and the fast (> 1 MeV) flux 9 x 10^{13} 1/cm^{2}s. The irradiation time was 1690 h, yielding a ^{6}Li burnup of 20 - 25 % and 0.7 dpa in Be.

Inpile tritium release at constant temperature did not show any unexpected phenomena. The results of a few temperature transients performed at the end of irradiation were:

1. From comparisons with the ceramic only sample it can be concluded that for LiAlO$_2$ there was no significant effect of Be on tritium release.

2. For Li_2ZrO_3 tritium release was similar as in previous inpile tests, indicating that also for this material tritium release is not significantly affected by Be.

3. For the Li_4SiO_4 pellets residence times of several h at 550 °C and of $>$ 100 h at 460 °C are estimated. Because reference data at beginning of irradiation or from ceramic only samples are not available, it is not clear if this pretty slow release is caused by Be or if it is characteristics for this charge. We tentatively assume that it is sample-characteristic because a similar slow release was observed for a few other Li_4SiO_4 charges in previous inpile tests (see section 4.6.3).

Extensive post-irradiation examinations at the involved laboratories (ANL, CEA and KfK) are planned and will include

- detailed examinations of Be/ceramic and Be/steel interfaces using optical microscopy, SEM, EPMA and SIMS

- phase identification of ceramics by x-ray diffraction

- measurement of tritium and He contents in ceramics and Be

- determination of Be swelling by dimensional measurements and immersion density.

Any irradiation effect on compatibility will be identified by comparison with out-of-pile tests carried out under conditions identical to SIBELIUS.

The first results from visual inspection of the Sibelius compatility irradiated samples indicate that at 550 °C there was no reaction between Li_4SiO_4 and Be, and only a slight reaction at the interfaces Be-Manet and Be-316 L.

Reference

[1] N. ROUX, M. BRIEC, M. BRUET, T. FLAMENT, C. JOHNSON, M. MASSON, A. TERLAIN, F. TOURNEBIZE, "The SIBELIUS Experiment: Study of the Irradiation Behaviour of Beryllium/Ceramic and Beryllium/Steel Compacts", to be published in J. Nucl. Mater.
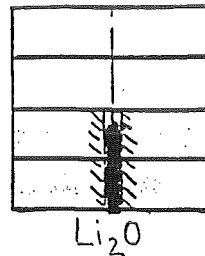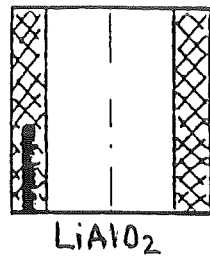
Fig. 4.7.3.1 Loading of SIBELIUS capsules

4.7.4   Irradiation effects (M. Küchle)

Beryllium has been used as a reflector and moderator in low temperature material testing reactors and was also considered for fuel cladding in power reactors. In this context the properties of irradiated beryllium were investigated at several places (see for instance / 1 - 10). This forms the bulk of information presently available on properties of irradiated beryllium but it suffers from some drawbacks:

1.   The measurements generally refer to hot pressed blocks with modest purity. This material exhibits a relatively large anisotropy, low ductility and large swelling. A significant beryllium development took place since 1970 leading to a fine grain, high purity material with improved properties.

2.   The irradiations often were made at low temperature ($\approx$ 100 °C) with post irradiation annealing at various temperature levels. This may be different from an irradiation at elevated temperature.

3.   The irradiations were made in fission reactors where the helium production is smaller for the same fast fluence than it is in fusion reactor blankets. The range relevant to Demo is not covered by the tests.

Neutronic calculations for different systems revealed roughly the following ratios:

-   for fusion systems   7000 appm He / 10^{22} cm^{-2}

-   for fission reactors   3500 appm He/ 10^{22} cm^{-2}

when the fluence of neutrons with energies E > 1 MeV is taken.

The most important irradiation effects in beryllium are swelling, embrittlement, and tritium production. Fig. 4.7.4.1 shows swelling data from the literature vs. fast neutron fluence. Most of the data refer to low temperature irradiation with swelling measured after annealing, the annealing temperature is indicated in Fig. 4.7.4.1 at the points. The lines correspond to model calculations given in [11] which are adjusted by changing one parameter to better agree with the measurements. In spite of the data scattering a large swelling at temperatures around 500 °C can be predicted for Demo fluence values.

Possibly the low temperature irradiation with post irradiation annealing gives a larger swelling than irradiation at high temperature. However, an evaluation of beryllium swelling data by Billone [12] which is primarily based on an EBR II irradiation experiment made at high temperature [13] comes to even higher swelling rates at 450 °C and above. New irradiation experiments with the best material presently available are urgently needed and are planned (see Section 5.2.2).

The situation is even more puzzling with respect to ductility. Irradiation at about 470 °C of cylindrical samples up to fast fluences of more than 10^{22} cm^{-2} in EBR II showed a residual

ductility of 14 % at temperatures of 450 °C and 550 °C and a plastic strain of 3 % at ambient temperature [13]. Earlier irradiations at different temperatures with annealing after the irradiation exhibit a large variability in the data with zero ductility in many cases for fluences of more than 10^{21} cm^{-2} (E > 1 MeV) [10]. Other measurements show for fast neutron fluences of 0.8 x 10^{21} cm^{-2} and for irradiation and annealing temperatures of 350 °C a residual elongation of 14 % [6]. This indicates that the data depend on the materials purity and processing parameters as well as the irradiation and test conditions.

Screening tests with irradiations to 1.5 x 10^{21} cm^{-2} (E > 1 MeV) at various temperatures are planned for the high purity fine grain size material now available (see Sect. 5.2.2).

Radiation hardening is observed in nearly all the irradiation experiments. It decreases for high fluences ($\phi\tau$ > 2 x 10^{22} cm^{-2}) and for higher temperature. At T $\approx$ 500 °C the values for the irradiated material nearly equal the values of the unirradiated one [2].

An important problem of beryllium in a fusion reactor blanket is also the tritium inventory. In the ^{9}Be (n, α) ^{6}He process ^{6}He is generated which immediately decays to ^{6}Li. In a next step tritium is generated by the ^{6}Li (n, α) T-reaction. For temperatures below 300 °C the tritium is completely trapped in the beryllium. It is partially released at about 400 °C but by far the largest fraction is released in a burst at 600 °C after an annealing time of a few hours [14]. A similar phenomenan was observed for the onset of swelling and the reduction in microhardness [16, 6] so that the migration of small helium bubbles may be the common cause for these three phenomena.

With beryllium in the blanket being always at temperatures below 600 °C a sudden tritium release under accident conditions should be envisaged, unless the new high purity fine grain material behaves better.

References

1. S.H. BUSH, "Irradiation Effects in Cladding and Structural Materials", American Society of Materials, Roman and Littlefield Inc., New York 1965.

2. M. KANGILASKI, "Radiation Effects Design Handbook, Section 7 Structural Alloys", NASA CR-1873, 1971.

3. J.M. BEESTON, "Properties of Irradiated Beryllium, Statistical Evaluation", TREE-1063 (1976).

4. J.B. RICH, G.B. REDDING and R.S. BARNES, "The Effects of Heating Neutron Irradiated Beryllium", Journ. Nucl. Mat. 1 (1959) 96.

5.   R. TROMP, "Swelling Threshold Temperature for Irradiated Beryllium", BNWL-128, (1965).

6.   G.P. WALTERS, "Effect of Neutron Irradiation on the Mechanical Properties of Hot Pressed and Extruded Beryllium". J. Less-Common Metals 11, 77 (1966).

7.   B.S. Hickman, G.T. Stevens, "The Effect of Neutron Irradiation of Beryllium Metal", AAEC/E-109 (1963).

8.   J.B. RICH, G.P. WALTERS, "The Mecahnical Properties of Beryllium Irradiated at 350 and 600 °C", The Metallurgy of Beryllium Chapman and Hall Ldt., London 1963.

9.   J.M BEESTON, "Gas Release and Compression Properties of Beryllium Irradiated at 600 and 750 °C", Effects of Radiation on Structural Metals, ASTM (1967) 135.

10.   J.B. RICH, G.P. WALTERS, R.S. BARNES, " The Mechanical Properties of Some Highly Irradiated Beryllium", J. Nucl. Mat. 4 (1961) 287.

11.   McCARVILLE et al., "Technical Issues for Beryllium Use in Fusion Blanket Applications", UCID-20319 (1985).

12.   M.C. BILLONE, R.G. MACAULAY-NEWCOMBE, "Design, Properties, and Testing of Beryllium Components for Breeder Blankets", Second Internat. Symposium on Fusion Nuclear Technology, Karlsruhe June 2 - 7 1991.

13.   J.M. BEESTON et al., "Comparison of Compression Properties and Swelling of Beryllium Irradiated at Various Temperatures", Journ Nucl. Mat. 122, 123 (1984) 802.

14.   D.L. BALDWIN, D.S. GELLES, and O.D. SLAGLE, "Tritium Release from Irradiated Beryllium at Elevated Temperatures", J. Nucl. Mat. 179 - 181 (1991) 329 - 334.
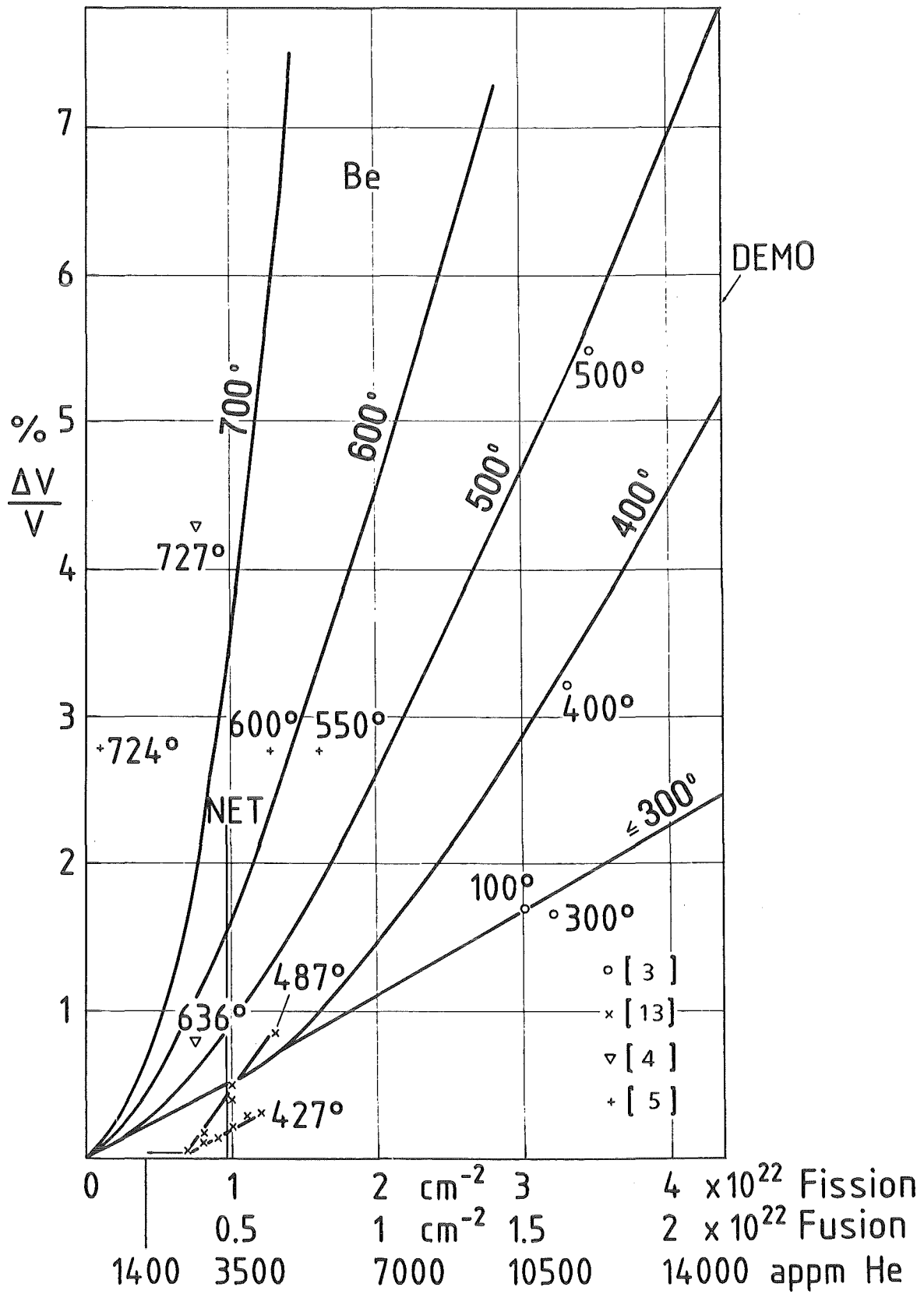
Fig. 4.7.4.1   Swelling of Beryllium vs. Fast (E > 1 MeV) Fluence

5. REQUIRED R. & D. PROGRAM PRIOR TO TESTS IN NET / ITER (M. Dalle Donne and M. Küchle)

The design and R. & D. work performed so far have shown that there is still a number of major technical issues to be solved. These may be divided in four parts:

a.   Design problems

b.   Material development and testing

c.   Non-nuclear tests of blanket components and blanket sections

d.   Nuclear tests of blanket-subsections.

The annual operation cost of ITER is presently estimated at about 300 M $/a. With the low availability expected, testing in NET / ITER will be very expensive and limited in scope. Moreover safety and reliability of NET should not, or only marginally be reduced by the incorporation of test blankets. Therefore an extensive blanket development and testing program has to be carried out prior to construction of the NET / ITER test modules.

Only the initial part of this program, running until 1994, has been specified up to now, for the rest not more than general ideas exist. The later part of the program will strongly depend on the concept which is selected for final development and testing.

5.1   Design Problems

Table 5.1 summarizes the work performed in 1989 - 91 and the proposed until 1994. This refers essentially to design modifications in view to improve the blanket reliability and, if necessary, to make the blanket more compliant with a large beryllium swelling. Detailed safety investigations have still to be performed for the Demo blanket and for the test modules. The development work for a computational system to calculate the Lorentz forces and stresses caused by disruptions in ferromagnetic structures (Manet) will continue until the end of 1994.

5.2   Material Development

The R & D relevant materials for the present solid breeder blanket are Li_4SiO_4, beryllium and Manet. With Manet development forming a separate part of the fusion R & D program, only the breeder material and beryllium will be discussed here.

In the area of material development the main issue will be the impact of long term irradiation effects on the material properties. Most of the material data measurements described

earlier in the paper (Sections 4.2 to 4.7)) have to be repeated with materials irradiated up to Demo relevant fluences.

5.2.1 Breeder material

The tritium release in-pile experiments at low burn-ups and the out-of-pile tests (mechanical, thermal cycle and heat transfer tests) performed so far show that the chosen reference solution of breeder material - Li_4SiO_4 pebbles in the diameter range 0.35 to 0.6 mm and fabricated by melting - does not present so far any feasibility problem. There is still work to be done on the effects of the presence of beryllium and Manet on the tritium release and some out-of-pile tests which will be discussed in the Section 5.4 (Non-Nuclear Tests), however the future work will be mainly concentrated on the effects of high burn-ups (Table 5.2). Of interest is the behaviour of the reference Li_4SiO_4 pebbles at high neutron fluences (10 at % total lithium burn-up, 22 dpa) in the temperature range 380 - 800 (900) °C and namely:

- mechanical stability

- tritium release and transport

- lithium transport

- thermal conductivity of the pebble bed

- compatibility with beryllium and with Manet.

In Manet and beryllium, helium, which is responsible for the material embrittlement, is generated in (n,α)-reactions which have a threshold at fairly high neutron energies. Therefore, here fusion reactor irradiations lead to much higher helium to dpa ratios than irradiations in a fission reactor. Thus fission reactors are not well suited for fusion reactor materials testing. This is not the case for breeder materials. In breeder materials helium is predominantly produced by the $^6Li(n,\alpha)$-reaction which has no threshold but a cross section which is increasing with decreasing neutron energy. The neutron fluxes in high perfomance fission reactors are also adequate for breeder materials testing.

In Table 5.5 quantities relevant to breeder material irradiations of a Demo reactor are compared with those of some fission reactors. The fission reactors are:

- a fast breeder (Phenix)

- a thermal reactor with the sample behind a cadmium screen (BR2)

- two thermal reactors without cadmium screen (OSIRIS, HFR).

Optimum irradiation positions were taken and quantities which characterize irradiation effects are given for Li_4SiO_4 and $LiAlO_2$. The material data used in Table 5.5 are compiled in Table 5.6. Definitions of the quantities of Table 5.5 and relations between them are given in Table 5.7. Lithium burn-up and neutron capture induced power density are not included in Table 5.5 but can easily be calculated with the formulas given in Table 5.7.

Displacements per atom are defined for monoatomic materials. In composite materials the recoil cascade will contain a sequence of collisions with atoms of different masses and a very large number of cascade possibilities exists. At KfK a simplified approach was used where only the primary knock-on processes were treated differently for the different atomic species and an effective mass was taken for all other collisions. [1]. A detailed model was developed by Alberman [2] and a benchmark calculation with a fission spectrum revealed that our model overestimates the neutron scattering induced damage rates by a factor of 1.54. This factor was used to adjust the KfK-calculations. As shown in Table 5.8 the ratio of the displacement rate $d_n = <\sigma_d>\phi_{tot}$ to the flux of neutrons with energies $E > 0.1$ MeV, ϕ (E > 0.1 MeV), is constant within 10 %. Therefore this ratio was adjusted, and the adjusted value was used to get backwards the new displacement data.

From the d_{tot}-values of Table 5.5 one can see that the thermal reactors create damage rates which are slightly lower than the Demo values, whereas the damage rates in Phenix are about a factor of 6 higher than those of Demo.

As shown in Table 5.2 two end-of-life irradiations are proposed by ECN-Petten and by CEA in the HFR and in the Phenix reactor respectively. Within the European collaboration both will contain samples of the KfK reference Li_4SiO_4 pebbles. In both reactors it is possible to achieve the objective burn up of 10 at %, however in the case of HFR the achieved fluence will be lower than the aimed one (5.8 against 22 dpa), while in Phenix it will be higher (39 dpa). Considering the preliminary work requirements, the irradiation in Phenix cannot be started before January 1994, so that the results of the post-irradiation-examinations will be available only at the end of 1995.

5.2.2 Beryllium

The design work for the Demo blanket has shown which are the problems related to the use of beryllium in the blanket. These are:

- swelling under irradiation

- embrittlement caused by irradiation

- tritium retention

- compatibility with Manet and Li_4SiO_4 pebbles

- behaviour of the interface between beryllium and cooling tubes under thermal cycling

As was pointed out in subsection 4.7.4 irradiation effects in beryllium were mostly determined on materials produced about 30 years ago. Most of the experiments were made on hot pressed blocks of relatively impure beryllium which had low ductility and anisotropic properties. Moreover the irradiations were mainly carried out at ambient temperature.

For the high purity more isotropic and ductile material now available a more favourable behaviour with respect to swelling and embrittlement can be expected. Therefore an extensive irradiation program with pre- and post test examinations is planned. The irradiations will be carried out at different temperature levels.

First short term irradiations up to a fluence of

$$\phi \, (E > 1 \text{ MeV}) \times t = 1.5 \times 10^{21}/\text{cm}^2$$

are foreseen to identify the impact of material purity and processing parameters on the properties. Quantities of primary interest are embrittlement and thermal conductivity, no swelling is expected at this dose level.

In Table 5.9 for the same reactors as taken in Table 5.5 the operation time is given to reach a fast neutron fluence of 1.5×10^{21} n/cm^2. This fluence was chosen to keep the irradiation time in thermal reactors acceptable even if the central position is not available.

At the same fast neutron fluence the helium produced in beryllium from (n, 2n)- and (α,n)-reactions is higher by about a factor of two in Demo than in fission reactors (Table 5.9). This is a consequence of the 14 MeV-contribution to the fusion reactor spectrum and the threshold of the (n, 2n) reaction which is around 2.5 MeV.

In order to verify the feasibility of blanket concepts which are using beryllium it is necessary to irradiate the material up to Demo end-of-life conditions. Blanket life time in Demo was specified to 20000 h or 2.28 FPY burn time. Table 5.9 shows the irradiation times needed in fission reactors to reach the same helium concentration (15000 appm He). These end-of-life irradiations have to be conducted in a fast reactor and Phenix is foreseen in the EC-program. Again extensive pre- and post test examinations are foreseen, including swelling and mechanical property determinations.

Table 5.3 shows the European beryllium program. The irradiation in the Phenix reactor covers the neutron effects expected in Demo, but not the complete range of temperatures (Table 5.10). This should be covered by the irradiation in the Siloe reactor, but at much lower neutron fluences. The proposed beryllium embrittlement irradiation covers the temperature range, but at much lower fluences than in the Demo blanket (Tables 5.3 and 5.10). It is

known that embrittlement occurs already at much lower fluences than swelling. These irradiations will also provide relevant information on the tritium retention in beryllium.

5.3   Non-nuclear Tests

In a fusion reactor the heat sources result from nuclear reactions and occur within the materials. This cannot be realistically simulated in non-nuclear tests. Moreover no tritium production and radiation damage effects occur in such tests. Nevertheless quite a number of important issues can be addressed in non-nuclear tests.

An attractive possibility for helium cooled solid breeder blankets consists in constructing a realistic mock-up of a blanket or blanket subunit, including the breeder material, and feeding the helium coolant system periodically with cold ($\approx$ 260 °C) or hot ($\approx$ 460 °C) helium. In this way the total structure will periodically be heated up and cooled down thereby simulating the thermal cycling effects of a Tokamak reactor. A possibility to technically realize the temperature changes is described in Section 4.5.1 for the HEBLO-loop.

If required, electrical surface heating could be added to better simulate the heat flow in the front part of the blanket.

The KfK design of a helium cooled ceramic breeder blanket has a large degree of modularization: Each segment is composed of 28 toroidally arranged canisters, each canister is subdivided by stiffening plates into subsections, each subsection containes a periodic structure of beryllium plates and slits filled with breeder material pebbles. Therefore testing of a subunit often is already characteristic for the whole system. The fairly complex geometrical arrangement makes fabricability tests important. The following sequence of developments is foreseen:

1.   Fabrication of canister subsections with cooled walls and characteristic structure.

2.   Thermal cycling tests with the canister subsection.

3.   Fabrication of a full canister filled with beryllium plates and ceramic breeder pebbles including helium coolant and purge flow system.

4.   Thermal cycling and other tests with the canister.

Thermal cycling is done by periodic variation of the coolant temperature.

Issues addressed by the subsection tests include:

-      investigation of the wall coolant connection

-      effective heat conductivity of the pebble bed

- local heat transfer coefficients and hot spot factors

- purge flow distribution and pressue drop

- local mass transfer (by simulation with pebbles made of sublimating material)

- hydrogen permeation into coolant

- effect of purge flow on lithium transport.

The full canister tests partly address the same issues but in addition they provide information on:

- blanket pressure drop

- flow distribution in the canister

- breeder / structure / multiplier thermal expansion interaction

- determination of fundamental frequency

- response to LOCA or other coolant transients

- response to structure failure, such as for instance, the break of an inner pressure tube.

With the HEBLO-loop canister subsection tests will be performed in the period 1992 - 1995. For the full size canister tests an existing helium loop will be used but details are not yet specified and the tests fall into the period after final solid breeder blanket concept selection.

Table 5.4 summarizes the non-nuclear tests performed and proposed in the period 1989 - 1995. Beside the HEBLO tests, also tests to measure the thermal conductivity and the wall heat transfer coefficient of a pebble bed in the test apparatus PEHTRA and thermal cycle tests of pebble beds in PETCY are being performed (Section 4.5.4 and 4.3.4).

Parallel to the thermal cycling tests fabricability tests of various components are being conducted (Section 4.5.2 and 4.5.3).

The helium coolant system is similar to what has been used for fission reactors and does not need special R & D work except for the thermal cycling operation which has to be tested.

5.4   Nuclear Tests

In principle it would be desirable to perform the tests mentioned under point 5.3 with nuclear heating also, so that a prototypic heat source distribution is obtained and the behaviour of tritium could be studied. However, inspection of the possibilities at existing research reactors revealed that this is not feasible.

The dimensions of NET / ITER are large compared to the radial thickness of the blanket region with a high neutron flux. Therefore the geometry could be simulated in experiments with a plane surface fast neutron source behind which a typical blanket structure is located. Such neutron sources only exist at the surface of research reactors, for instance at the pool side facility of the HFR-Petten. Unfortunately the fast neutron flux at this position is an order of magnitude below the value at the first wall of NET / ITER. Moreover the surface area available is by far too small to simulate the NET / ITER geometry.

In order to get prototypic neutron flux values one has to go right into the center of a reactor. Here the space is very limited, however. Thus, only a small subunit of a blanket structure can be used to study local geometry effects. In view of the high degree of modularization and periodicity of the structure such small size experiments are still quite valuable.

The minimum dimensions to represent the KfK solid breeder blanket configuration are: one 6 mm thick slab filled with breeder material pebbles, sandwiched between two beryllium plates which contain helium coolant tubes. The dimensions of the breeder material slab should be large compared to its thickness what means about 60 mm. A purge system with supply tubes at the ends of the slab should be provided.

The neutron flux, flux gradient, and neutron spectrum should be matched as closely as possible to the fusion reactor conditions, also the heat source should be simulated.

Practically only the thermal research reactors of the European Community are available for this type of experiments. But then the thermal neutron flux impinging on the test assembly has to be suppressed, otherwise the tritium production rate and the heat generation from the $^6Li(n, \alpha)$T-process would be by far too high when compared with other quantities (see Table 5.5 and 5.2). Therefore the test assembly has to be surrounded by cadmium.

A research reactor in which a large central loop and a test position covered by cadmium already exists, is the BR2. Therefore this reactor was taken for a first feasibility assessment. Only some neutronics calculations have been performed, a detailed engineering design does not yet exist.

Fig. 5.1 shows a horizontal cut throught the central region of the BR2 with the test loop and the blanket structure to be investigated. The dimensions of the test object are tentatively specified to 57 x 57 x 300 mm, located symmetric to the core midplane. In Table 5.11 are compiled some characteristic data of this test together with those of Demo, ITER, and the BR2 central position without the special test loop. The data are rough values and should only be used for a first orientation.

The loop reduces the neutron fluxes by about a factor of two, but because of the moderating effect of beryllium and of the water to cool the pressure tube the tritium production rate remains practically constant and is larger than the ITER value. The beryllium (n, 2n)-

reaction, which is responsible for the neutron source distribution in the vicinity of the breeder material, is much lower in the test section than in ITER. Gamma-heating probably will be higher in the test section than in ITER, but it has not yet been calculated.

In spite of the uncertainties and differences to ITER it can be concluded that the conditions are quite acceptable to get important informations on the nuclear behaviour of the blanket. Issues which could be addressed by such tests include:

- tritium release and transport by the purge flow system,

- tritium permeation to the coolant,

- lithium transport,

- beryllium / ceramic / steel compatibility under irradiation.

Similar or slightly degraded test conditions can be obtained in the core center of OSIRIS or HFR, provided that a cadmium covered loop can be tolerated there. With the expectation that no fundamental non-feasibility problem will be revealed by the nuclear tests they are postponed - mainly for economic reasons - to well behind the year 1994.

5.5 Conclusions

The essential tests to judge the feasibility of the Demo blanket, namely high burn-up irradiations of breeder material and beryllium and non-nuclear tests on blanket subsections, will be terminated in 1995. Only at this stage it will be possible to make a founded choice between the two European solid breeder blankets. This date was already foreseen in the program proposition to the FTSC in 1989. After 1995 more expensive tests will be necessary, namely out-of-pile canister or segment tests in already available large helium loops, and nuclear tests of blanket subunits in fission reactors. This would allow sufficient time for the design and construction of the test modules to be irradiated in NET/ITER in the foreseen time (2005 - 2010).

References

1.   U. FISCHER, M. KÜCHLE, "Ceramic Breeder Material Irradiation Test Requirements and Possibilities" KfK 4065 (1986)

2.   A. ALBERMAN personal communication, CEA Saclay, (1990)

Table 5.1   R & D program prior to tests in NET / ITER. Design

Activity / Milestones		1989	1990	1991	1992	1993	1994
1.	**Design**						
1.1	Demo blanket conceptual design						
	- Basic design	▽─────────────		▽ ▼			
	- Modification due to results of investigations				────────────		▽
1.2	Test module and relative ancillary loop conceptual design						
	- Basic design		──── ▼				
	- Modifications due to results of investigations				────────		▽
1.3	DEMO blanket safety investigations			────────	▽		
1.4	Design of He temp. and flow control for test module coolant loop				────	▽	
1.5	Safety investigations for test module and its ancillary loops				────	▽	
1.6	Definition of large scale tests and design of large helium loop for Non-Nuclear Tests					────	▽
1.7	Development of a computational system to calculate Lorentz forces and stresses caused by disruptions:						
	- For non-ferromagnetic structures (316LSS)-ELSA	────────		▼			
	- For ferromagnetic structures (MANET)-CARMA		────────────────────				▽

Milestones: ▽ planned   ▼ achieved

Table 5.2   R & D program prior to tests in NET / ITER. Breeder material

Activity / Milestones		1989	1990	1991	1992	1993	1994	1995
2.	**Breeder Material**							
2.1	Choice of reference Li_4SiO_4 pebbles		▼					
2.2	Reproducibility of tritium release results for reference Li_4SiO_4 pebbles		▼					
2.3	Further improvements of the Li_4SiO_4 pebbles							▽
2.4	Effects of beryllium and Manet presence on tritium release				▽			
2.5	Determination of released HTO / HT ratio				▽			
2.6	Effects of high burn-up: - EXOTIC 7 irradiation (ECN, Petten) - Phenix irradiation (CEA)						▽	▽

Milestones:

▽   planned

▼   achieved

Table 5.3   R & D program prior to tests in NET / ITER. Beryllium

Activity / Milestones	1989	1990	1991	1992	1993	1994	1995
3. Beryllium							
3.1 Theoretical investigations to model the swelling, embrittlement and tritium trapping of irradiated beryllium (KfK)							▽
3.2 Beryllium swelling irradiations (CEA) — in Siloe reactor (Begonia) — in Phenix reactor				▽			▽
3.3 Beryllium embrittlement irradiation (BR2 reactor)						▽	
3.4 Beryllium compatibility with ceramic and structural materials: — out-of-pile /CES, KfK — in-pile (Sibelius, CEA)			▽ ▽				

Milestones:

▽ planned   ▼ achieved

Table 5.4 R & D program prior to tests in NET / ITER. Non nuclear tests.

Activity / Milestones	1989	1990	1991	1992	1993	1994	1995
4. Non-Nuclear Tests							
4.1 "HEBLO" loop for test canister subsections:							
- Construction			▽				
- Operation							▽
- Fabrication of test sections			▽				
4.2 Pebble bed heat transfer rig (PEHTRA):							
- Tests on reference pebble bed			▼			▽	
- Tests on mixed Be-Li$_4$SiO$_4$ pebble bed			▽				
4.3 Pebble bed thermal cycle rig (PETCY):							
- Tests on reference pebble bed				▽			
- Tests on mixed Be-Li$_4$SiO$_4$ pebble bed						▽	

Milestones:

▽ planned

▼ achieved

Table 5.5   Breeder Material Irradiation Data

Reactor position		Demo peak	Phenix core center	BR2 cent. Cd-Loop	OSIRIS central	HFR 5 E5
Φ_{tot}	$n/cm^2 s$	1.04×10^{15}	6.5×10^{15}	9.83×10^{14}	7.92×10^{14}	6.94×10^{14}
$\phi(E > 0.1 MeV)$	$n/cm^2 s$	6.43×10^{14}	4.62×10^{15}	5.27×10^{14}	3.90×10^{14}	3.25×10^{14}
$\phi(E > 1 Mev)$	$n/cm^2 s$	3.04×10^{14}	1.29×10^{15}	2.30×10^{14}	2.07×10^{14}	1.72×10^{14}
Φ_{th}	$n/cm^2 s$	2.76×10^{8}	1.5×10^{2}	1.04×10^{8}	5.7×10^{13}	7.08×10^{13}
$< \sigma_{n,a} >$	$10^{-24} cm^2$	1.606	0.906	10.46	60.43	104.1
$< \sigma_d >$	$10^{-24} cm^2$	255	291	220	202	192
Li4SiO4 d_n	10^{-7} dpa/s	2.65	18.94	2.16	1.60	1.33
d_{a+T}	10^{-7} dpa/s	0.45 *	0.13	0.23	1.07	1.61
$d_{tot} = d_n + d_{a+T}$	10^{-7} dpa/s	3.10	19.07	2.39	2.67	2.94
TPR	$10^{13} /cm^3 s$	7.22 *	2.12	3.7	17.2	26.0
He / dpa	appm / dpa	2519	104	1585	9971	18071
$< \sigma_d >$	$10^{-24} cm^2$	341	390	294	270	257
d_n	10^{-7} dpa /s	3.55	25.4	2.89	2.14	1.78
LiAlO2 d_{a+T}	10^{-7} dpa /s	0.29 *	0.086	0.15	0.70	1.06
$d_{tot} = d_n + d_{a+T}$	10^{-7} dpa / s	3.84	25.5	3.04	2.84	2.84
TPR	$10^{13} /cm^3 s$	3.59 *	1.05	1.84	8.57	12.94
He / dpa	appm / dpa	1060	43.6	667	4197	7600

* = 90 % $^6Li/Li$, 7.5 % $^6Li/Li$ else

Table 5.6   Breeder Material Data used to Calculate Irradiation Effects

	Quantity	units	Li_4SiO_4	$LiAlO_2$
ρ	density (theoretical)	g/cm^3	2.39	2.615
M	molecular weight	g/mol	119.84	65.92
N_{Li}	lithium atomic density	$atoms / cm^3$	4.802×10^{22}	2.388×10^{22}
N_6	^6Li atomic density (7.5 %)	$atoms / cm^3$	3.60×10^{21}	1.791×10^{21}
N	atomic density	$atoms / cm^3$	1.0805×10^{23}	9.552×10^{22}
	N_6/N		3.333×10^{-2}	1.875×10^{-2}
ND	displacements per $^6Li(n,\alpha)$- reaction (material const.)		67	78

$$
\left.\begin{matrix} N \\ N_{Li} \\ N_6 \end{matrix}\right\} = \frac{6.02 \times 10^{23}}{M} \times \rho \quad \left\{\begin{matrix} \text{number of atoms per molecule} \\ \text{number of Li-atoms per molecule} \\ \text{number of } ^6Li\text{-atoms per molecule} \end{matrix}\right.
$$

Table 5.7 Definitions and Equations to Characterize Breeder Material Irradiation Effects

1. Displacement Rate from Neutron Scattering

$$d_n = \frac{\int_0^\infty \sigma_d(E)\,\phi(E)\,dE}{\int_0^\infty \phi(E)\,dE} \quad [\,dpa/s\,] \tag{1}$$

$\sigma_d(E)$ = displacement cross section [cm^2]

$< \sigma_d >$ = average displacement cross section

$$d_n = <\sigma_d> \times \phi_{tot} \qquad \phi_{tot} = \int_0^\infty \phi(E)\,dE \tag{2}$$

$< \sigma_d >$ is spectrum dependent

$$d_n = <\sigma_d^*> \times \phi_f \qquad \phi_f = \phi(E > 0.1\ MeV) \tag{3}$$

$$\phi_f = \phi(E > 0.1\ MeV) = \int_{0.1\ MeV}^\infty \phi(E)\,dE$$

$< \sigma_d^* >$ is only weakly spectrum dependent,
often assumed constant

2. $^6Li(n, \alpha)T$-process induced displacement rate

$$d_{\alpha+T} = N_D \times \frac{N_6}{N} <\sigma_{n,\alpha}> \phi_{tot} \left| dpa/s \right| \tag{4}$$

with

N_D, N_6, N from Table 5.6

$$\langle \sigma_{n,a} \rangle = \frac{\int_0^\infty \sigma_{n,a}(E)\,\phi(E)\,dE}{\int_0^\infty \phi(E)\,dE} \quad \left[cm^2 \right] \tag{5}$$

3. Tritium Production Rate (TPR)

$$TPR = N_6 \, \langle \sigma_{n,a} \rangle \, \phi_{tot} \quad \left[cm^{-3}\,s^{-1} \right] \tag{6}$$

4. Helium-to-dpa-Ratio He/dpa

$$\frac{He}{dpa} = \frac{N_6 \, \langle \sigma_{n,a} \rangle}{N \, \langle \sigma_d \rangle} \, x\,10^6 \qquad \left(\frac{appm\ He}{dpa} \right) \tag{7}$$

5. ^{6}Li Burn-up (BU)

$$BU = \frac{N_6(0) - N_6(t)}{N_6(0)} = 1 - e^{-\langle \sigma_{n,a} \rangle \, \phi_{tot} \, x \, t} \tag{8}$$

$N_6(t)$ = N_6 at the time t (sec) after start of irradiation

5a.   Li-Burnup

$$\frac{N_{Li}(0) - N_{Li}(t)}{N_{Li}(t)} = \frac{N_6(0)}{N_{Li}(0)} \times (1 - e^{-<\sigma_{n,\alpha}> \phi_{tot} \times t}) \tag{9}$$

6.   Power Density due to the 6Li(n, α)T-reaction

$$p = 7.68 \times 10^{-13} \times TPR \times \frac{\rho}{\rho_{th}} \quad \left| W/cm^3 \right| \tag{10}$$

Table 5.8 Adjustment of the Displacement Data to an Improved Model of Calculation

Part A: Procedure

The adjustment procedure is based on the observation that $\phi(E > 0.1$ MeV) is a good measure for the displacement rate d_n. Therefore the procedure goes as follows:

1. divide $< \sigma_d >$ by ϕ (E > 0.1 MeV) / ϕ_{tot} to form $< \sigma_d^* >$ which is nearly the same for all reactors,

2. take the average of $< \sigma_d^* >$ from the different reactors to get $< \sigma_d^* >_{av}$,

3. form

$$\frac{< \sigma_d^* > \text{Alberman}}{< \sigma_d^* > K/K} \; x < \sigma_d^* >_{av}$$

4. multiply this by ϕ (E > 0.1 MeV) for the different reactors to get $(d_n)_{corr}$

5. divide $(d_n)_{corr}$ by ϕ_{tot} to get $< \sigma_d >_{corr}$.

Table 5.8   Adjustment of the Displacement Data to an Improved Model of Calculation

Part B Numerical Data

1. Li_4SiO_4

reactor	$<\sigma_d>$ 10^{-24} cm^2	$<\sigma_d^*>$ cm^2	$(d_n)_{corr}$ dpa /s	$<\sigma_d>_{corr}$ cm^2
Demo	365.6	588 x 10^{-24}	4.35 x 10^{-7}	255 x 10^{-24}
Phenix	432.2	608 x 10^{-24}	18.94 x 10^{-7}	291 x 10^{-24}
BR2	353.5	658 x 10^{-24}	2.16 x 10^{-7}	202 x 10^{-24}
OSIRIS	330.3	672 x 10^{-24}	1.60 x 10^{-7}	202 x 10^{-24}
average		631.5 x 10^{-24}		
fission spectr.	KfK	685 x 10^{-24}		
	Alberman	447 x 10^{-24}		

2. $LiAlO_2$

reactor	$<\sigma_d>$ 10^{-24} cm^2	$<\sigma_d^*>$ cm^2	$(d_n)_{corr}$ dpa /s	$<\sigma_d>_{corr}$ cm^2
Demo	494.4	795 x 10^{-24}	5.82 x 10^{-7}	341 x 10^{-24}
Phenix	566.2	796 x 10^{-24}	25.4 x 10^{-7}	390 x 10^{-24}
BR2	472.7	880 x 10^{-24}	2.89 x 10^{-7}	294 x 10^{-24}
OSIRIS	445.3	905 x 10^{-24}	2.14 x 10^{-7}	270 x 10^{-24}
average		844 x 10^{-24}		
fission spectr.	KfK	942 x 10^{-24}		
	Alberman	610 x 10^{-24}		

Table 5.9   Beryllium Irradiation

reactor		Demo	Phenix	BR2	OSIRIS	HFR
position		peak	core cent.	centr. loop	central	E5
ϕ_{tot}	n /cm^2 s	1.04 x 10^{15}	6.5 x 10^{15}	9.83 x 10^{14}	7.92 x 10^{14}	6.94 x 10^{14}
ϕ (E > 0.1 MeV)	n /cm^2 s	6.43 x 10^{14}	4.62 x 10^{15}	5.27 x 10^{14}	3.90 x 10^{14}	3.25 x 10^{14}
ϕ (E > 1MeV)	n /cm^2 s	3.04 x 10^{14}	1.29 x 10^{15}	2.30 x 10^{14}	2.07 x 10^{14}	1.72 x 10^{14}
t	FPD	57	13.4	75	84	101
He/ϕt	appm He	994	588	560	552	516
t_{EOL}	FPY	2.28	0.91	5.4	6.4	7.8

t = irradiation time to reach a fast (E > 1 MeV) neutron fluence of 1.5 x 10^{21} n/cm^2

He/ϕt = appm He in Be when the fast fluence is ϕ = 1.5 x 10^{21} n/cm^2

t_{EOL} = irradiation time to reach Demo end-of-life He-concentration (14500 appm He)

Table 5.10   Beryllium irradiations: temperatures and fluences

	Temp range °C	Peak fluence (E > 1 MeV)	Peak fluence (dpa)	He content (appm)
Demo blanket	250 - 600	2.2×10^{22}	30 - 60	15000
Be-swelling irr.: - Siloe - Phenix	250 - 700 400 - 550	$\approx 2.2 \times 10^{21}$ $\approx 4 \times 10^{22}$	3 60	≈ 800 ≈ 15700
Be-embrittlement irr.: (BR2)	200 - 600	1.5×10^{21}	-	≈ 600
Be-compatibility	450 - 550	0.55×10^{21}	0.7	≈ 200

Table 5.11

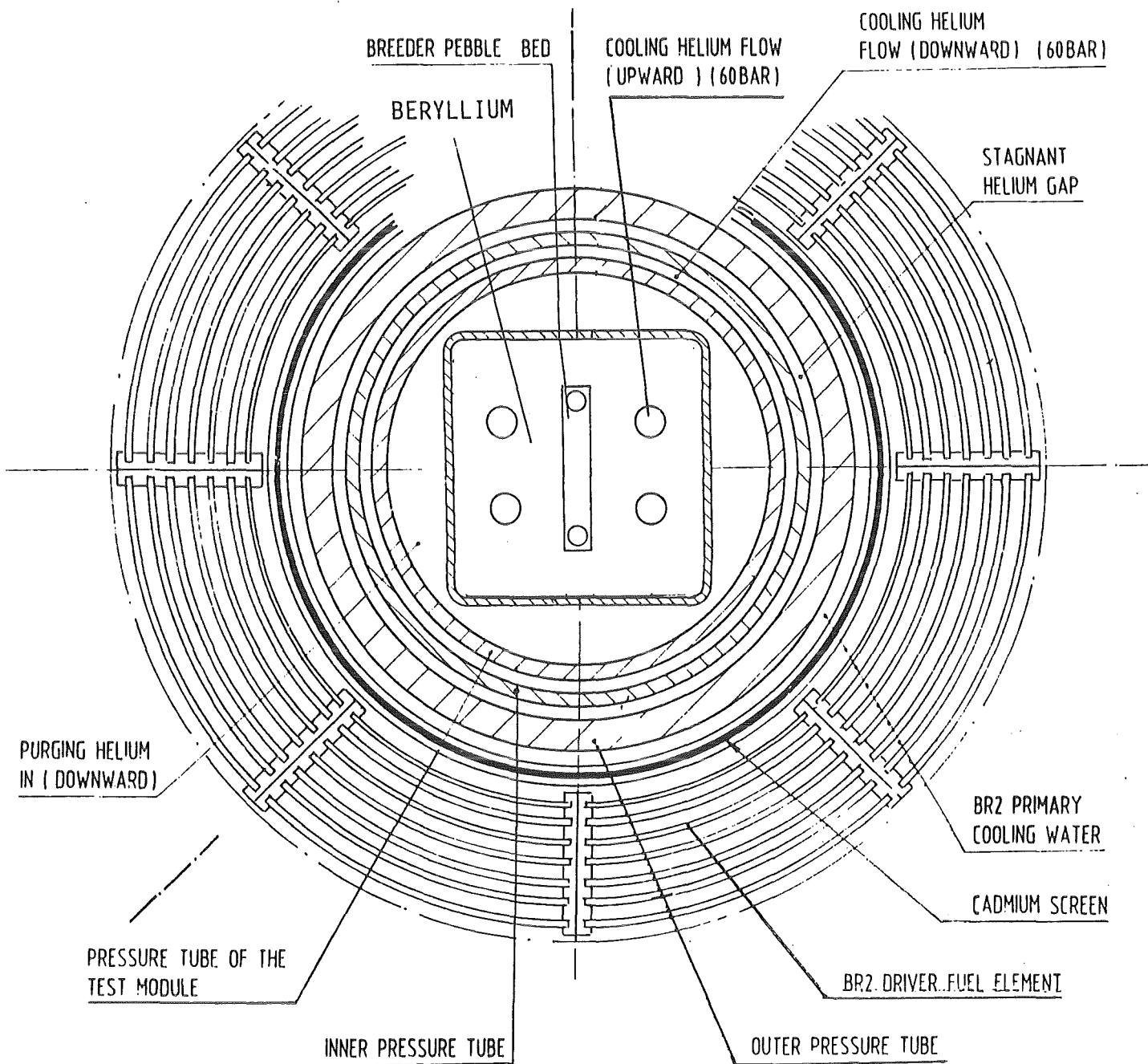|	Demo	ITER	BR2	BR2 Test	
ϕ_{tot}	1.04×10^{15}	3.78×10^{14}	9.83×10^{14}	5.87×10^{14}	$n / cm^2 s$
$\phi(E > 0.1\,MeV)$	6.43×10^{14}	2.34×10^{14}	5.27×10^{14}	2.74×10^{14}	$n / cm^2 s$
TPR ($\rho = 0.6\,\rho_{th}$)	4.33×10^{13}	1.57×10^{13}	2.2×10^{13}	2.2×10^{13}	$cm^{-3} s^{-1}$
Be (n, 2n)	1.54×10^{13}	5.60×10^{12}	3.97×10^{12}	1.9×10^{12}	$cm^{-3} s^{-1}$
$\phi (E > 1\,MeV)$	3.04×10^{14}	1.11×10^{14}	2.3×10^{14}	1.1×10^{14}	$n / cm^2 s$

SECTIONAL VIEW AT REACTOR MID-PLANE

Fig. 5.1 Cross section of Nuclear Test in BR2

6. TEST PROGRAM IN NET / ITER (M. Dalle Donne and M. Küchle)

6.1 Introduction

NET/ITER offers the unique possiblity to test simultaneously all aspects of a DEMO relevant blanket concept in the real geometrical configuration, with the real magnetic field, and with an incident neutron flux having the real neutron spectrum and spatial distribution. The main differences to DEMO are the lower wall load (1.0 MW/m^2 instead of 2.2 MW/m^2), and the shorter burn time, or lower fluence.

In spite of the lower power density the average temperature in the blanket can be adjusted to DEMO values by flow reduction. However, the local temperature distribution and temperature gradients in the materials will be different. Anyway, the most important use of NET/ITER is the comparison of the actual test object performance in NET/ITER with calculated predictions and to make code validations. Here testing in NET/ITER is only the last step of a design validation process which includes the R. and D. program described in Chapters 4 and 5.

Testing in NET/ITER will be extremly expensive and, because of the limited amount of tritium available for NET/ITER operation, also will be strongly limited in scope. Therefore it was tried to specify a test program which is sufficiently detailed to confirm the viability of the blanket concept for Demo and allows some blanket variations and modifications to be tested, but on the other hand keeps the NET/ITER burn time requirements sufficiently low.

In order to arrive at such a compromise the following procedure was adopted: First the critical issues of the blanket concept were identified. Then for the issues relevant to testing in NET/ITER the time constants to reach equilibrium conditions in NET/ITER-tests were estimated. From these the duration of a single test and the required mode of NET/ITER operation were deduced. Finally a test program was formulated and the total burn time to conduct the program was estimated.

6.2 Critical Issues of the B.O.T. Helium Cooled Solid Breeder Blanket

The subject of critical issues was discussed in the Finesse Study and in several ITER workshops. This will not be repeated here, only a list is given which may contain some arbitrary distinctions. Under critical issues we understand both, those which have an impact on the concept feasibility and those which refer to details of a particular design. For the KfK solid breeder blanket concept (see Chapter 5)these include:

1. Beryllium swelling and embrittlement

2. Response of the structure to plasma disruptions

3. Breeder material behaviour at high burn-up (mechanical integrity, thermal conductivity, tritium release)

4. Tritium inventory, tritium permeation and losses to the steam circuit,

5. Behaviour of the mechanical structure with welds and brazed connections under cyclic loads and with a volumetric heat source

5a. The same as 5. but with irradiated material

6. Temperature and flow distribution

7. Tritium self-sufficiency

8. Failure modes and reliability

9. Behaviour under abnormal coolant conditions

Points 1 and 3 do not only refer to material property data but also to the behaviour of the material in the blanket configuration. Thus, all the points are subject to testing in NET/ITER. Points 1, 3, 5a and 8 cannot be adequately covered in NET because of too low fluence and need extrapolation. Only a limited amount of abnormal operation conditions testing will be possible in NET/ITER. Post irradiation testing up to destruction may be needed in some cases.

6.3 Time to Reach Equilibrium Conditions

Important parameters which determine the minimum duration time of a test are the time constants to reach equilibrium conditions in the test object for temperature and tritium distribution after a step in power production.

An assessment of these time constants was made in the framework of two ITER workshops, and a general agreement was achieved on the values. They are based on a neutron wall load at the test blanket position of 1.2 MW/m^2 what corresponds to an average neutron wall load of 0.8 MW/m^2. In particular, the design of the test module for the KfK solid breeder blanket (see Chapter 3) has allowed to estimate the time constants of the various components and thus assess the requirements given by the testing of the test modules in the NET / ITER machine, Table 6.1 shows these requirements. The following text is essentially an explanation of this Table.

Time to reach thermal equilibrium

When nominal coolant flow conditions are imposed on the test blanket already from the beginning of power production, it takes a long time to reach thermal equilibrium in the

breeder material. To reduce this time it is necessary to heat up the blanket nearly adiabatically. This requires that the temperature and the flow of the helium coolant is controlled at the blanket inlet in the initial phase of the burn time and during the off-burn time. This procedure causes an increase of the thermal time constant during off-burn time and allows to have twice as long off-burn times ($\approx$ 1000 s). Of course this implies the presence of an external helium heating system. A redistribution of the temperature profiles and gradients will occur before the normal operation conditions are achieved.

This periodic inversion of the temperature gradients and the not well known temperature distribution makes, at least for some tests, the operation with constant nominal coolant flow conditions preferable. In this case the off-burn times should be shorter ($\approx$ 500 s).

The heat-up times depend on the power density and geometrical arrangement. For the B.O.T. concept with Li_4SiO_4 and nearly adiabatic heat-up t = 100 s are obtained for the blanket front part and t = 300 s for the back part. Thus, thermal equilibrium can well be obtained in one cycle of 1000 s burn time duration.

Time to reach tritium inventory equilibrium

The tritium inventory equilibrium is reached exponentially with the time constant τ (= tritium residence time) where τ is strongly temperature dependent. For Li_4SiO_4 and the KfK-design the residence time is rather short: In 1000 s burn time one already gets 50 % of the equilibrium tritium inventory. This is sufficient to verify the tritium inventory and release calculations, which therefore can be checked by a single shot. A much longer operation time is needed to reach equilibrium conditions in the tritium processing units and in the tritium permeation losses to the coolant. The time to reach equilibrium tritium inventory in the whole blanket is about 10 h while equilibrium tritium permeation to the coolant is about one day, for the purge gas system it is 6 h. Equilibrium in the tritium extraction system is reached in 2 h.

With equilibrium tritium losses to the coolant and well established tritium balance being important conditions for the tests one day of operation prior to the test will be needed.

6.4 Single Test Duration

Initially and each time when a new or modified test module is inserted, functional (shake-down) tests will be made to identify mistakes in the design, errors in component fabrication, and other effects leading to early failure or malfunction. For these tests it is not necessary to reach tritium equilibrium, thermal equilibrium is sufficient, thus a test duration of about 10 h appears appropriate. The possibility to measure tritium release over a certain

period of time and sufficient operation time to roughly calibrate and measure the most important quantities are required. For these tests a duration of 20 h burn time is specified as minimum requirement. Tests in which only the temperature and flow distribution are determined and some mechanical tests can also be conducted in 20 h. This time should be available in the form of continuous operation with back-to-back cycles.

The tests which are used for code validation and performance assessment should be 3 to 5 days long and need tritium equilibrium. With a duty cycle (burn time / (burn time + off-burn time)) of about 70 % this corresponds to 50 h and 80 h burn time, respectivly. A typical test sequence could be:

Instrumentation and data
acquisition check out,
power balance control,
calibration etc.   1-2 days

time to reach equilibrium
conditions   1 day

test duration   1-2 days
                                                                          _____
total   3-5 days

In principle it is also possible to calculate and compare a non-equilibrium situation but the interpretation in case of differences would be questionalbe and the accuracy would be limited. Observation over a few days of steady operation is desirable to assure that equilibrium and proper functioning is achieved. Moreover operational conditions may slightly be varied within one test.

The time should be available as continuous operation time with back to back cycles. When NET operation is interrupted and the blanket temperature decreases to below 100 °C, tritium distribution is frozen in and after machine restart tritium migration starts from this distribution. Interruptions of more than one day may lead to chemical modifications which make the interpretation of the measurements difficult. Interruptions of a week or longer make a continuation of the test impossible. Therefore it is specified that some interruptions of up to one day duration can be tolerated.

6.5 Mode of NET Operation Required for the Tests

The minimum duration of the burn time and the maximum duration of the off-burn time are dictated by the need to have a sufficiently high duty cycle. This is needed to keep the average breeder material temperature high enough for adequate tritium release. Even when inlet coolant temperature and flow control is foreseen the temperature distribution at off-burn time is different form the one with burning plasma. To get acceptable conditions also for the back row a minimum burn duration of 1000 s is needed. The off-burn time should be as short as reasonably achievable but not longer than 1000 s. This leads to a duty cycle of about 50%. During the later stages of the test program an off-burn time of 500 s and thus a duty cycle of 70 % would be preferable, because it would allow to operate without coolant flow reductions during off-burn periods and thus it would simulate better the temperature distributions and variations of the Demo blanket.

6.6 A NET Testing Program Scenario

A test programme for solid breeder blanket tests in NET was elaborated and with the test duration estimates mentioned above the burn time requirement for NET was calculated. The data are summarized in Table 6.2 and the following text explains essentially this table.

Blanket testing in NET does not mean to put a fully developed blanket module in a port and to study its behaviour. On the contrary, the test programme is the most important part of the blanket development process which serves to decide between design options, although only one solid breeder blanket concept will be tested.

The programme is subdivided into three steps of increasing risk and DEMO relevance which are implemented in sequence and in the following are called generations:

A   Test module with austenitic steel behind the NET first wall

B   Test module with austenitic steel with its own first wall

C   Test module with the martensitic steel Manet with its own first wall

In each generation functional tests of one day duration are foreseen which are followed by real measurements. Depending on the test objective these tests may last 3 days or 5 days. It is assumed that a few modifications will be tested to select the best one. Depending on the test objective, modules with different instrumentation and possibly also different design details will be required. Moreover the outcome of the test will lead to design changes so that some iterations are needed. By multiplication of the number of modifications, the number of test objectives and the number of design iterations the number of tests per type are deduced.

The realization of the tests is done in so-called test campaignes where - because of the two ports available for the solid breeder blanket concept - two tests are being conducted in parallel. The required burn time is deduced from the number and duration of the test campaignes.

In this programme no submodule tests are foreseen. It is not clear whether the large number of supply tubes with remote handling connections can be installed in the port. Moreover the solid breeder blanket module consists of subunits (canisters) which could be designed or instrumented differently. In difference to real submodules they all will have the same coolant inlet temperature what is a slight disadvantage.

From all the module tests the best design solution will be selected and a complete NET segment of this type will be constructed. With this segment longer duration tests will be made to accumulate experience, to have some failure statistics, and to study irradiation effects. The segment will be made of Manet with its own first wall as a box design similar to what is foreseen for DEMO. The segment should remain in place as long as possible and is subject to repeated careful measurements. Here 20 measurement campaignes of three days duration each are foreseen what leads to a test burn time of about 1000 h.

If only one port is available for the solid breeder blanket concept (ITER case) the number of tests is equal to the number of test campaignes and the integral burn time for the port test would be doubled. The number of positions in which test segments can be inserted is not so much limited. Therefore more positions can be taken when more concepts have to be investigated and the segment test time will remain unchanged.

The test program as summarized in Table 6.2 containes some margins. For instance, the number of modifications could be smaller since they will successively be ruled out. On the other hand experience shows that early tests of a new kind or with a new facility are often of poor quality and need repetition or modification, the learning period is quite significant. In addition test will be lost due to malfunction or interruption of the machine operation. Thus, the burn time requirement as deduced from Table 6.2 is not excessive but rather modest.

With this overall frame given, a more detailed test program could be formulated. However, in view of the lead time of more than 15 years and the many open questions - such as NET driver blanket and total burn time available - this was considered as premature. The general tendency of the test program should be to select as fast as is reasonably achievable the final blanket solution and to leave a segment of the selected blanket in NET / ITER as long as possible in order to gain operational experience and to accumulate radiation dose.

An irradiation of 7000 h instead of 1000 h would make the test much more Demo relevant. Demo mid-life conditions could be achieved with respect to embrittlement and stress relaxation, however the regime of onset of swelling will not be reached.

Table 6.1   Minimum requirements posed on NET / ITER operation by the testing of the BOT-HCSBB module

---

Time to reach:

	100 s in blanket front
- steady state temp. in the breeder *	
	300 s in blanket back

- fraction of steady state tritium inventory (tritum release) in the breeder*	50 % with 1000 s burn time shot length
	67 % with 3000 s burn time shot length

- equilibrium tritium permeation to the coolant	≈ 1 day
- steady state in purge flow and tritium extraction system	≈ 6 hours + test.

Duration of continuous operation

- during early technology phase*: 10 to 20 hours (duty cycle ≈ 50 %)
- at the end of the technology phase: 5 days (duty cycle ≈ 70 %)

Recommended cycle parameters during continuous operation*:

- burn time shot length   ≥ 1000 s
- duty cycle **   ≥ 50 %
- off burn time   ≤ 1000 s

---

* Coolant flow and inlet coolant temperature control during off-burn-time
** Duty cycle = (burn time / (burn time + off-burn time)) average

Table 6.2   Solid Breeder Blanket Testing Scenario

generation*	A			B			C			port tests total	segment
test duration	1d	3d	5d	1d	3d	5d	1d	3d	5d		3d
burn time	20h	50h	80h	20h	50h	80h	20h	50h	80h		50h
modifications	2	2	2	2	2	2	4	2	2		
objectives	1-2	1-2	1	1-2	2	1	1-2	2	1		
iterations	2	2	1	2	1	1	2	2	1		
tests	4-8	4-8	2	4-8	4	2	8-16	8	2	48	20
campaignes	2-4	2-4	1	2-4	2	1	4-8	4	1	24	20
integral burn time	60	150	80 290	60	100	80 240	120	200	80 400	930	1000

*A = test module with austenitic steel behind NET first wall

  B = test module with austenitic steel with own first wall

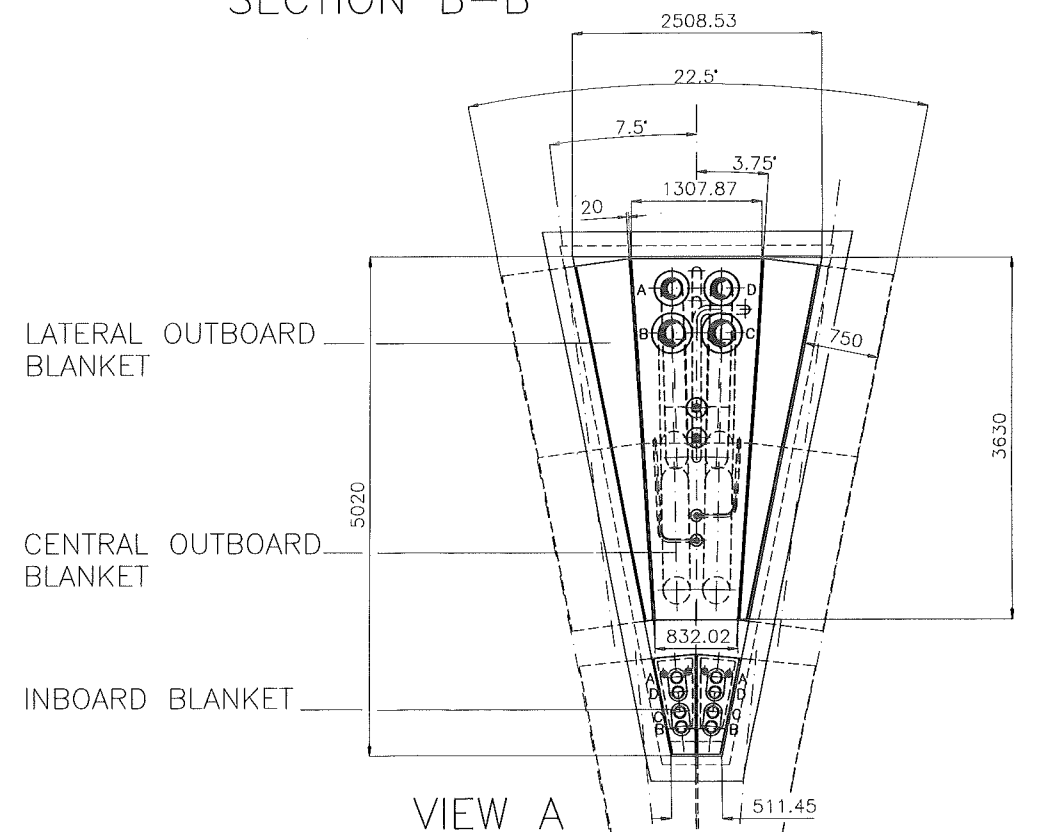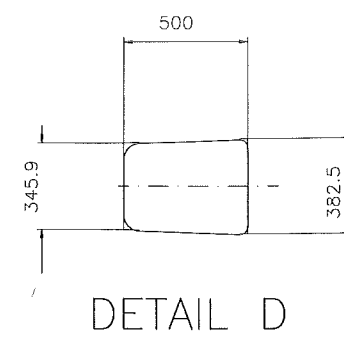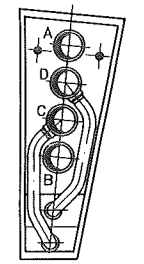 C = test module with martensitic steel with own first wall
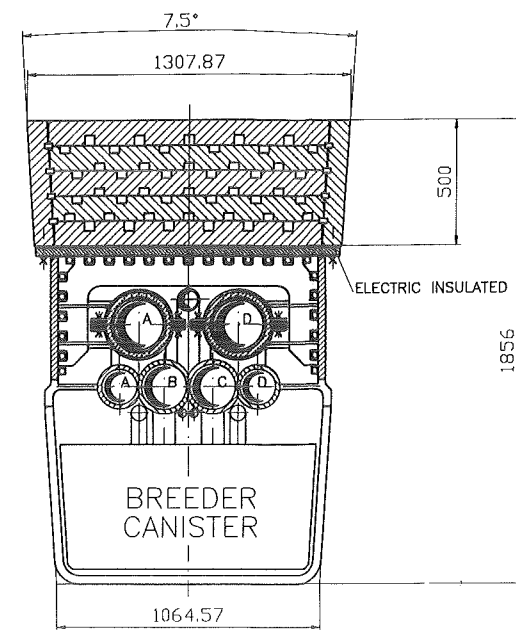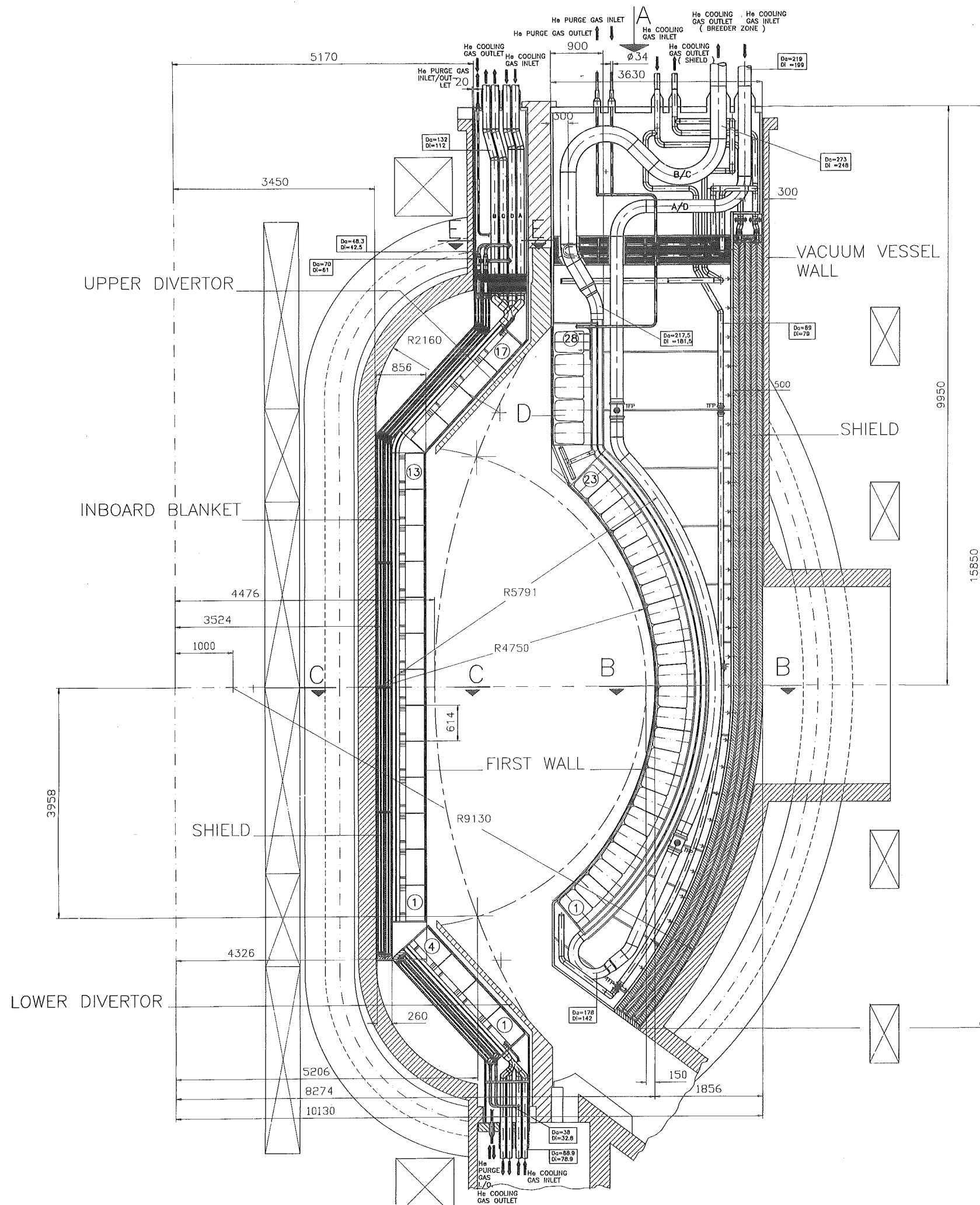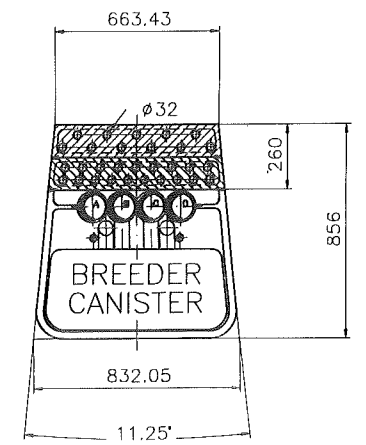
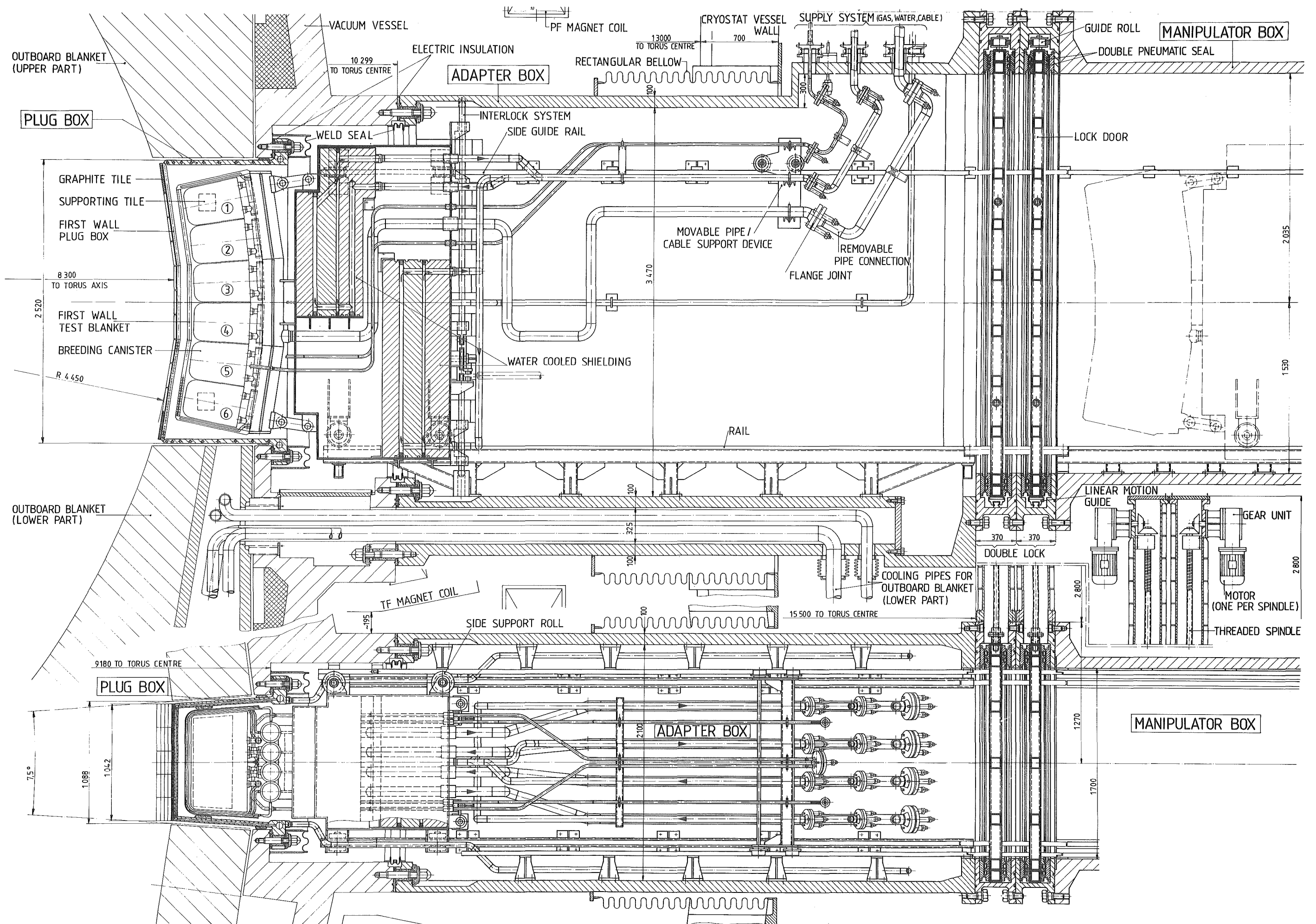Fig. 2.1.1 Vertical cross section of the Demo blanket (dimensions in mm).

Fig. 3.1.1 Vertical (upper picture) and horizontal (lower picture) cross section of the test module placed behind the first wall in a horizontal port of the outboard region. The figure shows also the shield. Test module and shield are shown also inside the manipulator box (dotted lines) in the position used for transportation to the hot cells (dimensions in millimeters).